Dublin City University
School of Electronic Engineering

For the Degree of Doctor of Philosophy

White Matter Volume Assessment in Premature Infants on MRI at Term - Computer Aided Volume Analysis

by

Michèle PÉPORTÉ

Supervisor: Prof. Paul F. WHELAN

February 2014

I hereby certify that this material, which I now submit for assessment on the programme of study leading to the award of Doctor of Philosophy is entirely my own work, that I have exercised reasonable care to ensure that the work is original, and does not to the best of my knowledge breach any law of copyright, and has not been taken from the work of others save and to the extent that such work has been cited and acknowledged within the text of my work.

Signed: __________ (Candidate)

ID No.: 57114340

Date: __________

Acknowledgements

First of all, I would like to thank Professor Paul F. Whelan for giving me the opportunity to work on this research project and for his support and guidance during my PhD study.

I would also like to express my gratitude to Dr. Dana E. Ilea for sharing her expertise and research insights which helped me tremendously in directing the course of my work.

I wish to thank many current and former colleagues from DCU and from the Center for Image Processing and Analysis (CIPA). It has been a pleasure discussing and sharing different experiences with them.

I would like to extend my thanks to the Temple Street Children Hospital, Dublin for supporting financially my research program. Special thanks go to Dr. Eilish Twomey for useful discussions and her assistance with medical topics.

Finally, I am grateful to my family for their permanent encouragement and support during this research journey.

Contents

1 Introduction **1**

1.1 Motivation 1

1.2 Objectives of this research 5

    1.2.1 Challenges 5

    1.2.2 Contributions 9

1.3 Overview of the proposed approach 11

1.4 Overview of the thesis 12

2 Literature Review **14**

2.1 Surface-Based Segmentation 15

2.2 Template- and Atlas-Based Segmentation 18

2.3 Intensity-Based Segmentation 22

    2.3.1 Fuzzy Clustering 24

    2.3.2 Probabilistic-Based Segmentation 25

2.4 Brain Segmentation Software 28

2.5 Conclusions 30

3 Brain Extraction **33**

3.1 Introduction 33

3.2 Overview 38

3.3 Data Pre-Processing 38

    3.3.1 Coherence Enhancing Diffusion Filter 40

    3.3.2 Intensity Standardisation 44

3.4 Mask Extraction 47

3.5 Region of Interest Segmentation 49

3.6 Post-Processing 52

    3.6.1 Refinement of the outer contours 52

    3.6.2 Lacrimal glands removal 54

3.7 Experiments and Results 55

    3.7.1 Evaluation Indices 58

3.7.2 Numerical Evaluation 59
3.8 Conclusions 60

4 Bias Field Correction **62**
4.1 Introduction 62
4.2 Overview 66
4.3 Data Pre-Segmentation 67
4.4 Intensity Maps 70
4.5 Low Pass Filter 71
4.6 Experiments and Results 75
4.6.1 Comparison to other algorithms 78
4.7 Conclusions 81

5 White Matter Segmentation **83**
5.1 Overview 84
5.2 Data Pre-Processing 85
5.3 Expectation-Maximization Segmentation 87
5.4 White Matter Pre-Segmentation 91
5.5 Cerebellum and Deep Grey Matter Detection 95
5.5.1 Extraction of the Deep Grey Matter surrounding the ventricles . 97
5.5.2 Detection of the Cerebellum 104
5.5.3 Locate the Middle Section of the Deep Grey Matter 108
5.6 Re-classification of the PVE and Diffused Contours 111

6 Evaluation **116**
6.1 1.5 Tesla Infant Data 116
6.2 Experiments 118
6.2.1 Evaluation Techniques 118
6.2.2 Numerical Evaluation 119
6.2.3 Discussion 125
6.3 3 Tesla Infant Data 132
6.3.1 Evaluation 133
6.3.2 Discussion 136

7 Conclusions and Future Work **139**
7.1 Contributions and Conclusions 139
7.2 Future Work 143

A State-of-the-Art Brain Extraction Comparison Methods **I**
A.1 Comparison Methods I
A.1.1 Brain Surface Extraction II

A.1.2 Brain Extraction Tool II
A.1.3 SPM8 III
A.2 Results III

List of Figures

1.1 A T2-weighted brain MR image of a two year old child, including the layout of the different brain regions. 2
1.2 T2 brain MR images of children at the age of approximately two years which suffer from cerebral palsy. It can be observed that the reduced brain tissue is replaced with cerebrospinal fluid. 3
1.3 Left: A MR brain image from a premature infant at the age of a few weeks; Right: A MR brain image of a child at the age of approximately two years. 4
1.4 Left: An original T2 brain MR image of a premature infant. Right: The same image where the contours of the white matter region are marked in red. The objective of this study is to automatically detect and measure the white matter volume. 4
1.5 On the left are the histograms of the corresponding images on their right. The top row shows an example of an MR image from an infant at term; the second row illustrate an image of the same child at the age of one year; the third row displays an image of the same child at the age of 2 years. The histograms reveal that the intensity distribution changes over time and the more structured the brain tissue is, the stronger is the differentiation between GM and WM. 6
1.6 The left example displays a bias field corrupted image in which the intensity values vary throughout the image. The three infant brain images illustrate shape and structure differences between patients. A more common dissimilarity in infant brain MRI data is the enlarged ventricles, which are the bright areas in the middle of the brain tissue. This is caused by stress during the premature birth but does not necessarily indicate ill health of the infant. 7
1.7 Differences in the deep grey matter between an adult (left) and infant (right) brain MR image. The contours of this region are marked in red. 8

1.8 Three contiguous images of a patient in which some of the partial volume voxels are marked with red arrows. The partial volume effects are related to the structure of the brain and they raise a challenge for the white matter segmentation algorithm. 9
1.9 An outline of the proposed approach. The brain extraction algorithm is underlined in green, the bias field correction algorithm is outlined in orange and the white matter segmentation is marked in purple. 12

3.1 An overview of the skull stripping algorithm. 39
3.2 Two images of the same patient. In the left image the intensity is manually adjusted, while the intensity of the right image has not been adjusted. 40
3.3 The left image shows an example of the original MR image, the other images are results after applying the CED filter using different diffusion parameters; second image: t=1; third image: t=10. 42
3.4 A representation of the intensity distributions after the application of the coherence enhancing diffusion filter using different diffusion times. . . 42
3.5 Left image shows an example of the original MR image, the other images are the results after applying the CED filter using different diffusion parameters; second image: t=1; third image: t=5; fourth image: t=10. . . 43
3.6 Results of the coherence enhancing diffusion using different diffusion times. The coloured lines represent the intensity values in the x-direction of the region marked in Figure 3.5, and the black line describes the changes in intensity values on the original image. The larger the diffusion time value is set, the stronger the image is smoothed with the risk of loosing information. 43
3.7 Left: a sample and its associated histogram before applying the intensity adjustment; the resulting image after the intensity adjustment was applied. The local maximum is expected to represent the grey matter tissue, which is set to the middle of the entire intensity range. 45
3.8 Improvements in the calculation of the brain tissue volume by comparing the results of the first and the second histogram analysis. The blue line presents the results of the first histogram analysis. The red line describes the outcome of the second histogram analysis which is smoother and more precise because the calculation of each image relies on the results obtained in the previous processed image in the volume. 46
3.9 Images detailing each mask step, starting with the original image, followed by the first mask, second mask and the final mask. The small bright part visible in the third image is a leftover of the lacrimal glands. 49

3.10 Overview of each step of the brain tissue segmentation using a region growing algorithm. 49
3.11 The histogram of one brain MR image illustrates the threshold results of the K-Means algorithm when it was used with different number of clusters. The focus lies on the threshold between the brain tissue and non-brain tissue (background and CSF). The black arrows indicate that if a larger number of clusters is used then the region of the brain tissue is larger. The green regions highlight the intensity values which are classified as background or CSF. 51
3.12 In this graph the threshold values of the Kapur, Otsu and K-means are shown. 53
3.13 An example of an image to illustrate the results before (A) and after (B) processing the inner edges of the brain. It can be observed that the brighter contour pixels in (A), which represent fluid pixels, have been removed in (B). 54
3.14 Overview of the algorithm which removes the lacrimal glands. 54
3.15 An example presenting results before (A) and after (B) the removal of the lacrimal glands. 55
3.16 A brain extraction result which indicates the presence of hairline shape cuts. These regions are outlined with red arrows. 56
3.17 Similarity Measurements of the brain extraction algorithm using Dice Similarity Metric. 59
3.18 False positive and false negative measurements. 60

4.1 Two examples from different patients that illustrate the intensity changes across the brain tissue. These intensity inhomogeneities have a severe effect on the segmentation outcome. 62
4.2 The overview of the bias field correction technique. 66
4.3 An overview of the Otsu decision tree that applies the Otsu algorithm three times. 69
4.4 Results obtained after applying the multiple Otsu algorithm. (Left) The technique was applied on the entire image. (Right) The result of the algorithm which was applied individually on small segments of the image. The red area represents class GM, and the dark blue illustrates the WM class. The partial volumes are represented in bright blue and yellow regions. The right image is an example of the final segmentation obtained by the multiple Otsu technique. The dark blue area represents an estimation of the white matter region and the grey matter is displayed in brighter blue. 70

4.5 Left: The intensity map computed from the grey matter region; Middle: The intensity map computed of the white matter region; Right: The combination of the two intensity maps. 71
4.6 Left image is an example of the calculated bias field, the middle image is the original image and the right image is an example after correcting the bias field variations. 73
4.7 The first row presents the results of the ILPF, the second row the GLPF and the third row the BLPF. In the first column D_0 was set to 0.5% of the image width, in the second column D_0 was set to 1% of the image width and in the right column the D_0 was set to 5% of the image width. 74
4.8 Two histogram examples where each presents the intensity distribution after using the BLPF and GLPF. 75
4.9 The top left image is the original image with the corresponding histogram at the right side; the bottom left image is the output after applying the bias field correction algorithm with its corresponding histogram at the right side. 76
4.10 Examples showing the intensity values in selected areas of the white matter before and after the bias field correction. Their corresponding histograms illustrate the intensity values in the selected regions. 77
4.11 Results of the bias field correction algorithm. The top images are the original images, whereas the bottom images are the corrected images. . 78
4.12 Examples showing the results obtained by the bias field correction algorithm called LEMS proposed by Salvado et al. The top images are the original images, whereas the bottom images are the corrected images. . 79
4.13 Some examples of the bias field correction algorithm proposed by Ahmed et al. The top images are the original images, whereas the bottom images are the corrected images. The last column is the result when the bias correction was applied to the middle column with the difference that in the first two columns the skull stripping process had been performed. 80
4.14 The intensity distribution obtained after bias field correction. The blue line presents the intensity distribution of the proposed method, whereas the red line is the result of the Fuzzy C-Means method, and the green line presents the results of the histogram-based technique. 81

5.1 An overview of the probabilistic segmentation technique for white matter segmentation. 84
5.2 Overview of the pre-processing steps. 85

5.3 Representation of the coordinates of the head in three dimensions. The example on the left presents an axial view, the middle image illustrates a sagital view and the right image shows a coronal view. The arrows indicate the coordinate system. 85

5.4 Three examples of sagital images taken from different patients. The top sample is from the first patient upon which all the other patients' datasets are adjusted to, whereas the examples below are sagital images from a patient in which the head position is estimated and then adjusted. 87

5.5 An outline of the EM process. 89

5.6 Combined final results are shown when the EM is used with different number of classes. Left: original image after bias field correction was applied. Magnified region from original image (A). The other images present results using (B): four classes; (C): eight classes; (D): ten classes; (E): twelve classes. 90

5.7 Expectation-Maximization results; Left: EM result based on the histogram analysis images; Middle: EM results based on the contrast enhancement images; Right: The result after combining both EM results. . . . 91

5.8 Overview of the pre-segmentation steps. 91

5.9 The steps required to extract the preliminary white matter mask. Top row, left: The pre-processed original image, middle: The result of the Otsu classification and right: The first white matter mask. Bottom row, left: The outer grey matter contour, middle: the result of the Canny edge detection and right: the preliminary white matter mask. 94

5.10 Top row illustrates a brain image of a two-year-old child where the brain structure has developed. The right side shows a magnified image of the deep grey matter. The bottom row introduces an infant brain image where the deep grey matter region has been magnified. In both examples the deep grey matter has been outlined by surrounding the region with a red line. 95

5.11 The deep grey matter is marked with a red arrow in each image. The green arrows identify the cerebellum and the yellow arrow indicates the brain stem. 96

5.12 A sagital brain image detailing the deep grey matter and the cerebellum, which is marked with a green line. The region is divided into three parts; the first part (1) represents the cerebellum connected to the brain stem, the second part (2) can include some end parts of the cerebellum, brain stem and deep grey matter and the third part (3) is the deep grey matter. The separation between the first and second part is defined when the size of the brain stem is the smallest and the third part is separated from the second step when the largest distance between ventricles can be measured. 97

5.13 The deep grey matter and its features. Left: sagital view of the deep grey matter. Right: the deep grey matter in the axial view taken from the location marked with a yellow line in the sagital image. 98

5.14 Overview of the steps needed to locate and extract the last part of the deep grey matter. 99

5.15 This illustration presents three examples of the four feature points (tl, tr, bl, br) which are identified in each image which contains the ventricles. The point between the four feature points is the centre point (C_0). . . . 100

5.16 An example that illustrates the angles needed for the estimation of a missing top left ventricle feature point. In the two graphs, the ventricles of two contiguous images are outlined in red. The left graph indicates the top ventricle points in the previous image (highlighted in green), whereas the right graph shows the points in the current image where the top left point is missing and needs to be estimated. 100

5.17 Two examples taken from different patients where the ventricle feature points have been located. Each located position is marked in a different colour including the centre of all four detected points. 101

5.18 An example that illustrates the radius of the small ellipse (r_s) and the distances (d_1 and d_2) which are added to the radius to form the large ellipse. 102

5.19 The left image is the original image which was pre-processed using the brain extraction algorithm and has the bias field corrected. The right image is the result showing the detection of deep grey matter (the detected area is marked in darker grey). 104

5.20 Overview of the cerebellum detection process. 104

5.21 Left: An image in the sagital view. Right: The image in the coronal perspective of the same patient. In both images the two extrema are displayed in yellow and the region of the cerebellum is outlined in green. 105

5.22 Two examples of images that are analysed during the localisation of the initial cerebellum image. The yellow points mark the extrema feature points of the cerebellum volume and the green points illustrate the extrema of the cerebellum in the current image. The left image displays the cerebellum at the beginning of the sequence; the right image illustrates the cerebellum at a later stage in the sequence where the cerebrum starts to connect to the cerebellum, which can be observed at the bottom of the image. 106
5.23 Each row presents an example of the cerebellum extraction; the left image displays the original pre-processed image; the middle image shows the extraction of the features and the right image presents the projection of the spline function results (in green) and the ellipse results (in red) onto the pre-processed image. 107
5.24 Magnified images describing the three steps of the cerebellum and deep grey matter detection. The first and the last images of the second step are presented, in which the RoI is outlined in green. From the first image the ellipse has been projected onto the last image, which illustrates the differences and the changes of the ellipse throughout the second step. . 108
5.25 Each column presents an example of the deep grey matter extraction; the top row displays the original pre-processed images, and the bottom row shows the pre-processed images, on which the interpolated ellipse (marked in red) and the corrected ellipse (marked in yellow) are projected on. If the interpolated ellipse does not need to be corrected, no corrected ellipse will appear as shown in the right bottom image. 110
5.26 Overview of the final step for white matter segmentation. 111
5.27 Image obtained after the Otsu algorithm is applied. This image is divided into six regions. 113
5.28 An example that illustrates the three scenarios for changes in the gp values. The lower the gp value the lower the contrast. The middle column presents magnified regions taken of the two images on the left and the right column illustrates the Otsu classification of these magnified regions. 114

6.1 Images from two different sequences of the same patient; Image A is a T2-weighted MR image; Image B is a T1-weighted MR image. 117
6.2 Accuracy of the white matter extraction algorithm using Dice Similarity Metric, plus the Dice Metric calculated for the entire system. 119
6.3 False positive and false negative rates obtained by the proposed white matter segmentation algorithm. 120

6.4 Two MR images of different patients are illustrated. For each image a smaller section is magnified to illustrate the differences between the manual (marked in green) and automatic (marked in red) segmentation results. Due to blurred areas, it can be observed that the automatic segmentation includes white matter and excludes grey matter where the manually annotated images show less precision in the separation of the white matter from the grey matter tissue. 121

6.5 Two images which illustrate the differences between the manually marked data (outlined in green) and the automatically segmented data (shown in red). 122

6.6 White matter volume measurements for control and preterm infant data; in blue are marked the preterm data measurements (86 patients); the red points illustrate the results for control datasets (12 patients). 123

6.7 White matter segmentation results for term-born infants. 125

6.8 Examples of the automatic segmentation results. 126

6.9 Examples of segmentation results where the red marking indicates the outer white matter contour identified by the proposed algorithm, and the green line represents the outer contour of the manually annotated data. Due to unclear intensity values, the images show differences between the two markings where the tissue could belong to the grey matter or the white matter. These regions are pointed out with yellow arrows. 127

6.10 White matter segmentation results obtained from infant brain data which present low contrast. The top row displays the original images and the bottom row shows the segmentation results. 128

6.11 White matter segmentation results obtained from infant brain data, which include large differences in brain structure and shape. 129

6.12 Three examples of preterm infant brain MR images in which the brain ventricles show atypical structures and dissimilarities. In the left image, the ventricles differ slightly from each other, whereas the image in the middle displays larger deviations between left and right ventricles. In the middle example, the under-segmentation can be observed, which is caused by the deep grey matter detection. The right image illustrates extremely enlarged ventricles which severely reduce the brain tissue volume. For this patient, the white matter segmentation failed. 130

6.13 Four magnified examples of different segmentation results, which show that the regions surrounded by the gyri are precisely extracted. 131

6.14 White matter segmentation results when applied to brain MRI for infants born at term. 132

6.15 White matter segmentation results using 3T infant brain MRI data. . . . 133

6.16 White matter segmentation results when the white matter segmentation method was applied to 3T infant brain MRI data provided by the Image Sciences Institute. Each row presents images of a different patient. . . . 137
6.17 Four magnified examples of different segmentation results performed on 3T datasets, which illustrate that the regions surrounded by the gyri are precisely extracted. 138

A.1 Results obtained for all brain extraction tools. Image (A) presents the original image, which is followed by the brain segmentation results BET2 (B), BSE (C), BET (D), SPM (E) and the outcome of the proposed approach (F). V

List of Tables

2.1 List of the available brain segmentation software developed for adult data (accessed 27/06/2013). 31

3.1 Images obtained after the skull stripping algorithm is applied. Each box represents a different patient, in which the left columns represent the automatic results and the right columns illustrate the corresponding manually segmented images. 57

6.1 Summary of the MRI data used in the experimental evaluation. 117
6.2 White matter segmentation results for preterm infant data. 124
6.3 Average white matter segmentation results for all algorithms that participate in the NeoBrainS12 challenge. The algorithms which are indicated by the Asterisk have used additional data provided by the NeoBrainS12 challenge. 135

A.1 Quantitative performance evaluation for four state-of-the-art implementations. Best results are highlighted in bold IV
A.2 Average values obtained for the entire database. V

List of Abbreviations

AAM - Active Appearance Model

AGMM - Adaptive Gaussian Mixture Model [133]

ASM - Active Shape Model

BCFCM - Bias Corrected Fuzzy C-Means

BEA - Brain Extraction Algorithm

BET - Brain Extraction Tool by Smith et al. [113]

BLPF - Butterworth Low Pass Filter

BP - Belief Propagation

BSE - Brain Surface Extractor by Shattuck et al. [109]

CED - Coherence-Enhancing Diffusion Filter by Weickert et al. [127] [128]

CP - Cerebral Palsy

CSF - Cerebrospinal Fluid

DBM - Deformation-Based Morphometry [6]

DSM - Dice Similarity Metric

DTI - Diffusion Tensor Images

EM - Expectation-Maximization algorithm

FCM - Fuzzy C-Means algorithm

FFD - Free-Form Deformation [100]

FLAIR - Fluid Attentuation Inversion Recovery

FN - False Negative

FP	- False Positive
GM	- Grey Matter
GMM	- Gaussian Mixture Modeling
HMRF	- Hidden Markov Random Field
HUM	- Homomorphic Unsharp Masking
JS	- Jaccard Similarity
kNN	- k-Nearest Neighbour [22]
LEMS	- Local Entropy Minimization with a spline model
LPF	- Low Pass Filter
MAC	- Magnetic Active Contour
MAP	- Maximum a Posterior
ML	- Maximum Likelihood
MP-RAGE	- Magnetic Prepared Rapid Gradient Echo [70] [36]
MR	- Magnetic Resonance
MRF	- Markov Random Field
MRI	- Magnetic Resonance Image
NIfTI	- Neuroimaging Informatics Technology Initiative
PVE	- Partial Volume Effect
rbHMM	- region-based hidden Markov Model
RoI	- Region of Interest
SPM2	- Statistical Parametric Mapping v.2 by Ashburner and Friston [8]
VBM	- Voxel-Based Morphometry [8] [6]
WM	- White Matter
WSEG	- Watershed approach by Merisaari et al. [89]

White Matter Volume Assessment in Premature Infants on MRI at Term - Computer Aided Volume Analysis

Michèle Péporté

Abstract

The objective of this study is the development of an automatic segmentation framework for measuring volume changes in the white matter tissue from premature infant MRI data. The early stage of the brain development presents several major computational challenges such as structure and shape variations between patients. Furthermore, a high water content is present in the brain tissue, that leads to inconsistencies and overlapping intensity values across different brain structures. Another problem lies in low-frequency multiplicative intensity variations, which arises from an inhomogeneous magnetic field during the MRI acquisition. Finally, the segmentation is influenced by the partial volume effects which describe voxels that are generated by more than one tissue type.

To overcome these challenges, this study is divided into three parts with the intention to locally segment the white matter tissue without the guidance of an atlas. Firstly, a novel brain extraction method is proposed with the aim to remove all non-brain tissue. The data quality can be improved by noise reduction using an anisotropic diffusion filter and intensity variations adjustments throughout the volume. In order to minimise the influence of missing contours and overlapping intensity values between brain and non-brain tissue, a brain mask is created and applied during the extraction of the brain tissue. Secondly, the low-frequency intensity inhomogeneities are addressed by calculating the bias field which can be separated and corrected using low pass filtering. Finally, the segmentation process is performed by combining probabilistic clustering with classification algorithms. In order to achieve the final segmentation, the algorithm starts with a pre-segmentation procedure which was applied to reduce the intensity inhomogeneities within the white matter tissue. The key element in the segmentation process is the classification of diffused and missing contours as well as the partial volume voxels by performing a voxel reclassification scheme. The white matter segmentation framework was tested using the Dice Similarity Metric, and the numerical evaluation demonstrated precise segmentation results.

Publications Resulting from this Research

Michèle Péporté, Dana E. Ilea, Eilish Twomey, and Paul F. Whelan. A Hybrid Approach to Brain Extraction from Premature Infant MRI, *Scandinavian Conference on Image Analysis (SCIA 2011), Lecture Notes in Computer Science (LNCS)*, Ystad, Sweden, 6688:719-730, 2011.

Michèle Péporté, Dana E. Ilea, Eilish Twomey, and Paul F. Whelan. A Morphological Approach for Infant Brain Segmentation in MRI Data, *Irish Machine Vision and Image Processing Conference (IMVIP 2011), IEEE*, Dublin, Ireland, 125-126, 2011.

Michèle Péporté, Dana E. Ilea, Eilish Twomey, and Paul F. Whelan. White Matter Segmentation of Brain MRI During Infancy, *BioPhotonics and Imaging Conference (BioPIC 2013)*, Dublin, Ireland, 2013.

Internal Presentations

Michèle Péporté, Dana E. Ilea, Eilish Twomey, and Paul F. Whelan. A Hybrid Approach to Brain Extraction from Premature Infant MRI, *Faculty Research Day, Dublin City University*, 2011. (Poster)

Michèle Péporté, Dana E. Ilea, Eilish Twomey, and Paul F. Whelan. White Matter Volume Assessment in MRI Data of Premature Infants, *Annual Rince Research Day*, 2012. (Presentation)

Michèle Péporté, Dana E. Ilea, Eilish Twomey, and Paul F. Whelan. White Matter Segmentation of Brain MRI during Infancy, *Faculty Research Day, Dublin City University*, 2012. (Poster)

Michèle Péporté, Dana E. Ilea, Eilish Twomey, and Paul F. Whelan. White Matter Segmentation of Brain MRI During Infancy, *Annual Rince Research Day*, 2013. (Poster) **(Awarded with the 1st Prize for Best Poster)**

Chapter 1

Introduction

This chapter introduces the motivation for the Magnetic Resonance Imaging (MRI) brain segmentation on premature infants. The difficulties and the fundamental challenges associated with the MRI segmentation task are discussed as minor and major contributions which have arisen during this research work. This chapter is finalised by describing the structure of this thesis.

1.1 Motivation

The main focus of this research work lies on the automatic segmentation and measurement of specific regions from infant brain Magnetic Resonance (MR) images. By analysing the resulting measurements, clinical experts are aiming to achieve an early diagnosis of neurodevelopment impairment with the focus on Cerebral Palsy (CP). An early intervention can benefit the children during their development and increase their state of life. However, the early identification of the infants who are at a high risk to develop a neurodevelopment impairment is a great challenge for clinicians. Harnsberger et al. [58] provides a useful insight into the development of the newborn brain MRI and the undergoing changes in the brain structure during the first years.

In the majority of cases, the neurodevelopment disability occurs in preterm infants. Marlow et al. [84] stated that approximately 40% of premature infants develop a neurodevelopment impairment such as cognitive, neurological or behavioural disabilities and that the underlying problems of cerebral abnormalities such as minor motor disability or attention deficit remain unclear. The earlier the infants are born prematurely, the higher the possibility that a neurodevelopment impairment occurs. Woodward et al. [130] stated that 5-15% of the premature infants develop cerebral palsy. The physical deficit condition called cerebral palsy was first described by William Little in 1843 and was defined by Bax et al. [18] as follow:

> *"Cerebral palsy (CP) describes a group of disorders of the development of movement and posture, causing activity limitation, that are attributed to non-progressive disturbances that occurred in the developing fetal or infant brain. The motor disorders of cerebral palsy are often accompanied by disturbances of sensation, cognition, communication, perception, and/or behaviour, and/or by a seizure disorder"*

One way for an early prognosis of the neurodevelopment impairment is the analysis of Magnetic Resonance Imaging (MRI). Several studies [61] [96] have revealed that neurodevelopment disabilities of preterm infants are caused by abnormalities in the white matter and grey matter regions. Figure 1.1 introduces a T2-weighted MR image[1] of a two year old healthy child. At this stage the brain regions are fully developed and visually distinguishable, which would not be the case for a few weeks old infants. In Figure 1.1 it can be observed that all white or very bright parts represent the cerebrospinal fluid (CSF) in the brain, the darkest grey regions define the white matter and the middle range grey level regions include the grey matter. The brain is surrounded by skull and fat.

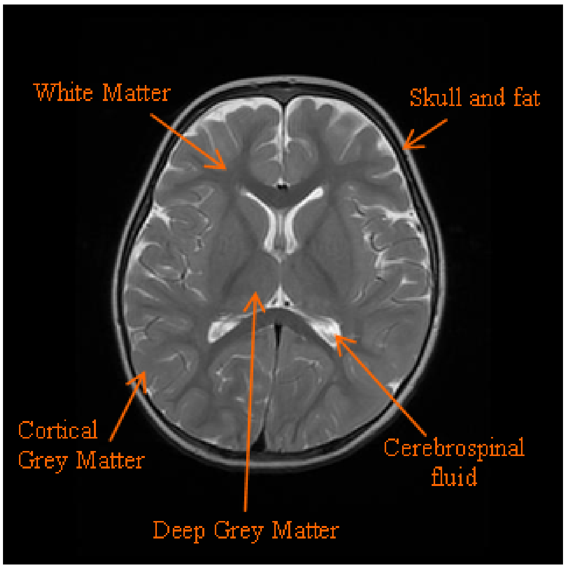

Figure 1.1: A T2-weighted brain MR image of a two year old child, including the layout of the different brain regions.

In the case of a developed cerebral palsy, this impairment can be visualised at the age of 24 months. Figure 1.2 displays T2-weighted brain MRIs of two children at approximately two years who suffer from cerebral palsy. It can be observed that the reduced brain tissue is replaced with CSF.

---

[1] T2-weighted MR images is one type of sequence which can be obtained by an MRI scanner. In T2-weighted MR images, the fluid is presented in high intensity values and fat is presented in low intensity values.

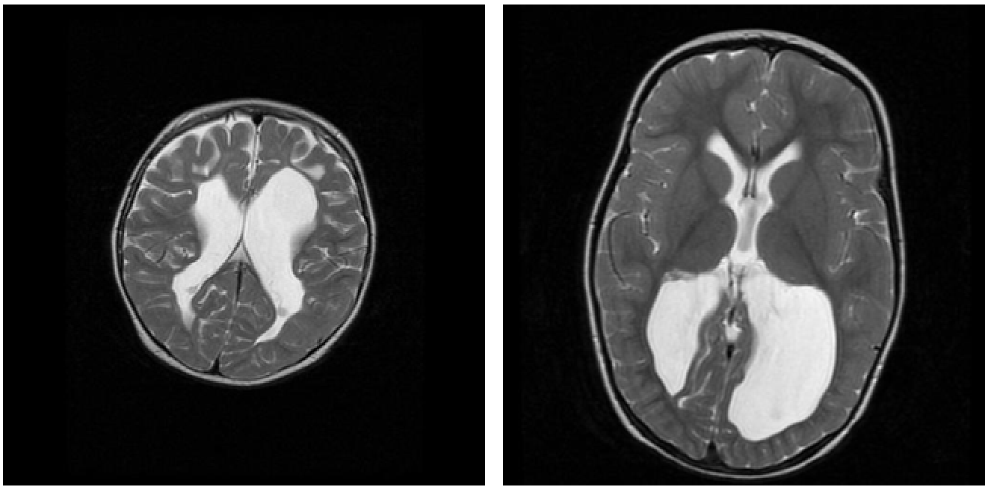

Figure 1.2: T2 brain MR images of children at the age of approximately two years which suffer from cerebral palsy. It can be observed that the reduced brain tissue is replaced with cerebrospinal fluid.

The brain structure of children younger than twelve months differs significantly in size and shape from the adult brain, in particular in the central part of the brain. This can be observed in Figure 1.3 where an image from a premature infant at the age of a few weeks and a second image from a child at the age of two years are shown. The MR images contain intensity non-uniformities, partial volume effects and noise which can be observed as intensity variations. Noise, intensity non-uniformities and intensity variations are introduced during the MR acquisition process. The partial volumes and the diffused contours are partially generated by the ongoing process of myelination[2] of the white matter and by the limitations on the resolution of the MR data. The intensity inconsistencies arise in preterm infants and cause the white matter to be extremely difficult to distinguish from the grey matter in various MRI sequences. On the other hand, the intensity inhomogeneities within the white matter tissue is higher in preterm infants compared to infants born at term [59]. Recent studies [21] have provided an insight into the differences between infants born at term and premature infants. The aim of these studies was to compare the evolution of the neurodevelopment impairment by analysing the data that is captured at different age stages. At the age of 2 years, the majority of the white matter has myelinated. Additionally, due to a higher level of fluid in the infant brain tissue, the MR images do not display clear boundaries between different brain regions, and this causes difficulties for clinical experts in establishing a precise and accurate diagnosis during the visual examination. In computer vision, this translates into a challenging segmentation task where, for example, methods which rely on probabilistic atlases generated from adult brain images can return large misclassification rates [91].

---

[2] The myelination describes the brain developing process in which the myelin sheath (a fatty substance) accumulates around a nerve fiber for a faster transmission of the nerve impulses.

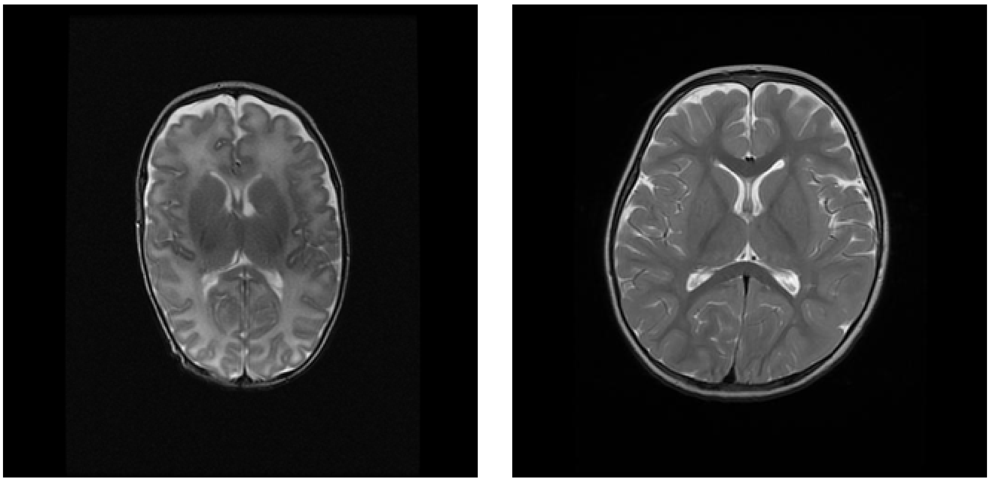

Figure 1.3: Left: A MR brain image from a premature infant at the age of a few weeks; Right: A MR brain image of a child at the age of approximately two years.

Most abnormal patterns are visible to experts. The challenge is to investigate small abnormalities which can been seen as intensity, shape or volume differences. These differing patterns can go undetected during the visual examination performed by clinical experts. To this end, the aim of this study is to develop a framework which identifies, extracts and measures the white matter volume. An example of original and segmented images is illustrated in Figure 1.4. The right image presents the original image in which the contours of the detected white matter volume is projected in red colour. The intensity variations within the white matter tissue and the diffused contours between the grey matter and the white matter are clearly visible in Figure 1.4. The following section outlines the challenges when segmenting premature infant brain MR images.

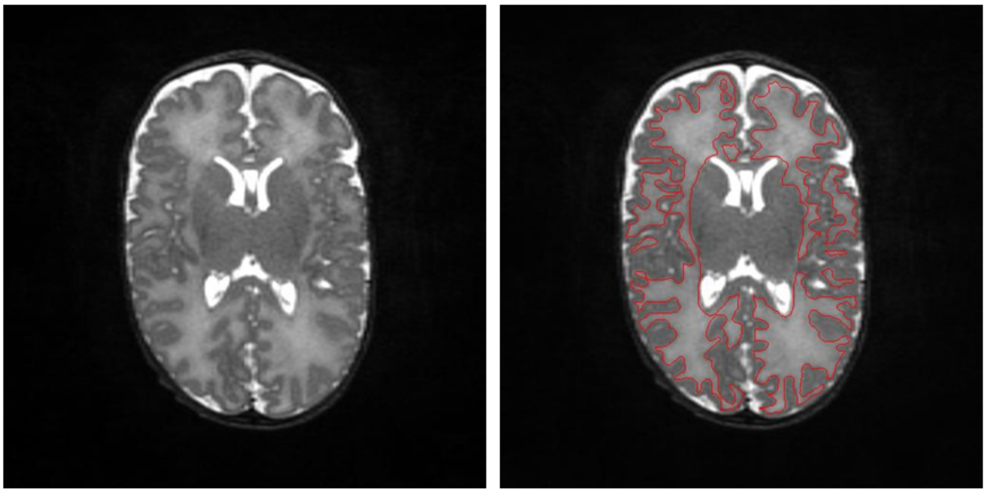

Figure 1.4: Left: An original T2 brain MR image of a premature infant. Right: The same image where the contours of the white matter region are marked in red. The objective of this study is to automatically detect and measure the white matter volume.

1.2 Objectives of this research

This study is a proof of concept for a preliminary study within a pre-defined clinical context. This project is built on a pilot study which was pre-defined by the Temple Street Children Hospital, Dublin, who also provided the medical insight and the data. The objective is the development of a white matter segmentation algorithm for premature infant brain MRI scans, which were captured on a 1.5 Telsa scanner with a resolution of 512×512 pixels and a thickness of 1mm. The approach will be used by the clinicians which allows them to perform research on the white matter volume measurements while focusing on the early diagnosis of the slow arising neurodevelopment impairments, especially cerebral palsy.

For this reason, this study focuses on the development of a brain segmentation approach for premature infant MR images. The majority of the state-of-the-art brain segmentation techniques have been developed for adult datasets. Consequently, their application to infant brain segmentation is limited. For that reason, this research work focuses on the robust segmentation of newborn infant MRI, which is an essential task in the study of diagnosing neurodevelopment disorders at an early stage.

1.2.1 Challenges

In Section 1.1 the visual differences between infant and adult brain MRI have been outlined. From a computer vision perspective, more challenges are encountered when dealing with infant MRI. Even though each brain tissue region is visually distinguishable in the MR images, the segmentation of corresponding areas is challenging due to intensity variations within regions, artefacts such as noise and motion, and partial volume effects (PVE).

To emphasise the development of the brain in the first two years of life, the intensity distribution and changes between the MR images taken from a child at birth, at the age of one year and two years are illustrated in Figure 1.5 (in the associated histograms for each image, the background pixels have been removed). The intensity distribution of the child MR images over time demonstrates significant changes. As a consequence, the differentiation of the brain tissue region in children at a young age is difficult. This comparison also reveals that the infant MRI presents a high level of artefacts. The older the child is, the more distinctive the differentiation of the brain tissues is. In an adult MRI, the distribution of the intensity in a histogram would present three peaks; grey matter (GM), white matter (WM) and CSF. The inversion of the WM/GM intensity values between newborns and older children/adults (as shown in Figure 1.5) is an additional complication when applying existing brain segmentation algorithms to newborn image data.

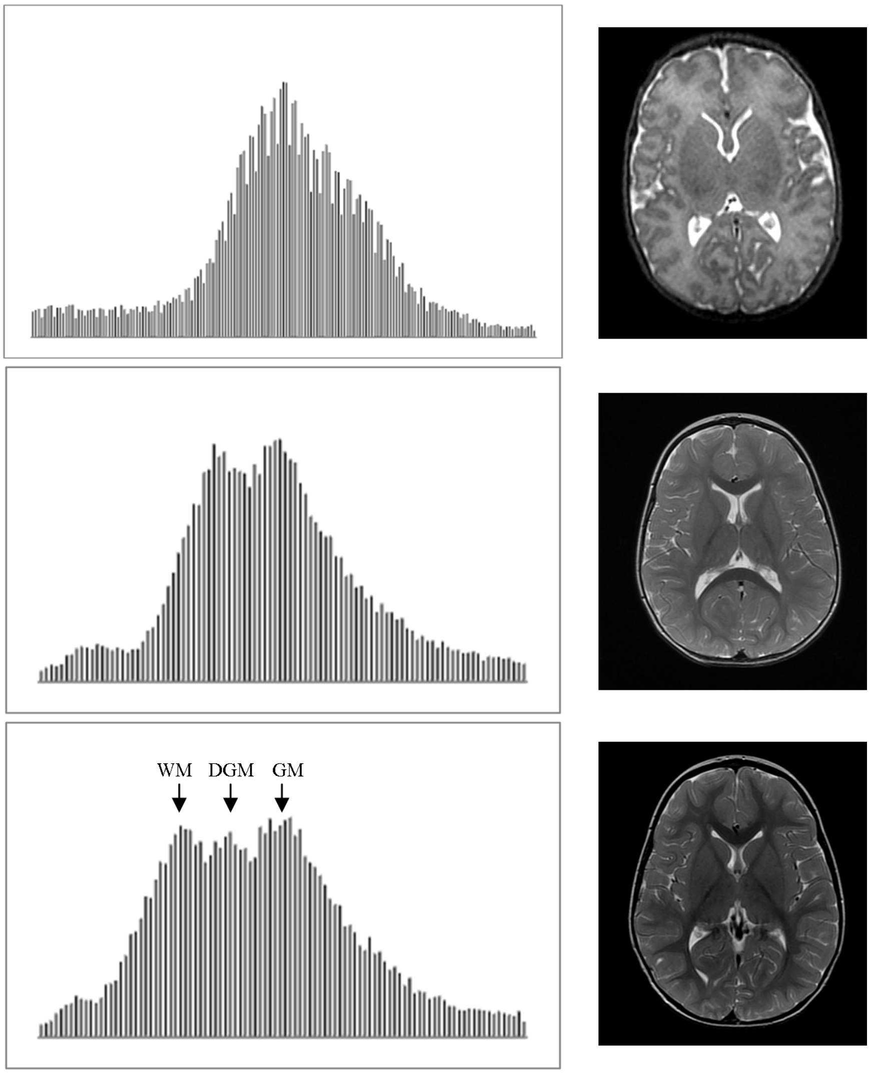

Figure 1.5: On the left are the histograms of the corresponding images on their right. The top row shows an example of an MR image from an infant at term; the second row illustrate an image of the same child at the age of one year; the third row displays an image of the same child at the age of 2 years. The histograms reveal that the intensity distribution changes over time and the more structured the brain tissue is, the stronger is the differentiation between GM and WM.

Most of the research work on brain segmentation has been done on adult data. The clinical overview in Section 1.1 has revealed large differences between adult and infant brain MR images. A common and demanding task required for MR brain segmentation (early born and adult) is the minimisation of the intensity inhomogeneities across the image, also called bias field correction. The bias field can be described as a low-frequency multiplicative signal which is caused by variations of the magnetic field during the MRI acquisition. Examples of images corrupted by bias field are presented in Figure 1.6.

In the early stage of the brain development, the brain tissue contains a high and inconsistent water content. This results in a non-uniform intensity distribution within the brain tissue and diffused contours. In addition, due to the stress of the premature birth, strong variations in the structure and shape of the brain tissues can appear. Both factors are illustrated in Figure 1.6.

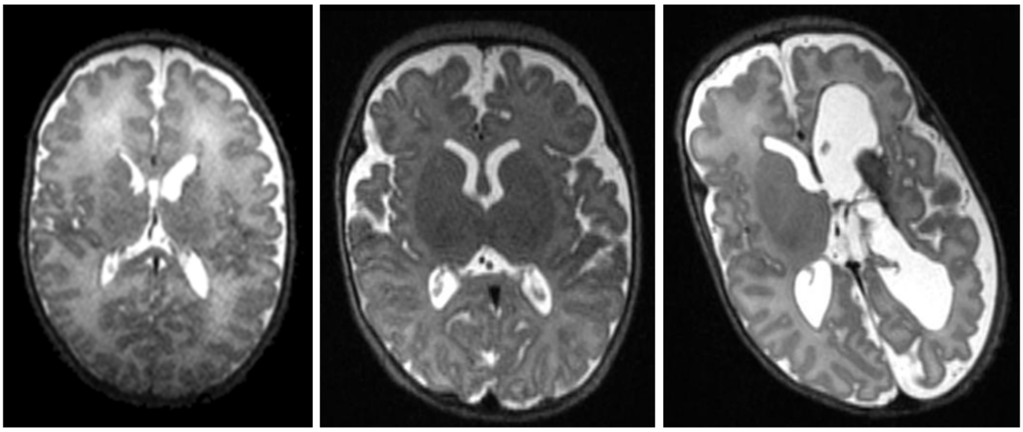

Figure 1.6: The left example displays a bias field corrupted image in which the intensity values vary throughout the image. The three infant brain images illustrate shape and structure differences between patients. A more common dissimilarity in infant brain MRI data is the enlarged ventricles, which are the bright areas in the middle of the brain tissue. This is caused by stress during the premature birth but does not necessarily indicate ill health of the infant.

Due to the small head size during infancy, the scanning procedure has to be performed at high resolution. In addition, the acquisition process is conducted rapidly because the infants tend to move. The high resolution and the short scanning time lead to a high level of noise and low contrast between the grey matter and the white matter tissue. This issue was illustrated in Figure 1.3 when comparing the adult and infant brain MR images.

A demanding task is the exclusion of the deep grey matter during white matter segmentation. In adult data, the deep grey matter is well defined and can be grouped in six smaller regions. During infancy, it is difficult to distinguish the white matter and the deep grey matter due to the high amount of water content within the brain tissue. In addition, the contours of the deep grey matter are often diffuse and sometimes missing. An example of the deep grey matter in adult and infant brain MRI data is displayed in Figure 1.7.

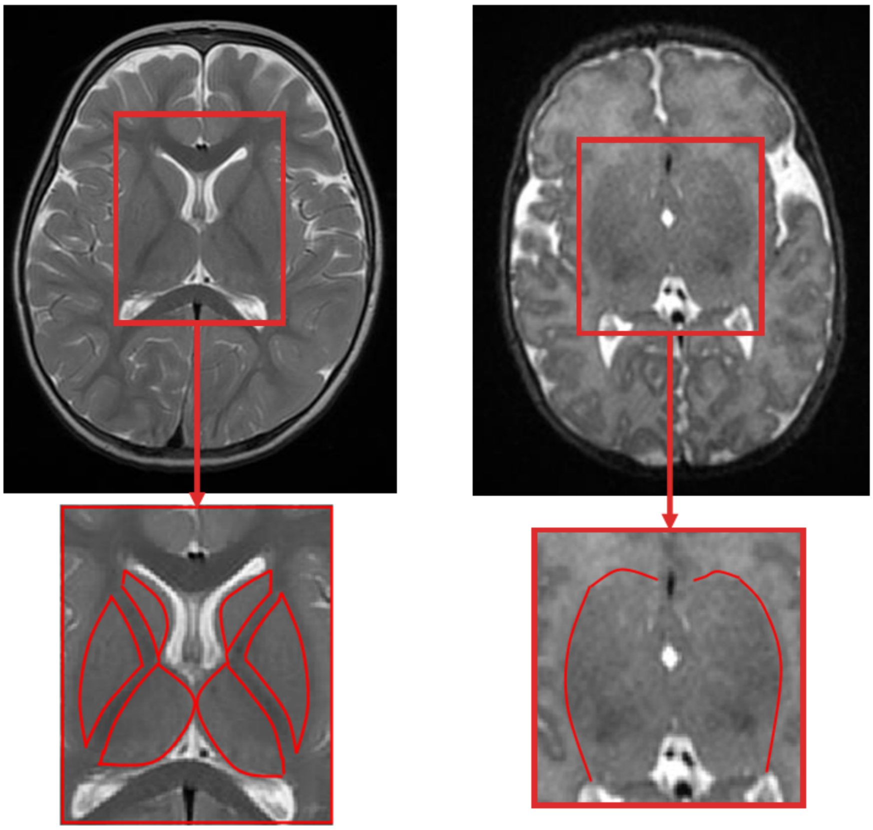

Figure 1.7: Differences in the deep grey matter between an adult (left) and infant (right) brain MR image. The contours of this region are marked in red.

If PVE is present, the intensity of the voxel is generated by more than one tissue and this has been a challenging problem for all steps of the proposed framework. First the PVE emerged in the skull stripping procedure where the boundaries between the brain tissue and non-brain tissue can be unclear. The aim of the bias field correction algorithm is to identify the intensity variations within each image, which can be demanding when containing large PVE. Finally, in the extraction of the white matter region, the PVE challenges the segmentation of the white matter tissue when distinguishing between WM and GM. The best way to illustrate the partial volume voxels is on contiguous images within a volume as displayed in Figure 1.8. The red arrows mark some regions which consist of partial volume voxels.

All these challenges characterise the brain segmentation of infant data as a demanding task.

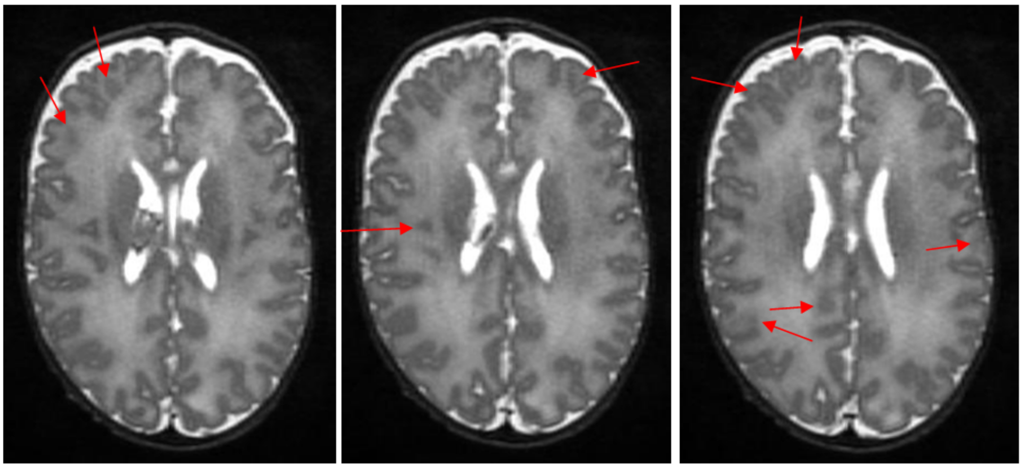

Figure 1.8: Three contiguous images of a patient in which some of the partial volume voxels are marked with red arrows. The partial volume effects are related to the structure of the brain and they raise a challenge for the white matter segmentation algorithm.

1.2.2 Contributions

The previous section has outlined the principal challenges which are involved in the segmentation of premature infant MRI data. The main aim of this research work is the development of a robust brain segmentation approach to extract the white matter region in preterm infant data. The focus lies on the measurements of premature infant data so that the underlying anatomical changes can be identified. When dealing with the previously mentioned challenges, different steps are required to achieve a precise brain segmentation technique.

The main contribution of this study is the development of an automatic framework for premature infant brain image segmentation. Due to the fact that the brains of premature infants tend to consist of large variations in shape and structure, the designed method is not guided by a pre-defined template or atlas. For this reason, the proposed approach includes three main steps; brain extraction, bias field correction and white matter segmentation. Another contribution is that this complex task was solved using fundamental techniques which were carefully combined in order to obtain a robust white matter segmentation framework.

A significant challenge is the poor quality of the infant brain MR images. One of the reasons is that the brain tissue of infants contains a large amount of fluid which generates intensity inconsistencies and less defined boundaries. The image quality can be improved by applying a filter to remove the noise. Another problem encountered during the MRI data analysis consists of the contrast variations which arise during the MR acquisition procedure. These intensity changes occur from one patient to the next but also during the same sequence. This issue can be decreased when enhancing the contrast between the grey matter and the white matter tissues. One way of diminishing the overlapping of intensity values between different regions, as demonstrated in Figure 1.5, is by removing all non-brain tissue. During this step, the missing and diffused contours between brain and non-brain tissues are addressed when generating a mask of the region of interest.

As mentioned in Section 1.2.1, the intensity inconsistencies within images, also called bias field, have a major impact on the segmentation procedure and this is, therefore, an important contribution to this study. The bias field causes a slow varying shading effect in the MR images. Assuming that the brain information consists of high-frequency signals, the intensity variations can be separated from the image by extracting the low-frequency information. The technique to adjust this type of artefact is called bias field correction.

A major contribution of this research involves a novel algorithm for the extraction and measurement of the white matter region. A common approach in brain segmentation is to use a template in order to extract the region of interest. Template-based algorithms have difficulties in the presence of severe pathologies and are, therefore, limited to large variations in shape and structure which is the common case in premature infants. This problem is solved here by not relying on template and, therefore, using local intensity-based methods. A technique independent of templates is less vulnerable to dissimilarities between the two cerebral brain halves, that can easily occur on premature infants data. A local intensity-based method can locate and regroup the partial volume voxels into their corresponding tissue class.

As mentioned in Section 1.2.1, the cerebellum and the deep grey matter consist of grey matter and white matter, and the high water content causes false segmentation when extracting the white matter tissue. As these brain regions are not of interest in this study, in this thesis a novel algorithm is proposed which localises and removes these regions from the WM data. The main idea followed in this work was to detect feature points such as contours and create an elliptical shape which corresponds to the region of interest.

Finally, the performance of the proposed approach is assessed by a quantitative and qualitative evaluation on a large database including preterm and term born infant brain MR images. To illustrate the generalisability of the proposed approach, the algorithm was tested on the large database of 1.5T MRI data which was given by the collaborating hospital and on public available 3T MRI datasets.

The outlined contributions are presented in various steps throughout this study. The following section will introduce an overview of the proposed approach.

1.3 Overview of the proposed approach

The main components of the proposed segmentation approach are presented in Figure 1.9. There are three main phases required to extract the white matter region in infant brain MRI data.

The framework starts with a novel approach for brain extraction (also called skull-stripping) and involves the removal of the non-brain tissue, which is explained in detail in Chapter 3. The proposed method reduces the image artefacts, generates binary masks, extracts the region of interest, and improves the results in a post-processing step. One of the challenges of this method is to determine the exact contours which differentiate the skull and fat from the brain tissue. Unlike the adult brain, the infants do not necessarily have a visible CSF region surrounding the brain tissue, which leads to unclear and diffused regions. For this reason, the mask is generated in three steps. Firstly to reduce the partial volume effects, secondly to remove disconnected small non-brain tissue, and then to generate the final mask with the aid of edge detection. To prevent under-segmentation, the final extraction of the brain tissue is performed in a region wise manner. For clarity all these steps are outlined in green in Figure 1.9.

The neonatal MRI data includes (besides noise and intensity inconsistencies) additional artefacts which cause substantial spatial intensity variations within an image. In order to address this problem, an approximation of each tissue region is necessary. Therefore, an automated thresholding algorithm is performed to classify the brain tissue into two regions (grey matter and white matter) by adding a probabilistic analysis. This is a key element because the grey matter belongs to a different intensity range than the white matter tissue. In this way, the intensity changes can be separately estimated for grey matter and white matter and then combined in a intensity map on which the bias field calculation is performed using a low pass filter.

The major component is the probabilistic approach for the final segmentation of the white matter region. In the proposed technique two separate clustering methods are performed with the goal to reduce the influence of the partial volume effects and diffuse boundaries. To speed up the final segmentation, the white matter volume is pre-segmented. As mentioned before, the cerebellum and the deep grey matter provide a great challenge during the segmentation procedure because they are composed of grey matter and white matter tissues. For this reason, both regions are separately detected by fitting an ellipse to the region of interest (RoI) in order to correct and prevent false classifications in the white matter volume. The final segmentation is performed by judging each voxel based on local re-classification which deals with partial volume voxels and diffused contours.

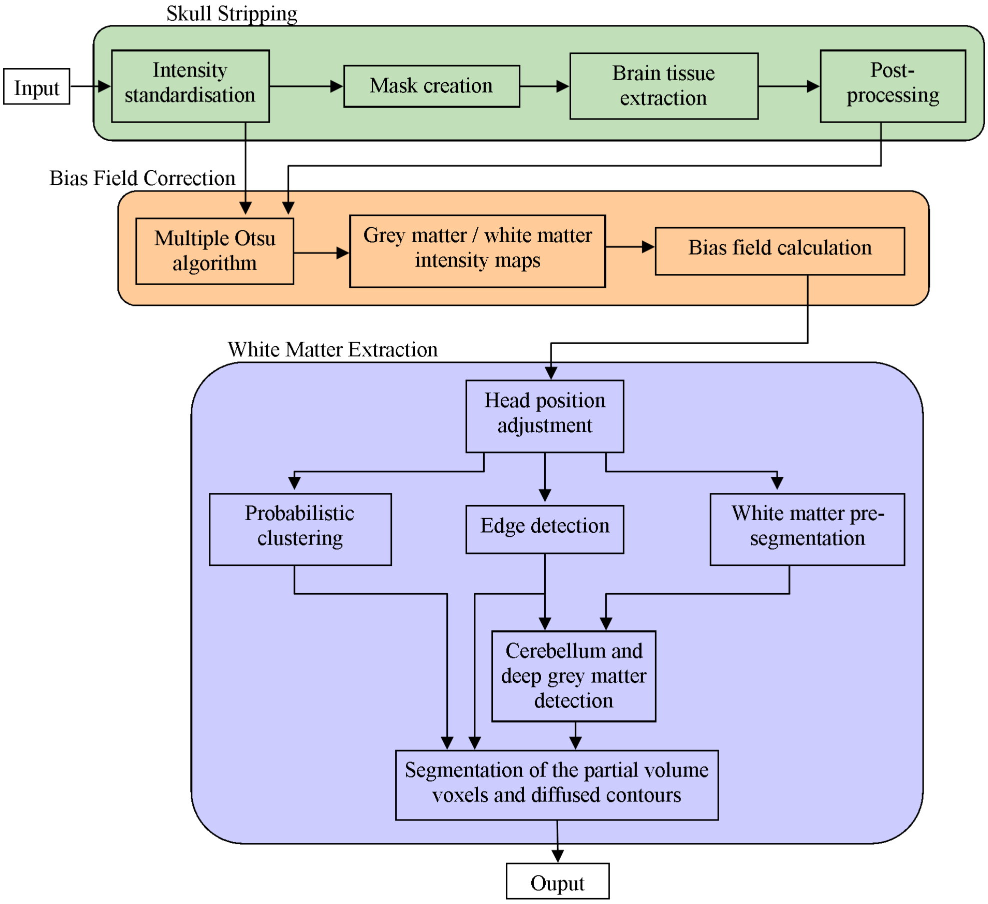

Figure 1.9: An outline of the proposed approach. The brain extraction algorithm is underlined in green, the bias field correction algorithm is outlined in orange and the white matter segmentation is marked in purple.

1.4 Overview of the thesis

This report is divided into seven chapters. The first chapter introduces the motivation of this research work and provides an insight into the challenging task of working with brain MRI of premature infants. The clinical overview in this chapter illustrates the risk of prematurity and the neurodevelopment impairment. An overview of the proposed approach is presented including the contributions that resulted from this study.

The second chapter presents an overview of the state-of-the-art approaches where the main emphasis is placed on discussing the problems associated with existing MRI brain segmentation algorithms. This allows the identification of the main directions of research and the methods required to solve these tasks.

The third chapter presents a detailed description of the proposed brain extraction algorithm. This chapter starts by briefly introducing the state-of-the-art methods and the purpose of the skull stripping technique. This is followed by a description of each stage of the developed algorithm in detail. To demonstrate the accuracy of the method, a numerical evaluation was performed.

The fourth chapter analyses the developed bias field correction technique. After briefly introducing the state of the art, the fourth chapter gives a detailed description for each step of the proposed approach. This includes the understanding of the varying bias field in MR images followed by the correction of the corrupted images. Chapter 4 ends with an experimental section that analyses the performance of the proposed method.

The fifth chapter presents the segmentation procedure which allows the extraction of the white matter region in the brain MRI of infants. The white matter segmentation is a difficult task in infant brain MR images because artefacts such as inconsistencies in intensity, structure and shape, change from one patient to another and also during a patient MRI sequence.

The sixth chapter includes experiments and a comprehensive quantitative and qualitative evaluation of the approach discussed in this thesis. The experiments were conducted on a large infant brain MRI database where the images were acquired when the infant reached the age of term equivalent. For example, if a preterm infant was born three months early then the scanning procedure was performed when the infant was three months old.

The seventh chapter summarises this research work while outlining the contributions resulting from this study. In the second part, the future work in relation to the proposed segmentation framework is discussed.

Chapter 2

Literature Review

The previous chapter introduced the clinical background of this research and presented the key challenges when working with infant MRI data. The aim of this chapter is to outline the state of the art on MRI brain segmentation techniques. The main work in brain segmentation has been conducted on adult brain MRI data. Only recently the interest in the segmentation of MRI data of young children and infants has received more attention. Therefore, the majority of the state-of-the-art methods presented in this chapter were developed for processing adult brain data.

Neurodevelopment impairment has a substantial impact on the personal, social and professional activities of patients and also on their family lives. The exact cause of the slow developing cerebral palsy is still unclear and the process is irreversible. By diagnosing the patient at an early stage of this neurodevelopment impairment, therapies can reduce the severity of these disabilities. The analysis of brain MR images is the most common method for this diagnosis. The segmentation of the brain MRI data has always been a great challenge and the measurement of regions in Magnetic Resonance (MR) images is a key task in the field of medical imaging. The process is important for a fast diagnosis, especially for an early detection of small anatomical abnormalities which might not be noticeable by visual examination.

As described in the previous chapter, the structure of the brain in infant MR images differs significantly from adult brain MRIs. Thus, the analysis and processing of infant brain MR images is an essential and difficult procedure. This process is partitioned into pre-processing and segmentation parts. The main pre-processing parts can be divided into three steps: brain extraction, bias field correction and registration. The first pre-processing step includes the removal of all non-brain tissue in MR images; this task is also called skull stripping or brain extraction. A state-of-the-art review of the brain extraction algorithms is presented in Chapter 3. Another pre-processing step consists of improving the image quality by reducing the influence of the bias field corruption. The bias field causes a slow varying shading effect in the MR images which arises from the inhomogeneity of the magnetic field during the MRI acquisition. A survey that focuses on the bias field correction techniques is presented in Chapter 4 and will, therefore, not be further discussed in this chapter. The third pre-processing step is called registration. The general idea of registering two images is to align them into the same space. One instance when registration becomes especially important is when MRI sequences are acquired from different MRI scanners. In this case, the registration algorithm transforms each patient data into the same coordinate system and allows a comparison of the results. Another reason is the incorrect positioning of the patient in the MRI scanner. During the MRI acquisition process, patients will never be located in the exact same posture. Thus, image registration maps a pair of images; one image will remain as a target or template and the other one, the source image, is transformed to match it. The registration process [8] calculates the transformation parameters and one image is transformed using these parameters. Some segmentation techniques are based on templates or models where an atlas is used as prior information to segment the region of interest in which case a registration algorithm is important. In our study, a registration technique is not essential for the segmentation of the white matter because the data is acquired in the same coordinate system and, therefore, a detailed description of this technique is beyond the scope of this thesis.

The segmentation of specific brain regions in MRI data represents a major field of research in medical image processing. The detected regions can be tumours, white matter lesions, ventricles, white matter or grey matter. State-of-the-art reviews [14] in different areas of brain MRI segmentation, such as the segmentation of cerebral cortical region [118] or multiple sclerosis lesions [81], outline the medical background of the developed technique along with their algorithm description. In each review the authors classify the developed methods in different ways. In this chapter, the segmentation techniques are categorised into three main groups: surface-based algorithms (Section 2.1), atlas-based methods (Section 2.2) and intensity-based segmentation (Section 2.3). After the developed brain segmentation methods have been introduced, Section 2.4 gives a short description of some available brain segmentation applications.

2.1 Surface-Based Segmentation

A popular segmentation approach for medical imaging applies surface-based methods such as active contours, deformable models, levelset, active shape models and active appearance models [4].

The active contour models, also called snakes, were first proposed by Kass et al. [68]. This method is applied to outline object contours in an image based on a curve.

The basic idea is to start with an initial curve and then to deform the curve to the contours of the object.

$$X(s) = [x(s), y(s)] \tag{2.1}$$

where s is an arc length commonly defined in a range of $[0, 1]$. It performs in a way that minimises an energy function that is composed of two terms:

$$E = E_{int}(X(s))ds + E_{ext}(X(s))ds \tag{2.2}$$

The term $E_{int}(X(s))ds$ is called the internal energy and controls the tension and rigidity of the deforming curve. The term $E_{ext}(X(s))ds$ describes the external energy and directs the curve toward the object boundary. The advantage of this method is its relative insensitiveness to contour initialisation, whereas on the other hand this method is time consuming when applied to a 3D volume. Additionally, the method is sensitive to weak or missing object contours.

Active Shape Models (ASM) [39] and Active Appearance Models (AAM) [38] are model based algorithms which perform a statistical analysis based on a training dataset to detect an object by its shape and grey level intensity values. To interpret an object in an image using a model, a set of parameters has to be found which describes the best match between the model and the object. In general, this set of parameters or landmarks describes the shape and position of the object in the image. Both methods learn the changes of the object by modelling the training set. The ASM fits a set of landmarks to a new image. Each point is fit to the new image by searching for the best match of the nearby points. The AAM deforms a model to fit the position of the landmarks and a region presenting the texture of the model. The AAM evaluates the difference between the new and the model image to update the parameters. Cootes et al. [37] investigated the differences of performing ASM and AAM on brain MR data. Both methods are limited for objects with large changes in shape, location and position of the objects. The model can only deform within the limits of the training set. Therefore, a problem occurs if the object displays untrained deformations which involve the difficulties of the labelling of training samples with sufficient anatomical variations to include specific conditions. Thus, this algorithm would be unsuitable for segmenting infant brain MRI data due to the large variations in structure, shape and intensity as well as unclear boundaries.

Deformable models [88] change their initially provided shape to match a target structure. The adaptation is estimated by computing the minimisation of an energy function (as in equation 2.2) which is composed of a weighted sum of internal and external energy terms. In general, deformable models are active contour models which change their shape in a 3D environment. Parametric deformable models have two limitations. Firstly, if the initial model and the required object differ greatly in shape and size, the model must be dynamically reparametrised for successful results. Secondly, the method has difficulties in adjusting to changes in structure such as splitting or merging. Generally, the deformable models suffer from the same limitations as the active contour models such as sensitiveness to weak or missing contours. Additionally, due to the 3D environment, the deformable models can be time consuming when applied to a large input data such as a brain MRI volume.

A related technique to the active contour model is the levelset method [4]. In both methods the same forces can be chosen to generate the contour. A major difference lies in the way the contours are represented. In the case of the active contour model, the boundaries are composed of contour points that parameterise the edges, while in the levelset method the boundaries are produced as the zero levelset of a higher dimensional function. Wang et al. [126] proposed a levelset algorithm by combining information of T1[1], T2 and DTI[2] data. The levelset energy function embeds a set of three features extracted from the data. Firstly, the local information of the intensity distribution is selected from T1, T2, and FA[3] images during the registration with a population based atlas, secondly, a cortical thickness constraint term that indicates the thickness of the cortical region and, finally, the longitudinal constraint term. The algorithm was tested on 22 datasets of children representing different age stages between two weeks and one year old. The results indicate that the partial volume effects prevent the extraction of the white matter surrounded by the gyrus.

Xie and Mirmehdi [131] proposed a Magnetic Active Contour (MAC) model which was applied on various medical images. In their technique, the object boundary and the active contour are charged with electric current. The magnetic field is caused by the image gradient of each of the currents' interactions and generates a force which acts as external force. The magnetic flux density at each pixel position is computed after estimating the direction of the active contour and the current in the object boundary. The active contour is defined as follows:

$$C_t = \alpha g(x)\kappa\hat{N} + (1-\alpha)(F(x)\hat{N})\hat{N} \tag{2.3}$$

where $g(x)$ is the stopping condition, $\hat{N}$ denotes the unit inward normal of the evolving contour, κ describes the curvature, α is a real constant and F is the magnetic force

---

[1] T1-weighted MRI is another MR sequence in which the fluid-containing tissues are presented in low intensity values.

[2] Diffusion tensor imaging (DTI) allows the measurement of the water flow and tracks the pathways of the white matter in the brain.

[3] The FA images present the fractional anisotropy images of the DTI data with the objective of providing information on the fibers.

defined as:

$$F(c) = I_c\Upsilon(c) \times B(c) \tag{2.4}$$

where $\times$ is the cross product, $B(c)$ presents the magnetic flux density, $\Upsilon(c)$ denotes the electric current vector, I describes the image and c is the active contour position. An advantage of this method is that the snake is less sensitive to its initial position and robust against complex structures. The method has provided positive results on various medical images. The technique performed well on 2D pre-processed data but showed erroneous segmentation in a 3D space.

2.2 Template- and Atlas-Based Segmentation

In template-based segmentation, a model of the object is applied to guide the segmentation procedure. For a more complex structure, an atlas-based technique [28] can provide a segmentation without the need of precise modelling. The algorithm performs brain segmentation using the information of an atlas to influence and guide the prior knowledge of anatomical structure, location, shape and the spatial relationships. Using data obtained from different patients, an atlas has a common anatomical map of the brain and is employed as prior information in an algorithm. After pre-processing data with a registration method, this map is then utilised as a template to segment the region of interest.

Morphometry in brain segmentation is applied to calculate and compare differences in brain size and shape across different MR images. This algorithm starts by aligning the data into the same space using registration. The registration provides the basis for Voxel-Based Morphometry (VBM) and Deformable-Based Morphometry (DBM). A third type is Surface-Based Morphometry which segments an image into tissue classes while converting the segmentation boundaries into parametric surfaces.

VBM [8] is employed to detect the main differences in the anatomy of the brain. In general, this method starts with a spatial normalisation of all images by registering every brain image to a template using a 12-parameter affine transformation. After registration, each voxel is defined with a probability which specifies the tissue class where it belongs by applying a modified mixture model cluster analysis technique. The modified mixture model cluster analysis technique used for the brain tissue segmentation was proposed by Ashburner and Friston [7] and iteratively partitions the images into grey matter, white matter, cerebrospinal fluid and three other background classes. During the segmentation process, the cluster parameters which includes the probability of the voxels, the variance and the weight of each clusters are estimated from the nonuniformity corrected image. Then the tissue probabilities are assigned based on the cluster parameters by using the Bayes' rule. These two steps are repeated until convergence. This is followed by a spatial smoothing which is obtained by convolving with an isotropic Gaussian kernel. Finally, statistical tests can be performed using the general linear model to identify regions which are used to show significant regional differences among populations. Corrections in the volume can be carried out by including the Jacobian determinant into the calculation. The VBM algorithm is incorporated in the well-known SPM tool which is freely available and allows performing a large number of statistical tests on brain MRI data. The SPM technique was investigated in this study in which the brain tissue on preterm infant data was obtained and evaluated. Kennedy et al. [69] implemented the VBM with the purpose to find age-related patterns in the brain structure. The authors stated that the few existing comparisons of VBM are limited by small datasets, limited selection and that the methods include manual measurements. Their aim was to overcome those limitations with a larger dataset of 200 subjects with an age range between 18-81 years. The limitations were also addressed by increasing the number of manually traced regions. The conclusion was that VBM performs poorly in the detection of age differences in the brain structure. Ashburner and Friston [10], and Bookstein [24] debated the use of VBM. Bookstein's main criticism was that, in case of systematic anatomical differences among subjects, the VBM method would only detect some of the features but not all. One of the main disadvantages of VBM is that it utilises a less precise image registration so that regional volumetric differences cannot be accurately localised.

The DBM [6] [29] aims to detect shape differences in the anatomical structure. In general, the local and global transformation will be calculated by registering the image to a template. The correction can be optimised by applying the normalised mutual information. A Jacobian determinant of the deformations can be applied to measure the regional tissue volume changes. An advantage of DBM is its ability to detect small changes. However, due to the wide range of registration methods, there is no standard technique for DBM. Boardman et al. [26] [27] and Aljabar et al. [2] designed DBM methods for brain MRI segmentation of premature infants. Their study included a comparison between pre-term infants data, acquired at term equivalent, and term-born infants data. Their method was based on DBM for the detection of abnormalities in breast data which was developed by Rueckert et al. [100]. The global transformation was generated using the affine transformation, and the local transformation was generated using the free-form deformation based on B-Splines. The authors utilised the normalised mutual information as a voxel-based similarity measure which has the advantage of not being sensitive to intensity changes. The results indicate that the non-rigid registration is better at finding the deformation than applying a rigid or affine transformation. The evaluation of the approach revealed sensitiveness to volume changes of the white matter tissue and partial volume voxels. The results also indicate that the partial volume effects and low contrast limit the extraction of the white matter surrounded by the gyrus. In 94% of the cases, two experts who examined the results stated that the non-rigid registration technique is preferable. In 4% of the cases, the results were influenced by the large motion in the images. Ball et al. [16] investigated the performance of DBM on infant brain MRI data to examine alterations in the development of the thalamic region associated with premature birth. The DBM algorithm developed by Ashburner et al. [11] was employed and the registration algorithm proposed by Rueckert et al. [100] was applied on their database which consists of 74 pre-term infants acquired with a 3T scanner. Their conclusion is that DBM is highly sensitive to volume changes, which was especially observed when measuring the CSF. Additionally, they stated that the current image registration techniques have limitations when applied to infant data.

In atlas-based segmentation, prior knowledge of the anatomical structure of the brain is applied to the segmentation method in the form of a probabilistic atlas. Similar to the template based procedures, a registration technique is needed as a pre-processing step in which the data is registered to the atlas. Atlas-based segmentation is widely used for brain segmentation where the anatomical structure information is embedded to influence the segmentation procedures.

The main challenge for atlas-based methods is the generation of a high quality atlas. Usually, in brain segmentation, a probabilistic atlas is composed of a template and three probability maps representing the grey matter, white matter and cerebrospinal fluid. In order to generate an atlas, multiple segmented brain volumes are aligned and then the average of the anatomical structure is used. In this regard, a probabilistic atlas represents the changes in the anatomical structure of the brain. A high number of patients is required to construct a good quality atlas. For example, the MNI305 atlas of the Montreal National Institute [43] was generated using 305 patients. The ICBM152 probabilistic atlas [87] was created by registering 152 scans to the MNI305 atlas. These atlases are constructed using adult MRI data.

Gousias et al. [50] [49] generated an atlas-based segmentation technique to employ prior information from healthy adult brain MR images to overlay them on two-year-old subjects. Their aim was not to extract the volumetric data of these regions but to demonstrate if the segmentation can be successful by applying atlases of adult MRIs to two-year-old subjects. The authors proved that the use of adult templates in the brain segmentation for two-year-old subjects results in erroneous segmentation. The segmentation of infant brain MRI data with the help of adult templates was also evaluated by Altaye et al. [3]. Their segmentation method included the generation of an adult-based template and prior information maps, which were then applied to segment infant brain MRI. The results demonstrated that the use of adult templates with infant data leads to misclassification. This is due to the different shape and size structures of the infant brains when compared to adult brains.

Only recently a technique was proposed by Murgasova et al. [73] with the aim of generating a 4D probabilistic atlas for the developing brain during different stages in early childhood (age between 29 to 44 gestational weeks). The method consists of a deformable atlas (created by manually aligning data to the atlas generated by the Montreal Neurological Institute (MNI)[4] using affine registration), atlas-based segmentation and intensity-based segmentation to locate the brain tissue regions using an Expectation-Maximization (EM) (a detailed description of EM is presented in Section 2.3.2). Most segmented regions show an average result of at least 90% similarity to manually segmented data. Due to the fast developing brain during childhood, the use of the altas is restricted to the age of the children it was generated from. This means that their atlas is only suitable for analysing infant brain MRI.

Shi et al. [110] designed a multi-region-multi-reference atlas technique to divide the brain into multiple anatomical regions. The semi-automated pre-processing step first applies two well-established brain extraction algorithms (BET and BSE) and then manually corrects the processed data to ensure accurate results. A subject-specific atlas is generated using an adaptive Fuzzy C-Means algorithm. This is followed by the application of a Gaussian model-based EM method which embeds the atlas information in the brain tissue segmentation algorithm. The method was evaluated on 3T T1-weighted neonatal, 12 and 24 months MRI data. The method uses the advantage of applying a combination of multiple Gaussian models in order to distinguish more precisely the tissue intensity distribution of each brain tissue. The generation of their own atlas which was based on their database performed well when used with the Gaussian-based EM algorithm. However, the results indicate that the method is sensitive to partial volume effects. Additionally, the results demonstrate false segmentation in the deep grey matter.

Another way to perform atlas-based segmentation was proposed by Boer et al. [22] who designed a segmentation approach to estimate the white matter lesion in adult MR images. After removing the non-brain tissue and correcting the intensity non-uniformity, the white matter lesion regions are segmented by applying a k-nearest-neighbour (kNN) classifier. The training samples have been obtained by atlas-based registration. The approach was developed for T1-weighted adult brain MRI. The results revealed that the detection of the cerebrospinal fluid (CSF) is influenced by the approach used to register the atlas to the brain MR images.

Prastawa et al. [95] presented an atlas-based segmentation method for newborn T1-weighted MRI data. This approach consists of three steps. Firstly, the technique estimates the white matter intensity parameters by computing the Gaussian distribution from previous detected parameters. This is followed by correcting the intensity inhomogeneity using spatial posterior probabilities to define a parametric classification. The segmentation is achieved by non-parametric kernel density estimation. The described

---

[4] more information can be found at http://imaging.mrc-cbu.cam.ac.uk/imaging/MniTalairach (date of access: 27/06/2013)

method is fully automatic and the results presented for 50 datasets illustrate that variations in the brain shape have no negative impact on the segmentation process. As a common problem of neonatal segmentation, the results indicate that the segmentation is influenced by the partial volume effects between the grey matter and the white matter along with misclassifications in CSF regions.

Gousias et al. [48] investigated the differences between infant and adult data, and the differences between pre-term and term-born infants' brain MRI. Therefore, T1- and T2-weighted MR images with a total of 18 pre-term and 5 term control datasets were manually segmented. A second aim of the study was to generate an atlas for newborn datasets. By comparing their results with adult datasets, the authors concluded that there are major differences between infant and adult MRI data such as the low contrast and high variability between patients within newborn datasets. Additionally, the newborn brain images have low contrast and are significantly affected by bias field corruption. The contrast between the GM and WM in infant images is only half of the adult data. This is caused by the higher resolution used during the image acquisition of infant data.

To deal with the segmentation challenges of the fast developing brain in early childhood, the methods presented in this section applied either templates or probabilistic atlases. Assigning prior knowledge to a segmentation algorithm is strongly dependent on the age of the patients. Atlas-based segmentation has provided accurate results when applied to healthy patients with little or no abnormal anatomical structure. Due to large differences in the brain structure and shape between the prematurely born and term-born infants, the atlas obtained from infants born at term can provide false segmentation in premature infant MR images [62]. Differences in the brain structure and volume were presented by Broadman et al. [26] using deformable-based morphometry. In template and atlas-based segmentation methods, the procedure is limited by the quality of the template or atlas and the precision of the registration process.

2.3 Intensity-Based Segmentation

Intensity-based methods classify voxels based on intensity information into different classes. When dealing with images with low contrast, noise, artefacts, partial volume effects and intensity inhomogeneities, brain segmentation can be a challenging task when using intensity-based methods. The following paragraphs introduce various intensity-based techniques that were used in brain segmentation. As mentioned before, most methods have been developed for adult MRI data.

In early segmentation techniques [79], intensity thresholds were employed to extract the region of interest. These methods manually select or automatically compute a threshold and then use it to segment the image by partitioning the MRI data. In this way, the threshold value allows the distinction between the region of interest and the background. Histogram-based segmentation [106] approaches are based on applying one or multiple intensity thresholds detected by histogram analysis to segment the desired region. These methods are often followed by morphological operations such as opening, closing, dilation and erosion, which are combined with connectivity analysis. These thresholds work well on regions with strong contrast differences. Brain MR images during infancy present blurred regions with diffused, unclear boundaries, a high level of noise, contrast variation and intensity overlapping between brain tissues. These image characteristics generate errors when performing thresholding. Histogram analysis has been considered and applied in different stages in this study with the purpose to extract primary information about the brain.

The Watershed algorithm [14] is a gradient-based segmentation technique and has been often used for MR segmentation [55] [54]. Merisaari et al. [89] designed an automatic brain segmentation method using watershed (WSEG). This approach initially removes the non-brain tissue with the help of a Brain Extraction Tool (BET) [113], then the brain region is segmented using the watershed algorithm, and finally, a Gaussian Mixture Modelling (GMM) classifies the brain tissue into three clusters (WM, GM and CSF). The outcome was analysed by experts from the University of Turku, Finland, who stated that the results were not sufficiently precise, as some CSF, WM and GM regions were misclassified. Gui et al. [52] have recently presented a morphological-based automatic segmentation algorithm for neonatal MRI brain data. After pre-processing the data with the bias field correction algorithm proposed by Mangin et al [83] and registering T1- and T2-weighted MRI data using the SPM8 tool, the procedure is divided into five steps: brain extraction, detection of subcortical grey matter, detection of GM, WM and CSF, detection of cerebellum and brainstem, and finally, the detection of the myelinated white matter. During these steps, the data is repeatedly processed by applying morphological operators such as erosion and dilation, followed by a marker-based watershed algorithm. The segmentation of the GM, WM and CSF is performed by utilising a region growing algorithm with a distance map as a stopping condition, and the seedpoints are located using the K-means algorithm. The framework has been successfully tested on 30 healthy infants data and four premature infant datasets acquired with a 3T scanner. This data has the advantage of stronger contours and less PVE. The algorithm is limited to locate regions close to the gyri, which are the convex shapes in the surface of the brain. In addition, the method also relies on knowledge about the brain structure which differs between patients, especially during infancy.

Another type of gradient-based segmentation is the semi-automatic live-wire technique [17], which has been applied to different areas of medical imaging such as segmentation, and classification of bones in MRIs [117] [80] and brain MRI segmentation [71] [72]. In general, the live-wire algorithm is a semi-automatic method that allows a simple and fast extraction of the region of interest (RoI) using user interaction. A few researchers [44] [56] developed techniques which extend the two dimensional procedure to three dimension (3D). In the 3D extended algorithm, the initial contours are created in a 2D image. Then, they are distributed in the volume by calculating the intersections with user defined contours. The live-wire technique relies on edges defined by the changes in the intensity values. For this reason, this method is not suitable for infant MR images due to unclear or missing contours.

2.3.1 Fuzzy Clustering

Clustering techniques are popular methods that were also applied to automatic brain segmentation. Clustering methods can be grouped into two classes: hard clustering and soft clustering algorithms. The hard clustering techniques [63] group the features into clusters (or classes) where each feature is assigned to one cluster only. Alternatively, in soft clustering, each feature is assigned to multiple clusters and each feature has associated membership levels. These membership levels define the association between the features and clusters. For this reason, the soft clustering is often employed in brain MRI segmentation.

One of the most widely applied fuzzy clustering technique in brain MRI is the Fuzzy C-Means (FCM) algorithm [1] [34] which uses the spatial relationship of the neighbouring voxels and boundary detection. The FCM optimises the association between voxels and clusters iteratively by recalculating the fuzzy membership function and the centres of each cluster.

Wieclawek and Pietka [129] embedded an interactive 2D live-wire method into a 3D FCM clustering procedure, which is then followed by morphological operations. The idea is to start with one image in the volume, called reference image, on which the features are extracted and then apply this information to the contiguous images in the volume. Kannan et al. [66] developed a Fuzzy C-Means to segment breast and brain MRI data. In this method, instead of computing the Euclidean distance, the authors propose to apply a kernel function to the feature space to reduce computational complexity. Ji et al. [65] developed a Fuzzy Local Gaussian Mixture Model (FLGMM) for segmentation of adult brain MRI data by minimising the energy function of the Gaussian Mixture Model (GMM) that is computed for every voxel in the image. Fuzzy memberships are applied to balance the information of each GMM and are, therefore, dependent on the mean and on the variance of the local Gaussian Mixture. A simplified Gaussian kernel function is implemented to establish the spatial constraint. In order to overcome the challenges caused by intensity inhomogeneities, a bias field correction model was embedded into the FCM. The segmentation was performed on 3T and 7T brain MRI data.

Ahmed et al. [1] applied a FCM technique where clustering is extended by embedding a bias field correction algorithm called Bias-Corrected FCM (BCFCM). This method modifies the membership function of a standard FCM and estimates the intensity inhomogeneities. Additionally, the approach facilitates the labelling of a voxel by considering the labels of its surrounding voxels. Therefore, the neighbour voxels act as a regulator and influence the final results. This method was used to segment brain MRIs into three classes; background, grey matter and white matter, and it was tested using adult MRI data. The results were compared with the results obtained by a traditional FCM and an Expectation-Maximization (EM) algorithm. Their output indicates that the BCFCM produces the same results as the EM but the BCFCM produces better results than EM in the presence of noise. This algorithm was tested on our database in Chapter 4 with the aim of correcting the bias field in the MR images.

FCM is based on clustering intensity values in an image and can be described as a computationally expensive and complex algorithm. On the positive side, the FCM algorithm can combine the segmentation process with the bias field correction which can then be strengthened with the influence of an atlas. One disadvantage of the FCM method is that it does not consider the spatial information, which may reduce its accuracy in the presence of noise. Although the embedding of local spatial information has improved its performance, the algorithm is also sensitive to initial parameterisation and can be trapped by local minima.

2.3.2 Probabilistic-Based Segmentation

In general, probability-based techniques assign a pixel to a class based on a probability value. A Markov Random Field (MRF) algorithm is a statistical model that allows computing spatial relations that exist between pixels and their corresponding neighbours. A segmentation method can employ MRF and it can decrease the influence of noise by using the neighbourhood information.

Bazin et al. [19] introduced a belief propagation based segmentation approach for Diffusion Tensor Images (DTI). Their work is based on MRF to model the diffusion properties and a Belief Propagation (BP) technique was used to estimate the most likely fiber tracts at voxel level. A prior atlas is generated and applied to influence the segmentation procedure. Their aim is to develop a method which can robustly identify the white matter lesions by tracing the fibers in DTI images. The experimental results indicate that the technique is sensitive to differences between patients, noise and head orientation. Additionally, the segmentation results are influenced by registration errors.

A more recent attempt of brain segmentation using a 3D region-based Hidden Markov Model (rbHMM) has been proposed by Huang et al. [60]. In the first step, a watershed algorithm is applied to define regions and the parameters for the rbHMM and the Maximum A Posteriori (MAP) states are estimated using the Viterbi algorithm [123]. The hidden states are initialised by applying a K-means clustering algorithm on the observed features which are defined by the mean values of the extracted regions. The approach was designed for T1-weighted adult MRI data that is available from the BrainWeb database[5]. A numerical evaluation has been performed and compared against a grid-based HMM. The rbHMM results show an improvement compared to the grid-based HMM. However, the output indicates under-segmentation in the subcortical structure, which implies segmentation difficulties on regions with weak contrast.

Supervised approaches have the advantage that the classification can be guided by the training data. On the other side, the generation of the training data is time consuming and difficult. The algorithm is limited to the trained structure and large variations could lead to false segmentation, which is especially the case in pre-term infants.

A more popular statistical model employed in brain segmentation, is the Expectation-Maximization (EM) algorithm in which the parameters are iteratively estimated with respect to missing or hidden data. The idea in an EM algorithm is to commence with an initial estimation of the model built upon the observable features and then the results are improved by adjusting iteratively the E-step and the M-step. During the E-step, the distribution of the hidden data is estimated by evaluating the current estimated parameters. During the M-step, the estimated parameters are updated by maximising the expected log-likelihood function which was computed in the E-step. The calculated parameters are then utilised to determine the distribution of the hidden data in the following E-step until convergence. A description of the EM technique is provided in Section 5.3.

In brain segmentation, the most commonly applied model to calculate the data distribution is the Gaussian Mixture Model (GMM) presented as a probability density function which estimates the distribution in each class.

Shattuck and Leathy [108] developed an approach called BrainSuite. The approach first uses an algorithm called Brain Surface Extraction (BSE) [109] to extract the brain tissue. Their bias field correction algorithm is based on a combination of global and local estimation of the tissue nonuniformity. The white matter and grey matter segmentation is achieved with the help of a Maximum A Posterior probability classifier. The approach was tested on T1-weighted adult brain MRI. The method is sensitive to the initial orientation of the brain volume and the technique allows user interaction for manual parameter adjustments.

The EM algorithm is sensitive to initialisation because it can only find the local extremum. Therefore, the common approach in brain segmentation is to use the EM with a probabilistic atlas. For this reason, the atlas is first registered to the new data and then

---

[5] available at http://brainweb.bic.mni.mcgill.ca/brainweb/ (accessed 14/04/2010)

employed as a weight during the EM calculations. Leemput et al. [77] and Ashburner and Friston [9], both perform an EM which is influenced by atlas to extract the grey matter and the white matter in adult brain MRI data. The weights obtained from an atlas are applied in different parts of the algorithm. In the EM algorithm proposed by Leemput et al., the weights are fixed probability values represented by the atlas and they influence the results during the E-step. On the other hand, the EM method developed by Ashburner and Friston recalculates the weights in each iteration during the M-step by combining them with the probability values acquired from the atlas.

Wells [125] was the first to propose an EM framework that is embedded with a bias field correction algorithm. The Gaussian distribution parameters are estimated from a histogram analysis during a pre-processing step. The authors then combined the bias field estimation and the classification as a non-linear optimisation. Grimson et al. [51] presented an adaptive algorithm to segment white matter, grey matter and cerebrospinal fluid. The EM approach includes a bias field measurement during the M-step, which is an equivalent to an MAP estimator of the bias field. The approach was evaluated on T2-weighted adult MRI data and presented successful results even without the additional influence of an atlas.

Murgasova et al. [90] [91] analysed the anatomical differences in the brain during early development. After an initial investigation that aimed to develop a brain atlas for young children [73], the authors proposed a population specific deformable and probabilistic atlas for brain segmentation. This technique applies registration, a template-based method to correct the intensity inhomogeneities and, finally, an Expectation-Maximization segmentation algorithm that is influenced by an atlas. The study focused on one and two-year-old children using 3T T1-weighted MR images. The registration errors were not included in the evaluation results. An advantage of this atlas-based method is the accurate segmentation results in the deep grey matter region.

Since most researchers have focused on the segmentation of the brain data with normal anatomical structure, Cardoso et al. [31] focused on processing infant brain MRI data with structural abnormalities. In order to perform the brain extraction, a population specific template based on T1-weighted MRI data is built and then combined with the atlas developed by Murgasova et al. [73]. A Maximum A Posteriori Expectation-Maximization algorithm is proposed which includes intensity nonuniformity correction and embeds the spatial dependence via a Markov Random Field. The authors state that an atlas-based segmentation method alone does not return acceptable results on preterm infant brain MRI data. The outcome illustrates some under-segmentation within the white matter and the CSF, on the other hand, the segmented grey matter regions demonstrate over-segmentation. These limitations are the result of the low contrast and the overlapping of intensity ranges between brain tissues. To overcome these issues the authors suggest to incorporate additional information from corresponding T2-weighted

MR images.

The advantage of the EM method is that the parameters are probabilistically adjusted and the EM technique can easily be extended by including other processes such as bias field correction. On the other hand, the convergence can be slow, depending on the amount of hidden data, and the results depend on the initial parameters. Nevertheless, the EM technique has provided accurate results when used for the segmentation of brain MRI data of young children and infants.

2.4 Brain Segmentation Software

A few researchers have made their developed software publicly available. In this section, tools including BrainSuite [108], FSL [40] [112], SPM8 [116], MRIcroN [99], ITK[6] and TurtleSeg [120] [121] are discussed and followed by a table which summarises the most important information.

- **Statical Parametric Mapping (SPM):**

  SPM is a well-established state-of-the-art tool and is used in various areas of medical image analysis. SPM99 is available since May 2001 and the latest version is SPM8 [116] which provides a large range of medical image analysis functions. For our study, only the segmentation part is of interest. The segmentation process uses Voxel-Based Morphometry (VBM) which performs region-wise volumetric comparisons among populations of subjects. SPM8 extracts three regions (GM, WM and CSF) and for each region a volume is generated.

- **BrainSuite:**

  BrainSuite [108] is an image analysis application designed for the identification of tissue types and surfaces in brain MR images. As mentioned above, each medical analysis tool has been designed for a specific task. BrainSuite was specifically developed for cortical surface extraction. This tool is easy to install and includes a user friendly interface which was implemented in C++ to allow a fast brain extraction process. To implement brain extraction, the Brain Surface Extraction (BSE) algorithm is embedded and this algorithm has been is described in detail in Section 3.1. This method is used in a stepwise manner which allows the user to adjust its parameters during brain segmentation. A negative aspect of BrainSuite is that during our experiments the software needed to be restarted for each patient data. BrainSuite was developed and tested on T1-weighted brain MRI data. This tool has been evaluated on four types of data; adults with depression, adults with Alzheimer, young control healthy patients and elderly control healthy patients.

---

[6] available at http://www.itk.org/ITK/project/welcome.html (accessed 02/07/2013)

- **FMRIB Software Library (FSL):**

  FSL is a library which consists of medical analysis methods for processing fMRI, MRI and DTI brain data. The brain segmentation technique is called FAST (FMRIB's Automated Segmentation Tool). This method commences with an initial segmentation using a tree-K-Means algorithm. The segmentation is then performed by a probability model which separates the tissue types based on their intensity distribution. Artefacts such as low resolution, noise, motions, bias field and overlapping intensity ranges between tissue types, complicate and limit the accuracy of the segmentation process. The software includes a technique to extract the brain tissue, called Brain Extraction Tool and this algorithm was discussed in Section 3.1

- **MRIcroN:**

  MRIcroN [99] is a simple and user friendly tool for medical image analysis which can be applied to generate 2D or 3D renderings of statistical overlay maps on brain anatomy images. An advantage is the integrated data format converter which allows the transformation of Dicom images into NIfTI format. This tool was originally developed to process T1-weighted adult brain MRI data. MRIcroN includes a brain extraction technique called Brain Extraction Tool which is the same as the method used by FSL.

- **Insight Segmentation and Registration Toolkit (ITK):**

  ITK toolkit[7] was developed to analyse and process medical images such as CT and MRI. By using a selection of well-known algorithms, the framework can process different types of medical images focusing on two main tasks: registration and segmentation. The segmentation procedure commences by performing the Perona-Malik algorithm in order to smooth the image while preserving the edge information. In addition, Canny edge detection or watershed algorithm can be applied for boundary detection. Then, region growing and deformable models such as levelsets can be employed for the segmentation procedure. ITK was implemented in C++ and enables interfacing with programming languages such as Tcl, Python and Java. Using a system (known as Dart), the toolkit can be extensively tested on a daily base. An advantage is that the framework can be applied to all operating systems, Unix, Windows and Mac Os X.

- **TurtleSeg:**

  TurtleSeg [120] [121] is an interactive and semi-automatic segmentation tool, developed by the Medical Image Analysis Lab at Simon Fraser University and the

---

[7] available at http://www.itk.org/ITK/project/welcome.html (accessed 02/07/2013) and a software guide is presented in http://www.itk.org/ItkSoftwareGuide.pdf (accessed 09/07/2010)

> Signal and Image Computing Laboratory at the University of British Columbia. This technique is based on a 2D live-wire which is used to semi-automatically trace contours on a set of images with different orientations. This is done by using manually selected seedpoints to generate intersections and contours on images using the live-wire technique. The information obtained from the selected images is then used to create a 3D segmentation using the Turtlemap 3D Live-wire algorithm.

All these described applications were developed for adult datasets and lead to erroneous segmentation when applied to infant brain MRI. VBM performs the registration using a template which is based on the adult brain structure. As mentioned in Section 2.2, the consequences are that regional volume differences cannot be accurately localised and all image registration techniques show limitations when applied to infant data. BrainSuite uses a spatial classification scheme to group the voxels in their tissue type. A major problem lies in the false classification of the deep grey matter and cerebellum regions. MRIcroN applies a brain extraction algorithm called BET which was examined on our database and the results are presented and discussed in Appendix A. FSL uses the algorithm called FAST for brain segmentation, which assumes that each tissue type has a corresponding peak in the histogram. However, the low contrast between the cerebellum and deep grey matter regions causes significant problems. The contrast in infant MRI is weaker than in adult brain data and the approach will return incorrect segmentation. ITK is an application which includes a wide range of techniques available for brain segmentation and their strengths and limitations have been outlined in this chapter. On the other hand, TurtleSeg, for example, relies on user interaction and the contours are detected using live-wire.

The brain extraction algorithms which are provided by some of these approaches (SPM, BrainSuite, FSL and MRIcroN) have been used as comparison methods in many skull stripping studies. For this reason, an investigation on their performance using infant data was carried out and the experiments are presented in Appendix A. A brief analysis of the brain segmentation tools discussed in this section is presented in Table 2.1.

2.5 Conclusions

This chapter provided a detailed review of the current state-of-the-art techniques for brain MRI segmentation. The methods are divided into three main categories: surface-based, atlas-based and intensity-based segmentation.

In Section 2.1 the surface-based methods such as active contour model, active shape model and levelset based algorithms are discussed. All of these methods have provided accurate results in many areas of medical image segmentation. Since these algorithms

Name	Purpose	Location	Data (adult)	Methods	Limitations when applied to infant data
SPM (2009)	This is a tool used to analyse various medical brain data	http://www.fil.ion.ucl.ac.uk/spm/	fMRI, MRI, PET, SPECT, EEG, MEG	Voxel-based morphometry	It is based on adult templates, which provides incorrect segmentation when applied to infant data
BrainSuite (2011)	This software identifies tissue types and surfaces in human brain MRI	http://www.loni.ucla.edu/Software/BrainSuite http://neuroimage.usc.edu/neuro/BrainSuite	MRI	Spatial classification	The low contrast regions lead to incorrect segmentation especially in the deep grey matter region
FSL (2012)	FSL is a comprehensive library of tools for analysis of brain data	http://fsl.fmrib.ox.ac.uk/fsl/fslwiki/	fMRI, MRI and DTI	FMRIB's Automated Segmentation Tool (FAST) based on hidden Markov Random Field model and EM algorithm	Overlapping intensity between tissues can cause problems
MRIcroN (2009)	Tool to analyse and visualise magnetic resonance images	http://www.mccausland center.sc.edu/mricro/mricron/	MRI and fMRI	Brain Extraction Tool (BET)	Only the brain extraction method of MRIcroN is related to this study
ITK (2012)	Tool to segment and register medical images	http://www.itk.org/	medical data	Perona-Malik filtering, Canny edge detector, watershed, region growing, deformable models	Incorrect segmentation in low contrast regions
TurtleSeg (2010)	Iterative segmentation tool for 3D images	http://www.turtleseg.org/	supports image formats such as DICOM, NIFTI, MINC, METAIMAGE and Analyze	Live-wire	Semi-automatic and presents problems when dealing with missing or diffused contours

Table 2.1: List of the available brain segmentation software developed for adult data (accessed 27/06/2013).

are sensitive to missing and diffused contours or rely on shape and structure, they have not been regarded suitable for infant brain segmentation.

In Section 2.2 template and atlas-based techniques were described. These methods have the advantage that prior knowledge of anatomical structure, location and shape is used for brain segmentation. In the presence of low contrast between different brain tissue, the atlas-based methods are an efficient choice. In brain segmentation, an atlas brings a common anatomical map of the brain to guide the segmentation. Since atlases are population specific, these methods generate erroneous segmentation when applied to brain MRI data of infants with anatomical abnormalities. Further, the quality of the atlas, which is dependent on large segmented databases, is crucial for a satisfactory segmentation. Apart from the quality of the atlas, the accuracy of these methods is influenced by the precision of the registration procedure, which has demonstrated limitations when applied to infant brain MRI data.

Basic intensity-based methods such as histogram analysis are useful for data with a strong contrast differentiation, which is characteristic for adult brain data but not for infant MR images. To improve performance, the watershed method has also been applied to medical images but tends to result in over-segmentation. The more popular methods are fuzzy clustering and EM segmentation, which have produced accurate results when used for brain MRI segmentation. FCM and EM are well-known for potentially getting trapped in local minima. The recent trend in infant brain segmentation is to implement the atlas-based EM technique. Due to the fact that the EM method has provided accurate results in processing infant brain MRI data, this study will further advance the application of the EM algorithm to premature infant data. A limitation of the atlas-based segmentation is the registration error. To avoid this limitation in the approach discussed in this thesis, the anatomical knowledge is locally used in various stages of the segmentation process.

The final section of this chapter gave an overview of popular applications developed for processing medical images. Some of these applications have been tested on our database and the results will be described throughout this thesis. Their main limitation is that none of them was developed and tested for the use of infant brain MRI data. Adult brain images provide a strong contrast between tissues and clear contours, which is not the case in infant data. For this reason, techniques developed for adult data generate incorrect results.

Chapter 3

Brain Extraction

3.1 Introduction

The previous chapter presented an outline on the state-of-the-art techniques of the brain MRI segmentation algorithms. Summarising all techniques, there are two major types of infant brain MRI segmentation. The first category of methods start with a registration procedure, for example as presented by Murgasova et al. [91] where after registering the data to an atlas, the bias field correction and segmentation are simultaneously performed using an EM algorithm. The second category of brain segmentation techniques include three steps, which consist of brain extraction, bias field correction and segmentation.

A common way of processing infant brain MRI is to bias the segmentation process with anatomic prior knowledge such as an atlas. Due to the lack of an available atlas for infant MRI data, the segmentation task described in this thesis is divided into three main steps. Firstly, a brain extraction algorithm is proposed, in which all non-brain tissues are removed. Secondly, a developed bias field correction method is presented, in which the intensity inhomogeneity within an image is adjusted and, finally, the brain tissue is segmented by introducing a white matter segmentation procedure.

This chapter will introduce the first stage of the brain segmentation, which involves the extraction of the brain tissue. This procedure is called brain extraction or skull stripping and requires the removal of all non-brain tissue such as skull, fat and cerebrospinal fluid parts. Consequently, the extracted region consists of the cortical grey matter, white matter, deep grey matter and cerebellum. The use of automatic skull stripping facilitates and speeds up the overall segmentation process. Due to inconsistencies in the MR images, brain extraction remains an essential and difficult step in brain segmentation. It is clear that due to the early development stage of the brain structure, this task is more challenging when using infant brain MRI data. This was outlined in Section 1.1 by introducing the differences in the anatomical structure between adult and infant brains.

Over the past thirteen years, various techniques have been proposed for unsupervised skull stripping such as histogram-based [15] [107], region-based [55] [109], boundary-based [113], graph-cut based [101], fuzzy-based [70] or hybrid approaches [105] [33]. Rehm et al. [98] divided some of the Brain Extraction Algorithms (BEA) into different categories such as intensity thresholding, edge detection, atlas based, deformable models and hybrid models. Most skull stripping approaches were developed for adult brain MRI and are outlined in this section. Many researchers who performed infant brain segmentation did not employ brain extraction because the procedure can be accomplished in a probabilistic classification by embedding prior knowledge such as atlases. For this reason, only a few brain extraction algorithms with the focus on infant data were developed and they will be explained after the description of the adult brain segmentation algorithms.

Intensity-based segmentation is a common way to extract the brain tissue. Shanthi and Kumar [107] propose to identify the brain and non-brain tissues using an histogram analysis. The use of T1-weighted axial MR images of adults has been chosen, because according to the authors, out of all data in their database these MR sequences have shown the best resolution. Balan et al. [15] expanded the histogram analysis method by adding binary mathematical morphology. This technique is based on the search of minima which are positioned in the intensity between two local maxima in a histogram. The background was removed using histogram partitioning. This partitioning was applied a second time on the resulting images to extract the brain tissue. At this stage, most of the brain tissue had been extracted. In order to finalise the results, the images are processed by simple morphological operations such as erosion, connectivity analysis, dilation and closing. Saha et al. [103] also applied histogram analysis for brain extraction. This method is based on histogram feature analysis, which is based on a visual inspection using the knowledge that the different regions of interest are distinct and, therefore, easily identifiable. In their brain extraction results, the CSF is not removed. Due to the complex anatomical structure of infant MRI data, a histogram analysis technique alone is not sufficient for accurate brain extraction. A more complex algorithm was proposed by Somasundaram and Kalavathi [115], who presented a brain extraction algorithm which is based on noise reduction by applying the mean filter, determining a primary mask for brain tissue and refining this mask by using a erosion operator. They improved their technique by adding 3D information to connect the multiple regions into a single brain tissue volume [114].

Another attempt to extract the brain tissue was made using a watershed algorithm. An example, is the algorithm proposed by Hahn and Peitgen [55] where the authors developed a 3D watershed algorithm for brain segmentation. In order to avoid the problems generated by intensity inhomogeneities and noise, the technique performs pre-flooding where the basins are filled to a certain height. Segonne et al. [105] extended Hahn and Peitgen's [55] technique by combining the watershed with a deformable surface technique to develop a robust skull-stripping approach. First, T1-weighted MRIs are analysed to localise a single white matter voxel to create a global minimum in the white matter. Then, the watershed algorithm is applied to 3D data to estimate the brain volume. At this stage, the algorithm generates a brain volume which includes most of the brain tissue and is followed by the application of an atlas-based contour model to correct the initial segmentation results. The final step is performed using a deformation-based surface model. After testing the algorithm on a dataset of 43 subjects, the authors stated that this method performs well even if the image is corrupted with noise. Rajagopalan et al. [97] designed a technique that uses a 3D watershed for an initial extraction of the brain tissue. In the second step, a parameter projection of T2-weighted to T1-weighted MRI space was applied, on which the watershed algorithm was performed to extract the final brain tissue volume. The authors' aim is to focus on the use of T2-weighted MR images. The watershed algorithm produced satisfactory results when used for brain extraction in adult MRI datasets. The reason for this is the clear identification of the CSF which surrounds the brain tissue. In infant brain MR images, the CSF surrounding the brain tissue can be so small that, due to partial volumes and noise, it appears that the skull is attached to the brain tissue.

Some of the well-established brain extraction methods have been embedded in software tools such as BrainSuite [108], SPM8 [116], MRIcroN [99] or FMRIB Software Library (FSL) [40] [112]. At this time, three state-of-the-art approaches outperform all the other developed methods. These are: Brain Surface Extraction, Brain Extraction Tool and Statistical Parametric Mapping, and they have been frequently used for comparison and testing.

Brain Surface Extraction (BSE) [109] is one of the well-established BEA and is integrated in the BrainSuite tool. BSE is an edge-based method which executes an anisotropic diffusion filter, followed by a Marr and Hildreth edge detector. The final segmentation is obtained by applying morphological operators to the edge map to enable the removal of the non-brain tissue. Zhao et al. [134] modified this method by replacing the edge detection step with a threshold and skeletonisation technique.

The second well-established BEA is embedded into the MRIcroN and FSL tool and is called Brain Extraction Tool (BET) [113]. This method is based on estimating the intensity threshold of the brain and non-brain regions, and it then determines the centre of gravity of the brain volume. This is followed by the definition of an initial sphere, which is based on the previously calculated centre of gravity. Finally, the technique deforms the initial sphere outwards to attach to the brain tissue boundaries. Lee et al. [75] compared the BET and BSE by testing 20 datasets of T1-weighted MRIs. The authors concluded that BSE is sensitive to the initial set of parameters. On the other hand, the BET yielded high false positive and false negative measurements because the technique was not able to eliminate all non-brain tissue such as the neck; furthermore, some of the brain tissue was incorrectly removed.

The third well-known brain segmentation approach is called Statistical Parametric Mapping (SPM) [46] and consists of registration, normalisation and segmentation steps. Realigning and normalisation were performed to transform the volume into the Talairach space [119]. As previously explained in Chapter 2, the segmentation extracts three regions (GM, WM and CSF) and for each region a volume image is generated. SPM is the only technique of these three which was not developed as a brain extraction approach in the first place since this technique was designed for GM-WM-CSF tissue segmentation. As SPM is one of the most popular tools to process medical brain images, an investigation was carried out on segmenting infant brain MRI using SPM. SPM does not include a brain extraction algorithm, but to analyse its performance when used for infant data, the white matter and grey matter results were combined in order to construct the brain tissue volume.

The outcome of this investigation is described in Appendix A. The skull stripping approaches developed for adult brain data rely on clear distinctions between brain tissue and non-brain tissue, which are indicated by strong contrast and boundaries. This is not the case in infant data and, therefore, these methods produce false segmentation when applied to neonatal brain MR images.

With regard to infant data, many researchers developed probabilistic approaches where a brain extraction algorithm is not required. However, a few researchers designed skull stripping algorithms with the focus on processing infant brain data. The brain extraction from infant brain MR images presents greater challenges than the adult brain MRI data. These challenges are, for example, the unclear boundaries between the brain tissue and the non-brain tissue, the high level of noise and intensity inhomogeneities that are present in infant MRI data. Only a few infant brain extraction methods have been developed. One of these approaches was proposed by Chiverton et al. [33], who presented a brain extraction algorithm that first removes the background using region growing and then applies parameter estimation to fit an intensity Gaussian Mixture Model to a predefined histogram. A 2D mask is created by using thresholding and region growing. The final segmentation is achieved using 3D morphological erosion and dilation operators and connectivity analysis. The results indicate a high level of errors when intensity ranges of different tissues overlap. This causes under-segmentation due to incorrect parameter estimation. Despotovic et al. [42] developed an approach that combines histogram analysis, morphological operators and active contours. Various steps are based on the combination of partial results obtained from T1 and T2-weighted MR images. As a consequence, the algorithm relies on the quality of the registration which is used in the pre-processing step. This algorithm is not suitable to address the intensity overlapping between WM and GM, which are common in infant brain MRI data. Kobashi et al. [70] used fuzzy rule-based active surface models. A surface model was achieved by connecting triangles and by allowing the surface to be deformed. The positions of the triangles were defined using fuzzy IF-THEN rules. The outcome revealed that small non-brain tissue parts remain in the extracted region. Additionally, the technique has not excluded the CSF from the segmented area. Mahapatra et al. [82] proposed a graph cut method with the aim of incorporating prior shape information from a pre-constructed atlas. The atlas is based on manually segmented datasets and is applied during the pre-processing step to identify the threshold between the background and the brain tissue. In addition to shape information, the gradient information is used during the segmentation process in order to optimise the graph cut algorithm. The approach was tested on 20 T2-weighted infant MRI data acquired with a 3T scanner and 77 T1-weighted adult MR images acquired with a 1.5T scanner. The results indicate over-segmentation in regions with low contrast and diffused contours.

The aim of this chapter is to present a novel skull stripping algorithm for infant brain MR images. The next section introduces an overview on the structure of the proposed technique. This is followed by a section on pre-processing, whose objective is to simplify the brain segmentation process. Section 3.4 describes the process of identifying the outer contour of the brain tissue in order to support the segmentation algorithm presented in Section 3.5. Two post-processing steps are required to refine the segmentation results and are presented in Section 3.6. Section 3.7 presents a numerical evaluation of the proposed approach. A numerical comparison between the three well-established brain extraction algorithms (BSE, BET and SPM) is presented in Appendix A. In the case of SPM, the resulting volumes of GM and WM were combined into one volume to obtain the skull stripping volume and then compared against the automatically segmentation results of the proposed approach. The outcome of this investigation demonstrates that the methods developed for adult data show false segmentation due to remaining non-brain tissue in the brain volume.

3.2 Overview

In the previous section, the challenges related to the extraction of the brain tissue in infant brain MRI data were outlined. Due to the large number of inconsistencies within the brain area that are caused by noise, artefacts, unclear boundaries and intensity inhomogeneities, the brain extraction procedure is a complex task. This section outlines the steps of the proposed brain extraction technique, which is composed of a mixture of 2D and 3D algorithms.

The first step deals with the attenuation of the intensity inconsistencies within the brain MR images, which arise during the image acquisition. This step is divided into two phases. Firstly, the image is filtered to reduce noise while maintaining the edges of each region. This has been solved using an anisotropic diffusion filter. The second part of the contrast standardisation implies an intensity adjustment within a patient sequence. In order to remove the intensity shifts between slices throughout the volume, a histogram analysis was applied. Both pre-processing steps are necessary to simplify the following segmentation process.

The contrast optimisation step is followed by the generation of a binary mask. Due to the fact that the shape and size of the premature infants' brain may vary, the binary mask has to be generated for each patient individually. The mask that is constructed in 3D is created in three steps. The first step aims to reduce the partial volume effects between the brain tissue and the skull and fat. In the second phase, small objects which are not connected to the main brain region are removed. Finally, edge detection identifies the outer boundaries of the brain tissues. This facilitates the removal of the CSF which surrounds the main brain region. Before the RoI is segmented using a 3D region growing algorithm, a seedpoint is automatically defined. At the same time, a threshold for each individual image in the volume is calculated. This allows a more precise discrimination between the brain and non-brain tissues. After the identification of the RoI, the final step is applied to refine the outer edges.

Figure 3.1 presents an overview of the main components of the developed approach and in the following sections each step of our developed approach is described in detail.

3.3 Data Pre-Processing

One challenge is generated by the inter-patient inconsistencies and intensity variations throughout the patient volumes which is caused after converting the MR signals into MR images. In MRI, the grey scale value attributed to a voxel depends on the relative

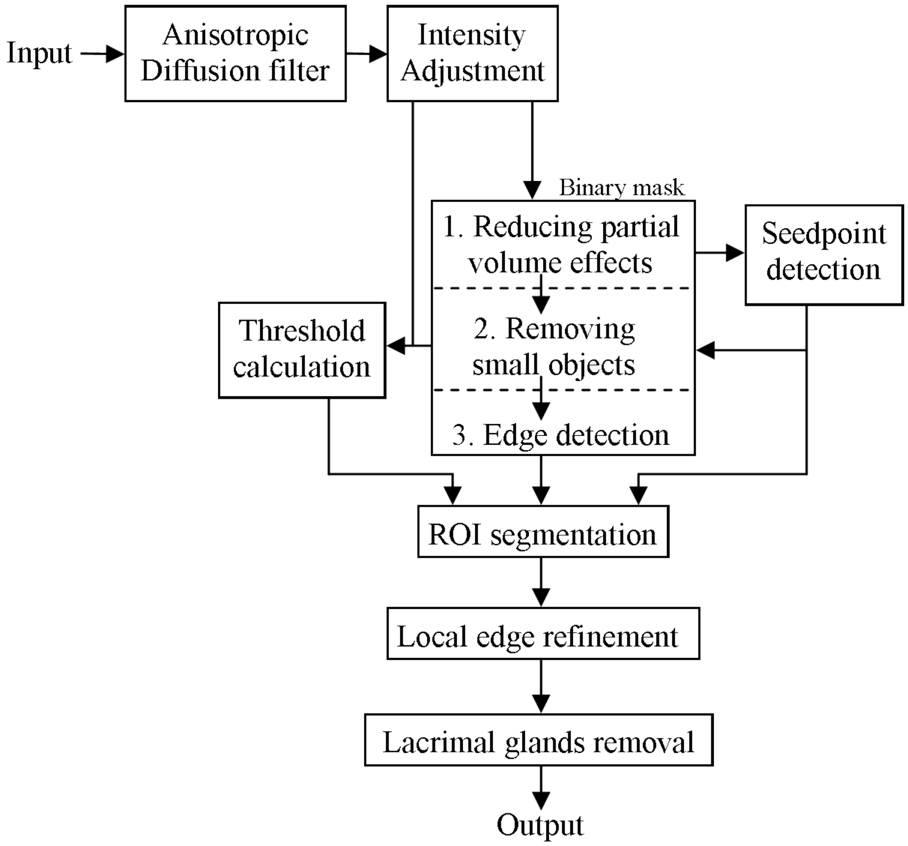

Figure 3.1: An overview of the skull stripping algorithm.

T2 values in other voxels, and is therefore not absolute. This is a relative process in a particular sequence or even within a single image and it is not similar across patients or different scans over time. For this reason, the intensity is manually adjusted by the clinical expert and this procedure is called windowing. The clinicians adjust the image intensities through a visual examination and in turn this may generate intensity inconsistencies. The intensity differences with and without windowing can be observed in Figure 3.2.

In order to avoid the user interaction in the proposed approach, the intensity range of the volume is calculated and each image is then adjusted to the same range. In order to address the noise and intensity variations, a two-step procedure was applied. The first step addresses the noise reduction while preserving the edges in the images as described in Section 3.3.1. The second step deals with the adjustment of intensity changes in all slices of the dataset as presented in Section 3.3.2.

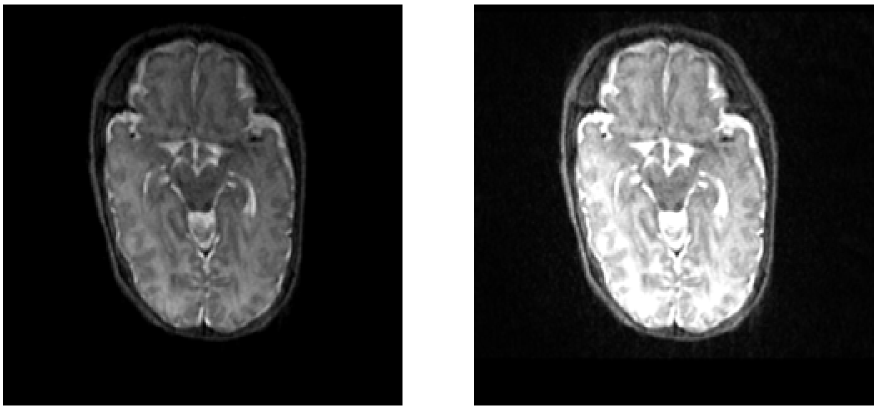

Figure 3.2: Two images of the same patient. In the left image the intensity is manually adjusted, while the intensity of the right image has not been adjusted.

3.3.1 Coherence Enhancing Diffusion Filter

MRI data is associated with noise artefacts which arise during the MRI acquisition. In order to acquire the brain data from a newborn, the patient has to be scanned using a high resolution, which leads to a high noise level and stronger partial volume effects [48] [52]. In the presence of a considerable amount of noise, the detection of anatomical structures emerges as a difficult task. Especially in infant MRI data, the strength of edges is substantially reduced and the level of noise and partial volume effects is high, which leads to a computationally demanding segmentation.

An anisotropic diffusion filter [109] [134] can significantly improve the image quality by removing the noise while preserving the edge details. The most common utilised filter in brain segmentation is the Perona-Malik filter [93]. Most nonlinear diffusion filters use a scale diffusivity and, therefore, remain isotropic. As a consequence, the information of diffused contours and partial volume regions are weakened. An investigation was performed by applying the Perona-Malik filter on our database. The outcome revealed several limitations by demonstrating the disappearance of useful information. For this reason, the Coherence Enhancing Diffusion Filter (CED) proposed by Weickert [128] was investigated. This filter allows the removal of noise without eliminating any useful information. Instead of using a scalar diffusion coefficient, this filter is guided by a diffusion tensor, which allows to optimally adjust the diffusion process in different directions. In this way, weak edges are maintained in the image. For this reason, the images are processed with the CED in order to facilitate the application of an edge detection method at a later stage as indicated in Section 3.4.

The CED algorithm is a noise reduction method in which a nonlinear diffusion filter is controlled by a structure tensor. The anisotropic diffusion equation is mathematically defined as follows:

$$\frac{\delta u}{\delta t} = div(D \times \bigtriangledown u) \tag{3.1}$$

where u is the input image, t denotes the time, div the divergence operator, $\bigtriangledown u$ describes the gradient of the image and D is the diffusion tensor. The diffusion tensor D is defined as a function of the structure tensor J_ρ, which is described as follows:

$$J_\rho(\bigtriangledown u_\rho) = K_\rho * (\bigtriangledown u_\sigma \bigtriangledown u_\sigma^T) \tag{3.2}$$

where K_ρ denotes the Gaussian kernel, ρ is the integration scale that controls the size of the Gaussian Kernel K_ρ is calculated and $\bigtriangledown u_\sigma$ is the gradient of the Gaussian-smoothed version of u_σ. In order to enhance the coherent structure, the smoothing should be performed along the coherence directions with a diffusivity λ. In m dimension, the eigenvalues are chosen by designing D so that it has the same eigenvectors v_1 and v_2 as J_ρ:

$$\lambda_1 = \alpha, \tag{3.3}$$

$$\lambda_2 = \begin{cases} \alpha, & if\ \mu_1 = \mu_2 \\ \alpha + (1-\alpha)\exp\left(\frac{-C}{(\mu_1-\mu_2)^{2m}}\right) & else \end{cases} \tag{3.4}$$

where α is a small positive parameter $\alpha \in (0,1)$ which defines the strength of the smoothing along the direction of the corresponding eigenvectors and C is a constant that influences the strength of the coherence. μ_1 and μ_2 are the corresponding eigenvalues of the eigenvectors v_1 and v_2 from J_ρ. The expression $(\mu_1 - \mu_2)$ is a measure of the local coherence.

The CED parameters were set to the following values: $\sigma = 0.5$, $C = 1$, $\alpha = 0.001$. By increasing the noise scale σ, a stronger blurring occurs, which leads to difficulties when enhancing the contours. The integration scale parameter ρ controls the size of the Gaussian Kernel K_ρ and is usually set to a larger value than σ. The author has set the variable ρ at 2,4 and 6 when investigating different types of images. A strong increase of ρ leads to a strong flow-like character in the image, which may have an impact on the segmentation procedure. The best results on the database of this study were obtained when $\rho = 4$. Figure 3.3 displays an image where the CED algorithm was applied using different time parameters. When applying a larger time step size t value, the image reveals some artefacts.

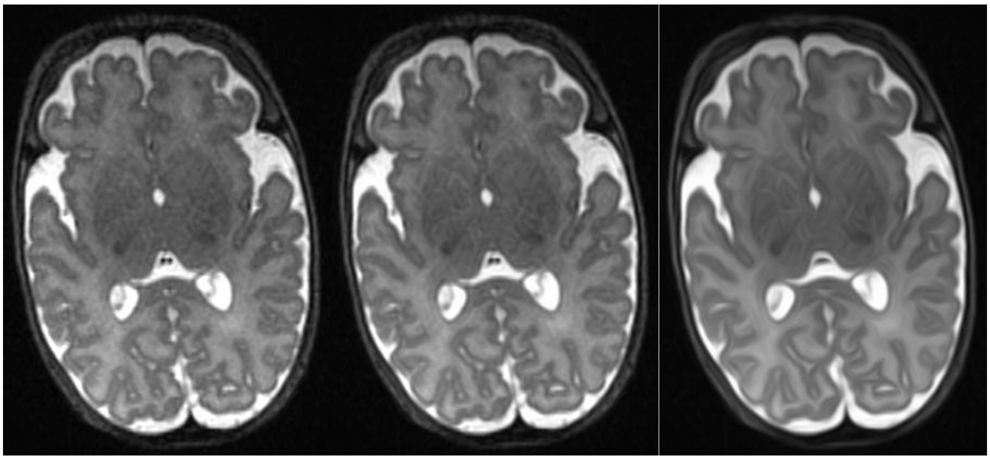

Figure 3.3: The left image shows an example of the original MR image, the other images are results after applying the CED filter using different diffusion parameters; second image: t=1; third image: t=10.

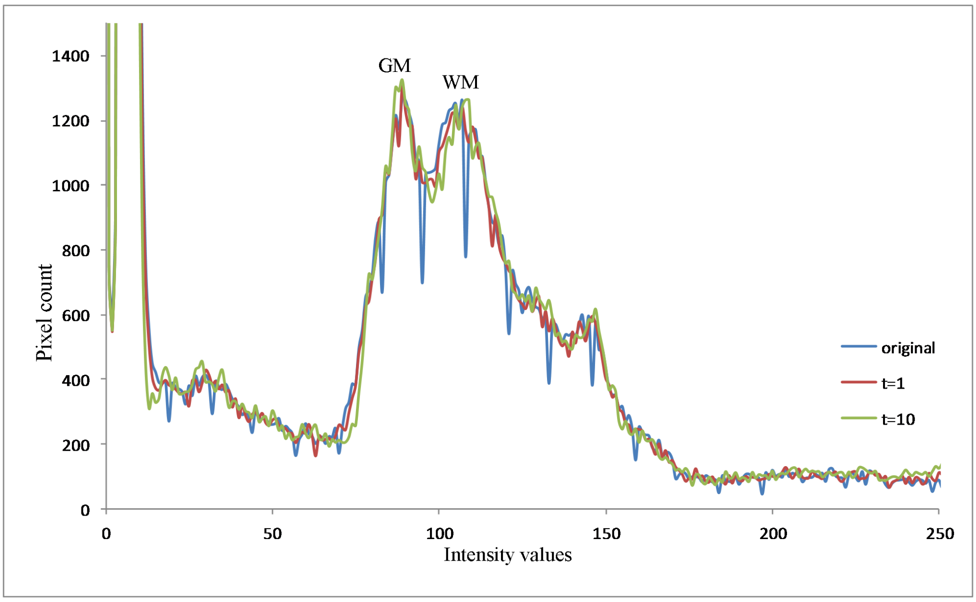

Figure 3.4: A representation of the intensity distributions after the application of the coherence enhancing diffusion filter using different diffusion times.

Figure 3.4 illustrates the intensity variations given by the use of the CED algorithm when the diffusion time is varied as shown in Figure 3.3. According to this finding, the diffusion time should be set high to smooth the image and enhance edges. However, after further investigations, results have shown that due to partial volume effects important information is lost when the diffusion time is too large. An example is presented in Figure 3.6, which shows edge attenuation when t increases.

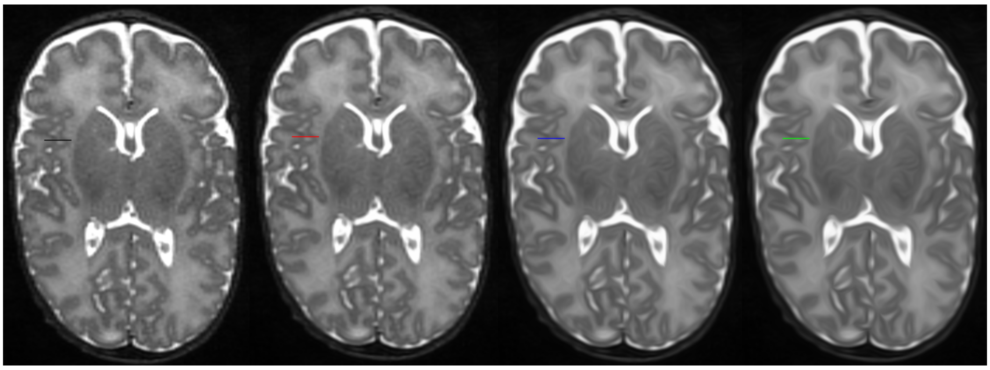

Figure 3.5: Left image shows an example of the original MR image, the other images are the results after applying the CED filter using different diffusion parameters; second image: t=1; third image: t=5; fourth image: t=10.

In this study, the diffusion time was set to 1 since this setting has strongly reduced the noise without the appearance of flow-like structures and the reduction of useful information due to partial volume effects.

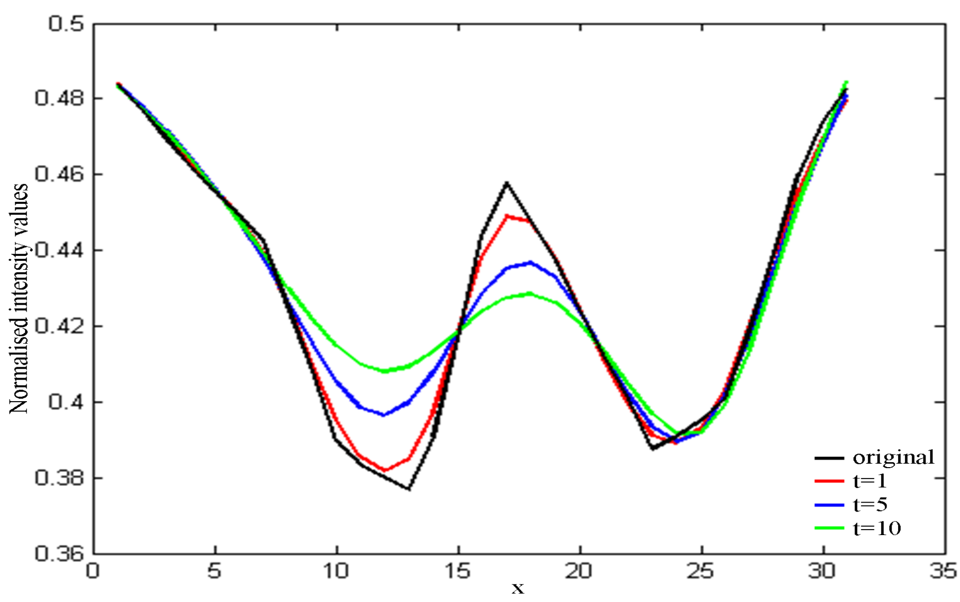

Figure 3.6: Results of the coherence enhancing diffusion using different diffusion times. The coloured lines represent the intensity values in the x-direction of the region marked in Figure 3.5, and the black line describes the changes in intensity values on the original image. The larger the diffusion time value is set, the stronger the image is smoothed with the risk of loosing information.

3.3.2 Intensity Standardisation

Due to the characteristics of the MRI acquisition procedure, MR images include intensity inconsistencies. One inconsistency is called bias field and consists of intensity inhomogeneities within each image in the volume. The second challenge is generated by the intensity changes between one patient and another and also across a data sequence. The aim of this step is to automatically adjust the intensities of the brain tissue into the same range throughout a patient sequence. Thus, the algorithm sets the intensity of various patients into the same grey level range.

As mentioned in Chapter 2, several researchers used histogram analysis to extract a threshold for the brain tissue segmentation. In infant brain MRI the intensities of the different regions tend to overlap, which complicates the segmentation process. This challenge was described in Section 1.2.1. Additionally, the intensity range of the brain tissue tends to change from one image to the next within the brain volume. This is caused by a high and inconsistent distributed water content in the brain tissue. For this reason, the focus of intensity standardisation is on locating the intensity range of the brain tissue in each image of the volume.

In the first step, the background is removed by employing a thresholding procedure where all background pixels are set to 0. This is obtained by localising all pixels with a lower value than the local minima detected between 0 and 10,000. In the second step, the intensity of the foreground region is automatically adjusted in each image individually. The approximate region of the brain tissue is detected using histogram analysis. The histogram analysis is important since it allows the adjustment of the intensity ranges as well as to receive useful information about the brain tissue, which will be further evaluated throughout this study. In each histogram, one local maximum and two local minima of the RoI are detected using a min-max search. By knowing the location of the RoI in the histogram, the region is shifted into the same intensity range for each image. To avoid a cut-off in the bright intensity, that area will be stretched out, so that a smooth transition is still maintained. Figure 3.7 presents an example where an image is taken before and after the intensity adjustment.

The approximate RoI lies between two local minima that are clearly visible in this histogram (see Figure 3.7). The intensity range in a MR image lies between 0 and 65,535. The histogram also illustrates the removal of the background pixels which are set to 0 after performing a thresholding procedure. Due to the left shift of the brain tissue intensity range, the distinction between brain tissue and CSF is strengthened which can be observed towards the high intensity values in the histogram.

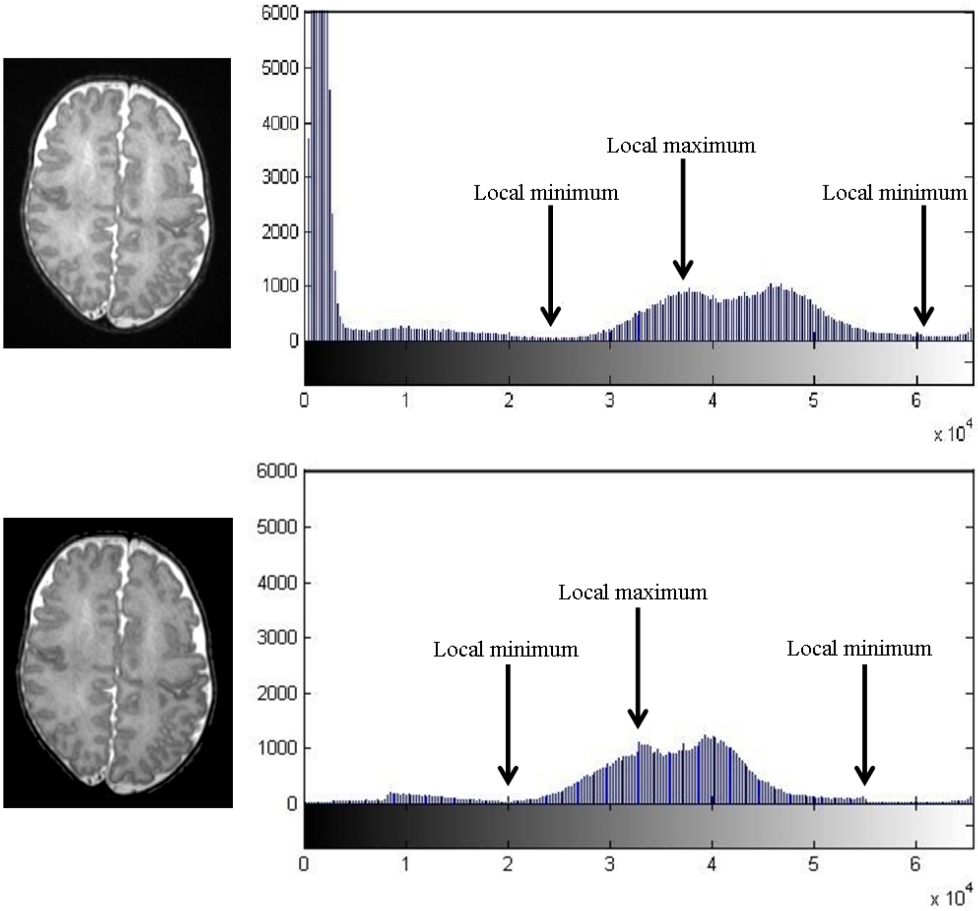

Figure 3.7: Left: a sample and its associated histogram before applying the intensity adjustment; the resulting image after the intensity adjustment was applied. The local maximum is expected to represent the grey matter tissue, which is set to the middle of the entire intensity range.

The histogram analysis is applied twice. During the first iteration, an approximation of the brain tissue volume is computed from each image starting with the first image in the sequence. In this way, the local maximum and minima are computed without any associations with the calculated values in the previously processed image. Due to a high amount of non-brain parts in the first images of the sequence, the estimation of the maximum and minima values can be incorrect, which is illustrated in Figure 3.8. In the second iteration, the analysis starts on the image with the largest number of brain tissue pixels. This is done because the image with the largest brain tissue includes the smallest number of non-brain tissue pixels and the intensity distribution facilitates the localisation of the brain tissue intensities. The measurement of the maximum and minima values for the contiguous images is based on the previous calculations, which results in a more precise detection of the RoI. This can be observed in Figure 3.8. The graph illustrates the region of interest determined in the first iteration (displayed in blue), which was not homogeneous and the detection of the brain tissue was not accurate in the first few images of the sequence. The first iteration is important for two reasons. First, to find the image with the largest brain tissue volume which is later used during the seedpoint detection. Second, the initial measurement of the brain tissue volume in each image is used as a guidance during the second iteration. The high number of non-brain tissues in the first images of the volume is the reason for an incorrectly determined threshold. The adjustment of the intensity does not mean that each region has the same intensity throughout the volume but it implies that each region can be expected to have a normalised intensity range. The problem which remains to be addressed is that the GM and WM still overlap in their intensity ranges.

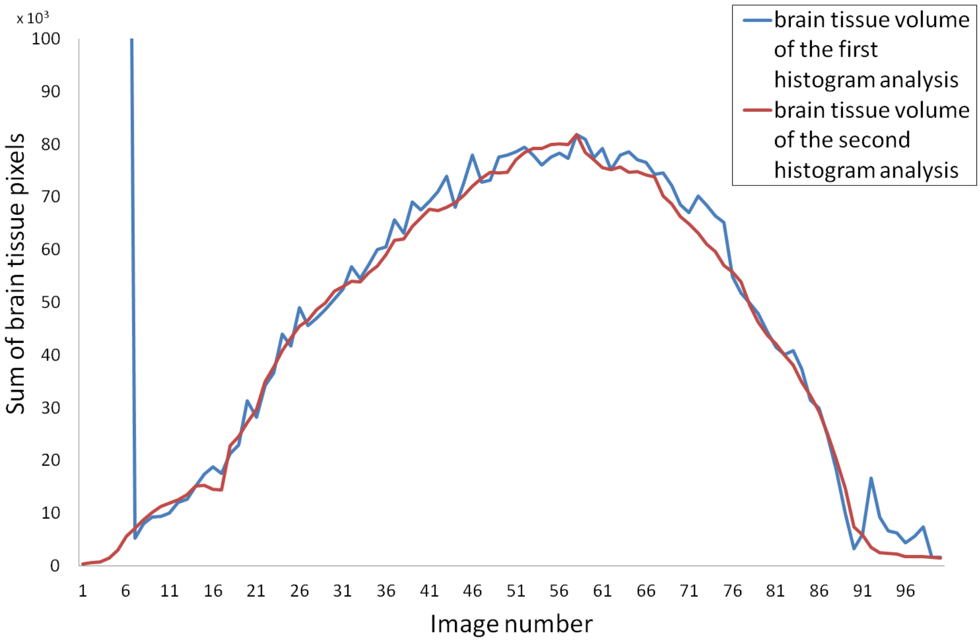

Figure 3.8: Improvements in the calculation of the brain tissue volume by comparing the results of the first and the second histogram analysis. The blue line presents the results of the first histogram analysis. The red line describes the outcome of the second histogram analysis which is smoother and more precise because the calculation of each image relies on the results obtained in the previous processed image in the volume.

3.4 Mask Extraction

The purpose of generating a mask for each patient is to find the outer contours which differentiate the brain tissue from the non-brain tissue. This idea has been applied by many researchers [109] [33] [115] in order to improve the removal of the non-brain tissue. In this study, the three steps illustrated in Figure 3.1 are required to generate the final mask, and they are defined as follows:

1. Reduction of errors caused by partial volume effects
2. Removal of small disconnected objects
3. Edge detection

In the first stage, a primary mask of the brain region is constructed with the intention of reducing the partial volume effects between brain and non-brain tissue. This is achieved by bringing the region of interest into the foreground and the other regions into the background using erosion and dilation operators with a kernel size of 20 voxels. In the output image, the foreground region will be defined by different intensity values when compared to the background region. The bias field can prevent the removal of all non-brain tissues due to intensity changes across images. An estimation of the presence of the bias field is obtained by applying the K-means algorithm (described in Equation 3.8) on each image using three clusters. The first class describes all background pixels, the second class includes the entire grey matter tissue and the third class contains all white matter pixels. In relation to the grey matter, in each image the detected foreground is divided into three parts in the y-axis direction. The estimation of the bias field is computed by comparing the percentage p of the grey matter existent in the top part of the image gt against the grey matter pixels located in the bottom part of the image gb using the following formula:

$$p = \left(\sum_{N} \left| \frac{\sum gt}{\sum ga} - \frac{\sum gb}{\sum ga} \right| \right) / N \tag{3.5}$$

where ga denotes all grey matter pixels in the image and N is the number of images. Note that the closer p is to zero, the less the volume is corrupted by intensity inhomogeneity. After performing a large number of experiments, it has been deduced that a minor presence of intensity changes has no impact on the brain extraction algorithm. Therefore, the volumes with a p higher than 0.1 are regarded as affected by bias field. In cases where no intensity inhomogeneity is contained in the image, the image is processed individually. However, if the bias field is present, each part of the divided image is processed by removing the remaining non-brain parts.

For each image in the volume a histogram is calculated. In order to find the lower grey intensity threshold, the smallest count of grey intensity values is taken where the grey intensity is larger than the local minimum (calculated in Section 3.3.2). In this way, the background is separated from the grey matter tissue. All pixels which have a lower intensity than the calculated threshold are set as background.

The purpose of the second step is to remove regions such as the eyes. In T2-weighted MRI data, the body parts such as the eyes and teeth appear as high intensity pixels. Consequently, these areas are still maintained in the volume after histogram analysis. Knowing that the brain tissue is always connected, this step focuses on removing all disconnected regions using a fast 3D binary region growing algorithm. The automated seedpoint detection executed in the second step is explained in Section 3.5.

In order to generate the final brain mask, the Marr and Hildreth edge detector [85] is applied on the second mask, which was first modified by projecting the intensity values on the RoI, and enhancing them using Equation 3.9. The Marr and Hildreth edge detector has proven successful when applied on adult brain extraction techniques [109] and was considered in this study. Advantages of employing this edge detection are its low computational cost and its affinity to return closed contours. Other edge detection algorithms such as the Canny edge detection can be applied instead. However, in some regions the edges produced by Canny are not closed and multiple edges can appear in the same region due to the low resolution of the image, which can complicate the detection of the correct anatomical boundaries.

The Marr-Hildreth edge detector first runs a Gaussian low pass filter followed by detecting the boundaries using the Laplacian edge operator.

$$C(k) = \nabla^2(G_\sigma(q) * I(k)) = \nabla^2 G_\sigma(q) * I(k) \tag{3.6}$$

$$G_\sigma(q) = \frac{1}{\sqrt{2\pi}\sigma} \exp^{-\frac{\|q\|^2}{2\sigma^2}} \tag{3.7}$$

where I is the input image, q indicates the point in the volume, ∇^2 is the Laplacian operator, * denotes the convolution operator and G describes the Gaussian kernel with the variance σ, which was set to 2. When increasing the value of σ, the blurring kernel gets wider and only strong edges such as those between the grey matter and the CSF, remain in the image. In infant brain MR images, the CSF between the grey matter and skull is not always clear and the boundaries are diffused. When the σ values are small, then the narrow filters produce more edges in the images. The purpose of this final step is to remove the large fluid areas that are located on the outside of the brain region. Due to partial volume effects and diffused boundaries, in some cases the edge detector may not find the correct contours and it may find edges between the grey matter and the white matter. This problem was also described by Shattuck et al. [109] and was overcome by using morphological closing operation.

The images corresponding to each mask generation step are given in Figure 3.9, starting with the original image followed by the first mask, second mask and third mask. In the proposed algorithm, the generation of the binary mask is essential since it will be used as a boundary stopping condition in the next procedure.

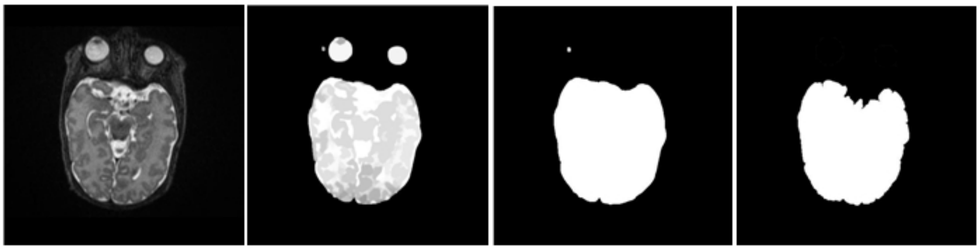

Figure 3.9: Images detailing each mask step, starting with the original image, followed by the first mask, second mask and the final mask. The small bright part visible in the third image is a leftover of the lacrimal glands.

3.5 Region of Interest Segmentation

The segmentation of the brain tissue is performed by applying a region growing algorithm to the previous extracted information. The region growing method includes the neighbourhood pixels which fit specific criteria. Figure 3.10 illustrates each component needed for the segmentation of the brain tissue.

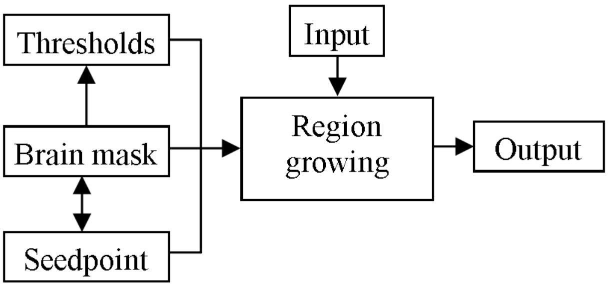

Figure 3.10: Overview of each step of the brain tissue segmentation using a region growing algorithm.

The technique starts at an initialised pixel called seedpoint. During the intensity adjustment, the seedpoint in the z-axis direction is determined by selecting the image with the largest connected region of the brain tissue. Within the image where the seedpoint z is selected, the x and y coordinates are obtained by extracting the largest connected region associated with the dominant intensity, which is retrieved as the local maximum in the histogram. One pixel will be taken from the extracted region and defined as seedpoint with the coordinate (x,y,z).

To extract the RoI, a region growing algorithm is applied on the MRI sequence. Pohle et al. [94] proposed an adaptive region growing algorithm to segment regions in medical images using two runs of the region growing. However, if particular conditions such as shape differences or intensity changes within the region of interest are not well defined, then the method does not work sufficiently well. Li et al. [78] proposed a different region growing method to address this problem. Therefore, an adaptive threshold, which is based on the mean value and standard deviation of the RoI, is used to classify the current pixel into brain tissue or non-brain tissue classes.

Different thresholds have been examined in this study such as the adaptive threshold proposed by Li et al. [78] and those based on estimated tissue values. These thresholds have generated erroneous segmentation in several volumes. It was concluded that the use of one threshold for the entire volume is not as efficient as calculating thresholds for each slice individually. The range of the intensity values in the RoI is still large. By finding a threshold in each image, the segmentation for different parts of the volume can be determined more precisely. During the seedpoint detection within the brain extraction procedure, Gui et al. [52] successfully performed a K-means thresholding algorithm on neonatal brain MR images. In the proposed approach the K-means algorithm is applied to calculate the threshold values for each image. The K-means is a clustering technique which iteratively partitions the data into a number of clusters (or classes). The clustering process ends when no elements are exchanged between clusters and is mathematically described as follows:

$$J = \sum_{j=1}^{K} \sum_{n \in S_j} |q_n - \mu_j|^2 \tag{3.8}$$

where the data points are clustered into K disjoint classes S_j each containing n_j data points, where q_n is the observation and μ_j is the centroid of the data points in the cluster S_j.

After several investigations, it became clear that three clusters (background, brain tissue and CSF) were not sufficient for an accurate extraction. The best results were empirically obtained with a total of eight clusters, which were assigned to partition the intensity range in each image. The idea was to better divide the large brain tissue intensity range in order to achieve a more precise threshold estimation for the extraction of the brain tissue.

This detailed investigation was performed on a large database in order to examine the variations of the K-means results while changing the cluster number. Figure 3.11 illustrates an example when using the K-Means with different number of clusters on a brain MR image.

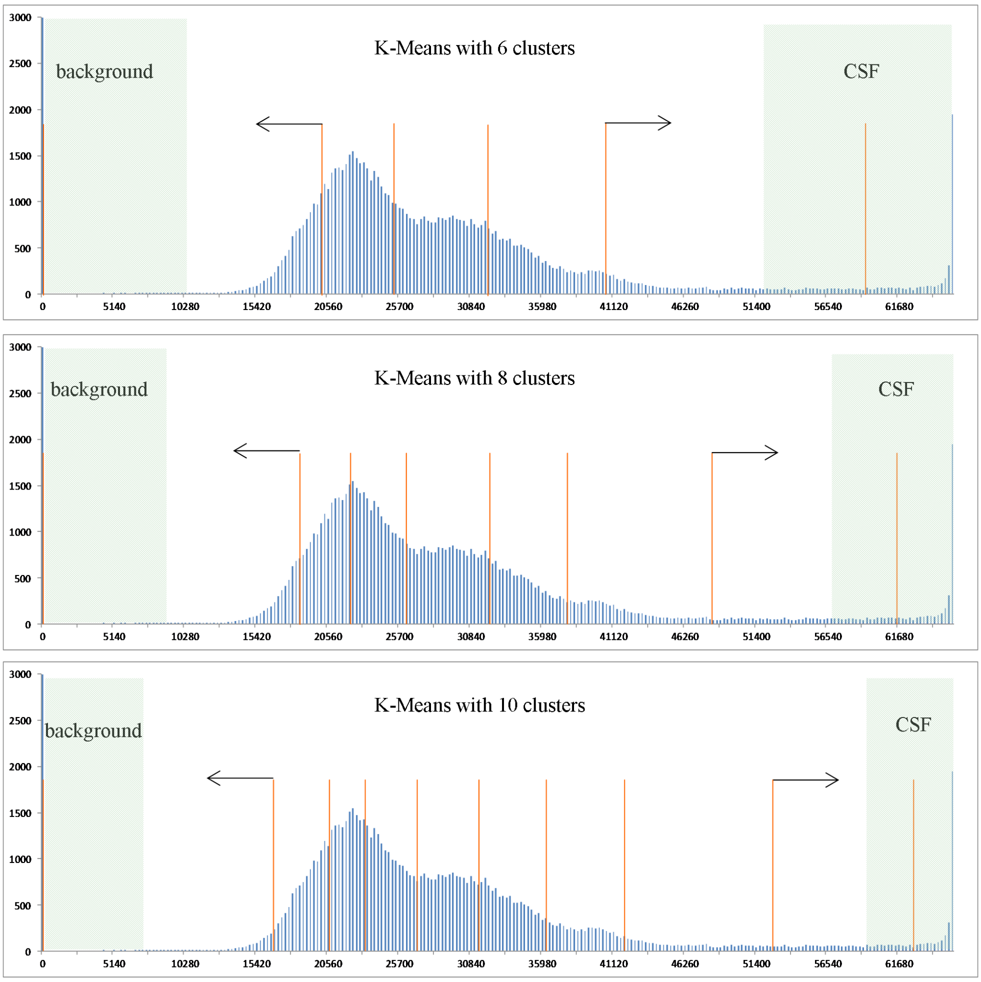

Figure 3.11: The histogram of one brain MR image illustrates the threshold results of the K-Means algorithm when it was used with different number of clusters. The focus lies on the threshold between the brain tissue and non-brain tissue (background and CSF). The black arrows indicate that if a larger number of clusters is used then the region of the brain tissue is larger. The green regions highlight the intensity values which are classified as background or CSF.

The main focus lies on the two regions between the brain tissue and non-brain tissue (background and CSF). If the number of clusters is too small, then the brain tissue is classified as non-brain tissue. On the other hand, if the number of clusters is too large, then the non-brain tissue is segmented as brain-tissue. The optimal number of classes was set to eight after a large investigation using the 1.5T neonatal database.

In this study, each cluster was initialised with a predefined value. Two clusters were defined with the lowest and highest intensity values of the image representing the background and the brightest CSF region. The other six clusters were initialised with a value extracted from the RoI intensity range, which was equally divided into six parts. During the extraction procedure, the class, to which the current voxel is assigned, indicates if the voxel is part of the brain or non-brain tissue.

For the extraction of the brain tissue, a region growing method with two thresholds as stopping conditions is performed. The first threshold is employed for the identification of the outer boundaries between RoI and CSF, in which case the final binary mask is utilised. In this way, the expansion during the region growing process is restrained by the mask area. The second threshold is used to differentiate the RoI and the non-brain tissue within the volume by applying the previous calculated array of thresholds. In order to assign the current voxel to a class in that array, the smallest distance between the current voxel and the class centroids is evaluated.

3.6 Post-Processing

The investigation of the segmentation results concludes that two post-processing steps are required to obtain accurate results. In the first step, the contours of the extracted brain volume are refined so that some left over CSF regions can be removed. The second step focuses on disconnecting and removing the lacrimal glands regions.

3.6.1 Refinement of the outer contours

The first task investigates the edges of the extracted brain tissue. In order to solve this task, the image intensity is stretched to enhance the contrast between the brain tissue and the CSF. The intensity expansion was achieved using the following formula:

$$v(x, y) = u(x, y) - \|c - u_{LPF}(x, y)\| \tag{3.9}$$

where u defines the resulting image from the region growing step and LPF describes the Low Pass Filter. c is a parameter which is used to distinguish the white matter from the CSF. Out of all those local minimum values which were acquired during the histogram analysis from the intensity adjustment step in Section 3.3.2, the mean value is calculated to initialise the parameter c. Then, the gradient magnitude of each contour pixel is computed. In order to distinguish between fluid and non-fluid pixels, a threshold is defined as follows:

$$threshold = min(gm(e) > k^*)) \quad e \in B \tag{3.10}$$

where gm is the gradient magnitude of the edge values e, B defines the brain tissue mask and k^* is the threshold value of the Kapur entropy [67]. Several threshold algorithm such as K-means, Otsu [92] and Kapur entropy were evaluated and as Figure 3.12 illustrate, different values were obtained.

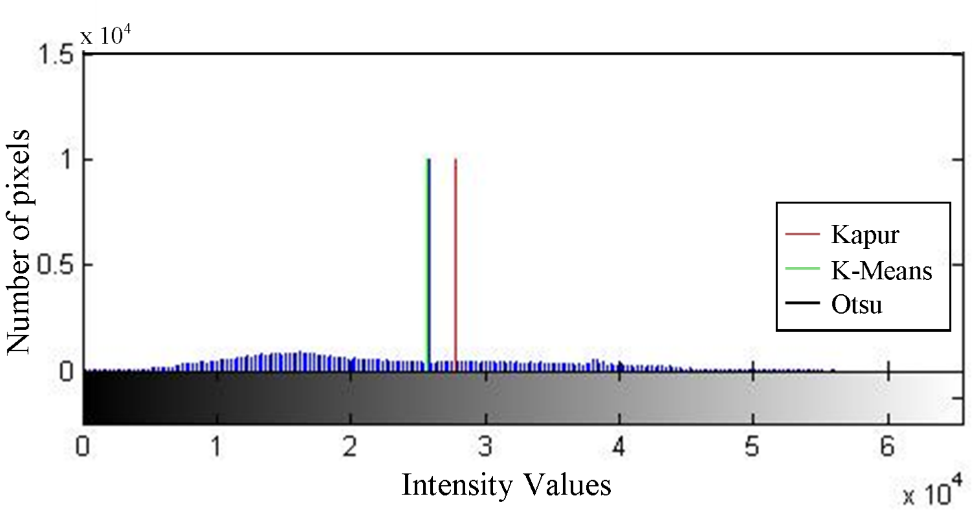

Figure 3.12: In this graph the threshold values of the Kapur, Otsu and K-means are shown.

In a first attempt, the K-means algorithm, which previously provided accurate results, was used to compute the threshold. The outcome was insufficient because the threshold value is too low and causes misclassification of the grey matter. The Otsu thresholding algorithm, which will be introduced in Section 4.3, was also investigated in this step and yielded similar results as the K-means. Comparing the outcome of the Kapur threshold with the two previous methods, it can be concluded that the Kapur algorithm provided the best threshold value for this task. In Figure 3.12, the threshold is calculated by using the minimum of the gradient magnitude values which are larger than the Kapur entropy threshold. The Kapur entropy threshold is calculated as follows:

$$k^* = argmax_{k=1}^{N}\{\lg(\sum_{i=1}^{k} p_i) + \lg(\sum_{i=k+1}^{L} p_i) - \frac{\sum_{i=1}^{k} p_i \lg p_i}{\sum_{i=1}^{k} p_i} - \frac{\sum_{i=k+1}^{L} p_i \lg p_i}{\sum_{i=k+1}^{L} p_i}\} \tag{3.11}$$

where p_i describes the probability of grey level *i* and *L* defines the total number of grey levels. k^* is the threshold that maximise the total entropy. Figure 3.13 illustrates the results before (A) and after (B) processing the inner edges to eliminate the remaining CSF regions.

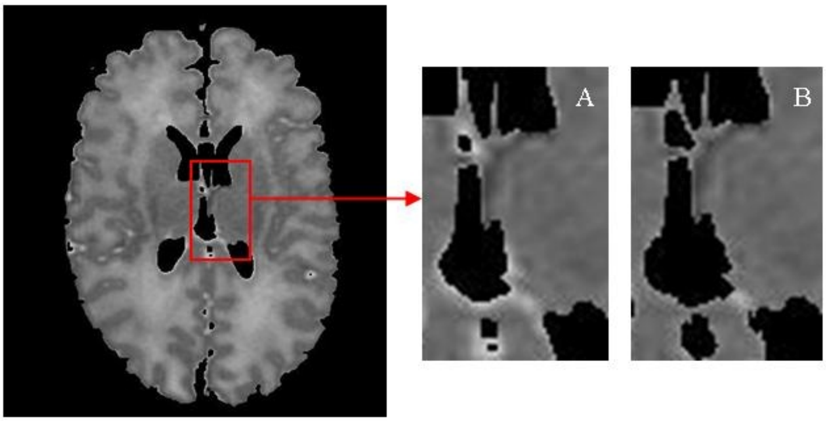

Figure 3.13: An example of an image to illustrate the results before (A) and after (B) processing the inner edges of the brain. It can be observed that the brighter contour pixels in (A), which represent fluid pixels, have been removed in (B).

3.6.2 Lacrimal glands removal

In infant brain MR images, the boundaries between the brain tissue and the lacrimal glands are ambiguous. In addition, the lacrimal glands are composed of the same intensity values as the brain tissue. Consequently, the region growing algorithm will include these parts into the brain tissue volume as shown in Figure 3.15 (A). Figure 3.14 presents an overview on the removal of the lacrimal glands.

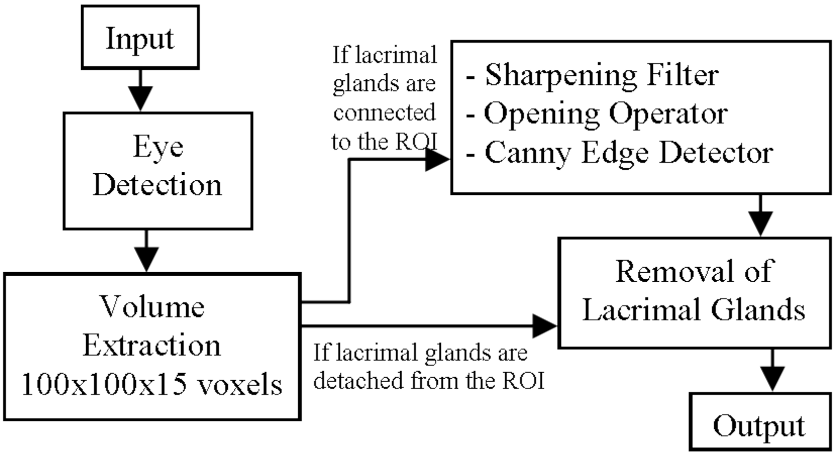

Figure 3.14: Overview of the algorithm which removes the lacrimal glands.

First, the positions of the eyes are determined by locating circular objects in the first mask that is determined using the procedure explained in Section 3.4, using the following expression:

$$R = \frac{4\pi \, area}{perimeter^2} \tag{3.12}$$

where the value $R = 1$ describes a perfect circle. After locating the eyes, the focus lies on the region above them in order to identify the lacrimal glands. Therefore, two volumes are extracted and each of them has a size of $100{\times}100{\times}15$ voxels. The window size parameter 100 is approximately twice the diameter of an infant eye which was measured using the entire database. The number of images was set to 15 in order to reduce the processed volume of data because in the majority cases the lacrimal glands appear only on seven to ten images and then the algorithm stops. The window size was experimentally chosen with the purpose to assure that the RoI includes all areas of interest. By analysing the MRI data, we observed that the lacrimal glands are detached from the brain in the first few images until they connect. In order to detach the connected parts, a sharpening filter and an opening operator with a kernel of $2{\times}2$ is applied and followed by a Canny edge detector (the scale parameter σ = 1, the low threshold = 0.01, and the high threshold = 0.2). Finally, the voxels identified as lacrimal glands, are removed by marking them as background voxels.

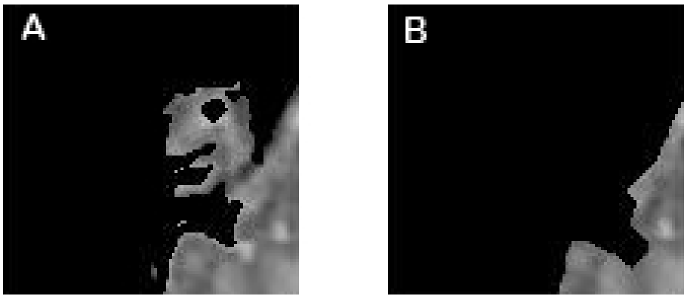

Figure 3.15: An example presenting results before (A) and after (B) the removal of the lacrimal glands.

3.7 Experiments and Results

The proposed brain extraction technique, described in this chapter, has been tested on fifteen T2-weighted MRI datasets (ten male and five female infants). In order to perform a comprehensive quantitative evaluation, fifteen datasets of our database (total of 1444 images) were manually segmented under the guidance and validation of a consultant paediatric radiologist working in neonatal MRI in Temple Street Children Hospital, Dublin. The premature infants were born approximately three months early and the data was acquired when the infant reached the term equivalent age. Detailed information on the data and the manual segmentation is provided in Section 6.1.

This section presents an evaluation of the proposed skull stripping algorithm. In order to determine the performance of the proposed method, the results of our skull stripping algorithm are compared against the manually segmented data. Some results obtained by the skull stripping algorithm are shown in Table 3.1 where each box presents images of one patient, in which the left columns represent the automatic results and the right columns illustrate the corresponding manually segmented images.

After a visual inspection of the results, it can be observed that the best performance is obtained for the data with the lowest bias field corruption. A general observation for all the tested datasets indicates that small cerebrospinal fluid parts appear within the brain volume. Due to partial volume effects, the intensity of remaining CSF parts lies often within the intensity range of the white matter and is, therefore, not distinguishable from the brain tissue. A second observation determines that some results indicate the presence of a hairline shape cut into the outer contour of the brain tissue across the volume or on single images as shown in Figure 3.16 (the hairline shape cuts are marked with red arrows).

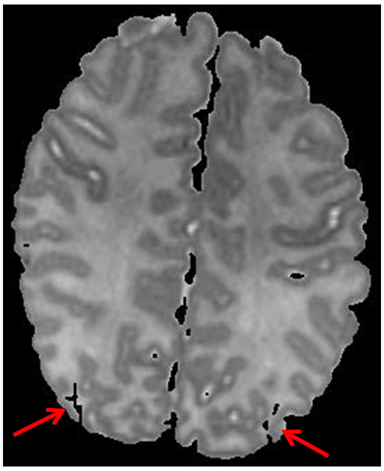

Figure 3.16: A brain extraction result which indicates the presence of hairline shape cuts. These regions are outlined with red arrows.

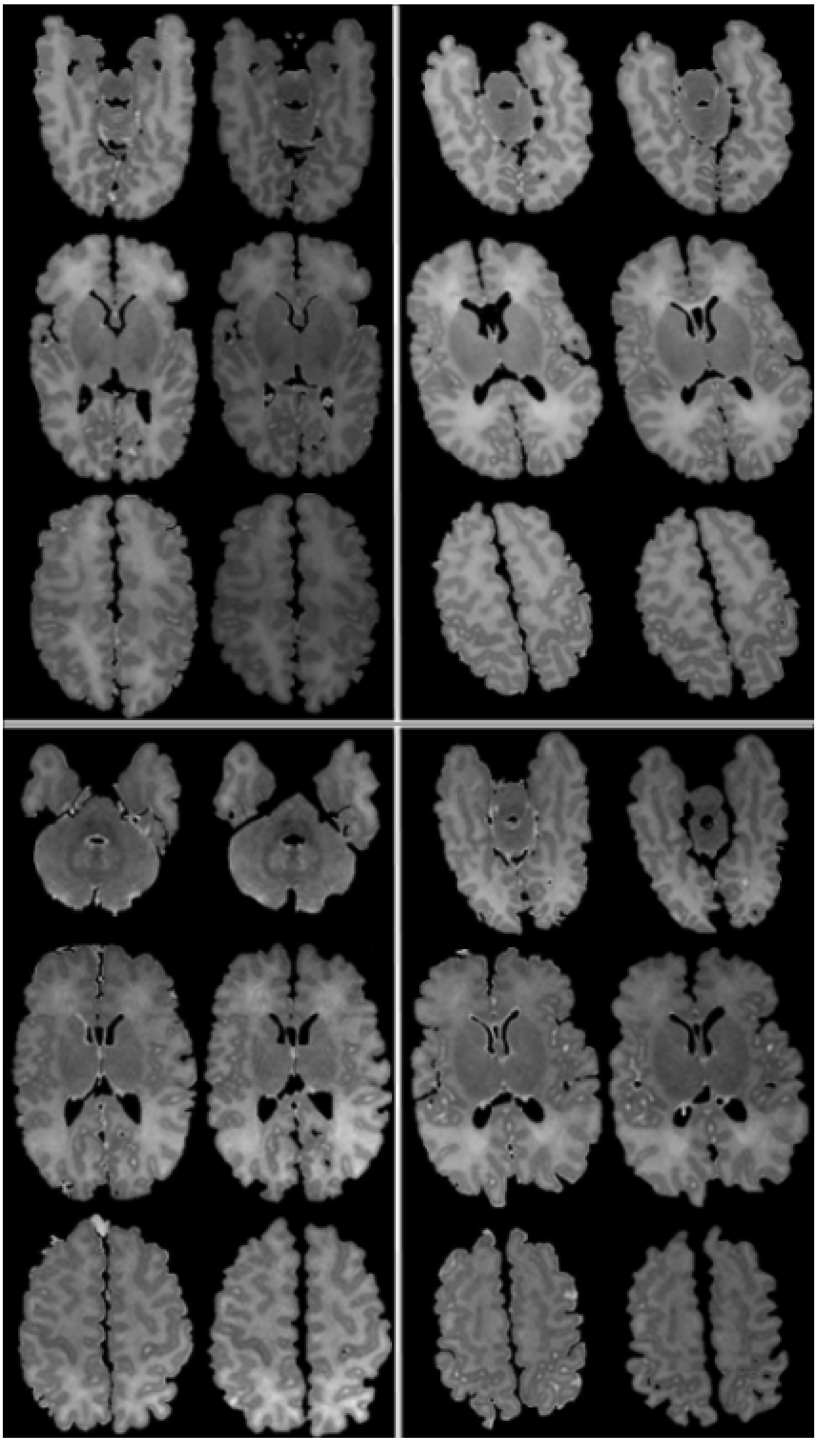

Table 3.1: Images obtained after the skull stripping algorithm is applied. Each box represents a different patient, in which the left columns represent the automatic results and the right columns illustrate the corresponding manually segmented images.

3.7.1 Evaluation Indices

The evaluation was performed by calculating three different indices such as Dice Similarity Metric, False Positive and False Negative. The Dice Similarity Metric is a popular comparison metric used for evaluation in many brain MRI segmentation approaches [13] [23] [95] [101] [109] and it describes the similarity between the manually segmented data and the automatically segmented data. The last two calculations describe the percentage of falsely segmented pixels as defined by [75] [101] [109].

1. The first set of tests is carried out by using the Dice Similarity Metric (DSM), which describes the amount of overlap between the manually segmented data and the automatically segmented data. The mathematical formula to calculate this metric is described as follows:

$$DSM = \frac{2|M_1 \cap M_2|}{|M_1| + |M_2|}, \tag{3.13}$$

   where M_1 is the automatically segmented volume and M_2 is the manually segmented volume. $|M_1|$ denotes the number of voxels with the value 1 in the binary volume M_1.

2. The over-segmentation is calculated using the false positive rate as defined by [101]. This formula calculates the percentage of voxels which were identified as a part of the RoI but does not belong to the RoI. The false positive rate was calculated as follows:

$$FP = \frac{|M_1 \setminus M_2|}{|M_2|} \tag{3.14}$$

   where $|M_1 \setminus M_2| = \sum_{(x,y)} f(M_1(x,y) = 1 \ \ \&\& \ \ M_2(x,y) = 0)$ where (x, y) are the pixel coordinates, $f(a) = \begin{cases} 1 & if\ a = true \\ 0 & if\ a = false \end{cases}$, M_1 is the automatically segmented volume and M_2 is the manually segmented volume, $|M_2|$ denotes the number of voxels with the value 1 in the binary volume M_2.

3. The under-segmentation is calculated using the false negative rate as defined by [101]. This formula calculates the percentage of voxels which were not identified as part of the RoI but would belong to the RoI. The false negative rate was calculated as follows:

$$FN = \frac{|M_2 \setminus M_1|}{|M_2|} \tag{3.15}$$

   where $|M_1 \setminus M_2| = \sum_{(x,y)} f(M_1(x,y) = 1 \ \ \&\& \ \ M_2(x,y) = 0)$
   and $f(a) = \begin{cases} 1 & if\ a = true \\ 0 & if\ a = false \end{cases}$

3.7.2 Numerical Evaluation

Figure 3.17 gives an overview on the numerical results. A database of 15 patients (with a total of 1444 images) was manually marked under the guidance and validation by one clinical expert. Figure 3.17 displays the dice similarity measurements for each subject. The Dice Similarity Metric varies between 95% to 96.5% when the skull stripping algorithm was applied to data with low bias field corruption. The similarity measurements obtained from bias field corrupted data varies between 93.4% to 95%.

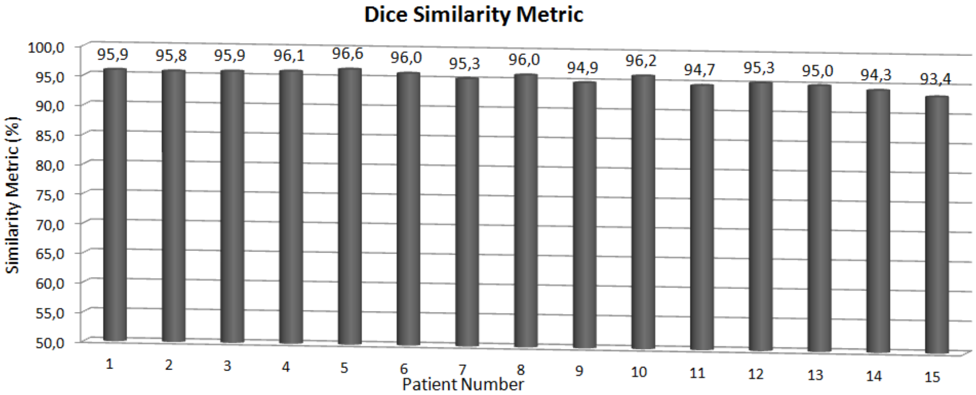

Figure 3.17: Similarity Measurements of the brain extraction algorithm using Dice Similarity Metric.

The average result of the Dice Similarity Metric is 95.4%. The skull stripping algorithm was optimised so that the partial volume effect and the bias field corruption have a minor influence on the brain extraction approach. By comparing these results to other developed infant brain extraction techniques, Chiverton et al. [33] obtained a DSM between 89% to 93% while Despotovic et al. [42] presented a DSM of 90%. Mahapatra et al. [82] stated a DSM of 98.9% similarity. During their experimental evaluation their method was compared with two well-established techniques, BET and BSE. They obtained a DSM of 96.1% for BET and 95.1% for BSE. A comparison of these two techniques was performed on our database and resulted in an average DSM of 87.94% (BET) and 87.67% (BSE). The experimental results obtained from our investigation are presented in Appendix A. Comparing the BET and BSE results obtained by Mahapatra et al. and the results obtained in our study, nearly ten percent difference was observed between these two sets of results. These variations can be explained by the use of data acquired with scanners with different magnet strength (3T MRI Mahapatra et al. and 1.5T data in our study).

Figure 3.18 presents the over- and under-segmentation measurements. The average false positive rate is 4.69% and the false negative rate is 4.48%. To better understand the error rate results, a global error was calculated, which demonstrates the error rate when the segmented brain volume surface is one pixel smaller than the manual segmentation. Due to the large surface of the brain tissue, the brain volume shows an error rate of 7.83%.

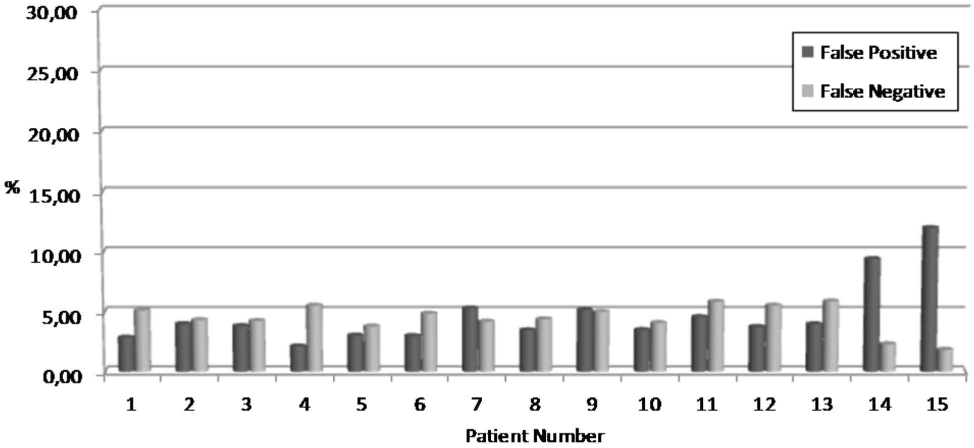

Figure 3.18: False positive and false negative measurements.

It can be observed that the datasets with stronger bias field corruption present larger number of false positive voxels. This is the consequence of some CSF parts lying in the intensity range of the white matter and, therefore, the algorithm has difficulties in distinguishing between the white matter and CSF in those regions. The remaining CSF voxels inside the brain tissue volume are often caused by PVE, which can be difficult to classify, even when using a visual examination.

In general, the false negative measurements reflect missing brain tissues in the segmented volume, such as the mentioned hairline shape areas. Additionally, for images of some patients (patients 4, 6, 11, 12 and 13) the brainstem is missing. This happens because some brain tissue volumes consists of darker, low intensity values and the brainstem is assigned as part of the background. Since the brainstem is not a relevant feature for this clinical study, no further investigation is considered to address this issue.

3.8 Conclusions

This chapter proposed a novel, automatic brain extraction algorithm for infant MRI data. The skull stripping method has overcome several challenges. The image quality was improved by reducing the noise level and adjusting the intensity inconsistencies across the volume. In order to minimise the influence of the partial volume effects between the brain and the non-brain tissues, a mask of the RoI was generated. For the segmentation of the brain tissue, a seedpoint and multiple thresholds are automatically calculated.

Two post-processing steps are required to refine the segmented data. A number of experiments indicate that the algorithm shows robustness to image quality, partial volume effects and intensity inhomogeneities.

The brain extraction method is the first part of the white matter segmentation framework. In order to facilitate the white matter segmentation, the bias field has to be corrected and a novel technique is presented in the next chapter.

Chapter 4

Bias Field Correction

4.1 Introduction

The most challenging artefact in MR images is the bias field which can be described as a low frequency multiplicative signal arising from the inhomogeneity of the magnetic field during the MR acquisition. The bias field causes a slow varying shading distortion in the MRI within the same tissue. An example of this artefact is illustrated in Figure 4.1. In the left image, the bottom of the brain tissue is darker than the top, while in the right image the bottom is brighter than the top. The process related to the removal of these intensity inhomogeneities is called bias field correction.

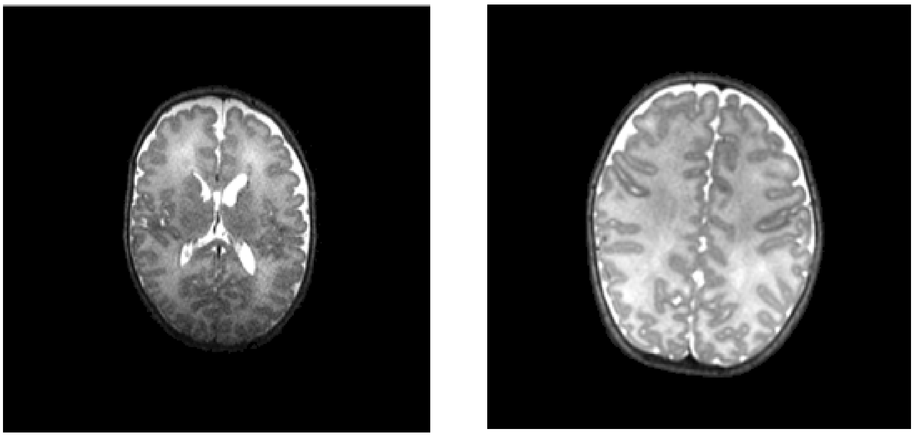

Figure 4.1: Two examples from different patients that illustrate the intensity changes across the brain tissue. These intensity inhomogeneities have a severe effect on the segmentation outcome.

The intensity inhomogeneities have a severe effect on the results of the segmentation techniques. The model, which is commonly used to describe corrupted data, is mathematically defined as follows:

$$v = u\,b + n \tag{4.1}$$

where v denotes the corrupted image, u represents the true intensity image, b describes the bias field and n indicates the additive noise. Numerous methods [20] [124] have been proposed to correct the intensity non-uniformity and these can be divided into two groups. The prospective correction methods deal with the MR signal received from the scanner during the acquisition, while the retrospective approaches process the data after the signal has been acquired and reconstructed into MR images. The advantage of the prospective methods is that the information used for correction is closely related to the problem. A disadvantage is that in many cases additional scans are needed. In this study, the data acquisition had been completed, therefore, the prospective methods are beyond the scope of this study and will not be further discussed.

The retrospective methods have been classified into four main categories [124]: filtering, surface fitting, segmentation and histogram analysis.

Filtering: The earliest retrospective techniques [25] [35] for bias field correction are based on low pass filtering. These methods assume that the image is composed of high frequency information and the bias field is generated by low frequency signals. For this reason, the intensity non-uniformity can be separated and corrected using low pass filtering. An advantage is that this technique is fast. Axel et al. [12] proposed a fast and simple correction algorithm called Homomorphic Unsharp Masking (HUM). The algorithm applies a 2D low pass filter LPF on the observed image $v(x)$. The correction is obtained by dividing the intensity values of the observed image with the intensity values of the LPF image. In order to achieve a correction in the appropriate intensity range, the resulting image is multiplied by a constant value c representing the mean or median of the image. The correction technique is mathematically expressed as follows:

$$u(x) = \frac{v(x)}{b(x)} = c\,\frac{v(x)}{LPF(v(x))} \tag{4.2}$$

A disadvantage is that this method considers no intensity overlapping between different regions. Given that this is usually not the case, the filtering process generates new artefacts [64]. An improved low pass filtering can be achieved by combining the filtering process with a segmentation algorithm.

Surface Fitting: In [83] [74], a parametric surface is constructed from selected image features which contain information about the intensity of the dominant region. The resulting surface represents the bias field. A disadvantage of the surface fitting is that the method depends on the selection of the feature pixels. Secondly, as the correction assumes one region in the image, the region has to be large and uniformly distributed across the entire image. Due to these disadvantages, the surface fitting is not commonly applied for brain MRI processing and, therefore, these methods are not analysed in this thesis.

Segmentation: The brain segmentation algorithms and bias field correction methods rely on each other. A precise segmentation makes the intensity inhomogeneity correction insignificant, whereas on the other hand the achievement of complete segmentation results depends on the accuracy of the pre-processing steps. In this regard, inhomogeneity correction algorithms and segmentation techniques are merged so that both methods benefit from each other and achieve the best results. To this end, statistical methods are employed to merge the segmentation and the bias field correction algorithms. The two most common methods are the Expectation-Maximization (EM) [53] [76] [8] and Fuzzy C-Means (FCM) [1]. These procedures iteratively correct the intensity artefacts while segmenting the required regions. A disadvantage of both methods is that these techniques are computationally expensive. The EM techniques calculate probability values based on the intensity distribution of labeled voxels. The maximum-likelihood (ML) [76] or the Maximum A Posteriori (MAP) [125] criterion are commonly implemented within EM. The Expectation step calculates the tissue probabilities when assuming the bias field is known while the Maximization step computes the updated set of parameters. Wells et al. [125] proposed the first EM segmentation with an embedded bias field estimation. The algorithm uses a finite Gaussian Mixture Model and an MAP. Leemput et al. [76] proposed an Expectation/Conditional Maximization (ECM) algorithm in which a normal distribution model describes each tissue class. The bias field is calculated as a linear combination of smooth fourth-order polynomial basis functions. In order to improve the EM calculations, a brain atlas with a prior probability map for each tissue class is integrated. Guillmaud et al. [53] modified the EM so it replaces the distribution of each class by a uniform probability density function. In general, in an EM algorithm, the initialisation step remains critical. As mentioned in Chapter 2, the outcome of an EM technique can be improved by the influence of a brain atlas which implements a priori probability map for each tissue class.

The Fuzzy C-Means (FCM) method is a soft classification algorithm which allows voxels to be classified into multiple classes. This technique modifies the object function to adapt to intensity inhomogeneities. A modified FCM (MFCM) technique was proposed by Ahmed et al. [1], which segments adult MRI data into three classes (background, white matter and grey matter). In order to improve the general FCM, two components were added. The first component is a regulator which includes the spatial coherence of the tissue classes and enables the class membership of each voxel to be influenced by the corresponding neighbourhood voxels. This constraint term was optimised using the Lagrange multipliers technique. The second component optimises an additional parameter which corrects the bias field. This method was applied on our database and results are shown in Figure 4.13 in Section 4.6.

Histogram: In histogram-based approaches, the information required for bias field correction is extracted from the histogram. The advantage is that these methods need little or no initialisation and can, therefore, be applied to a large range of different images. A well-known histogram-based correction method is the nonparametric nonuniformity normalization (N3) proposed by Sled at al. [111]. The correction is achieved by finding a smooth multiplicative field which maximises the high frequency of the intensity distribution of the histogram of the ideal image. The histogram of the ideal image is iteratively approximated from the current histogram by estimating a parametric bias field with a histogram sharpening function. A disadvantage of this method is that, if the intensity variations are stronger than the contrast between the brain tissues, the N3 algorithm results are not precise [90] [64]. The reason for this is the sharpening function which prevents a good approximation of the histogram from the ideal image. Salvado et al. [104] proposed a correction technique for adult brain MR images using a Local Entropy Minimization with a bicubic spline model. The algorithm called LEMS approximates the initial bias field using a fourth-order polynomial function. The bias field is then modelled as a bicubic spline and is optimised so that the entropy of the image is minimised. A disadvantage of this method is the long processing time. This technique has been tested on our database and results are presented in Section 4.6.

The aim of this Chapter is to evaluate the issues generated by the bias field corruption and to analyse the most common algorithms that are applied to remove the bias field in the neonatal brain MR images. Following an investigation on the performance of the technique proposed by Ahmed et al. [1] and the approach developed by Salvado et al. [104], the outcome revealed that both methods failed to correct the bias field corruption when applied to our database. For this reason, it was decided that the filtering technique should be further investigated to improve the bias field correction. Our database is composed of data with a low contrast between tissue classes and high intensity inhomogeneities. This combination presents a great challenge and the proposed algorithm performs a pre-segmentation of the brain tissue before applying low pass filtering. The next section introduces an overview on the structure of the developed technique.

4.2 Overview

Regarding the bias field corruption, a difficult challenge in infant brain data is given by the additional inconsistencies in the white matter tissue, which arise due to an inhomogeneous distribution of the water content in the tissue [52]. The previous described algorithms were developed for adult brain segmentation and they fail in distinguishing between grey and white matter in infant brain MRI. However, the key problem for bias field correction is to extract the intensity inhomogeneities within each region. In the experimental section of this chapter, results for bias field correction are illustrated. The idea behind the proposed bias field correction algorithm is, first, to partition the brain tissue into grey and white matter regions, followed by the extraction of the intensity inhomogeneities within each region and, finally, correct the image. Figure 4.2 presents an overview of the main components of the developed approach.

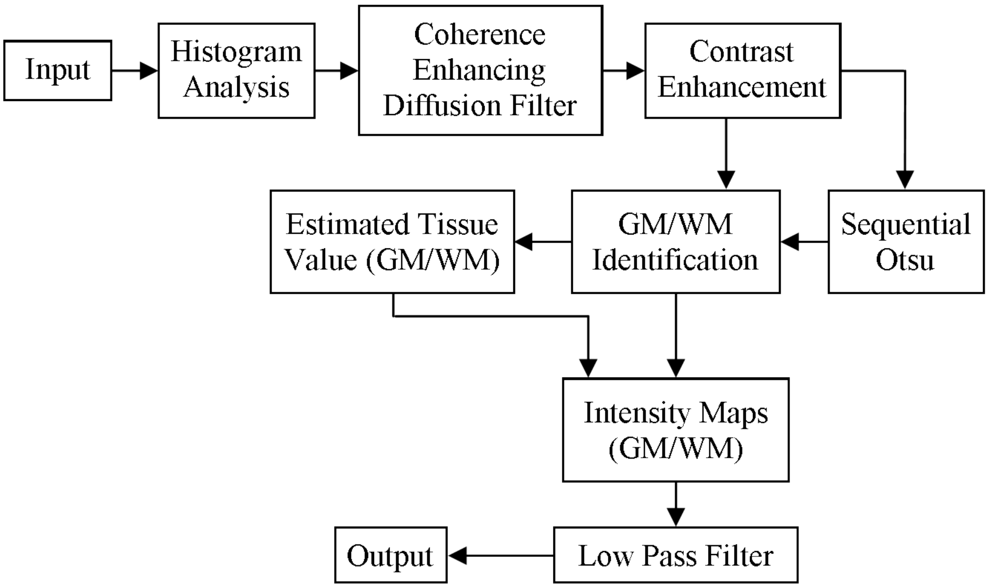

Figure 4.2: The overview of the bias field correction technique.

The bias field correction technique proposed in this study starts by dealing with the attenuation of the intensity signal within the brain images. The first step adjusts the intensity within the volume, using histogram analysis, while the second step reduces the noise by applying an anisotropic diffusion filter. This is followed by enhancing the contrast to improve the identification of the grey matter and the white matter regions. The use of a low pass filter across all brain tissues has resulted in the generation of additional artefacts and the disappearance of low contrast contours. For this reason, the proposed technique performs a pre-segmentation of the white matter and the grey matter. The two regions are estimated by segmenting the brain tissue using an Otsu thresholding algorithm. In order to reduce the influence of the partial volumes, the thresholding results undergo a probabilistic calculation. In order to obtain a bias field in which the intensity variations across the image are eliminated, a specific value for each tissue class is computed. Based on the tissue classes and their corresponding values, a intensity map is computed for each region. The two intensity maps for grey matter and white matter are merged to form the image on which the bias field is determined by applying a low pass filter. In order to achieve accurate results, the technique can only be applied on data in which all non-brain tissues have been removed.

4.3 Data Pre-Segmentation

In the data pre-processing step, a histogram analysis is performed, which is similar to the algorithm presented in Section 3.3 but with a different focus. The intensity adjustment in the skull stripping method addressed first the challenge related to the identification of the brain tissue and, subsequently, to correct the intensity values of the region of interest into the same intensity range. Additionally, in the skull stripping intensity standardisation step, the high values were stretched out, so that a smooth transition is maintained. At this stage, the non-brain tissue had been removed, which facilitates the identification of the intensity distribution of the brain tissue. The Coherence Enhancing Diffusion filter proposed by Weickert [128] has previously been used and explained in detail in Section 3.3. The contrast enhancement calculation was discussed in Section 3.6.

An investigation was performed by applying a low pass filter across the brain tissue. The results indicated the appearance of new artefacts and the disappearance of low contrast contours between the grey matter and the white matter. For this reason, it was decided that in the proposed technique a pre-segmentation of the white matter and grey matter is necessary.

The segmentation of the two regions was achieved by applying an Otsu thresholding [92] algorithm. The Otsu technique provided accurate results when applied to neonatal brain MRI data during the brain extraction process [52].

In this step, the Otsu thresholding algorithm was applied after a comprehensive comparison between the K-means and Otsu techniques on eighteen datasets of this study. The Otsu approach has provided better and more robust results than the K-means method when dealing with the bias field corruption and intensity variations. During this investigation it has been observed that the K-means algorithm performed well when the number of clusters were manually adjusted for each patient. This manual interference was dependent on the intensity variations and on the strength of the contrast in the MRI data. The Otsu method is a parameterless global thresholding technique which calculates a threshold value by assuming the presence of two distributions in an image. This means that the optimal threshold is calculated by separating the two classes so that their combined spread is minimal. Therefore, the optimal threshold t^* is computed when the variance between σ_B^2 is maximised. This is mathematically defined as:

$$\sigma_B^2(t^*) = argmax\left[p_0\, p_1\, (\mu_1 - \mu_0)^2\right] \tag{4.3}$$

where p_0, p_1 denote the class probabilities and μ_0, μ_1 describe the class means. Due to the early stage of brain development, the contrast between grey matter and white matter can overlap, which results in erroneous classifications. For this reason, the Otsu threshold algorithm is applied three times on different parts of the brain tissue, which results in four classified regions as illustrated in Figure 4.3. Performing the Otsu algorithm three times provides a stronger focus on the partial volume voxels, diffused contours and intensity variations within regions. One of these classified regions defines the white matter and the second one the grey matter. The two remaining classes consists of partial volume voxels.

Experimentally, we concluded that after the first application of the Otsu algorithm, the class corresponding to high intensity values is composed of white matter pixels only. Hence, the next Otsu thresholding is carried out on the class with low intensity values, which separates the grey matter from the partial volume pixels. For a more precise GM/WM identification, the partial volume class is divided into two classes using the Otsu algorithm for the third time. Figure 4.3 presents an overview of the proposed method for grey matter and white matter estimation.

After a global segmentation, Xue et al. [132] split the brain image into several parts to deal with the white matter intensity variations. This idea was also used in this classification algorithm to receive a good estimation of the white matter and grey matter. In this study, each brain tissue volume in each image is divided into 18 parts. The 18 parts allow the image to be segmented locally which improves the separation of grey matter and white matter without the negative influence of the bias field corruption. In addition, the size of each region permits the inclusion of both regions (GM/WM) which prevents misclassifications. The previously described Otsu thresholding is performed on each part individually. In this way, local intensity variations can be incorporated. The division of 18 sections proved to be optimal for this task. The outcome difference between performing the Otsu thresholding globally or locally is illustrated in Figure 4.4.

A probability judgment is employed to classify the two classes of the partial volume voxels into the grey matter and the white matter classes. Thus, two probability measurements are computed, the grey matter and the white matter, and each of which is compared

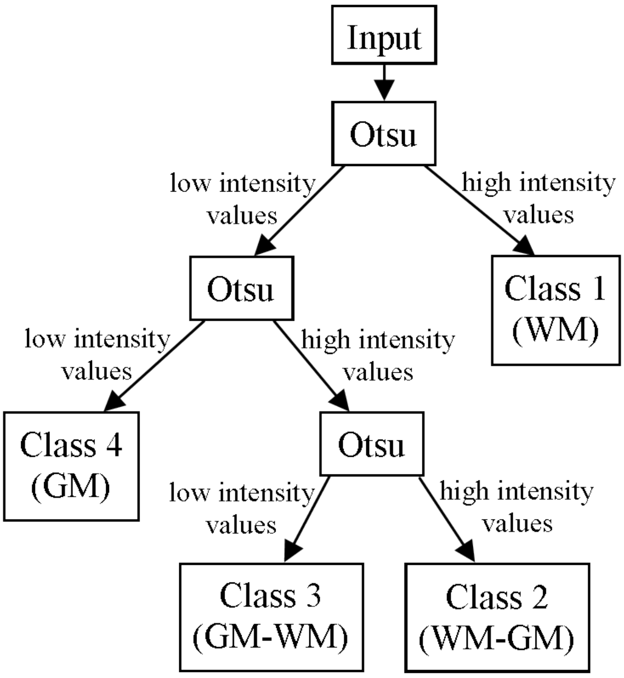

Figure 4.3: An overview of the Otsu decision tree that applies the Otsu algorithm three times.

to the partial volume pixels. The probability judgment is mathematically expressed as follows:

$$probGM = \frac{\sum q_{cl=4}}{\sum q_{cl=2} + \sum q_{cl=3}} \qquad probWM = \frac{\sum q_{cl=1}}{\sum q_{cl=2} + \sum q_{cl=3}} \tag{4.4}$$

where q_{cl} is the number of pixels in the class cl. The assumption is that class 4 describes the grey matter, class 1 defines the white matter and class 2 and 3 indicates the partial volume voxels and diffused contours. The probability calculation $probGM$ indicates the number of grey matter pixels compared to the number of partial volume pixels. The second probability $probWM$ computes the ratio between white matter pixels and partial volume pixels.

In order to classify the partial volume classes, two case scenarios are taken into account:

1. **probGM > probWM :** A higher percentage of grey matter pixels indicates a dark region in the image, in which the partial volume pixels of classes (WM-GM) and (GM-WM) are categorised into the white matter class.
2. **probGM ≤ probWM :** If the percentage of grey matter pixels is lower than or equal to the percentage of the white matter pixels, it means that this area in the image is brighter. In this case, class (GM-WM) is classified as grey matter and class (WM-GM) is defined as white matter.

Figure 4.4 presents an example obtained after applying the Otsu method. The left image represents the result if Otsu is applied to the entire image and the middle sample is the results after applying Otsu on 18 parts of the image. The right image presents the final Otsu results. The bias field correction algorithm does not require the achievement of a complete segmentation. At this stage, the two regions have been separated up to a point where the intensity variations can be precisely computed.

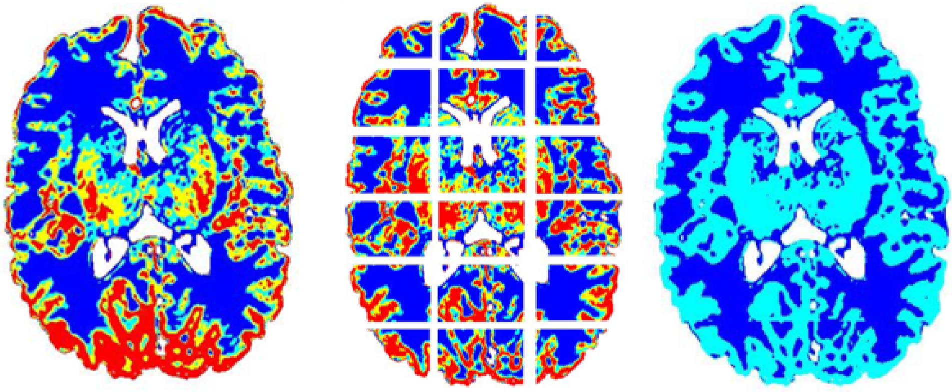

Figure 4.4: Results obtained after applying the multiple Otsu algorithm. (Left) The technique was applied on the entire image. (Right) The result of the algorithm which was applied individually on small segments of the image. The red area represents class GM, and the dark blue illustrates the WM class. The partial volumes are represented in bright blue and yellow regions. The right image is an example of the final segmentation obtained by the multiple Otsu technique. The dark blue area represents an estimation of the white matter region and the grey matter is displayed in brighter blue.

4.4 Intensity Maps

At this point the images consist of two main regions; grey matter and white matter. In the proposed bias field correction algorithm, it is important to differentiate between the grey and white matter because each region consists of different intensity ranges. An attempt of applying the bias field correction algorithm to one global region resulted in a false correction and the borders between grey and white matter were unclear. As a consequence, two maps (GM and WM) are computed and then reconstructed into one resulting image. This allows the processing of each region in its intensity range without the influence of the other region. These maps reflect the intensity variations within each region.

The measurements of intensity variations are based on an estimated value for each processed region. Brinkmann et al. [25] investigated the differences on brain MRI after applying the median or the mean filtering. Their results show that for human brain MR images the mean filtering outperformed the median filtering. An investigation on our database using both filtering techniques provided no significant differences in the results. In this regard, two estimated tissue values, one for grey matter and one for white matter, are computed by applying the mean filtering on the intensity values of each tissue region. For each segmented tissue region, the difference between the pixels and their corresponding estimated tissue value is calculated. At this stage, the two tissue types have been processed individually and the results are presented in two individual images, which are referred to as intensity maps. In order to receive a global interpretation of the intensity variations, the two intensity maps are merged into one image by summing both images. Figure 4.5 presents an example of the two computed intensity maps and the reconstructed final intensity map. It can be observed that in the bottom of the image the intensity values change within both regions which appear because the images are locally processed. These changes have no effect on the correction process because the further processing steps smooth these regions before the correction of the bias field.

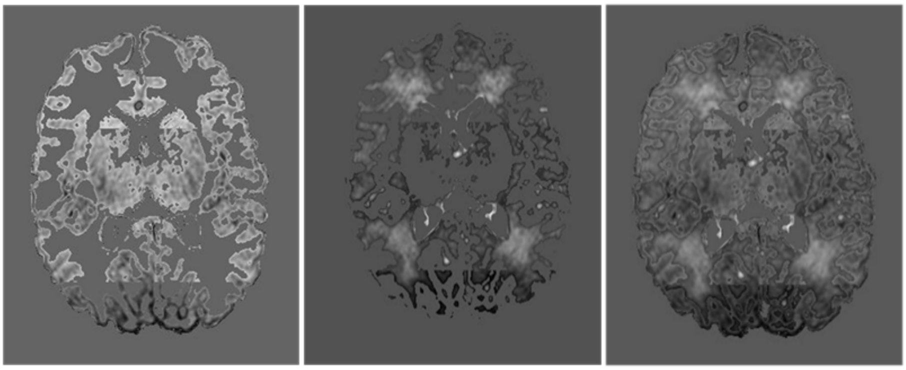

Figure 4.5: Left: The intensity map computed from the grey matter region; Middle: The intensity map computed of the white matter region; Right: The combination of the two intensity maps.

4.5 Low Pass Filter

The aim of the low pass filter [47] is to suppress the high frequencies and to maintain low frequencies unchanged. As mentioned in Section 4.1, the filtering-based bias field correction algorithms assume that the image is constructed of high frequency information, whereas the bias field is composed of low frequency signals. In this regard, the suppression of high frequencies permits the isolation of the intensity changes across the brain MR images.

The low pass filtering process is based on transforming an image into the Fourier domain, followed by multiplying with a filter function and with a retransformation into the spatial domain using the inverse Fourier transformation. In this study, the Fourier transformation is applied to the intensity map image described in the previous section and the Butterworth low pass filter is used as the filter function.

The 2D discrete Fourier transform $F(u, v)$ is defined as follows:

$$F(m, w) = \sum_{x=0}^{M-1} \sum_{y=0}^{W-1} v(x, y) \exp^{-j2\pi(mx/M+wy/W)} \tag{4.5}$$

where i represents the input image at the coordinate (x, y) , M and W denote the image size, $0 \leq m \leq M-1$ and $0 \leq w \leq W-1$.

The Butterworth Low Pass Filter (BLPF) is mathematically described as follows:

$$H(u, v) = \frac{1}{1 + \left[\frac{D(m,w)}{D_0}\right]^{2c}} \tag{4.6}$$

where D_0 describes the cut-off frequency, c defines the order of the filter and $D(m, w)$ is the distance from the origin. The Butterworth filter has a smooth transfer function without any discontinuity. In our study, D_0 was initialised with 1% of the image width and in order to reduce the ring artefact, c was set to 1. Some results of the low pass filter, including different parameter initialisation, are illustrated in Figure 4.7, in which the Butterworth low pass filter is displayed in the third row.

In order to obtain the bias field in the spatial domain, the result image $R(x, y)$ consists of the multiplication between $F(m, w)$ and $H(m, w)$, and it has to be retransformed using the inverse discrete Fourier transform (idFt). This is mathematically expressed as follows:

$$b(m, w) = \frac{1}{MW} \sum_{x=0}^{M-1} \sum_{y=0}^{W-1} R(x, y) \exp^{-j2\pi(mx/M+wy/W)} \tag{4.7}$$

The filtered image represents the bias field. In order to correct the intensity inhomogeneities, the bias field $b(x, y)$ image values are first inverted, then each pixel value is divided by the mean value of the image and finally, this image is multiplied with the image $v(x, y)$ on which the noise was reduced using the coherence enhancing diffusion filter.

$$u(x, y) = v(x, y)\, b(x, y) \tag{4.8}$$

Figure 4.6 presents an example of the computed bias field. The left image represents an example of a bias field image, the image in the middle is the image before correction and the right image is the bias field corrected image.

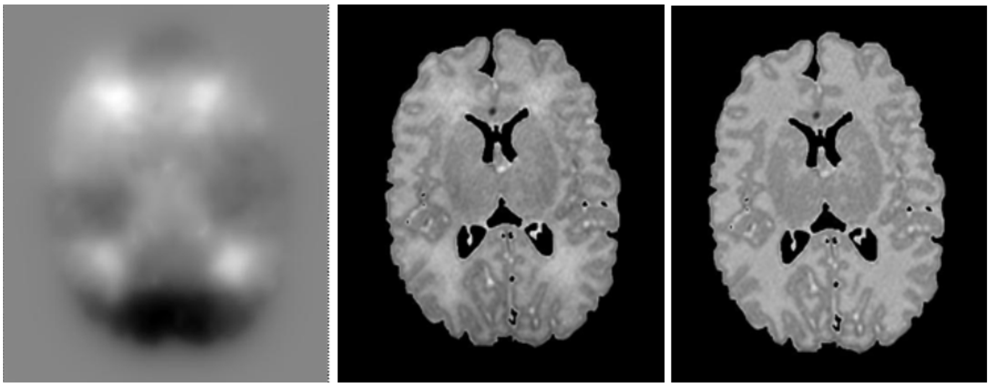

Figure 4.6: Left image is an example of the calculated bias field, the middle image is the original image and the right image is an example after correcting the bias field variations.

The decision to apply the Butterworth low pass filter was made after the investigation of three low pass filters (Ideal low pass filter; Gaussian low pass filter and Butterworth low pass filter). Mathematically, the Ideal Low Pass Filter (ILPF) and the Gaussian Low Pass Filter (GLPF) are described as follows:

$$ILPF : H(m,w) = \begin{cases} 1 & ifD(m,w) \leq D_0 \\ 0 & ifD(m,w) > D_0 \end{cases} \tag{4.9}$$

$$GLPF : H(m,w) = e^{-D^2(m,w)/2\sigma^2} \tag{4.10}$$

where $\sigma = D_0$. A drawback of the ideal low pass filter is a ringing effect which occurs along the edges of the filtered spatial domain image [47]. The Gaussian low pass filter and the Butterworth low pass filter have provided similar results. In our study, apart from the bias field, the intensity values of the white matter are inconsistent due to an inhomogeneous water content in the tissue. GLPF is known for smoothing the image more effectively than other filters because the intensity curve in the frequency domain and the spatial domain are the same [47]. However, BLPF has the advantage that it reduces this local intensity inconsistency stronger than the GLPF. A few samples of the low pass filter results are presented in Figure 4.7. The first row presents the results of the ILPF, the second row shows GLPF results and the third row the BLPF results. In the first column the D_0 was set to 0.5% of the image size, in the second column D_0 was set to 1% of the image size and in the right column the D_0 was set to 5% of the image size.

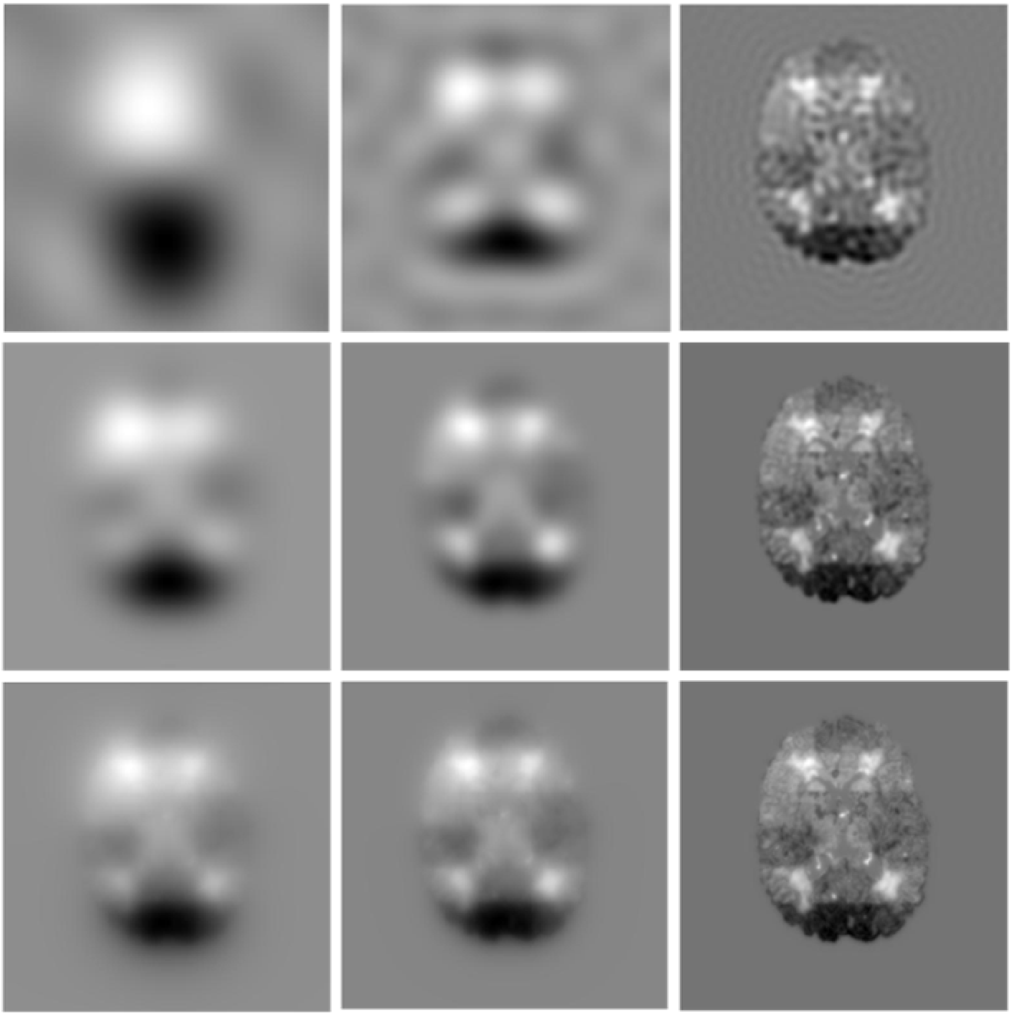

Figure 4.7: The first row presents the results of the ILPF, the second row the GLPF and the third row the BLPF. In the first column D_0 was set to 0.5% of the image width, in the second column D_0 was set to 1% of the image width and in the right column the D_0 was set to 5% of the image width.

After examining these images no visual differentiation between GLPF and BLPF could be observed. When comparing its corresponding intensity distribution in an histogram, the Butterworth low pass filter yielded the best results and is, therefore, used in this study. Figure 4.8 presents the comparison of the results obtained by the Butterworth low pass filter and the Gaussian low pass filter. Visually, the images do not reveal any differences, however when the intensity distribution is compared, then minor differences can be observed.

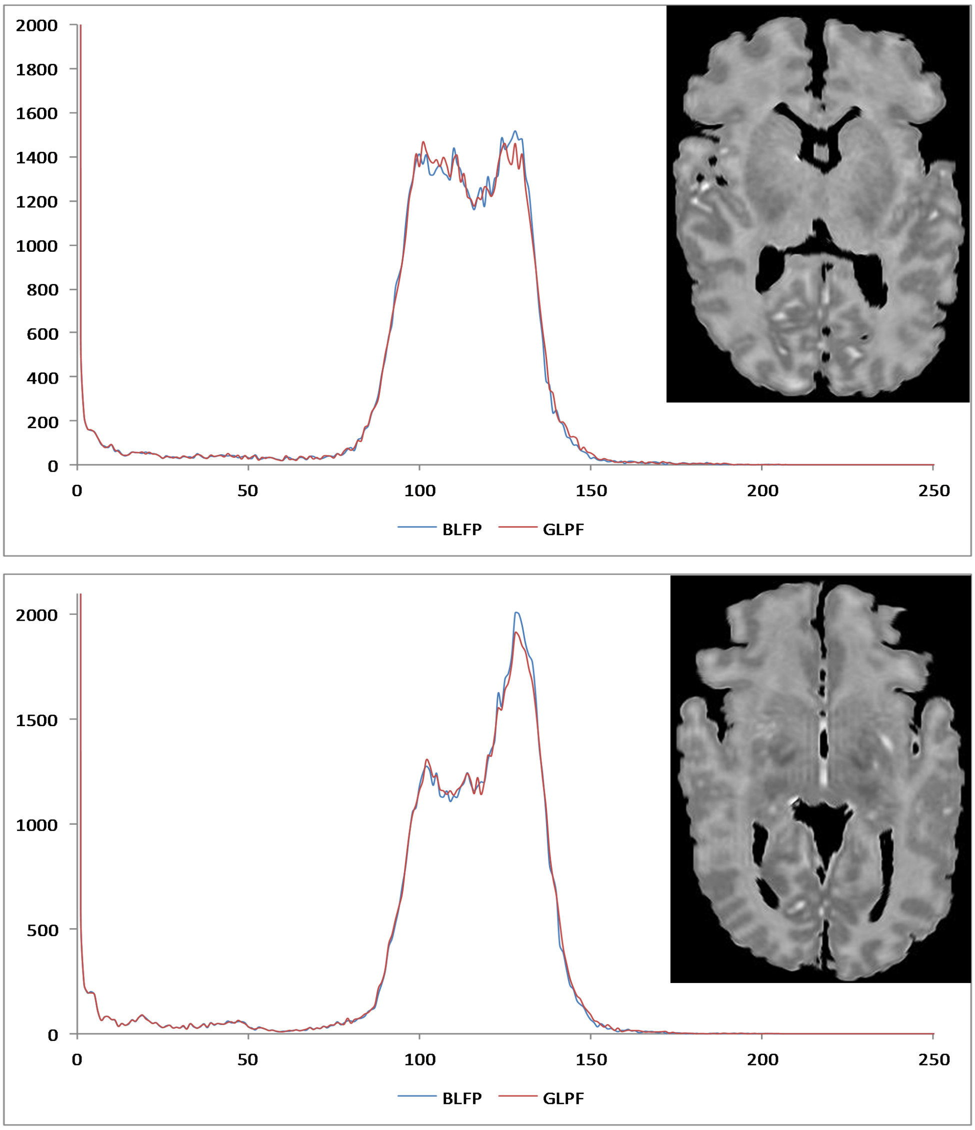

Figure 4.8: Two histogram examples where each presents the intensity distribution after using the BLPF and GLPF.

The results obtained by the proposed method are presented in the next section, as well as, a comparison against two other techniques; histogram-based and segmentation-based methods.

4.6 Experiments and Results

The bias field correction algorithm discussed in the previous sections of this chapter has been applied to our database. The outcome revealed that for each patient the intensity inhomogeneities were corrected while the edge information was retained. The tests on our database were performed on images with different strengths of bias field corruption, and show accurate results. Figure 4.9 gives an example that presents images before and after the application of the bias field correction algorithm. Their corresponding histograms are displayed beside each image and they illustrate the changes in the intensity distribution. It can be observed that the intensity variations have been corrected without attenuating the edge information or inducing additional artefacts.

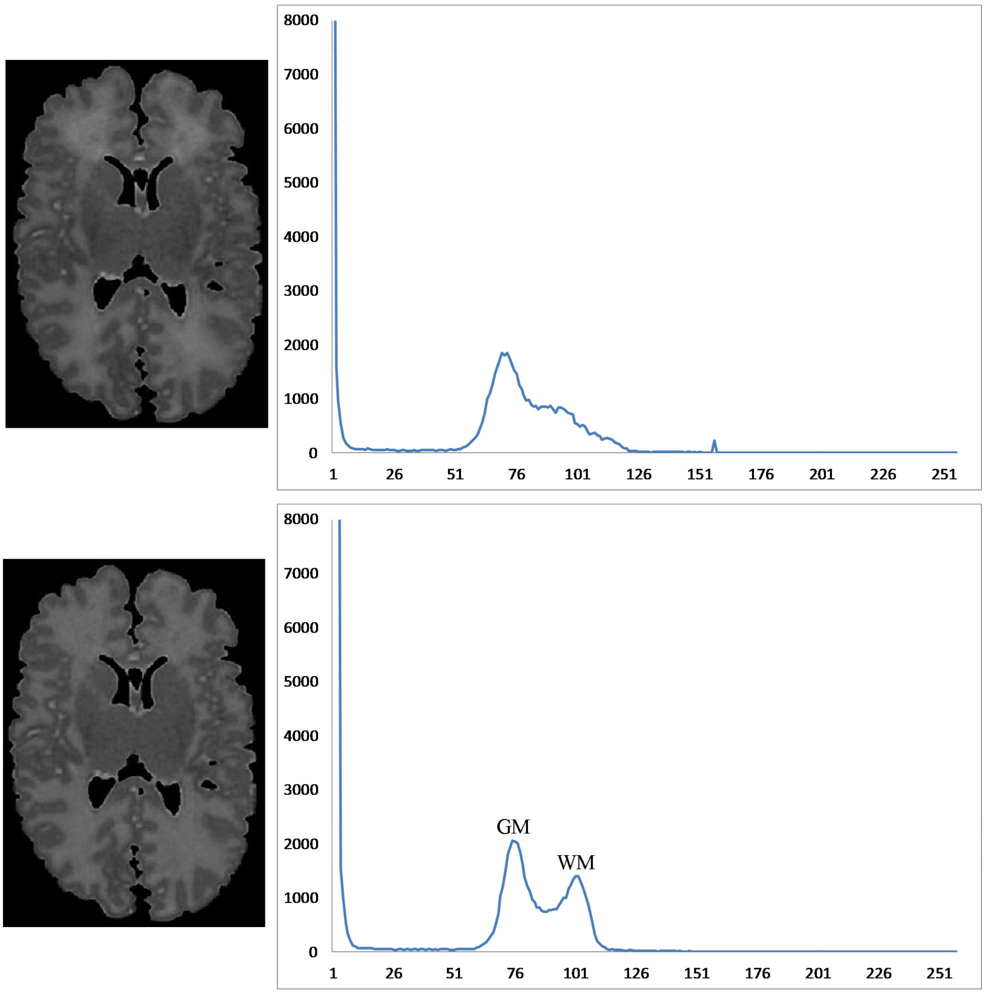

Figure 4.9: The top left image is the original image with the corresponding histogram at the right side; the bottom left image is the output after applying the bias field correction algorithm with its corresponding histogram at the right side.

Figure 4.10 gives an other example that shows the images before and after performing the bias field correction algorithm, while focusing on the local changes within the white matter region. Their corresponding histograms illustrate the intensity changes in the selected areas and demonstrate an accurate correction.

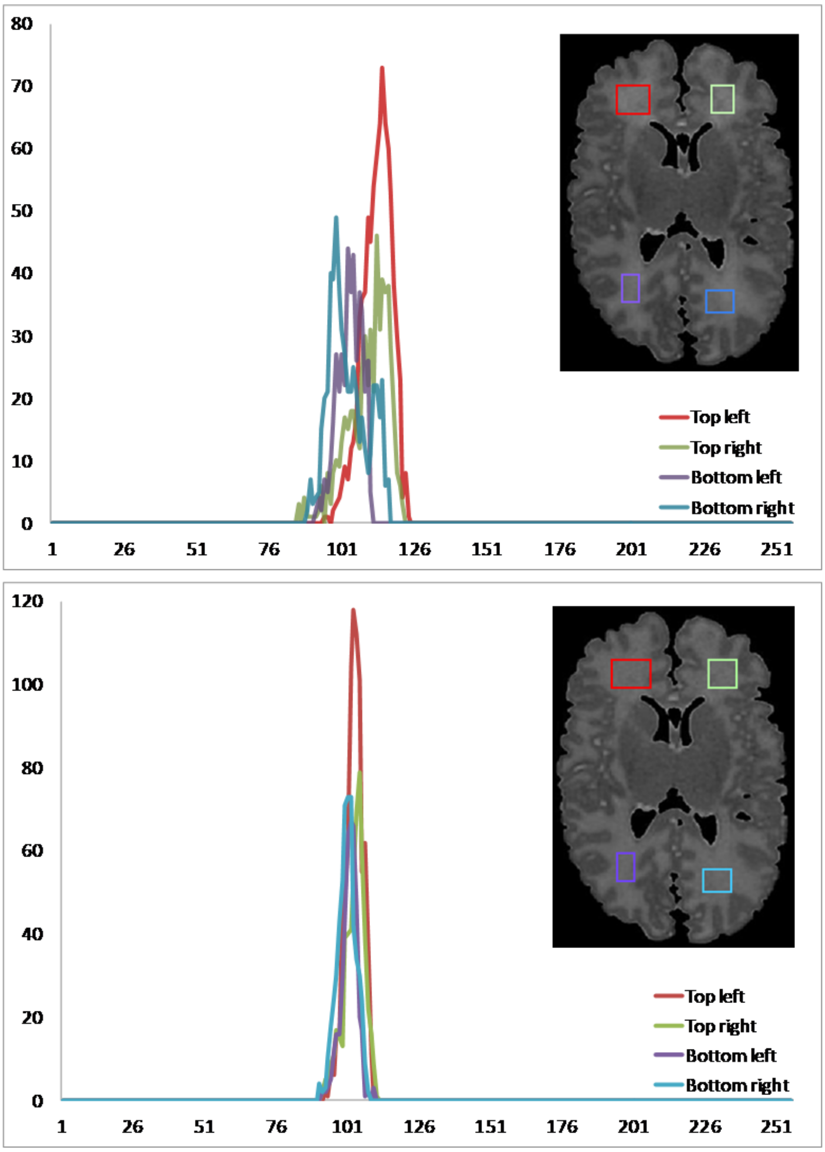

Figure 4.10: Examples showing the intensity values in selected areas of the white matter before and after the bias field correction. Their corresponding histograms illustrate the intensity values in the selected regions.

Figure 4.11 displays three examples of different patients on which the bias field correction algorithm was applied. Similar to the example in Figure 4.9, the three columns illustrate a high performance in correcting the bias field that is achieved by the proposed method. The influence of a strong bias field on the skull stripping algorithm can result in small remaining CSF parts in the brain tissue volume. Given that the proposed bias field correction method segments the brain tissue into two regions, the high intensity values of small remaining CSF parts that are attached to the grey matter tissue are classified into the white matter tissue. An example of this occurrence is illustrated in the second column of Figure 4.11.

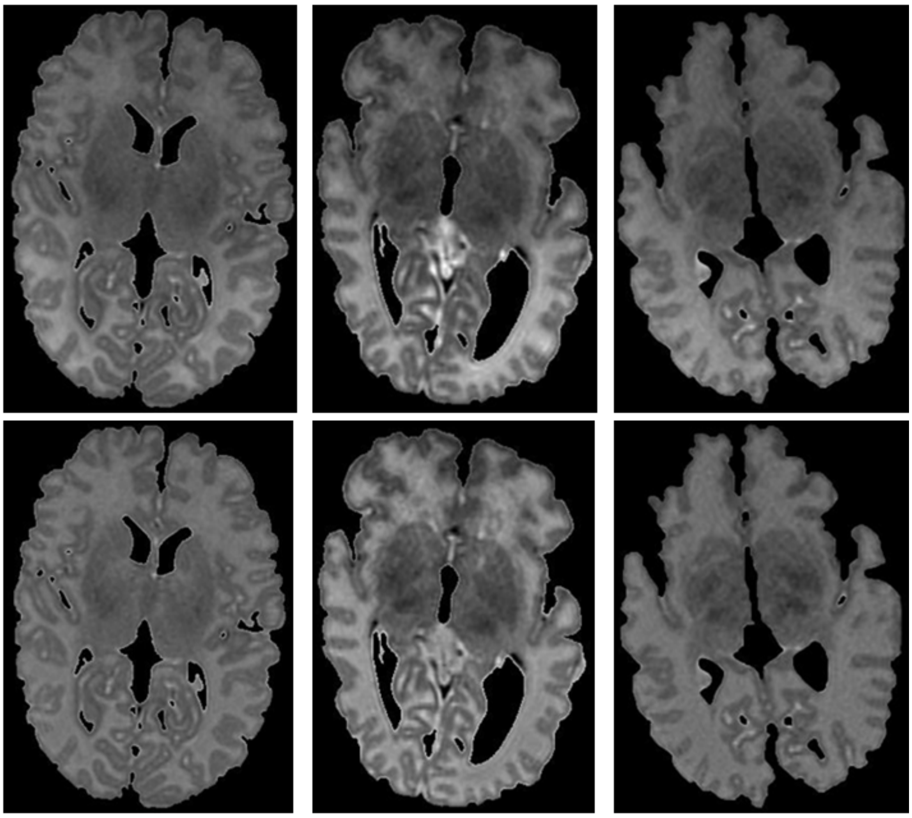

Figure 4.11: Results of the bias field correction algorithm. The top images are the original images, whereas the bottom images are the corrected images.

Given that the proposed method is based on filtering, the technique is less computationally demanding than the segmentation or histogram-based approaches. For this reason, the method proposes an attractive way to correct intensity variations.

4.6.1 Comparison to other algorithms

In order to demonstrate the effectiveness of other types of bias field correction algorithms, an investigation was performed on two techniques that are categorised into histogram and segmentation based methods. In order to perform a fair comparison, their implementation was used during this evaluation.

The first algorithm analysed is called LEMS and was proposed by Salvado et al. [104]. LEMS is a histogram-based technique and utilises a Local Entropy Minimization. Additional information is presented in Section 4.1. The algorithm provided by the authors functions in a stepwise manner, which allows the user to adjust its parameters to obtain the optimal results. LEMS was developed to adjust the bias field in the original image without pre-segmentation. As it can be observed in Figure 4.12, this approach has two disadvantages.

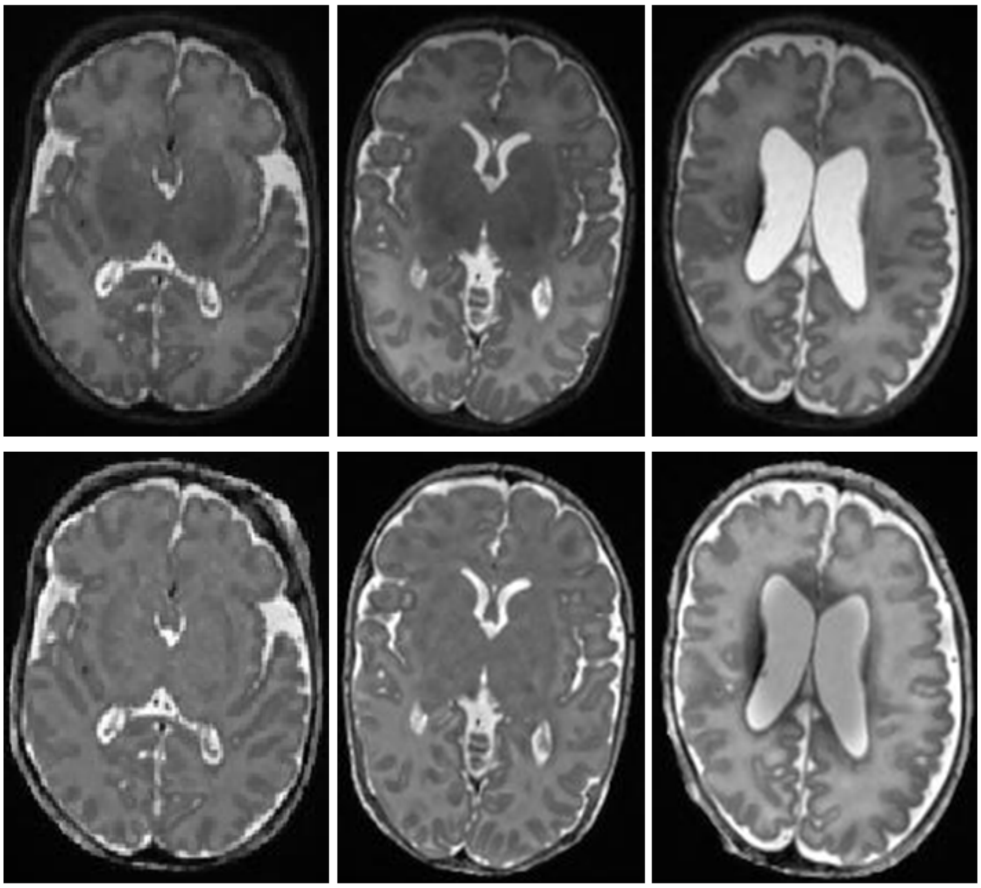

Figure 4.12: Examples showing the results obtained by the bias field correction algorithm called LEMS proposed by Salvado et al. The top images are the original images, whereas the bottom images are the corrected images.

Firstly, the edge information associated with the deep grey matter is weakened, which can be observed in the result images shown in the first and second columns. In the third column, it can be observed that the intensity values of the CSF within ventricles were falsely corrected and new artefacts appeared. These results can be explained by the fact that the histogram-based entropy measurement algorithm is prone to local minima localisation errors and sensitive to regions with low contrast. In addition, the authors state that the performance is degrading when the noise is descreased. Secondly, LEMS is computationally expensive and requires 20 minutes to process one image. In comparison, the proposed method processed the brain volume of a patient in 52 seconds.

The second comparison method is the bias field correction algorithm proposed by Ahmed et al. [1]. This technique is categorised as a segmentation-based algorithm that uses a modified Fuzzy C-Means algorithm. The algorithm is explained in detail in Section 4.1. During the evaluation of the technique, the parameters were adjusted in order to achieve the best results. The algorithm was first tested on the images obtained after skull stripping. As it can be observed in Figure 4.13, the structure in the brain tissue is unclear and the intensity values of the grey matter and white matter are adjusted into the same intensity range. A second test was performed, in which the algorithm was applied on the original image. The result image in the third column indicates that no useful information within the brain tissue remains. This is caused by the low contrast differentiation between the GM and WM in conjunction with the large contrast between brain tissue and CSF which hinders the differentiation of GM and WM tissue.

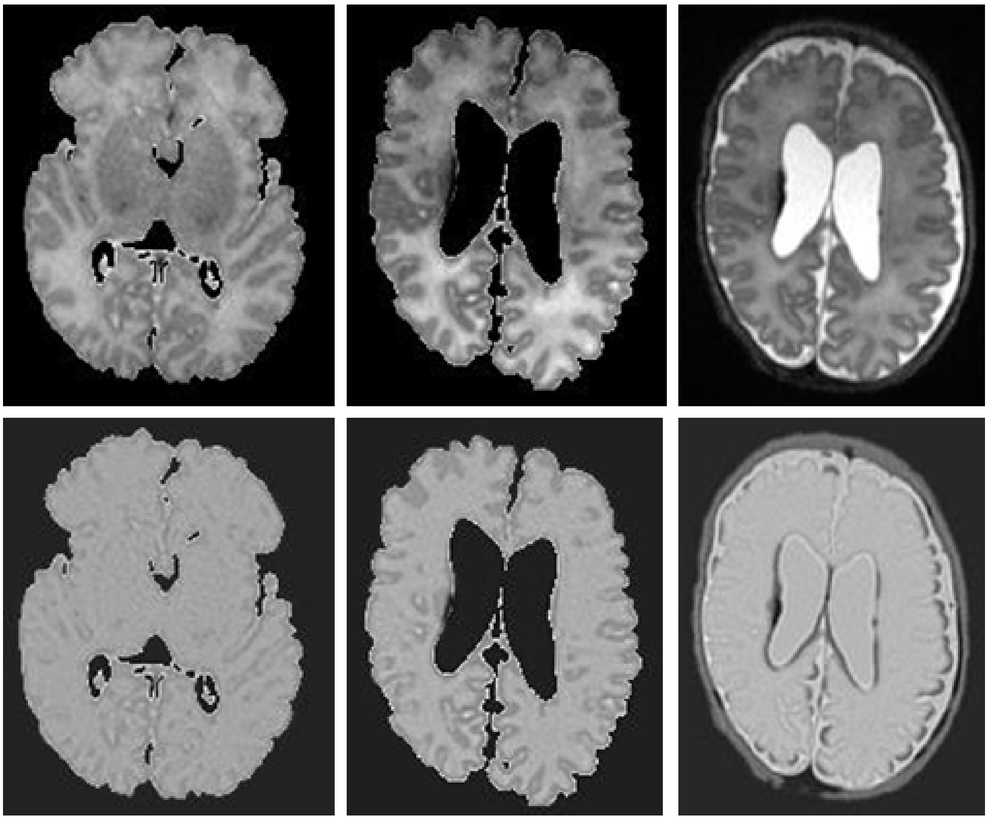

Figure 4.13: Some examples of the bias field correction algorithm proposed by Ahmed et al. The top images are the original images, whereas the bottom images are the corrected images. The last column is the result when the bias correction was applied to the middle column with the difference that in the first two columns the skull stripping process had been performed.

FCM is known for having convergence problems and to overcome these issues spatial constraints were incorporated. A negative effect of these spatial constraints is that low contrast details have been eliminated due to the blurring. In combination with a stronger level of noise in premature infant data, the algorithm fails to distinguish between GM and WM. In the last example on the right in Figure 4.13, the CSF was falsely identified because the CSF was segmented as WM.

The differences between the proposed methods and the other two algorithms was examined on a large database and an example of this investigation is illustrated in Figure 4.14 where the histogram was created from an example of the results that were generated by each method. Similar results as those presented in Figure 4.14 are obtained for all datasets where a clear difference in the intensity distribution of each image can be noticed. The blue line indicates the results for the proposed method where the differentiation between grey matter and white matter is illustrated by two peaks. Two peaks can also be observed from the results produced by Fuzzy C-Means algorithm displayed in red. However, in that case, the largest peak presents the background pixels and the smaller peak describes all brain tissue. This is similar to the results of the histogram-based technique displayed in green where the low level intensity peak presents the background and the high level intensity presents everything else. The outcome demonstrates that the most accurate results are given by the proposed method.

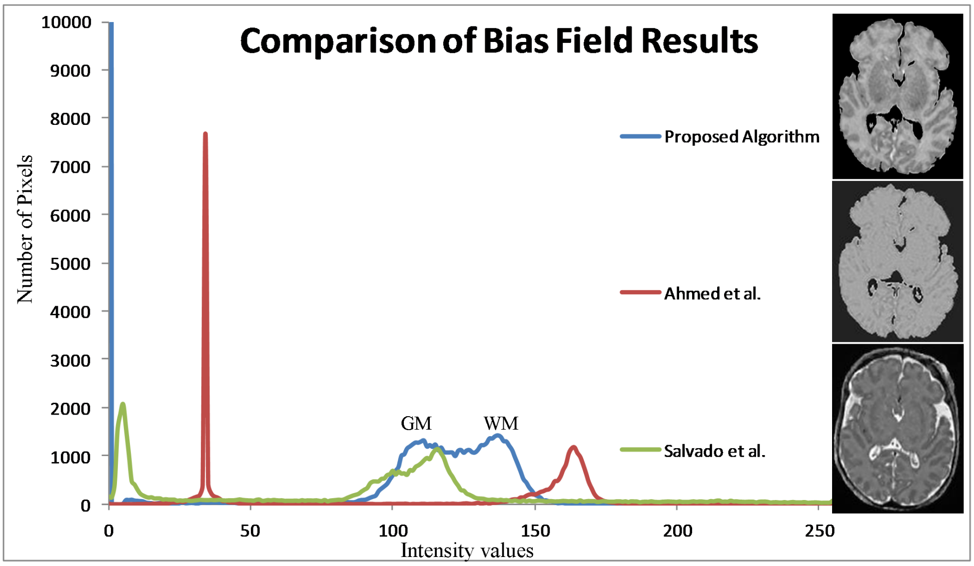

Figure 4.14: The intensity distribution obtained after bias field correction. The blue line presents the intensity distribution of the proposed method, whereas the red line is the result of the Fuzzy C-Means method, and the green line presents the results of the histogram-based technique.

4.7 Conclusions

This chapter proposed a bias field correction algorithm for infant brain MRI data. In this technique, the data is pre-processed using histogram analysis, a coherence enhancing filter and contrast enhancement. A pre-segmentation using a sequentially performed

Otsu algorithm with the combination of a probability calculations, allows the generation of an intensity map for each region (white and grey matter). The bias field is computed by applying a Butterworth low pass filter on the intensity map. The original image is corrected by multiplying the calculated bias field with the original image. A number of experiments indicate that the algorithm reduced the intensity variations without any attenuations in the edge information.

Chapter 5

White Matter Segmentation

As introduced in Chapter 2, the process of segmenting a specific tissue in brain MRI data is a challenging task. The majority of the developed segmentation algorithms were designed for the segmentation of adult brain MR images. Due to the early stage of the brain development in infancy, the application of these algorithms to infant MRI data has limitations. The segmentation of infant brain MRI data is difficult because of the low contrast between tissues, partial volume effects and the lack of clear edges. As a consequence, the segmentation requires carefully selected features. Some researchers combined the segmentation with prior information that are presented in form of an atlas. These segmentation algorithms rely on the quality of the atlas and a large amount of manually segmented data is required to generate an accurate prior brain model.

In our study, the anatomical structure information presented as a prior atlas for infant brain MRI data was not available, and the proposed algorithm is constructed as a combination of multiple intensity-based methods. The segmentation algorithm is the third part of the framework presented in this thesis. At this stage, the white matter tissue can be segmented after the non-brain tissue has been removed and the intensity inhomogeneities in the images have been corrected. In this chapter, a novel and fully automatic segmentation algorithm for brain MRI data during infancy is presented. The next section outlines an overview on the designed technique and is followed by a detailed description of all computational steps of the proposed method. A quantitative evaluation of this approach is presented in Chapter 6.

5.1 Overview

Figure 5.1 outlines the structure of the proposed segmentation algorithm which aims to extract and measure the white matter region in infant brain MRI data. During the first stage, the data is pre-processed by adjusting the intensity distribution in the same way as explained in Section 4.3. The pre-processing part was extended by one step which analyses and corrects the head position. This is followed by two Expectation Maximization (EM) algorithms. The first EM evaluates the results obtained from histogram analysis and the second EM uses the images from the contrast enhancement step. In order to improve the EM classification, the two EM results are combined, which amplifies the discrimination between the white matter and the grey matter.

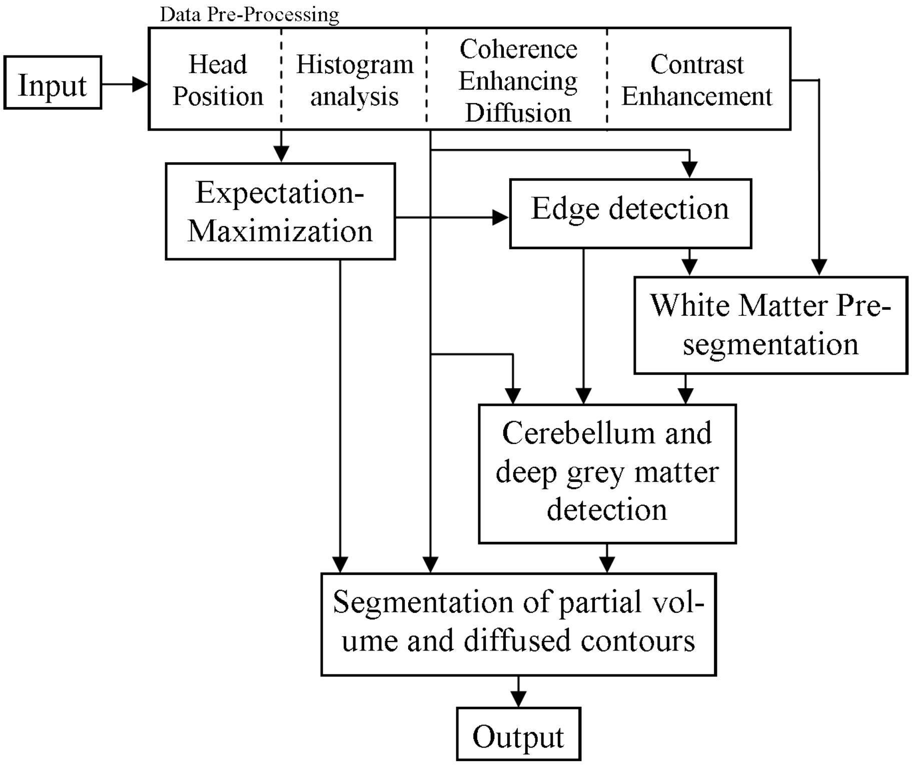

Figure 5.1: An overview of the probabilistic segmentation technique for white matter segmentation.

Next, an Otsu thresholding algorithm is applied as previously introduced in Section 4.3. The Otsu segmentation allows a preliminary identification of the white matter region on which the main segmentation step is based. Given that the deep grey matter consists of white matter and grey matter tissues, this area is detected in a separate step with the intention of improving the segmentation results. To completely extract the white matter and correct the segmentation errors, a re-classification of the partial volume voxels and of the voxels situated on diffused contours is performed.

5.2 Data Pre-Processing

The data pre-processing step is composed of adjusting the head position, histogram analysis, Coherence Enhancing Diffusion and contrast enhancement, as shown in Figure 5.2. These methods are applied in the same way as it was described in Section 4.3, except for the first step. The main addition to this pre-processing step is an analysis of the head position within the volume. This step was only developed to aid the precision of the cerebellum and deep grey matter detection which adjusts the position of the right and left ventricles (this will be presented in Section 5.5). Without this step, important indicators required to detect the cerebellum and the deep grey matter can disappear, and by adjusting the head position, the localisation of these features is improved.

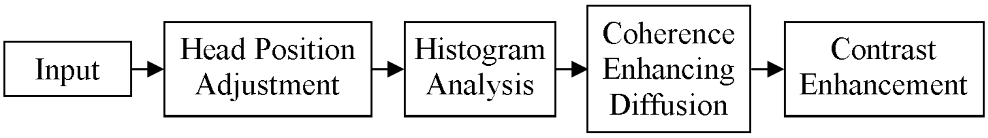

Figure 5.2: Overview of the pre-processing steps.

In order to facilitate the description of the techniques performed in this chapter, an understanding of the coordinates of the brain MRI data is necessary. Figure 5.3 illustrates images in the axial, sagital and coronal views for one patient, in which the arrows indicate the 3D coordinate system.

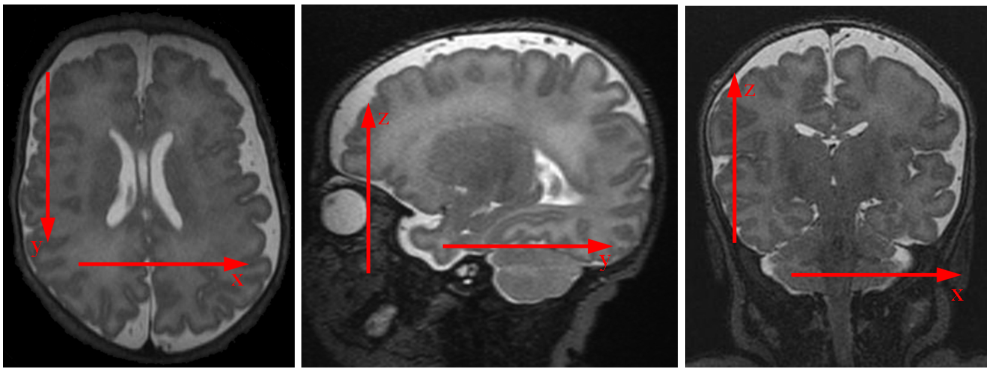

Figure 5.3: Representation of the coordinates of the head in three dimensions. The example on the left presents an axial view, the middle image illustrates a sagital view and the right image shows a coronal view. The arrows indicate the coordinate system.

The initial correction step attempts to calculate the angle of the head position in the z-axis direction. This can be visually illustrated when a patient has the head tilted forward or backward during the acquisition. This step is essential for the proposed 2D cerebellum detection algorithm because the features on which the cerebellum and deep grey matter extraction is based, may change or disappear in different head positions. This adjustment is required in the pre-processing step because different volumes are generated from the pre-processed data.

The variations in the x-axis direction (e.g. if a patient turns the head to one side) do not have an impact on the algorithm and have, therefore, not been investigated in this step. Therefore, to simplify the procedure, it was decided that the adjustment of the head position in the z-axis direction is sufficient.

The algorithm commences by selecting the image with the largest brain tissue area at the position of the seedpoint in the z-axis direction in the volume. In this image, the lowest and the largest y coordinate of the brain tissue are located. These two locations describe the front and the back of the head, as shown by the points a_1 and a_2 in Figure 5.4. The angle of the head is measured by the lowest y-coordinate represented as a_1 and the largest y-coordinate illustrated as a_2. The following formula is used to calculate the angle of the head in the sagital view,

$$angle = \arctan \frac{z_{a_2} - z_{a_1}}{y_{a_2} - y_{a_1}} \tag{5.1}$$

where z and y are the coordinates of the points a_1 and a_2, displayed in the sagital plane in Figure 5.4. As an ideal position, the angle of the first patient in this study (approximately 1.5 radians or approximately 86 degrees) was taken because the head position of this patient provided the optimal orientation for the extraction of useful information. A sagital image from the first patient with the two computed points is displayed in the top section of Figure 5.4. In order to reduce the resampling errors, it was determined that the angle of the head can vary within a range of 1.6% (meaning 0.05 radian in each direction of the initialised head position) without being adjusted. If the head angle is within this range, it has been determined that the features were detectable. Therefore, only where the head orientation is outside this range, the head position is recalculated. The reorientation step of the algorithm applies a volumetric rotation that involves an affine transformation and cubic interpolation which minimises the problems generated by non-isometric voxels. When dealing with non-isometric data the process related to volume rotation is always associated with loss of data. To maintain the same size of voxels after the rotation, the resulting 3D data is adjusted to the original 3D matrix dimension.

Figure 5.4 introduces three examples of the position of the head. The sample on the top is a sagital image with points a_1 and a_2 of the first patient, on which the other angle is adjusted to. The second example is a sagital image of another patient before correction, and the third is a sagital image presenting the second example after the head position is corrected.

The following steps of the white matter segmentation method presented in this chapter are a combination of 3D and 2D algorithms, and the 2D procedures process the data in the axial view.

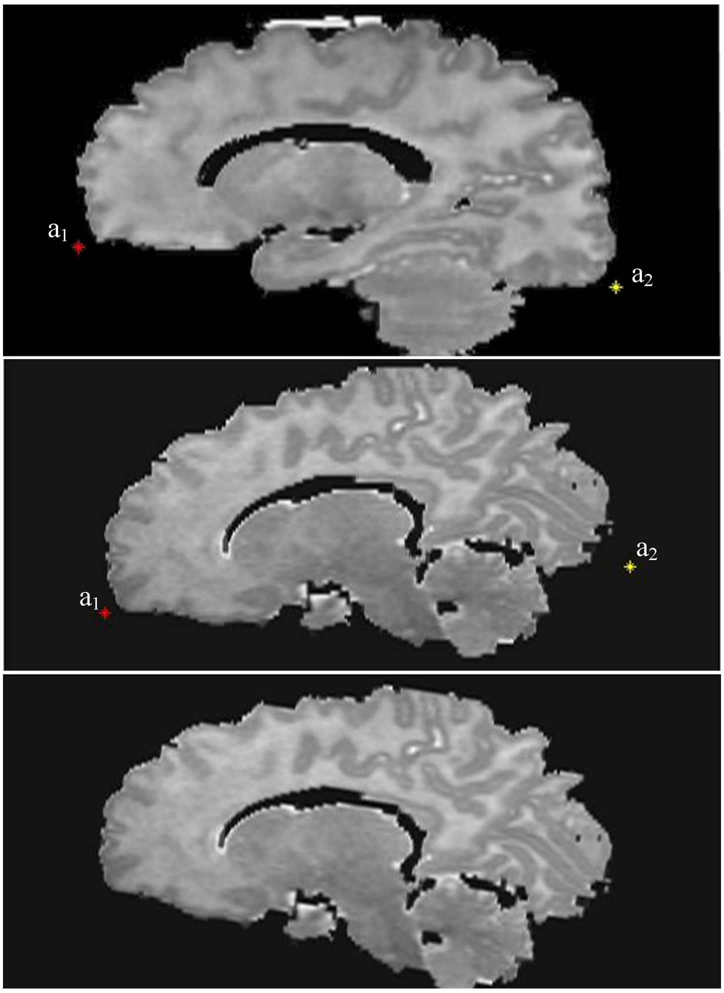

Figure 5.4: Three examples of sagital images taken from different patients. The top sample is from the first patient upon which all the other patients' datasets are adjusted to, whereas the examples below are sagital images from a patient in which the head position is estimated and then adjusted.

5.3 Expectation-Maximization Segmentation

As mentioned in Chapter 2, the Expectation-Maximization (EM) technique generates accurate segmentation results on infant brain MRI [91], while other methods are known to be less precise [52]. For this reason, it was decided to investigate the accuracy of the EM method when applied to infant brain MRI segmentation.

The Expectation-Maximization (EM) algorithm is a general technique which provides an iterative computation of the maximum likelihood estimation in tasks where the data is incomplete. The EM calculates the maximum likelihood parameter using an estimation of the hidden data based on the current parameter approximation. Then, the estimated complete data which is composed of observed and missing data is utilised to recalculate the parameters by maximising the likelihood of the complete data. In this study, a Gaussian Mixture Model (GMM) is employed in the EM with the purpose of estimate the distribution of the data.

The EM algorithm can be summarised as follows:

1. Initialise parameters
2. E-step: computes the posterior probabilities (p_{ij}) of the hidden data using the observed data and the current parameter estimation

$$p_{ij}^{m+1} = \frac{G(y_i^m, \mu_j^m, \sigma_j^m) c_j^m}{\sum_{k=1}^{K} (G(y_i^m, \mu_k^m, \sigma_k^m) c_k^m)} \tag{5.2}$$

$$and\ \ G(y, \mu_k, \sigma_k) = \frac{1}{\sqrt{2\pi}\sigma_k} \exp \frac{-(y-\mu)^2}{2\sigma^2} \tag{5.3}$$

   where p_{ij} denotes the posterior probabilities at iteration $m+1$ and expresses the probability of the voxel i to belong to the cluster j. $G(y, \mu, \sigma)$ is the Gaussian function with the standard deviation σ, y describes the intensity value, μ denotes the mean, c is a weight and K is the number of tissue classes.

3. M-step: calculates the maximum likelihood parameters for the measurement of the complete data

$$\mu_j^{m+1} = \frac{\sum_{i=1}^{n} y_i p_{ij}^{m+1}}{\sum_{i=1}^{n} p_{ij}^{m+1}} \tag{5.4}$$

$$(\sigma^{m+1})^2 = \frac{\sum_{i=1}^{n} (y_i - \mu_j^{m+1})^2 p_{ij}^{m+1}}{\sum_{i=1}^{n} p_{ij}^{m+1}} \tag{5.5}$$

$$c_j^{m+1} = \frac{1}{n} \sum^{n} p_{ij}^{m+1} \tag{5.6}$$

   where n is the number of voxels.

4. repeat steps 2 and 3 until convergence.

The EM iterates between the E-step and the M-step and converges when the maximum likelihood parameter is obtained for the observed data. The optimisation of the parameter ϕ includes the identification of μ and σ and is defined as the maximum likelihood estimation of the parameters using the observed data with their corresponding weights c. The likelihood maximisation can be mathematically expressed as follows:

$$L(\phi) = \sum_{i=1}^{n} \log \sum_{k=1}^{K} G(y_i, \mu_k, \sigma_k) c_k \tag{5.7}$$

$$\phi = \arg\max_{\phi} L(\phi) \tag{5.8}$$

where L describes the likelihood and ϕ denotes the current parameters.

EM is one of the most common algorithms in brain segmentation and mostly used on adult MRI data for which the GMM was optimised by using an atlas as prior information [76] [8]. Over the past few years, the EM technique has received significant interest when used for the segmentation of young children [91] and neonatal brain MR images [31]. The popular choice is to combine EM with an atlas which influences the segmentation procedure. As mentioned before, these atlases are population dependent and an atlas generated from adult data cannot be applied to infant brain images [50]. In this study, the EM is utilised to extract information from the brain tissue. For this reason, the classification is computed in two Expectation-Maximization procedures, where each EM is applied to different input volumes and both results are then combined subsequently. Figure 5.5 outlines the different steps of the proposed EM process.

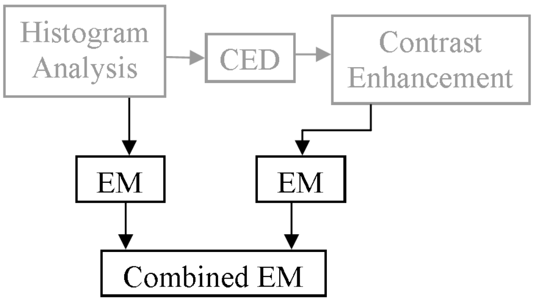

Figure 5.5: An outline of the EM process.

The partial volume effects negatively influence the segmentation results. As a consequence, two clusters are insufficient to identify the grey matter and white matter in the MRI data. Following a detailed investigation, it was decided to initialise each EM algorithm with ten classes. A selection of lower than ten classes resulted in errors that were caused by the partial volume voxels as well as the inconsistent intensity distribution of the white matter tissue. Initialising the EM with a higher number than ten classes has demonstrated no differences in the classification outcome when compared to the results obtained with ten classes. An example that emphasises the selection of the number of classes for EM is illustrated in Figure 5.6.

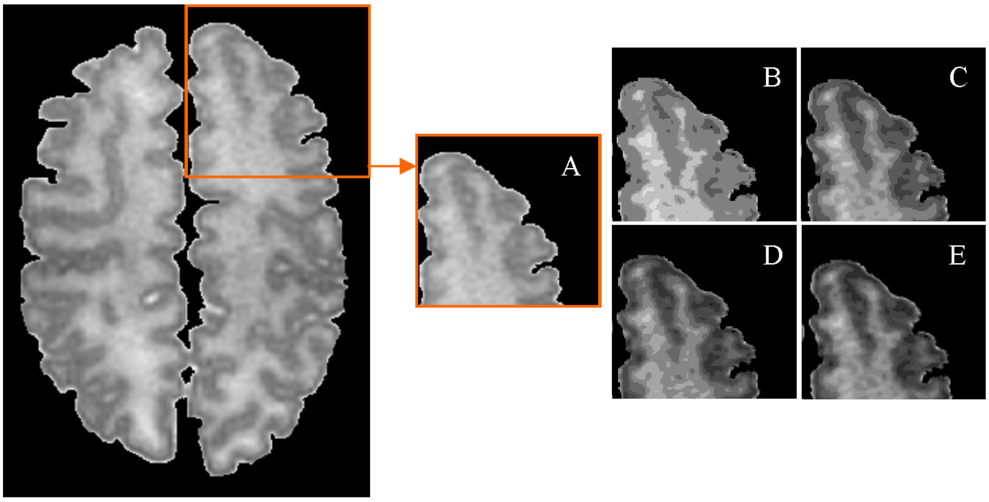

Figure 5.6: Combined final results are shown when the EM is used with different number of classes. Left: original image after bias field correction was applied. Magnified region from original image (A). The other images present results using (B): four classes; (C): eight classes; (D): ten classes; (E): twelve classes.

In this approach, the EM algorithm was, therefore, used with ten classes and the μ_i were initialised using the K-means algorithm (as described in equation 3.8) in the same way as presented by Xue et al. [132]. The EM is performed once on the intensity adjusted data and once on the contrast enhanced data. Figure 5.7 presents an example of each applied EM algorithm and the combined result. The left image is the EM result which was based on the histogram analysis. It can be observed that the grey matter provides a more homogeneous region than in the result where EM was applied to the contrast enhanced image. On the other hand, when the EM algorithm is applied to contrast enhanced images, the results provide a more homogeneous white matter region. In order to enhance both regions, the two results images are combined using pixel by pixel multiplications.

Due to the fact that the EM algorithm could not properly classify the partial volume voxels, the EM results are used in conjunction with a re-classification scheme. The generation of a preliminary white matter volume detection, on which the re-classification step is built upon, is described in detail in the next section.

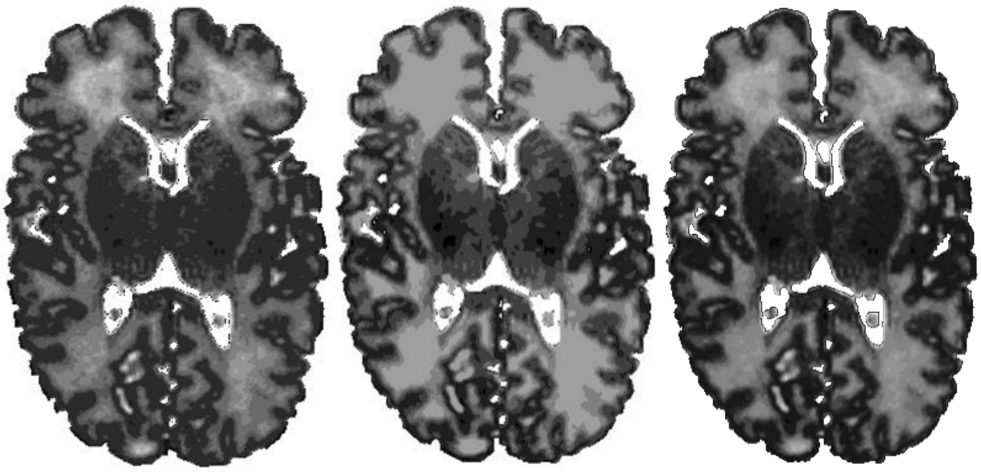

Figure 5.7: Expectation-Maximization results; Left: EM result based on the histogram analysis images; Middle: EM results based on the contrast enhancement images; Right: The result after combining both EM results.

5.4 White Matter Pre-Segmentation

In this part of the WM segmentation algorithm, a preliminary white matter mask is generated and an overview of each step is illustrated in Figure 5.8. This step is essential because the outcome of the EM algorithm has not provided sufficient accurate results. The inaccuracies in the EM results were caused by partial volume effects and the diffused boundaries between brain tissues. Therefore, this preliminary segmentation step is performed with the aim of generating an initial white matter volume which is corrected and finalised by applying two algorithms which will be explained in Section 5.5 and 5.6.

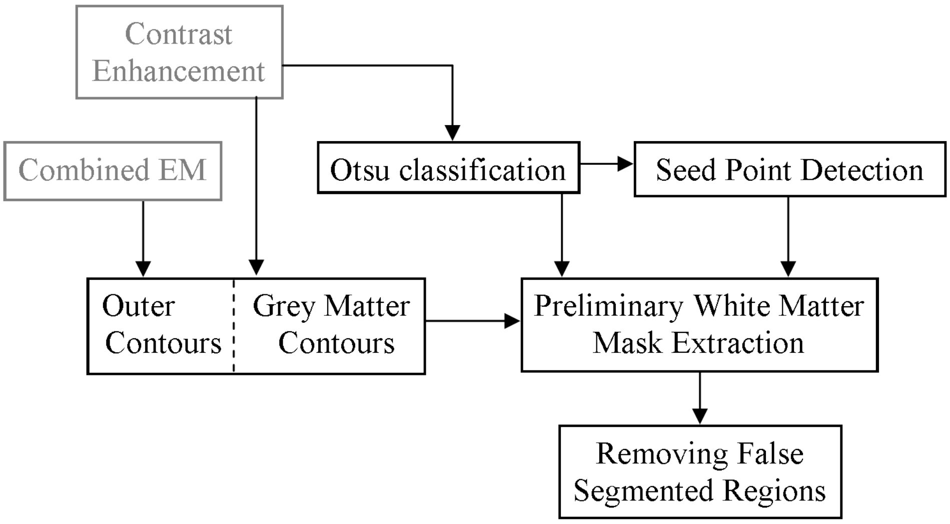

Figure 5.8: Overview of the pre-segmentation steps.

Otsu Classification: The Otsu algorithm is used in a similar way as it was performed in Section 4.3. The image is first divided and each part is then categorised into four classes using the Otsu thresholding method. The difference in the use of Otsu classification between the bias field correction algorithm and this step is that, at this stage, the four classes are not further processed. The advantage of this classification is that the two middle classes, class two and three, are generated by the diffused boundaries and the partial volume voxels, which will be closely examined in the reclassification step that will be discussed in Section 5.6. For this reason, the white matter pre-segmentation step focuses only on the first class of the Otsu classification representing the white matter tissue. An example that presents a result image can be observed in Figure 5.9 (middle image of the top section).

Preliminary Mask Extraction: The extraction of the preliminary mask is based on the application of a three dimensional binary region growing algorithm to the voxels of the first class of the Otsu classification. From an anatomical perspective, the white matter tissue is connected throughout the volume. In this regard, this procedure is necessary because it eliminates small non-connected regions which are wrongly classified into the white matter class.

Seedpoint Detection: The seedpoint of the region growing is automatically selected. During the intensity adjustment step, the seedpoint in the z-axis direction is determined by selecting the image with the largest brain tissue. Within the image that contains the seedpoint z, the x and y coordinates are obtained by extracting the largest connected region associated with the class one of the Otsu results, which represent the white matter tissue. One pixel is taken from the extracted region and is defined as seedpoint.

Contours: From an anatomical view, the white matter tissue is surrounded by the grey matter tissue. Using this knowledge, the elimination of the non-white matter tissue is achieved by considering the contours of the grey matter tissue as a stopping condition. Two different contour volumes are computed.

1. The first contour volume represents the outer contours of the grey matter tissue that are connected to the background. The determination of the grey matter contours is based on the final Expectation-Maximization results in combination with the contrast enhanced results. The first approximation of the grey matter is computed by combining the lower intensity classes of the EM results until the number of voxels reaches a threshold. This threshold is set as $4/7^{th}$ of the brain tissue volume. Using a threshold which returns just above the half of the volume, enables the inclusion of partial volume voxels and the voxels situated close to unclear boundaries. These initial contours are also used in the second phase, where the

inner contours are calculated.

Due to the early stage of brain development, the grey matter has a small thickness, which can lead to unclear borders between white matter and grey matter. The consequence is that small grey matter parts have the same intensity as the white matter and are, therefore, excluded from the contour. In order to determine the final outer contours, the located boundaries are enclosed using morphological operators.

2. In the second phase, the inner contours are calculated. An investigation was carried out using the Marr-Hildreth edge detector to find the contours between the grey and white matter. The outcome reveals that the Marr-Hildreth algorithm is not precise enough and the enclosed contours can lead to false segmentations. The Mar-Hildreth algorithm is known for returning a high level of false positives. Shattuck et al. [109] pointed out these issues and they tried to overcome them by using morphological operators. This was possible for brain extraction but not for white matter segmentation. Therefore, the contours are extracted by applying the Canny edge detector on the contrast enhanced images. The Canny algorithm is applied with σ, which is set to one and two thresholds, the low threshold is set to 0.01 and the high threshold is set to 0.2. These values were experimentally estimated. The edges are enclosed using morphological operators, followed by merging the results with the previously calculated grey matter contours. The preliminary white matter segmentation results are shown in Figure 5.9 (first and second image in the bottom row).

Removal of False Segmented Regions: Due to small brighter areas in the brain tissue, which cannot be clearly classified, since they might be residues of CSF, additional processing of the results is necessary and is achieved by removing small false segmented areas. For this reason, the non-brain tissue (background) boundaries are examined. This is based on the assumption that the white matter is surrounded by the grey matter. The falsely segmented areas are composed of cerebrospinal fluid, which appears with the same intensity as the white matter and are, therefore, misclassified. In this regard, all regions defined as white matter and connected to the background are evaluated. The focus lies on the contour of the analysed region. Three values are determined and then compared. These values are composed of the sum of the contour voxels which connects to background ($bgcont$), secondly the sum of the contour voxels of the located region ($regioncont$) and thirdly the sum of the contour voxels which connect to the grey matter region ($gmcont$).

$$pbg = \frac{\sum bgcont}{\sum regioncont} \qquad pgm = \frac{\sum gmcont}{\sum regioncont} \tag{5.9}$$

The idea is to exclude the small regions using two criteria. Firstly, the pbg (probability of the background) has to be higher than a threshold (experimentally the threshold has been set to 0.4). The pbg describes the percentage of contour pixels connected to the background. Secondly, if the region is connected to a grey matter contour with less than twice the threshold, the region is detached and removed from the white matter mask. In case the white matter is connected to the outside background voxels but does not fulfil the requirements of being removed, the connected area is reduced by three pixels in width from the contour which connects to the background. This is essential because the white matter has to be surrounded by grey matter and the presence of artefacts can prevent the accurate distinction between the grey and white matter.

This segmented white matter volume marks the basis for the following probabilistic segmentation where the partial volume voxels are classified. Figure 5.9 illustrates an example that details the steps of the preliminary white matter extraction. It can be observed that the majority of the false segmented voxels lie in the deep grey matter region (see the region marked with a rectangle in Figure 5.9). This issue will be dealt with as an additional stage of the segmentation procedure and will be explained in the next section.

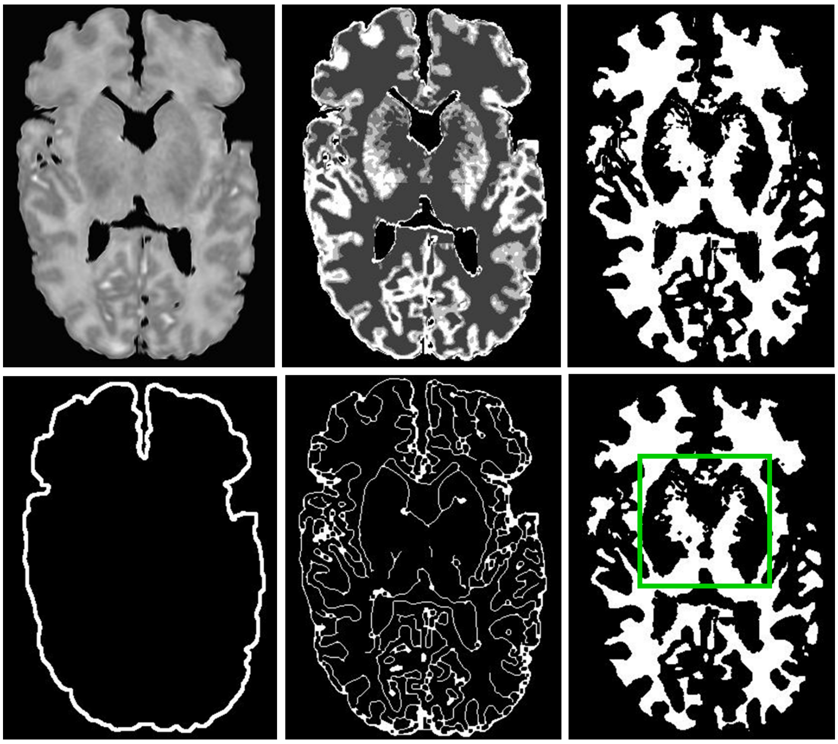

Figure 5.9: The steps required to extract the preliminary white matter mask. Top row, left: The pre-processed original image, middle: The result of the Otsu classification and right: The first white matter mask. Bottom row, left: The outer grey matter contour, middle: the result of the Canny edge detection and right: the preliminary white matter mask.

5.5 Cerebellum and Deep Grey Matter Detection

One of the major difficulties while processing MR images of the developing infant brain is the deep grey matter. This step is not an issue when using a global segmentation such as atlas-based [91] on healthy patients. When dealing with neonatal MRI data, there is a high probability that large variations in the brain structure may be present. Cardoso et al. [31] stated that an atlas-based segmentation alone does not provide sufficient results when applied to premature infants. This issue has been analysed by Shi et al. [110] who evaluated the application of atlas-based segmentation on infants brain. Therefore, the aim of the deep grey matter and cerebellum detection is to examine this problem by a non atlas-based approach in order to overcome the disadvantages of applying an atlas-based algorithm on preterm infants with abnormal brain structure. When applying a local segmentation algorithm, the inconsistent water content in the deep grey matter and cerebellum can cause false segmentations in the proposed algorithm as well. To overcome this problem, an additional deep grey matter and cerebellum detection algorithm has been proposed. Figure 5.10 illustrates the difference in the deep grey matter between an MR image of an infant and a two-year-old child.

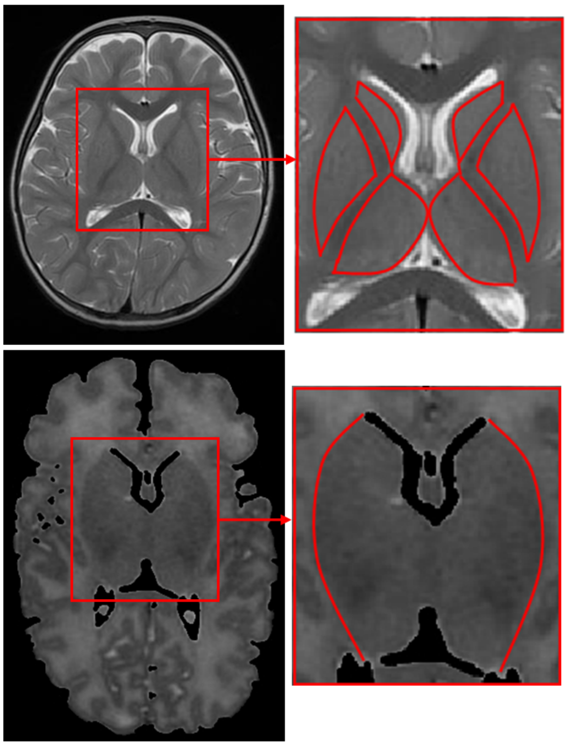

Figure 5.10: Top row illustrates a brain image of a two-year-old child where the brain structure has developed. The right side shows a magnified image of the deep grey matter. The bottom row introduces an infant brain image where the deep grey matter region has been magnified. In both examples the deep grey matter has been outlined by surrounding the region with a red line.

In adult MRI data, the deep grey matter is well structured and can be displayed in six smaller regions. During infancy, it is difficult to distinguish the white matter and the deep grey matter due to a high amount of CSF within the brain tissue.In Figure 5.10, the magnified deep grey matter region is highlighted by a red line. The atlas-based techniques have one advantage in the deep grey matter segmentation process. Information of the myelinated white matter is incorporated in the atlas and is then used to influence the segmentation for the extraction of this region. This is often not possible in intensity-based segmentation because there is not enough information within the deep grey matter region for the detection of the myelinated white matter tissue. The absence of myelinated white matter information is especially present in 1.5T data.

Given the fact that the region is composed of white and grey matter which results in intensity inconsistencies and diffused boundaries, the segmentation poses a great challenge. Therefore, in this study, the clinicians decided to assign this entire region as deep grey matter. Figure 5.11 illustrates several images from different views of the brain in which the investigated regions are indicated by arrows. The red arrows point at the deep grey matter where it can be observed that there are no clear contours when they are attached to the white matter tissue. The cerebellum is indicated with green arrows and the brain stem is identified by a yellow arrow.

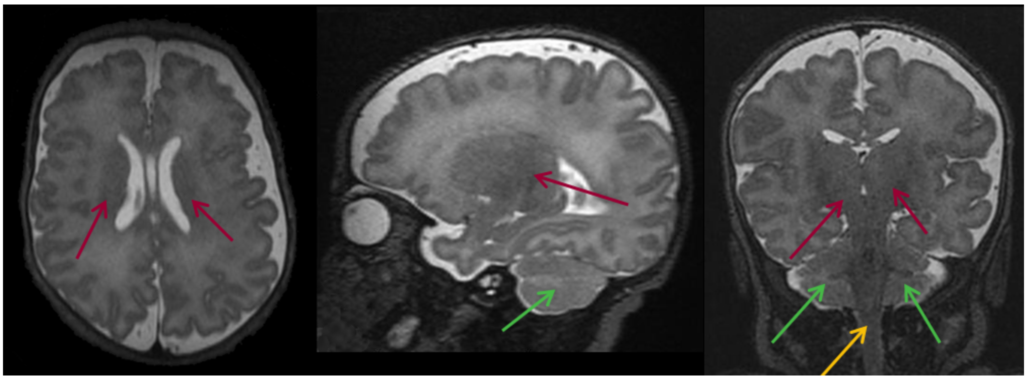

Figure 5.11: The deep grey matter is marked with a red arrow in each image. The green arrows identify the cerebellum and the yellow arrow indicates the brain stem.

Several researchers [41] [102] have performed investigations on the detection of the brainstem and cerebellum on adult MRI using active contour models or analysing the intensity distribution. Gui et al. [52] used the watershed technique to extract the deep grey matter, cerebellum and brainstem on neonatal MRI data. However, their method is not entirely automatic and a seedpoint that marks the cerebellum had to be manually selected. Their data was acquired with a 3T scanner, which provides images with increased contrast between the grey matter and the white matter.

In MR images shown in Figure 5.11, the cerebellum and the deep grey matter merge at some point and it is difficult even for clinical experts to detect the exact position that separates them. Therefore, in this step, the two parts are regarded and extracted as one object. Figure 5.12 illustrates an example of a sagital brain image which shows the analysed region, which is marked with a green line.

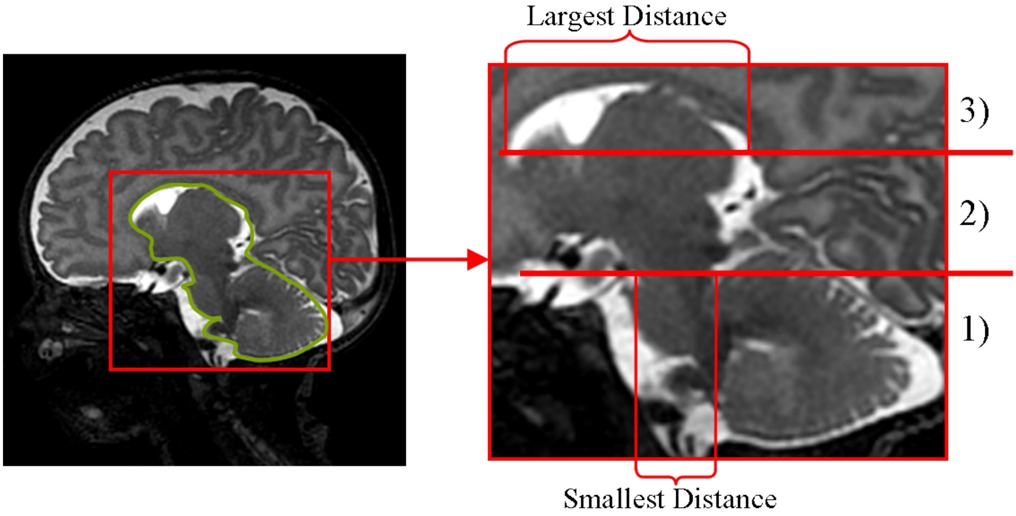

Figure 5.12: A sagital brain image detailing the deep grey matter and the cerebellum, which is marked with a green line. The region is divided into three parts; the first part (1) represents the cerebellum connected to the brain stem, the second part (2) can include some end parts of the cerebellum, brain stem and deep grey matter and the third part (3) is the deep grey matter. The separation between the first and second part is defined when the size of the brain stem is the smallest and the third part is separated from the second step when the largest distance between ventricles can be measured.

The fully automatic detection process is divided into three parts where each part focuses on different features of the brain. The first part, the extraction algorithm, indicated by 3 in Figure 5.12, identifies the deep grey matter by examining the information related to the brain ventricles. The second step, marked as 1, locates the cerebellum, and the final step is the region between the cerebellum and the lower part of the deep grey matter. For the first two steps, the idea is to start with one estimated image, on which the features have been detected, and to apply this information to the contiguous images. In the last step, the information of the first and second step is used to estimate the connected region.

5.5.1 Extraction of the Deep Grey Matter surrounding the ventricles

The main idea used in the deep grey matter (DGM) extraction (indicated with 3 in Figure 5.12) is to detect the Region of Interest (RoI) by locating the brain ventricles which provide the essential information.

Using the knowledge provided by clinical experts, a few assumptions are established in order to detect the deep grey matter. These are summarised as follow:

- Ventricles are always present.
- In the axial view, as illustrated in Figure 5.13, the deep grey matter is always attached to the ventricles.
- The mid line between the brain ventricles, which is marked with an orange line in Figure 5.13, maintains the same position throughout the volume.

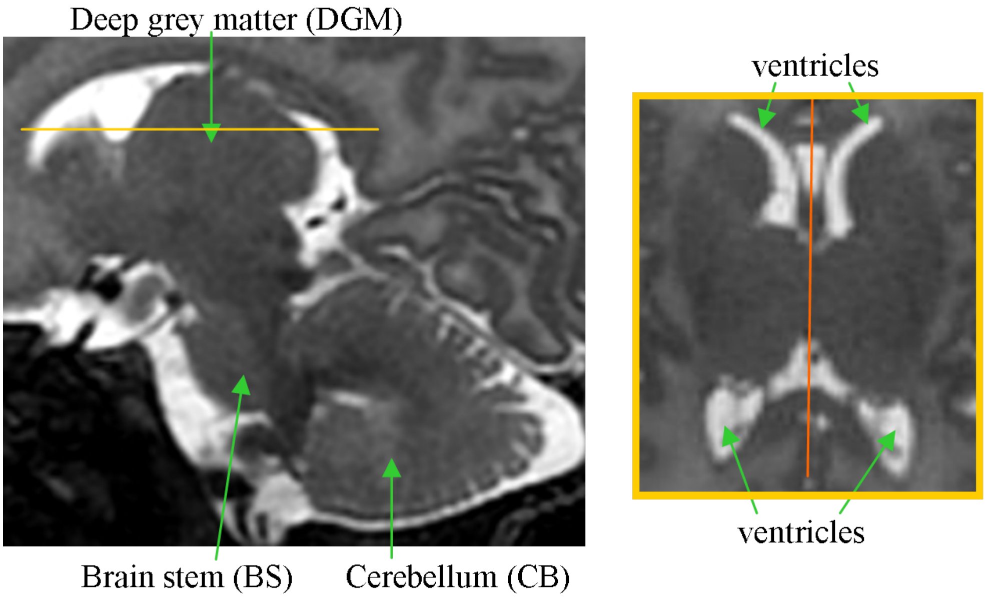

Figure 5.13: The deep grey matter and its features. Left: sagital view of the deep grey matter. Right: the deep grey matter in the axial view taken from the location marked with a yellow line in the sagital image.

In this part of the brain, the ventricles are strong feature points on which the DGM identification can be based. The idea is to fit an ellipse within the region of interest, which allows the detection of the DGM. This approach has a clear advantage since the information of the ventricles can be projected on other locations in the volume where less strong features appear. Figure 5.14 illustrates an overview of the steps that are performed to extract the DGM. The method commences by locating the RoI and the ventricles information. The ellipse is fitted to the examined region using the knowledge about contours and information related to the ventricles.

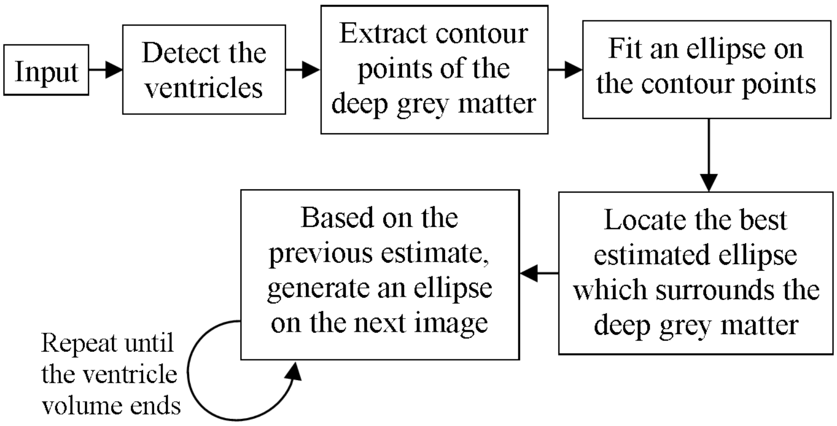

Figure 5.14: Overview of the steps needed to locate and extract the last part of the deep grey matter.

Region of Interest and Feature Extraction: In the first step, the estimation of the RoI is determined based on the identification of the brain ventricles. The ventricles are firstly detected by converting the pre-processed images into binary and then by locating the largest CSF parts inside the brain volume. In a minority of cases, it can be observed that the two ventricles are not connected to each other. In these cases, the two largest CSF regions form the ventricles. The image selected for this procedure is obtained by determining the image in which the top points of the ventricles are farther apart from the bottom ventricle points. The RoI is obtained by generating a box that surrounds the ventricles, where on the y-axis is the length of the ventricles. Regarding the x-axis, the largest distance between the outer ventricles points is calculated and one third of the distance is added to each side. In order to obtain the best estimation of the RoI, an initial angle of the head position in the x-axis direction is estimated. The angle is computed in the same way as described in Equation 5.14. Due to the fact that the ventricle feature points are precisely located after the RoI is extracted, the calculation of the angle provides an initial estimation.

After the ventricles are located, four feature points are identified in each image which contains parts of the ventricles, as shown in Figure 5.15. These points represent the initial feature points that will be used for finding the outer contour of the deep grey matter.

These feature points are constructed using a min-max search for all pixels identified as ventricle. The challenge increases if parts of ventricles are missing as shown in Figure 5.17 (see the right image). For example, if one of the ventricle parts from the top is missing, the feature point can be estimated using the angle α of the previous image $i+1$ and the angle β of the current image i. As mentioned before where the assumptions were outlined, the angle α does not change throughout the volume and can, therefore, be

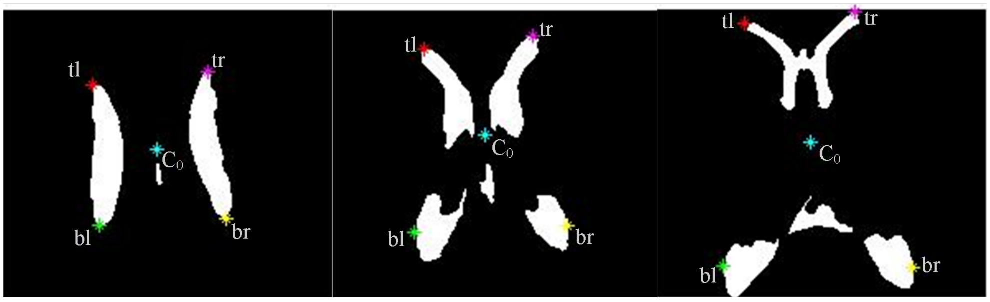

Figure 5.15: This illustration presents three examples of the four feature points (tl, tr, bl, br) which are identified in each image which contains the ventricles. The point between the four feature points is the centre point (C_0).

applied in continuous images where the information is missing. An example that shows the computed angles in both images is presented in Figure 5.16.
The formula used to calculate the angle α and β is as follows:

$$\alpha = \arccos \frac{< \overline{v_1} \; , \; \overline{v_2} >}{|v_1| \cdot |v_2|} \qquad \beta = \arccos \frac{< \overline{v_3} \; , \; \overline{v_2} >}{|v_3| \cdot |v_2|} \tag{5.10}$$

where v_1 describes the vector between $c_{(i+1)}$ and $C_{0(i+1)}$, and v_2 denotes a horizontal vector. The angle β is calculated in the same way as α except that v_3 describes the vector between the centre C_0 and the located top ventricle feature in the current image, which is the top right ventricle point tr in Figure 5.16.

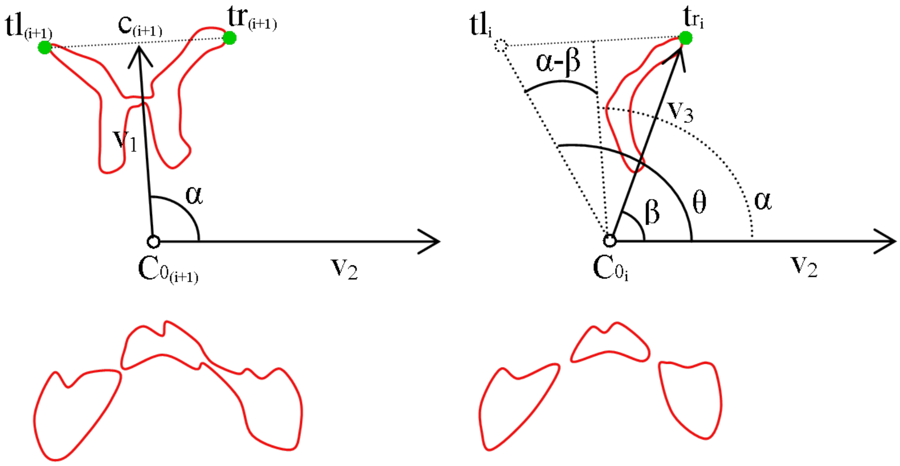

Figure 5.16: An example that illustrates the angles needed for the estimation of a missing top left ventricle feature point. In the two graphs, the ventricles of two contiguous images are outlined in red. The left graph indicates the top ventricle points in the previous image (highlighted in green), whereas the right graph shows the points in the current image where the top left point is missing and needs to be estimated.

The angle θ is used to rotate the identified feature point so that the unknown ventricle point can be estimated.

The angle to estimate the left ventricle point is calculated as follows:

$$\theta_l = 2 * (\alpha - \beta) + \beta \tag{5.11}$$

The angle to estimate the right ventricle point is calculated as follows:

$$\theta_r = \alpha - 2 * (\beta - \alpha) \tag{5.12}$$

The x and y coordinates of the missing point for left or right is then estimated by:

$$t_{x_{l,r}} = C_{0x} + \cos\theta_{l,r} * rad \qquad t_{y_{l,r}} = C_{0y} - \sin\theta_{l,r} * rad \tag{5.13}$$

where rad is the radius between the detected ventricle point and the centre C_0. An example of the located ventricle points is displayed in Figure 5.17, whereas the right image presents an example in which one part of one ventricle is undetected.

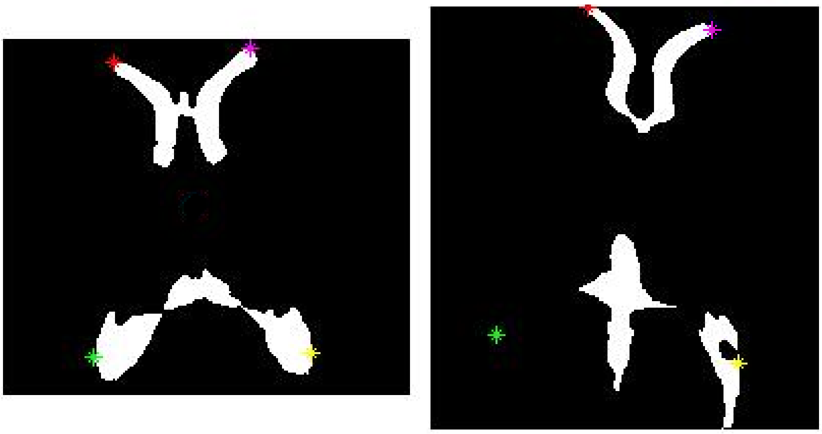

Figure 5.17: Two examples taken from different patients where the ventricle feature points have been located. Each located position is marked in a different colour including the centre of all four detected points.

Create an Initial Ellipse: After detecting all necessary ventricle points, an initial ellipse is constructed in two phases. This is accomplished by firstly locating the contours of the deep grey matter and then fitting an ellipse which is based on the detected contour points.

Due to the high water content in the brain tissue, the boundaries between the DGM and the white matter are unclear and diffused. For this reason, the contour images are generated by extracting the edges of the preliminary white matter mask. The guiding idea in this step is to mark the region which surrounds the contour points of the DGM and then select the edge points in this area. In order to find the required region, two ellipses with different sizes are constructed, which are based on the centre point that is calculated from all four ventricle features.

- The smaller ellipse is defined as a circle where the radius (r_s) is based on the Euclidean distance between the centre point and one of the located ventricle features as shown in Figure 5.18.
- The larger ellipse is determined as follow. The short radius of the larger ellipse is set as the radius (r_s) plus the distance (d_1) between the centre point and the ventricle in x-axis direction. For the long radius, the radius (r_s) is enlarged by adding half the distance (d_2) between centre point and the ventricle in the y-axis direction.

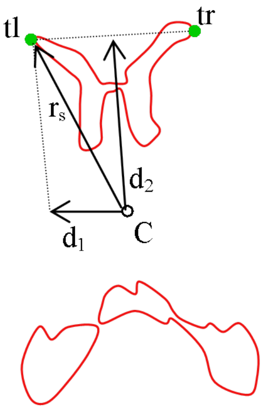

Figure 5.18: An example that illustrates the radius of the small ellipse (r_s) and the distances (d_1 and d_2) which are added to the radius to form the large ellipse.

The contour points, between the two ellipses, are used in the estimation of the preliminary ellipse.

The angle of the ellipse is computed using the information of the ventricle points. This is important because it allows the adjustment of the fitted ellipse in case the angle is too far off. This can occur if not enough contour points are found. The angle is calculated using the following formula:

$$\vartheta = \arctan\left(\frac{c_y - C_{0_y}}{c_x - C_{0_x}}\right) \tag{5.14}$$

where c describes the top middle point between t_l and t_r and C_0 defines the centre point for all ventricle points. This calculation is essential because the angle is applied throughout the deep grey matter extraction algorithm.

Ellipse Fitting to Feature Points: In order to find the best fitted ellipse for a given set of data points, the estimation is carried out using the least squares method and applied without the use of any weights [57]. This means that the best least squares fit is optimised by minimising the sum of the squared difference between the given values and the fitted values [45]. For the fitting process, the conic ellipse is utilised so that the computed curve is obtained by an intersection with a cone. In this case, the ellipse is a general conic fitting of an implicit second order polynomial and is mathematically described as follows:

$$F(A;X) = AX = ax^2 + bxy + cy^2 + dx + ey + f = 0 \tag{5.15}$$

where $A = [a\ b\ c\ d\ e\ f]$ describes the parameters of the conic equation and $X = [x^2\ xy\ y^2\ x\ y\ 1]$ describes the conic equation. $F(A;X)$ describes the algebraic distance of a point (x,y) to the conic F(a;X)=0. The fitting of a general conic can be approached by minimizing the sum of the squared algebraic distance $\sum_{i=1}^{N} F(X_i)^2$ of the curve to the N data points X_i.

Extract the Deep Grey Matter: The ellipse fitting is applied only to the images in which the ventricle features can be detected. It is apparent that the higher the number of feature points (ventricles and contours), the better the ellipse is aligned to the given set of points. Since the boundaries between DGM and the white matter tissue can be unclear and difficult to detect, the ellipse fitting is performed in conjunction with the calculation of the dice similarity measure (DSM). This means that for each constructed ellipse the DSM is measured in the current and the next image. Due to the fact that the ellipse changes in size within the volume, it was decided that if the DSM is higher than 95%, then the image and ellipse information is stored. In order to perform an accurate detection of the DGM, the centre point and the angle information are determined using their average values of the stored ellipses.

To finalise the DGM volume, a primary ellipse is selected by choosing the largest ellipse of the stored information. The ellipse is then projected to the contiguous images while adjusting the ellipse size in agreement with the changes of the ventricles. This means that the differences in the location of the top ventricle points between the current and the previous image are measured and used to scale the ellipse in the current image. The brain tissue volume delineated by ellipses in each image is marked as DGM. Figure 5.19 illustrates an example of the final outcome where the detected DGM is marked with a darker grey intensity value.

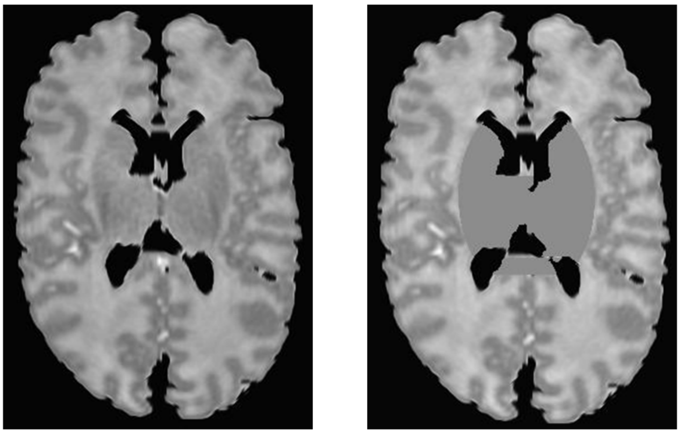

Figure 5.19: The left image is the original image which was pre-processed using the brain extraction algorithm and has the bias field corrected. The right image is the result showing the detection of deep grey matter (the detected area is marked in darker grey).

5.5.2 Detection of the Cerebellum

In this part of the algorithm (indicated as part 1 in Figure 5.12), the cerebellum and the brain stem are identified and then removed from the white matter segmentation. The cerebellum consists of white matter and grey matter tissues, which can be distinguished in a fully developed brain but is unclear at birth. For this reason, parts of the cerebellum are wrongly segmented as white matter tissue. Figure 5.20 introduces the steps that are performed to identify the region of the cerebellum.

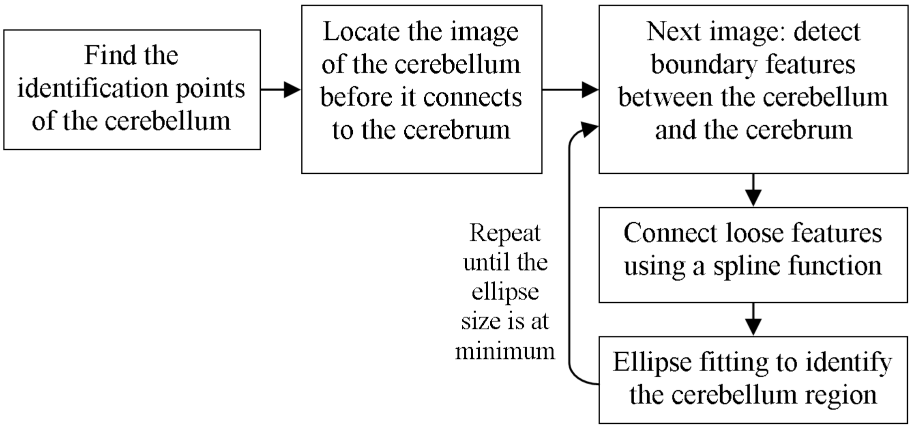

Figure 5.20: Overview of the cerebellum detection process.

In order to simplify explanations, the RoI in this part of the brain is referred to as cerebellum because both regions, the cerebellum and the brain stem are connected and extracted as one region.

Select the Cerebellum Image Before it Connects to the Cerebrum: The guiding idea is to first locate the axial cerebellum image, just before the cerebellum connects to the cerebrum. The advantage of this is that from the axial view, the cerebellum, has the largest size and the exact shape and contours can be estimated. In addition, in the following images the cerebellum increasingly connects to the cerebrum which complicates the RoI detection because the contours between the cerebellum and cerebrum are often unclear and can only be estimated. In order to assure that the cerebellum maintains the same shape for each patient, the re-positioning of the head, described in Section 5.2, is essential.

As mentioned before, the idea is to locate the image of the cerebellum just before connecting to the cerebrum. This was done by analysing the volume and contour changes of the cerebellum. However, this process was not precise enough when the changes are not large. Knowing that the cerebellum contains the largest 2D volume before connecting to cerebrum, the goal is to identify the most outer contour points in the x and the y-axis direction. These points can be found on the coronal and sagital views as shown in Figure 5.21.

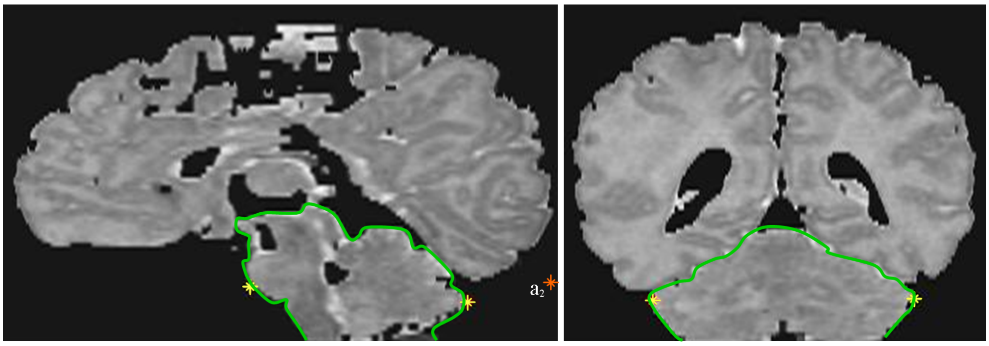

Figure 5.21: Left: An image in the sagital view. Right: The image in the coronal perspective of the same patient. In both images the two extrema are displayed in yellow and the region of the cerebellum is outlined in green.

To identify the outer cerebellum contour points, a min-max search is applied on the sagital and coronal views by considering the brain tissue below the point a_2 which was calculated in Section 5.2 after brain orientation correction. Due to the new head position, only the cerebellum and the brain stem remain below point a_2 which facilitates the min-max search. Figure 5.21 illustrates an example in coronal and sagital views where the cerebellum and the brain stem are outlined in green and the outermost cerebellum points are indicated in yellow and the point a_2 is indicated in red.

After locating the outermost cerebellum contour points, the next step is to find the image of the cerebellum before it connects to the cerebrum. The axial perspective is the only view where all contour points are present and, therefore, the algorithm continues to proceed in the axial perspective. In order to find the cerebellum volume, the points (top, bottom, left and right) of the cerebellum are measured in each image individually and then compared to the outermost contour points. The target image is found when the outermost contour points fit the measured points as illustrated in Figure 5.22. In this figure, the left image presents an example where the cerebellum has not reached the maximum size which is shown by the markers. The yellow points indicate the contour points of the cerebellum volume while the green markers present the contour points of the cerebellum image. In this figure, the right image presents an image where the cerebellum has connected to the cerebrum and therefore the local markers (in green) have exceeded the extrema contour points (marked in yellow). The following steps in the cerebellum detection are based on this located image.

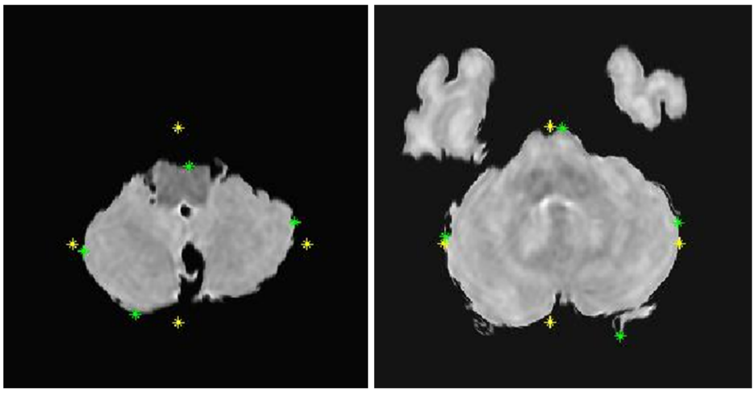

Figure 5.22: Two examples of images that are analysed during the localisation of the initial cerebellum image. The yellow points mark the extrema feature points of the cerebellum volume and the green points illustrate the extrema of the cerebellum in the current image. The left image displays the cerebellum at the beginning of the sequence; the right image illustrates the cerebellum at a later stage in the sequence where the cerebrum starts to connect to the cerebellum, which can be observed at the bottom of the image.

Feature Detection: In the following images, the cerebellum increasingly connects to the cerebrum. As a consequence, it is difficult to distinguish between these two regions and to locate the exact contours. For these reasons, new features which differentiate the two regions, have to be located. One of these features are the contours between the non-brain tissue and the brain tissue, which are mostly defined by strong contrast and high gradient. In order to reduce the complexity and the number of parameters, the Sobel edge detection, which uses 2D spatial gradient measurement to emphasise high spatial frequency regions, was applied. This allows the generation of the four outer contour points of the cerebellum. Some contours between the cerebellum and cerebrum are not visible because the connection appears in the same brain tissue. However, to gain as much information as possible, the Sobel contour results are combined with the extracted cerebellum information in the previous image. An example of the extracted features is presented in Figure 5.23 in the second column.

Region Estimation: In order to estimate the cerebellum region, the missing contour information is interpolated using a spline function on the extracted edge features. This function fits a smooth curve to a set of noisy data points using a spline function. The weights for the smoothing spline function are set to one. An example of the interpolated spline results is displayed in Figure 5.23 (right column). The spline results are marked in green.

Cerebellum Identification: The best features are recovered by extracting the intersection points between the spline results and the edge image which contains the Sobel edge information of the current, previous and next images in the volume. An ellipse is then fitted to the selected set of features using the least square fit in the same way as previously described. Two examples of the final results are presented in Figure 5.23, in which the right images include the spline function (marked in green) and the ellipse results (marked in red).

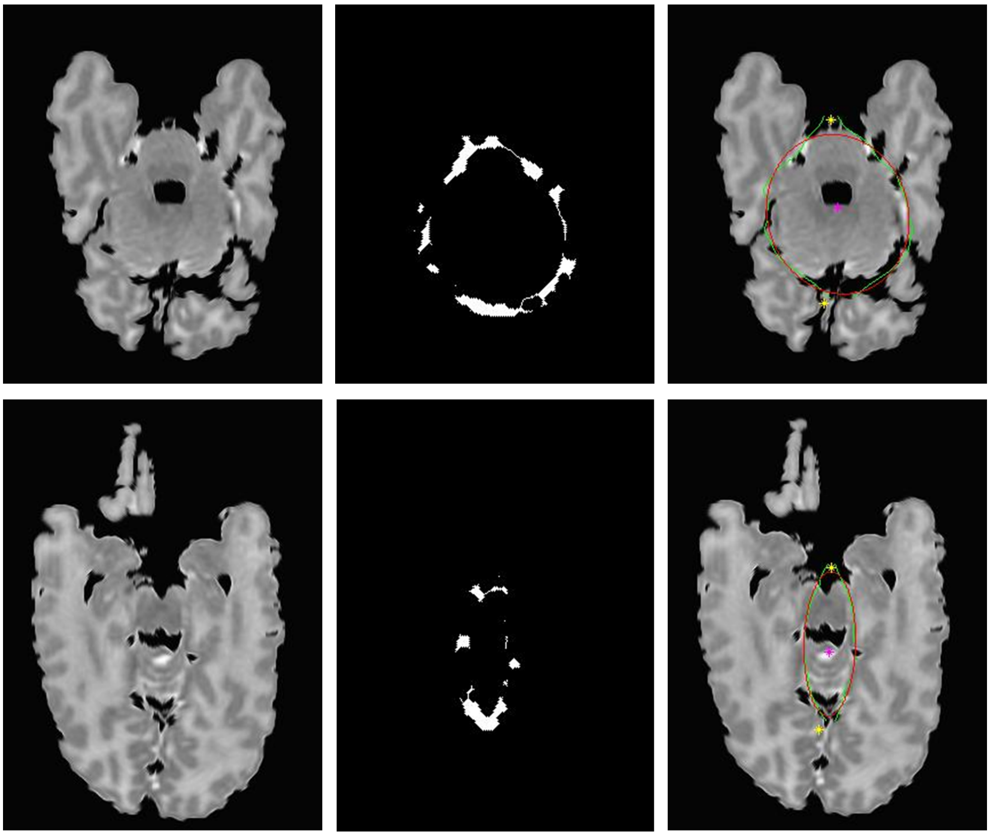

Figure 5.23: Each row presents an example of the cerebellum extraction; the left image displays the original pre-processed image; the middle image shows the extraction of the features and the right image presents the projection of the spline function results (in green) and the ellipse results (in red) onto the pre-processed image.

5.5.3 Locate the Middle Section of the Deep Grey Matter

After detecting the cerebellum and the deep grey matter, the part which connects both regions, can be estimated. Figure 5.24 presents a magnified image in which all steps of the cerebellum and deep grey matter detection are illustrated. Due to the fact that the brain stem and the deep grey matter are connected, they are merged into one region. The detection is accomplished in two steps. First, the ellipse is estimated, and second, the estimation of the parameters is refined.

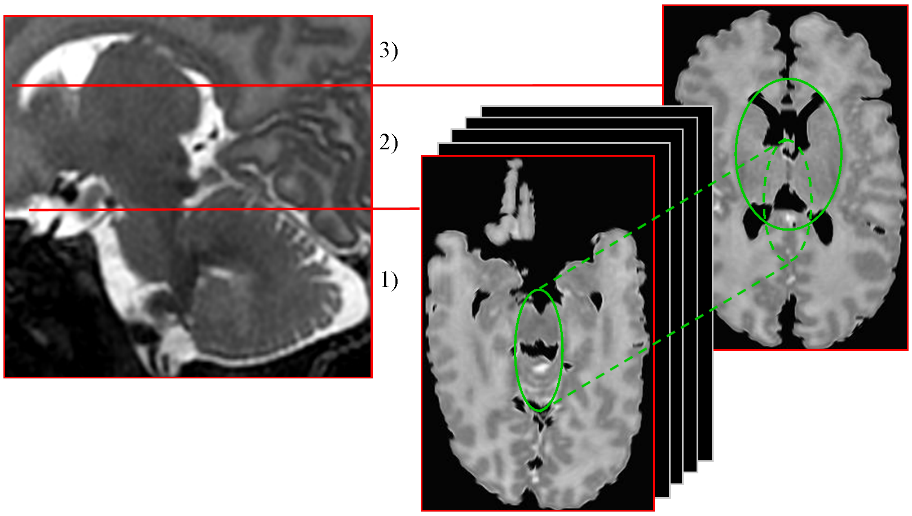

Figure 5.24: Magnified images describing the three steps of the cerebellum and deep grey matter detection. The first and the last images of the second step are presented, in which the RoI is outlined in green. From the first image the ellipse has been projected onto the last image, which illustrates the differences and the changes of the ellipse throughout the second step.

For the automatic estimation of the ellipse, the changes of the feature positions from the cerebellum towards the ventricles are calculated. The estimated features are the parameters of the ellipse such as the centre point, the long radius r_1, the short radius r_2, the top and bottom points.

Throughout the volume of region 2, it has been determined that the ellipse does not change in a linear manner. After an investigation, it was concluded that the parameters have minor changes at the beginning of the sequence and larger changes towards the end. The curve which presents the best estimation of the ellipse changes within the volume of interest, has been determined as follows:

$$f = 2^{\left(\frac{\log_2(N)}{N*n}\right)} \tag{5.16}$$

where N is the total number of images and n describes the current image number in the volume. The function f describes a slow increase for low values of n and a fast increase when n is getting closer to N. This behaviour has provided the best approximation for the changes in the ellipse from one image to the next. The coordinate of the current parameter val is based on the parameters of the first image in this step and is computed as follows:

$$val = x_2 - 2^{\left(\frac{log_2(d)}{f}\right)} \tag{5.17}$$

$$and\ \ d = x_1 - x_2 \tag{5.18}$$

x_1 describes the parameters (centre point, r_1, r_2, the top point and bottom point) of the largest ellipse located during the deep grey matter detection and x_2 presents the parameters of the smallest ellipse identified during the cerebellum detection.

A negative issue associated with the curve function f is that the value for the first image has already shown an increase. For example, if the volume has 30 images and $n = 1$ the function f has an increase of 1.12. However, when analysing the first image, the brain stem does not change the position compared to the previous image. For this reason, a simple stretch formula is used to remap the curve function that it does not show an increase for $n = 1$.

$$output = (input - inlo) \times \left(\frac{outla - outlo}{inla - inlo}\right) + oulo \tag{5.19}$$

where $inlo$ and $inla$ denotes the input range lowest and largest value. The $outlo$ and $outla$ represents the output range lowest and largest value. This formula was applied to calculate the new coordinate of the parameter which prevents changes when analysing the first image ($n = 1$). The formula is described as follows:

$$fv = (val - dist) \times \left(\frac{d}{d - dist}\right) + x_2 \tag{5.20}$$

$$where\ \ \ dist = d - 2^{\left(\frac{\log_2(x_1 - x_2)}{2^{(y)}}\right)} \tag{5.21}$$

$$and\ \ \ y = \frac{\log_2(N)}{N} \tag{5.22}$$

where fv describes the new coordinate of the point in the y-axis direction, $dist$ presents the changes between the iterations. This formula allows the best estimation of the changes of the ellipse where the modifications are slow at the beginning and rapid at the end of the volume.

Due to the fact that the structure of each patient varies slightly in its appearance, the ellipse estimation is only an approximation and for a few patients inaccurate results have been produced. For this reason, the second step of this algorithm checks if each parameter is correctly estimated.

- The high and low points, indicates the intersection points of the long axis with the outline of the ellipse. These points are further examined by searching the nearest contours with respect to the two estimated points in order to locate the optimal position. The new high and low points allow to inspect the long radius r_1.
- The short radius r_2 is checked; CSF components which surround the DGM are detected. The distance between the centre and each component after they were projected to the r_2-axis of the ellipse is calculated. The mean value of all the calculated distances is assigned as the new short radius.

Figure 5.25 presents a few results obtained by the proposed algorithm. The top row presents the pre-processed images, while the images on the bottom row display the ellipses that are projected onto these images. The ellipses marked in red displays the interpolated ellipses, whereas the ellipses marked in yellow represents the corrected ellipses (if correction is not necessary only the interpolated ellipse is displayed). The three investigated regions are of the cerebellum, deep grey matter and brain stem, which allow the removal of the false segmented regions from the preliminary white matter mask.

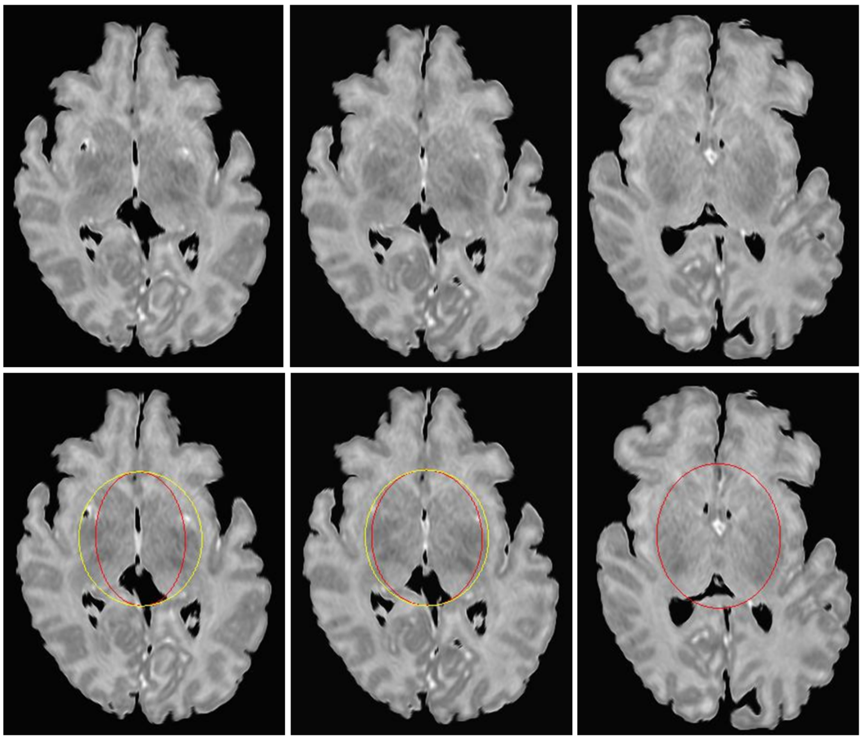

Figure 5.25: Each column presents an example of the deep grey matter extraction; the top row displays the original pre-processed images, and the bottom row shows the pre-processed images, on which the interpolated ellipse (marked in red) and the corrected ellipse (marked in yellow) are projected on. If the interpolated ellipse does not need to be corrected, no corrected ellipse will appear as shown in the right bottom image.

5.6 Re-classification of the PVE and Diffused Contours

A common problem in infant brain segmentation is the classification of the partial volume voxels and the diffused contours. Gui et al. [52] applied a region growing algorithm to segment the brain tissue. This method tend to get trapped in local minima which is demonstrated by the white matter under-segmentation in the regions of the gyri. Shi et al. [110] stated that their method is sensitive to partial volume voxels. To overcome these issues, additional re-classification of the PVE and diffused contours has been developed in the proposed approach.

The EM results have shown misclassifications due to intensity variations within regions and similar intensity values for different tissue types. This occurs when the EM segmentation using GMM is not constrained with prior information, which can easily converge to incorrect local maxima. Given the fact that both processes, the EM and the Otsu algorithm, have not provided sufficient accuracy on their own, the final segmentation step applies a re-classification step to combine the findings of these algorithms in order to obtain a more precise segmentation of the white matter tissue. Due to the fact that PVE can differ from one image to the next within the volume, this step of the algorithm involves two dimensional image calculations. Figure 5.26 provides an overview of the final segmentation step.

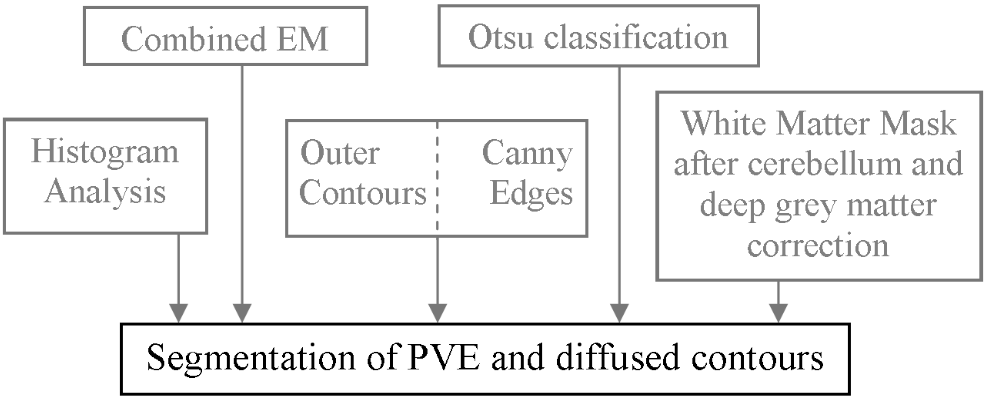

Figure 5.26: Overview of the final step for white matter segmentation.

This algorithm starts by extracting the contours of the preliminary white matter mask, which have been corrected by the application of cerebellum and the deep grey matter detection procedures. The idea is to evaluate the neighbours for each contour pixel to decide if the pixels belong to the white matter tissue or not. Multiple estimations are computed and applied to make a judgment about the state of the current pixel.

- By examining the changes between pixels and their corresponding neighbourhood, the information is used to determine if the pixel is excluded from the white matter region or not. In case the difference between the two pixels increases too rapidly, the pixel is excluded from the white matter region, otherwise the pixel is further considered for classification. Experimentally, it has been determined that if the difference between the two pixels is lower than ten percent of the maximum number of the EM classes tem, then the pixel will be further processed.

- Using the image obtained from the Otsu classification algorithm, the outcome contains the brain tissue divided into four classes. On each image the brain tissue volume is then divided into six equal regions and the following formula is applied to each region.

$$gp = \frac{\sum n_{cl=4}}{\sum n_{cl=2} + \sum n_{cl=3} + \sum n_{cl=4}} \tag{5.23}$$

  where n is the number of pixels defined in class cl. The gp results indicate if a region in the image has a high or low contrast. The division of the image into six regions yields a more precise estimation especially if the region contains partial volume voxels. The smaller the region, the more local and precise is the estimation. In our case, using a partition of six regions returns a good approximation for the four class distribution. Additionally, as displayed in Figure 5.27, the division of the image into six parts ensures that each divided region contains grey matter and white matter, and allows a better discrimination in the regions next to the deep grey matter. The contrast between the two brain hemispheres can differ and therefore, by dividing the two halves, the global estimation of the contrast and partial volume voxels is more precise. A more local estimation of each pixel is performed in combination with the global estimation. This is described below:

- When approaching the blurred contours where the intensity changes slowly, the two previously described calculations are not sufficient. Therefore, local judgments for each pixel and its surrounding neighbourhood are required.
  - The same Otsu calculation as described above is performed with the difference that this time the neighbourhood region of the current pixel consists of a window size of 20×20 pixels. This window size ensures that the information corresponding to class two, three and four is included in the calculation which allows a local estimation when dealing with low contrast and diffused contours. In this case, the changes in the surrounding pixels are taken into account using equation 5.23. The threshold value $gp_{20\times20}$ was set to 0.5 and allows to balance the number of grey matter tissue within the investigated

area.

- The neighbouring pixels of the current location in the EM results are analysed. In this calculation a window size of 3×3 is applied. The mean value of the EM pixels inside the detected white matter volume $emv1$, is compared to the mean value of the EM pixels outside the white matter volume $emv2$.

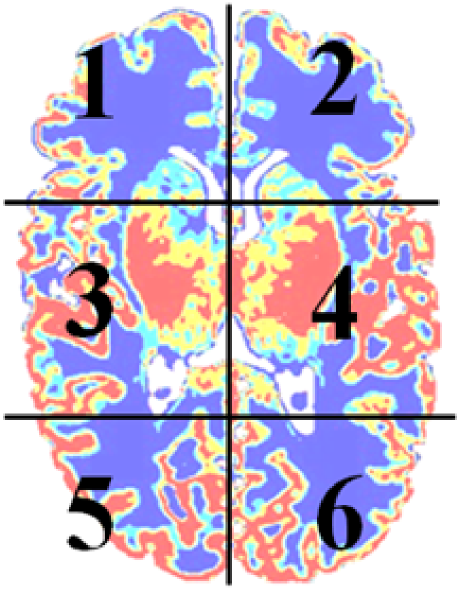

Figure 5.27: Image obtained after the Otsu algorithm is applied. This image is divided into six regions.

The analysed pixel has to be consistent with some general criteria. Firstly, in the Otsu image, the pixel can be in any of the classes except class four, which defines the grey matter (marked in red in Figure 5.27). Secondly, the pixel cannot belong to background, a Canny contour nor to an outside contour marked pixel. Finally, the EM class difference between the white matter contour pixel and the analysed neighbour pixel has to be lower than ten percent of the maximum number of the EM classes tem.

The pixels are further processed when they fit the first criteria. For further evaluation, the re-classification scheme is partitioned into two case scenarios; first $gp > 0.6$ and second $0.5 < gp \leq 0.6$. In case of $gp < 0.5$, the contrast is extremely low and the pre-segmented white matter region has provided accurate results. This conclusion was made after observing the same behaviour throughout the database. One example that presents different cases is illustrated in Figure 5.28. The dark grey value is the region that is defined as white matter. The white region is classified as class four (or grey matter) and the grey values between represent the diffused contours and the partial volume voxels.

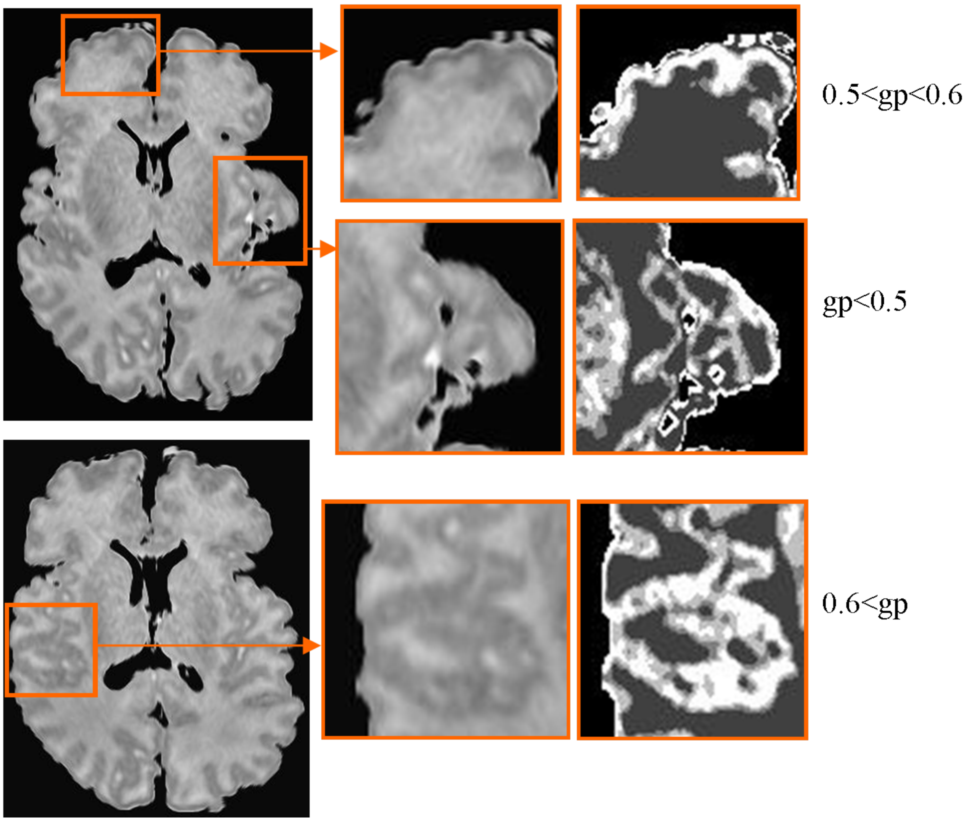

Figure 5.28: An example that illustrates the three scenarios for changes in the gp values. The lower the gp value the lower the contrast. The middle column presents magnified regions taken of the two images on the left and the right column illustrates the Otsu classification of these magnified regions.

The following listing details the two cases where the neighbourhood pixels are included in the re-classification process.

1. The first case deals with a region characterised by a high number of grey matter pixels and a small number of partial volume pixels. It was experimentally estimated that this appears when the gp value is larger than 0.6. In this instance, all pixels with a higher $gp_{20\times20}$ than the threshold, as well as the pixels of class two and three of the Otsu results, $emv1$ has to be smaller or equal than $emv2 + tem$ in order to be included in the white matter volume.

2. The second case investigates the region where the grey matter pixels only slightly outnumbers the partial volume pixels, which indicates a lower contrast. This is the case when the gp value is between 0.5 and 0.6. All the thresholds are analysed in the same way as in the previous case, except that the pixels which lie in the third Otsu class are defined as grey matter.

The application of these conditions has provided an optimal approach to classify the partial volume voxels and voxels situated on diffused contours. A quantitative evaluation of the framework is presented in the next chapter which demonstrates that this re-classification algorithm provides accurate results that overcome the difficulties generated by PVE and diffused contours.

Chapter 6

Evaluation

In order to evaluate the performance of the proposed approach, a quantitative and qualitative analysis is necessary. This chapter commences by introducing the 1.5T MRI data which was provided for this study by the clinical partners from the Temple Street Children's Hospital, Dublin, Ireland. This is followed by an experimental section where the proposed algorithm is numerically evaluated. The outcome of testing is analysed and a discussion about the strengths and limitations of the developed method is presented. Section 6.3 presents an investigation which was preformed using independent 3T datasets provided by the Image Sciences Institute[1].

6.1 1.5 Tesla Infant Data

Brain volume MRIs of premature infants have been acquired at full term equivalent in the Children's University Hospital, Dublin, Ireland. During the MRI acquisition of the preterm infants' head, the children were sedated, whereas the infant born at term were not sedated. Several sequences were acquired from each patient. The proposed algorithm is developed for T2-weighted MRI volume because from all acquired MRI sequences received from the Hospital, the T2-weighted images produced the best contrast differences between the different anatomical brain structures. Figure 6.1 gives an example of the two most common sequences T2- and T1-weighted MR images used in medical image processing.

The developed approach has been tested on T2-weighted MRI (TR: 2660; TE: 142.7; FOV: 16 $\times$ 26 cm) datasets using a 1.5 Tesla scanner General Electric HDx. Each MRI slice has a thickness of 1 mm and a resolution of 512 $\times$ 512 pixels. The acquisition matrix has a size of 320 $\times$ 320 mm^2. This leads to a voxel size of:

---

[1] available on the web page: www.neobrains12.isi.uu.nl (accessed 20/11/2013)

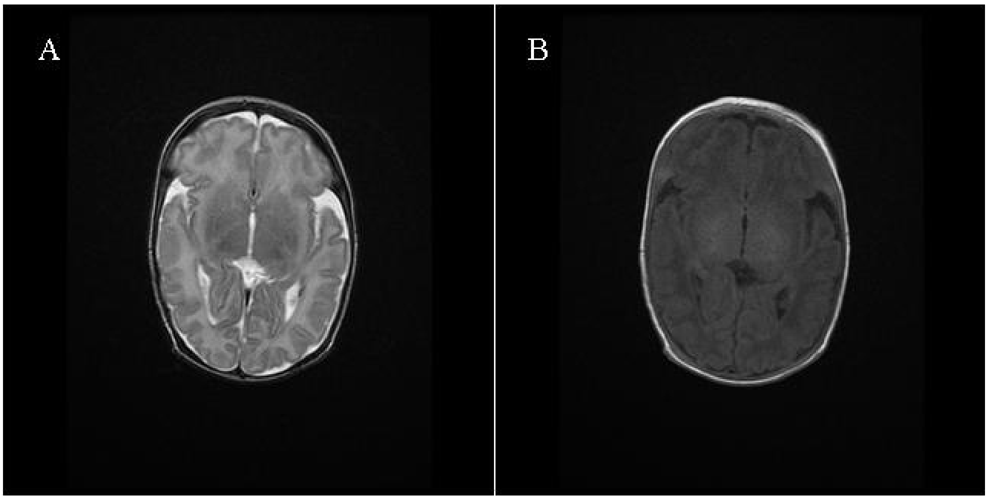

Figure 6.1: Images from two different sequences of the same patient; Image A is a T2-weighted MR image; Image B is a T1-weighted MR image.

$$\frac{160}{320} \times \frac{260}{320} \times 1 = 0.40625mm^3 \tag{6.1}$$

Our database consists of a total of 86 preterm datasets and 12 control datasets. The premature infants were born about three months early and the MR images were acquired when they reached the term equivalent age. The scans were taken starting at the cerebellum and finishing at the top of the head. Out of the 86 volumes 15, which contain a total of 1444 images, were manually annotated by a consultant pediatric radiologist from the Temple Street Children Hospital, Dublin, which is an expert in the evaluation of neonatal MRI data. These manually marked white matter volumes were employed for numerical evaluations of the proposed technique. Strong motion artefacts, noise and incorrect scaling during the acquisition were the reason to exclude some datasets from our evaluation. A summary of our database is presented in Table 6.1.

Category	Male	Female	Total
Term born	4	8	12
Preterm born	47	39	86
Manually marked	10	5	15

Table 6.1: Summary of the MRI data used in the experimental evaluation.

6.2 Experiments

The experiments are performed in two steps. Firstly, a numerical evaluation is conducted where the outcome of the automatic segmentation is compared to our manually annotated database. In the second step, the segmentation framework is applied to a large database of premature infants and infant born at term. The results of all experiments are presented and the strengths and limitations of the proposed approach are analysed.

6.2.1 Evaluation Techniques

The evaluation was performed by calculating four different measurement indices such as Dice Similarity Metric (first for the extracted white matter region and second for the entire approach), False Positive and False Negative. The first metric describes the similarity between the manually segmented data and the automatically segmented data. The last two calculations measure the percentage of false segmented pixels also called error rate. The Dice Similarity Metric, False Positive and False Negative measurements were previously introduced in Section 3.7.1 where they were used to evaluate the brain extraction algorithm. One additional Dice Similarity Metric is introduced in this chapter, which measures the similarity of the framework.

2. In order to measure the similarity of the framework, an adaptation of the Dice Similarity Measurement is employed. This measurement computes the similarity between the manually annotated data and the automatically segmented data by including the uncommon voxels of the brain extraction and white matter segmentation. This is achieved by dividing the number of shared voxels by the number of all the voxels. The shared data in the framework is defined by the common voxels of the brain extraction volumes minus the dissimilar voxels between the automatic and manual WM segmentation data. To calculate the number of all voxels, the two brain extraction volumes are added but the dissimilarity between the two WM volumes has to be subtracted. The mathematical formula to calculate this metric is described as follows:

$$DSM_{approach} = \frac{2 * (|MBE_1 \cap MBE_2| - DWM)}{|MBE_1| + |MBE_2| - DWM}, \tag{6.2}$$

where MBE_1 describes the automatic brain extraction results and MBE_2 is the manually annotated data. DWM denotes the dissimilarity between the manually and automatically white matter segmented volume and is defined as follows:

$$DWM = |MWM_1 \setminus MWM_2| \tag{6.3}$$

where $|MWM_1 \setminus MWM_2| = \sum_{(x,y)} f(MWM_1(x,y) = 1 \ \&\& \ MWM_2(x,y) = 0)$ where (x, y) are the pixel coordinates, where $f(a) = \begin{cases} 1 & if\ a = true \\ 0 & if\ a = false \end{cases}$, MWM_1 is the automatically white matter segmented volume and MWM_2 is the manually white matter segmented volume.

6.2.2 Numerical Evaluation

The numerical evaluation was accomplished by comparing the segmentation results against the manually annotated data which were marked by our collaborating clinical experts. In the first step the similarities between the automatically and manually marked datasets were computed. The outcome is shown in Figure 6.2 and presents the Dice Similarity Measurements calculated for the white matter volume and the system similarity results.

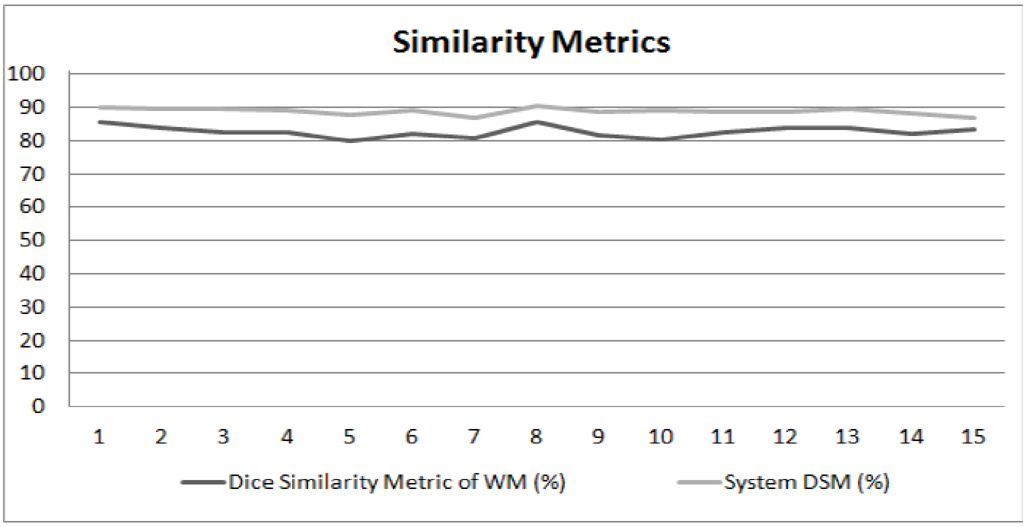

Figure 6.2: Accuracy of the white matter extraction algorithm using Dice Similarity Metric, plus the Dice Metric calculated for the entire system.

The proposed approach indicated an average Dice Similarity Measurement (DSM) of 88.9% for the system and 82.8% for the white matter volume. By comparing these results with other developed segmentation techniques, Wang et al. [126] stated a white matter DSM between 85% to 90%, Xue et al. [132] presented a white matter DSM of 79.4% where Gui et al. [52] produced a white matter DSM of 94%. Prastawa et al. [95] divided the white matter into myelinated and nonmyelinated white matter and the DSM was 69% for the non-myelinated white matter and 67% for the myelinated white matter. These results illustrate the difficulties and challenges associated with the segmentation of neonatal MRI brain data. To the best of our knowledge all segmentation methods developed to process infant brain MR images were designed for data acquired with a 3T scanner, which show improved contrast to MR data acquired with 1.5T scanners.

Some researchers [2] [90] performed studies that analysed the growth of the young children's brain. The DSM results for white matter segmentation at the age of two years were 87% but at this stage the brain is more developed than at birth. These studies reveal the great challenge of segmenting brain MRI data, not only during infancy, but also during the entire childhood until the brain is fully developed.

The experimental results presented in Figure 6.2 indicate that the system has high similarity measurements. The following graph shown in Figure 6.3 outlines the error rates by comparing the automatically extracted white matter volume against the manually segmented data.

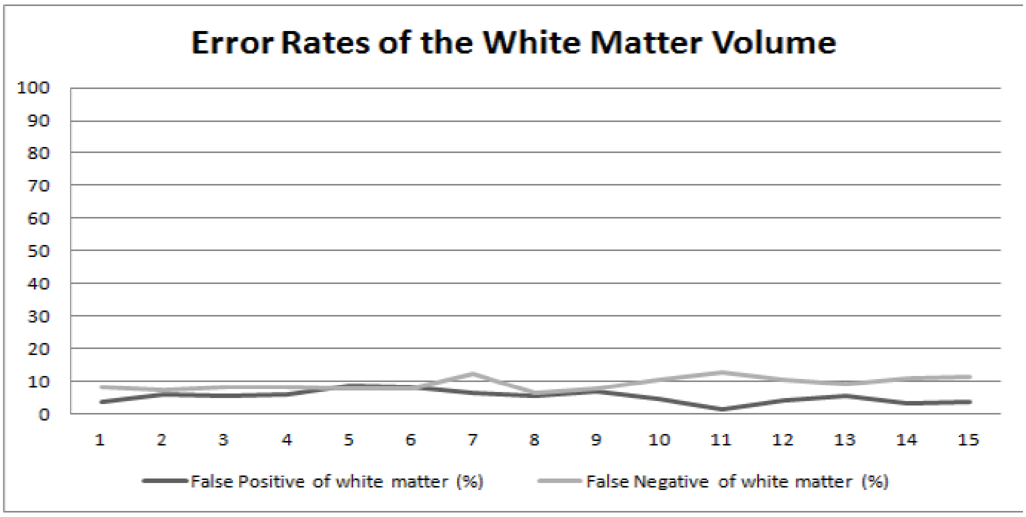

Figure 6.3: False positive and false negative rates obtained by the proposed white matter segmentation algorithm.

One issue that should be considered when analysing the false positive and false negative rates is the influence of the partial volume voxels which were differently interpreted in the manually annotated data compared to the automatically results. Figure 6.4 illustrates two brain MR images of premature infants where the manually marked and the automatically segmented results are overlaid on the original data. The outer contour of the manually annotated white matter is marked in green, whereas the contours of the automatic segmented white matter is delineated in red. Two regions were magnified and indicate that in those areas the automatic segmentation results illustrate a more precise segmentation than the manually marked data. The reason for this is the low contrast structure, noise and partial volume effect, which produce a great challenge for clinical experts when tracing the unclear contours.

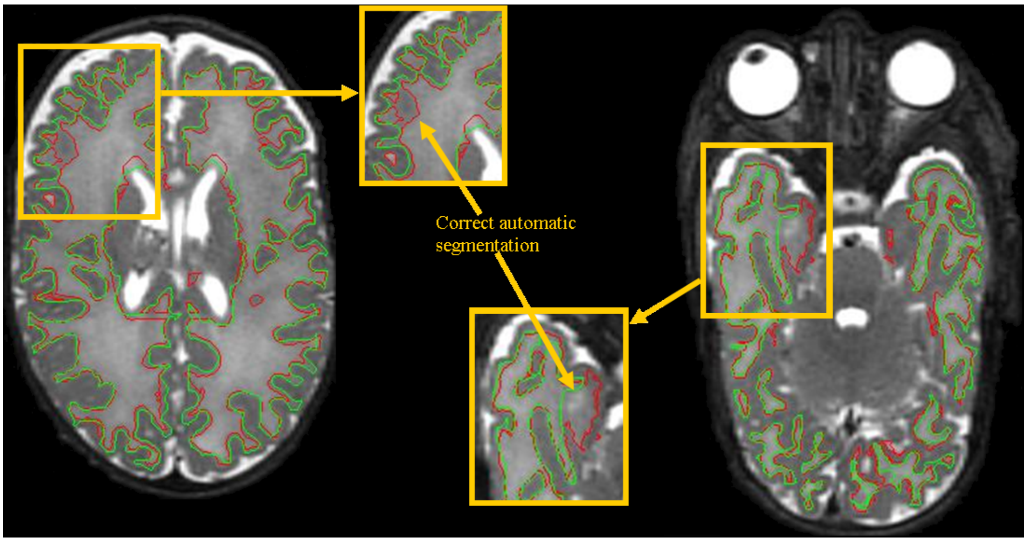

Figure 6.4: Two MR images of different patients are illustrated. For each image a smaller section is magnified to illustrate the differences between the manual (marked in green) and automatic (marked in red) segmentation results. Due to blurred areas, it can be observed that the automatic segmentation includes white matter and excludes grey matter where the manually annotated images show less precision in the separation of the white matter from the grey matter tissue.

To better understand the error rate results, a global error was calculated. Based on the manually annotated data, a new error is computed for the case in which the automatically segmented white matter volume surface is one pixel smaller than the manual segmentation. The white matter volume shows an error rate of 14.96%, the brain extraction (skull stripping) algorithm has an error rate of 7.83%, and the entire framework has an error rate of 13.58%. This was calculated as follows:

$$error = 1 - \frac{\sum im_{eroded}}{\sum im_{original}} \tag{6.4}$$

where im_{eroded} is the original image ($im_{original}$), from which one pixel of the surface was removed. An interesting outcome was presented by Prastawa et al. [95] where they analysed the manually annotated data performed by two different clinical experts. The DSM demonstrated a similarity of 73.625% for myelinated WM and 75.825% for non-myelinated WM. An example where the annotated and automatic contours do not match is presented in Figure 6.5. For clarity reasons, the contours are overlaid onto the corresponding original image where red indicates the automatic contours and the green lines present the annotated volume contours. Due to the blurred edges between the grey matter and the white matter, the contours can differ slightly from each other. As previously explained, these deviations can have a major effect on the similarity measurements and on the False Positives and False Negatives error rates.

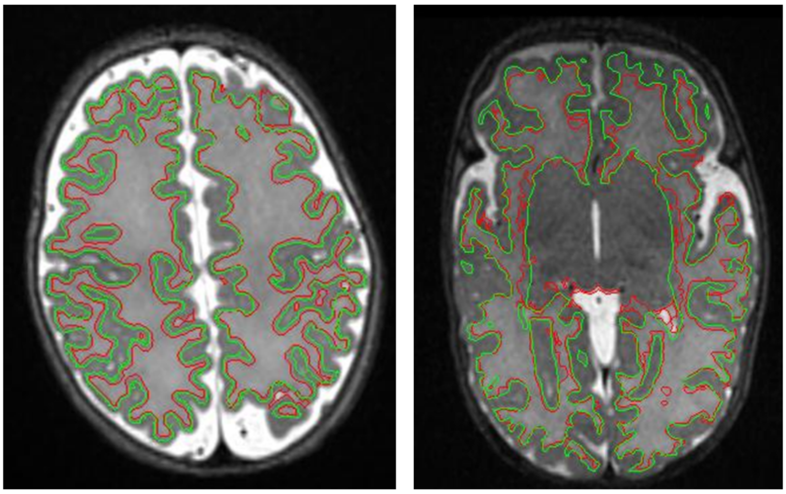

Figure 6.5: Two images which illustrate the differences between the manually marked data (outlined in green) and the automatically segmented data (shown in red).

To allow a more detailed evaluation, the white matter volumes for all patients included in our database were compared to each other and are illustrated in Figure 6.6. The red points indicate the results for the control data, whereas the blue points define the results for preterm infants. The two lines presents the average values corresponding to each category. Several studies [26] [62] [27] stated that the brain volume of preterm infants is smaller than the volume of the infants born at term. This finding is consistent with our results. It is still unclear if the reduced brain volume of the preterm infants is caused by the premature delivery or if there is a connection to ill health [48]. The clinicians from Temple Street Children Hospital, Dublin, aim to use the volume information as an indicator for neurodevelopment impairment with the focus on cerebral palsy. Mathur et al. [86] evaluated the brain injuries and neurodevelopmental impairment in premature infant where the brain volume changes for various tissues are analysed over time. They state that it is likely that volume changes in grey matter and white matter and intensity variation in white matter reflect to neurodevelopmental impairments which are a consequence of the grey matter and/or white matter injuries.

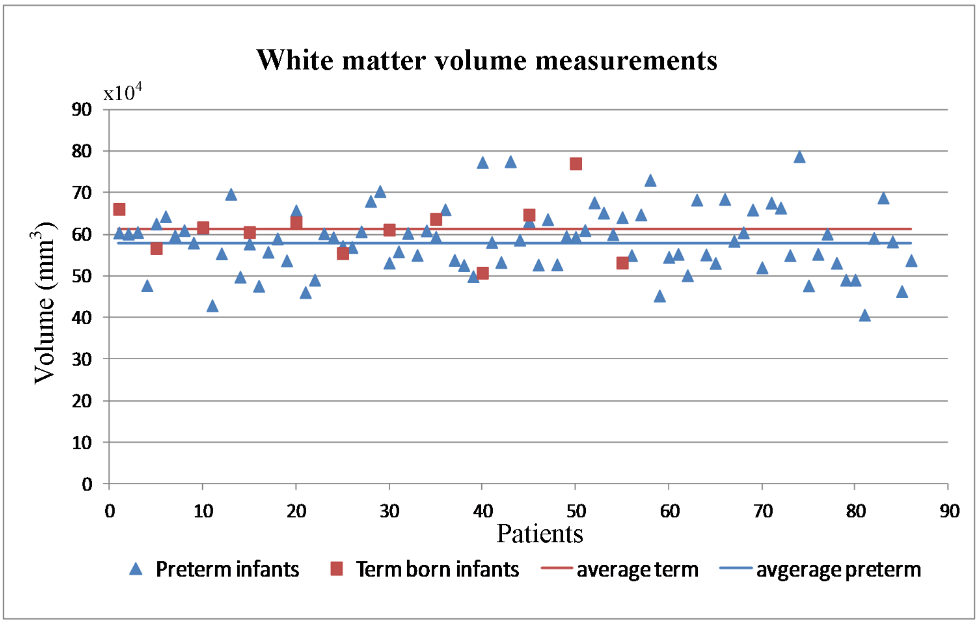

Figure 6.6: White matter volume measurements for control and preterm infant data; in blue are marked the preterm data measurements (86 patients); the red points illustrate the results for control datasets (12 patients).

Table 6.2 shows additional results when the proposed white matter segmentation algorithm was applied to premature infant MRI datasets. Each row illustrates examples of one patient. The contours of the extracted white matter volume was projected on the original input data. In these images it can be observed that the variations between patients, intensity inhomogeneities and partial volume effects have no impact on the outcome of the segmentation procedure.

Following the experiments conducted with preterm infant data, the proposed white matter segmentation algorithm was applied to brain MRI datasets of infants which were born at term. Figure 6.14 illustrates these results and they also demonstrate an accurate white matter segmentation.

A clinical expert from the Temple Street Children Hospital, Dublin, has evaluated the segmentation results. The clinician stated that the results indicate an overall accurate segmentation when compared to the manually annotated data. The diffused contours and the partial volume effects have been precisely segmented and the deep grey matter and cerebellum region were accurately detected.

The following section provides a discussion about the strengths and limitations which arose during the examination of the white matter segmentation results.

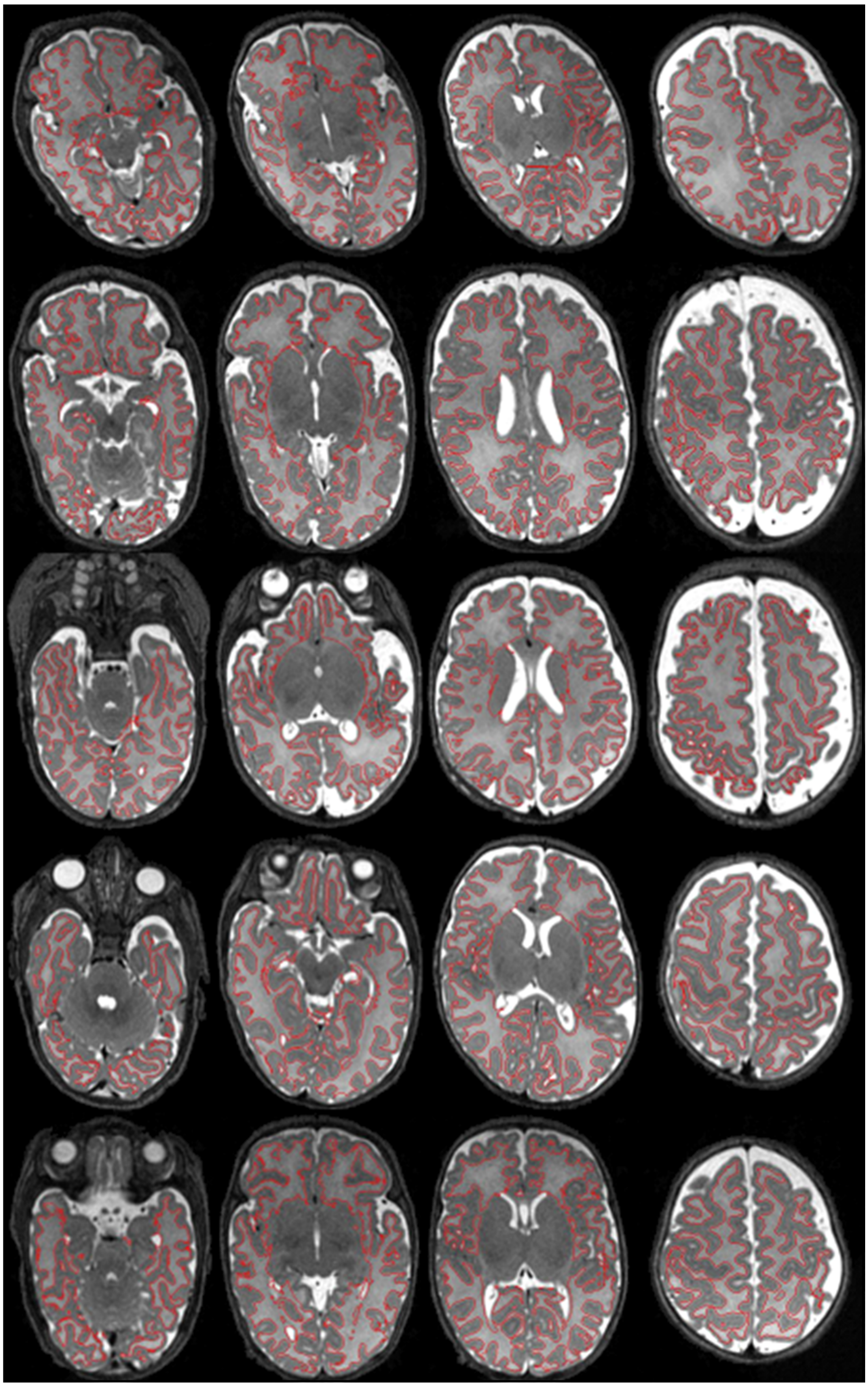

Table 6.2: White matter segmentation results for preterm infant data.

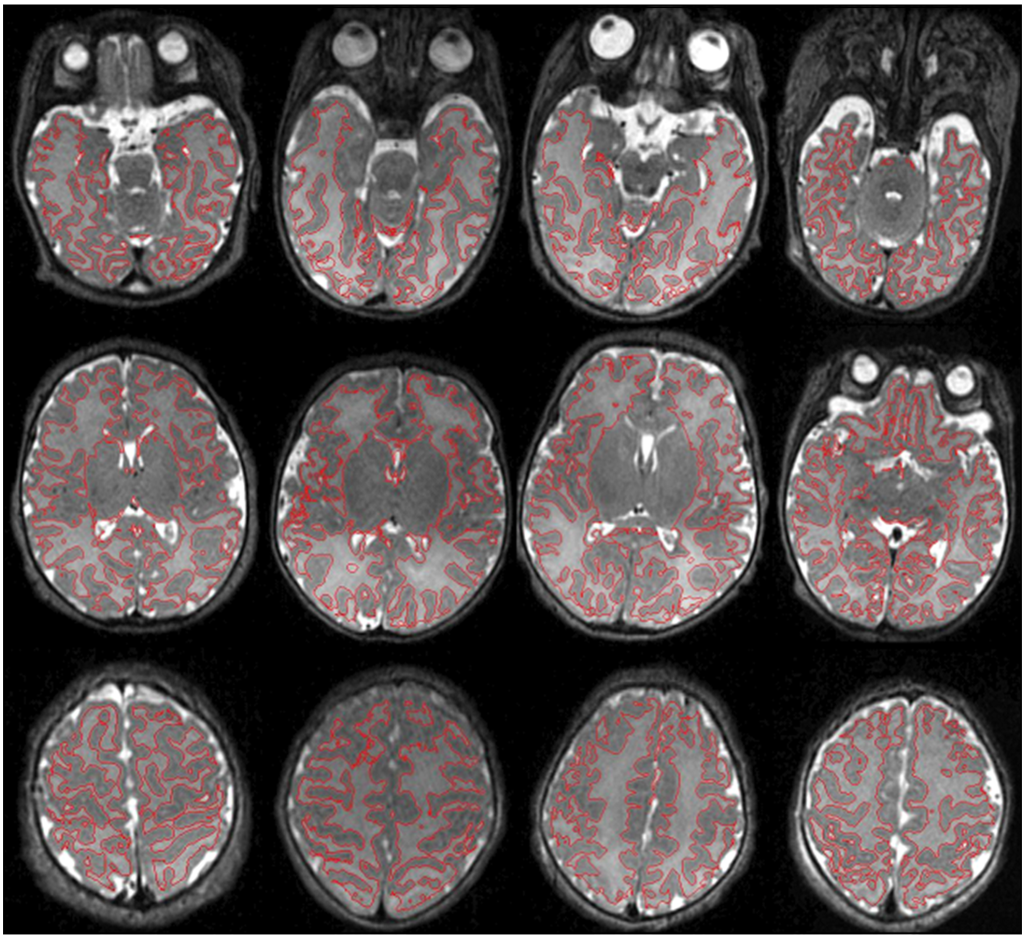

Figure 6.7: White matter segmentation results for term-born infants.

6.2.3 Discussion

The evaluation of the automatic segmentation results for infant MRI data is difficult because a gold standard does not exist. The production of manually annotated data is a demanding task that is substantially complicated by low-contrast structures, noise and partial volume effects. As introduced in Chapter 2, the brain segmentation needs to address many challenges when processing infant brain MRI data. The main challenges can be summarised as follows:

- The scanning procedure has to be performed in a short time because the infants tend to move during the data acquisition. In addition, the small head size requires a high resolution acquisition process. Both factors lead to a reduced contrast to noise ratio, which results in a low contrast between the grey matter tissue and the white matter tissue.

- In this study, the preterm infants were sedated during the acquisition. Sedated or not, the newborns tend to move during the scanning procedure, which generates motion artefacts that can affect the segmentation process.
- Each tissue type presents a significant level of intensity inhomogeneity which is caused by the inhomogeneous magnetic signal during the scanning process and also by the atypical biological characteristics of the preterm brain.
- Different tissue types show an overlapping between their intensity range. Therefore, in some situations the localisation of the brain tissue may be extremely difficult to achieve.

The main goal of this thesis is the development of a fully automatic intensity-based approach for the segmentation of the white matter volume in brain MRI data of preterm and term-born infants. The method has provided accurate results by processing the blurred contours between the white matter and the grey matter. Some typical examples that illustrate segmentation results are displayed in Figure 6.8. Although the shape, structure and intensity distribution are inconsistent in preterm MRI, the proposed approach produces precise segmentations without prior information about shape or structure. This is important because both, the structure and the shape varies between patients.

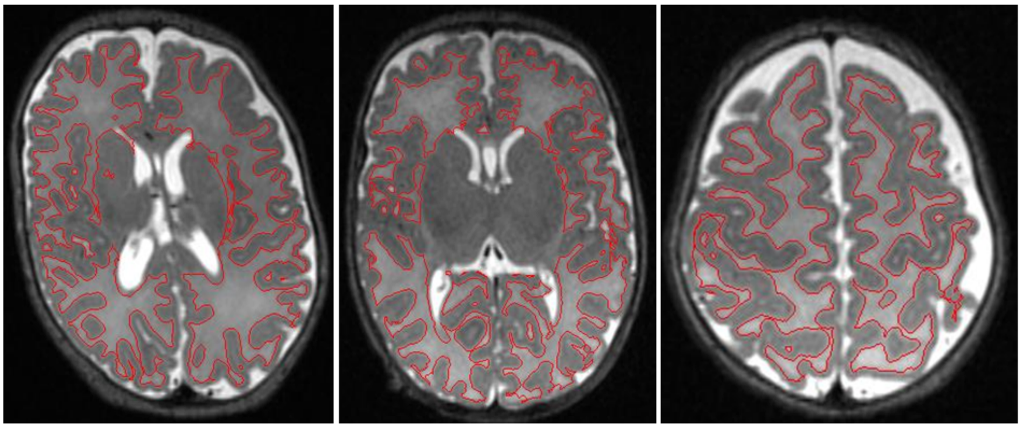

Figure 6.8: Examples of the automatic segmentation results.

The images in Figure 6.8 display three white matter segmentation results when dealing with blurred contours and partial volume effects and these issues will be analysed in detail in the remainder of the chapter

The Partial Volume Effect (PVE) has a significant impact on brain segmentation methods. For example, it can induce errors when applying atlas registration and classification techniques [22], as well as watershed-based techniques [52] to brain MRI. In the case of voxel-based morphometry, each voxel belongs to one class only. When a voxel contains the signal of more than one intensity tissue, this hypothesis is not valid anymore and can result in false classification [6]. As explained before, the PVE can affect the numerical evaluation. An example that illustrates the PVE is displayed in Figure 6.9 where the manually marked data is compared to the automatic segmentation results. Due to unclear intensity values, voxels could belong to either grey matter or white matter. These regions are pointed out with yellow arrows. The proposed approach deals well with the PVE. One reason for this is that the EM algorithm is performed twice and each time based on differently pre-processed brain volumes. The aim of this is to enhance the contrast between the grey matter and the white matter. An additional reclassification process was also included to help the precise identification of the white matter even when the boundaries between the grey matter and the white matter are unclear.

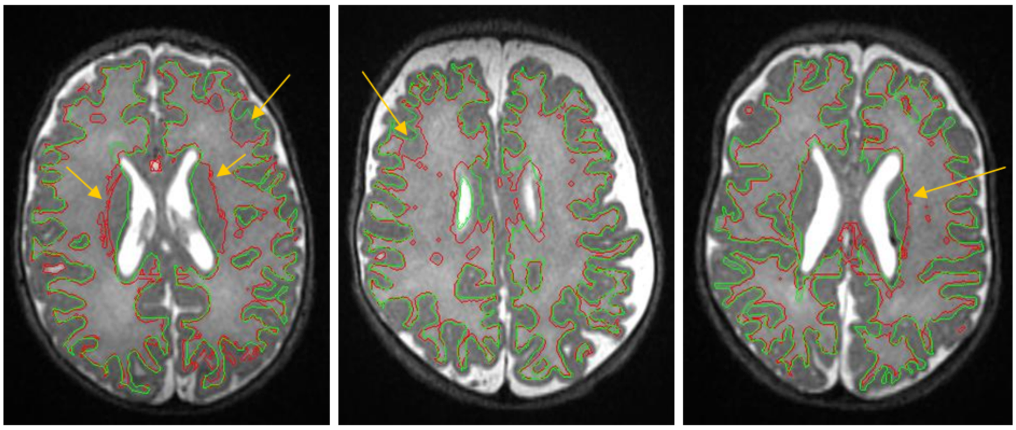

Figure 6.9: Examples of segmentation results where the red marking indicates the outer white matter contour identified by the proposed algorithm, and the green line represents the outer contour of the manually annotated data. Due to unclear intensity values, the images show differences between the two markings where the tissue could belong to the grey matter or the white matter. These regions are pointed out with yellow arrows.

Apart from the high level of PVE in infant brain MRI data, a major challenge is the low contrast of the brain tissue. The proposed algorithm has provided accurate results when dealing with low contrast between the grey matter and the white matter tissue. This has been achieved by using a local reclassification of the voxels. Figure 6.10 illustrates white matter segmentation results when dealing with this issue. The top row in Figure 6.10 illustrates the original images and the bottom row displays the white matter segmentation results.

In contrast to adult brain MRI data, the early stage of the brain development leads to large shape and brain structure variations between patients. The proposed approach has

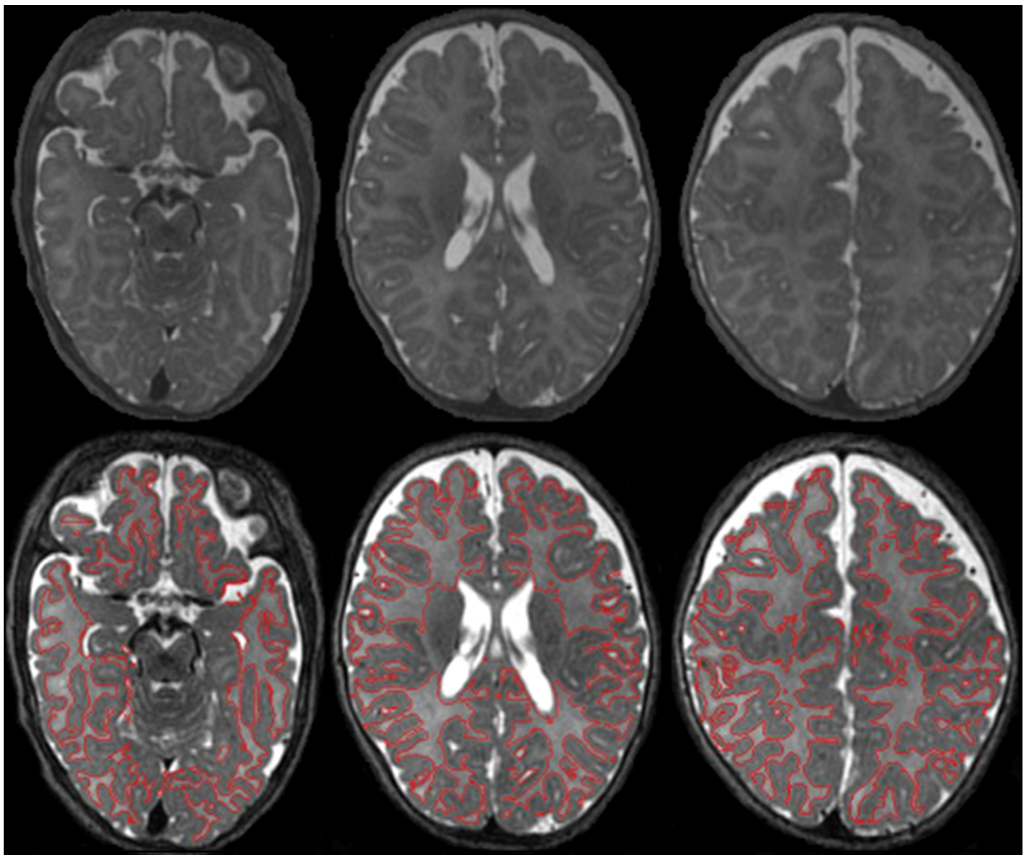

Figure 6.10: White matter segmentation results obtained from infant brain data which present low contrast. The top row displays the original images and the bottom row shows the segmentation results.

provided accurate results when dealing with variations in shape and structure. The main reason is that the algorithm does not rely on prior information. In addition, adult brain segmentation algorithms often rely on contours and contrast differences between tissues and for this reason, these techniques generate incorrect segmentation when applied to infant brain data. Figure 6.11 illustrates several white matter segmentation results performed on infant brain data, which include variations in brain structure and shape. Each column in the figure presents results for one patient.

During this investigation, the proposed technique was tested on data which shows strong variation in the structure of the ventricles, as displayed in Figure 6.12. Cerebellum and deep grey matter detection show precise detection on most of the analysed data. However, the approach can deal with a certain amount of dissimilarity between the two ventricles. The part of the algorithm, where a large dissimilarity can cause problems, is the deep grey matter detection, because it uses the ventricle features for DGM extraction. For a few patients under-segmentation occurs when strong dissimilarities between the two ventricles are present. The left image in Figure 6.12 illustrates small errors in

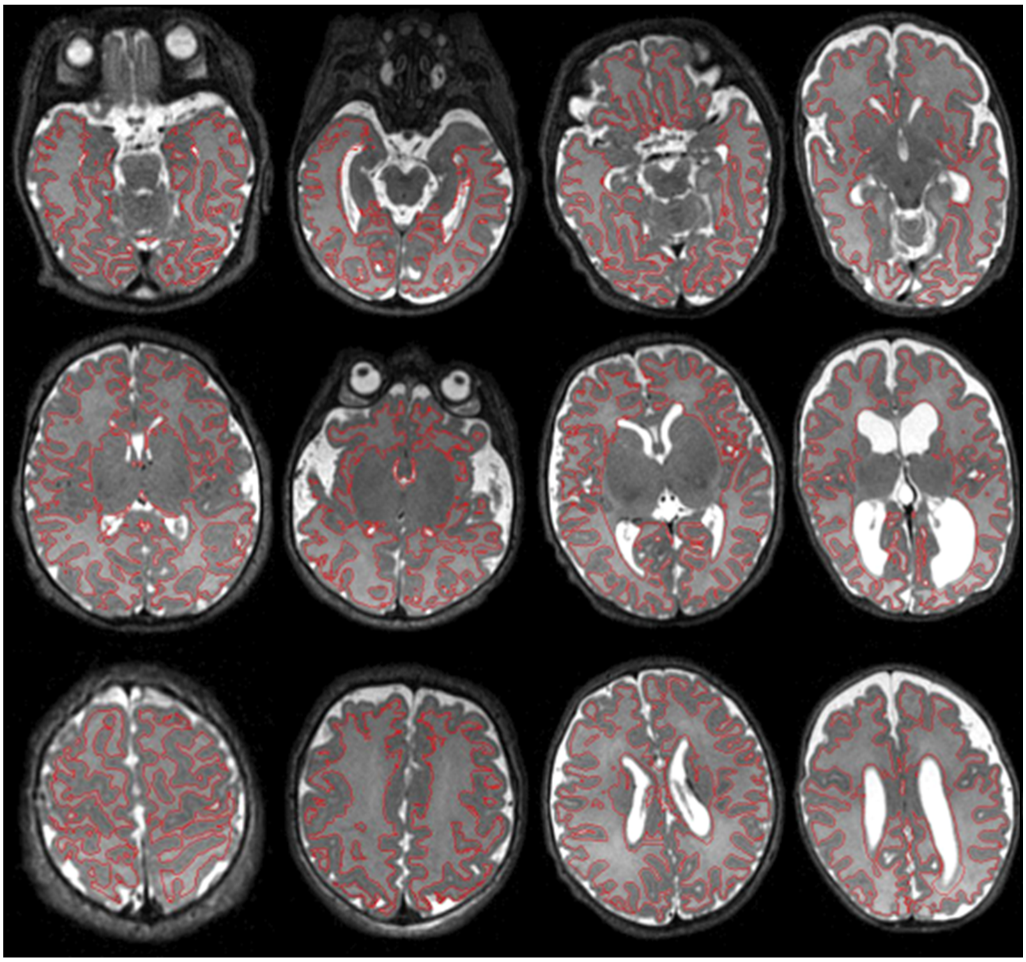

Figure 6.11: White matter segmentation results obtained from infant brain data, which include large differences in brain structure and shape.

the deep grey matter detection because the left ventricle is slightly increased compared to the right ventricle. However, in the middle image of the figure, both ventricles differ significantly from each other, which has negative effects on the segmentation results. A better solution can be obtained by processing the two ventricles separately, so that for each ventricle an ellipse would be generated instead of one ellipse for both. For one dataset this procedure failed, and this can be observed in the right image in Figure 6.12. This is caused by the enlarged ventricles which are falsely classified as brain tissue during the brain extraction algorithm. Due to the large volume of CSF, and no distinction between grey and white matter tissue, the brain extraction algorithm detects the CSF as brain tissue which compromises the segmentation procedure. Our database contained only one patient with this atypical ventricle enlargement and was, therefore, excluded from evaluation.

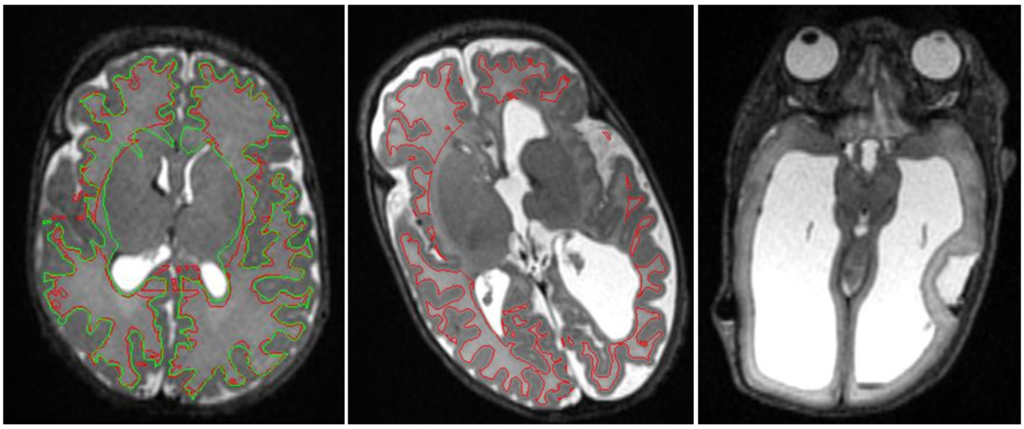

Figure 6.12: Three examples of preterm infant brain MR images in which the brain ventricles show atypical structures and dissimilarities. In the left image, the ventricles differ slightly from each other, whereas the image in the middle displays larger deviations between left and right ventricles. In the middle example, the under-segmentation can be observed, which is caused by the deep grey matter detection. The right image illustrates extremely enlarged ventricles which severely reduce the brain tissue volume. For this patient, the white matter segmentation failed.

A common characteristic in infant brain data is the intensity overlapping between brain tissues, which complicates the segmentation process. In this study, the intensity overlapping is reduced by the bias field correction and the procedure of merging two EM results which are based on two different pre-processing steps. By combining the two EM results, the resulting tissue regions are enhanced and easier to separate. The local voxel classification substantially reduces the occurrence of segmentation errors.

Some methods [2] [26] have shown difficulties to locate the white matter tissue surrounded by gyri, which results in under-segmentation. This limitation can appear when guiding the segmentation with templates or atlases on data which contains low contrast and PVE. In order to address this issue, a local tissue classification is performed, which prevents under-segmentation and allows a precise segmentation in these regions. Figure 6.13 illustrates four different examples of regions surrounded by gyri, which highlight the precise segmentation obtained by the proposed algorithm. It can be observed that the white matter segmentation process generates accurate results when dealing with narrow and diffused regions.

Several studies [26] [62] [86] have not only emphasised the variations of preterm infant brain MRI but they have also shown that there are differences in brain features between the premature infants and the infants born at term. These variations include differences within regions, small anatomical structures and rapid changes that occur during the brain development [95]. The term-born infant brain is in a more advanced stage of the deve-

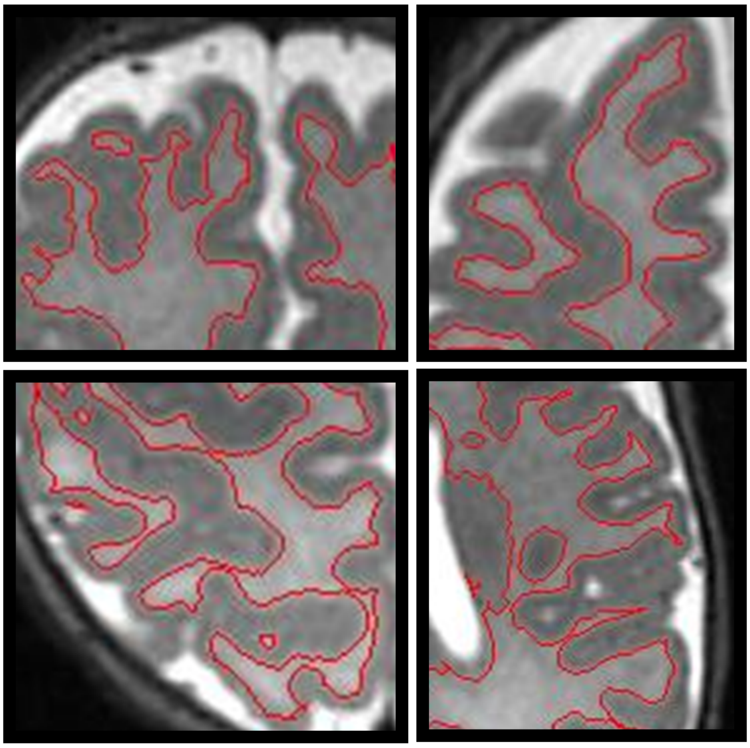

Figure 6.13: Four magnified examples of different segmentation results, which show that the regions surrounded by the gyri are precisely extracted.

lopment and the MR images present less intensity variations within the white matter tissue and less shape differences. In this study the term-born infants were not sedated and therefore the data consists of stronger distortions such as noise and motion artefacts. In general, it is less likely for term-born infants to show abnormalities in the brain such as enlarged ventricles. Regardless of the variations between preterm and term-born infants, the outcome of the proposed white matter segmentation algorithm shows adequate results for both categories. Figure 6.14 illustrates some white matter segmentation results when applied to infants born at term.

The proposed approach is a fully automatic parameter-driven white matter segmentation technique. No registration process is required, which avoids the introduction of supplementary errors when aligning the data to the template.

The results also reveal that the proposed technique can cope with diffused boundaries and partial volume effects. The advantage of our method is its independence to atlases or templates. This increases the potential of applying it to a broader range of infant data with large variations in brain shape and structure including abnormalities. The methods that utilise prior anatomical knowledge in forms of atlases or templates cannot be directly employed to infant brain MR images [3] [50].

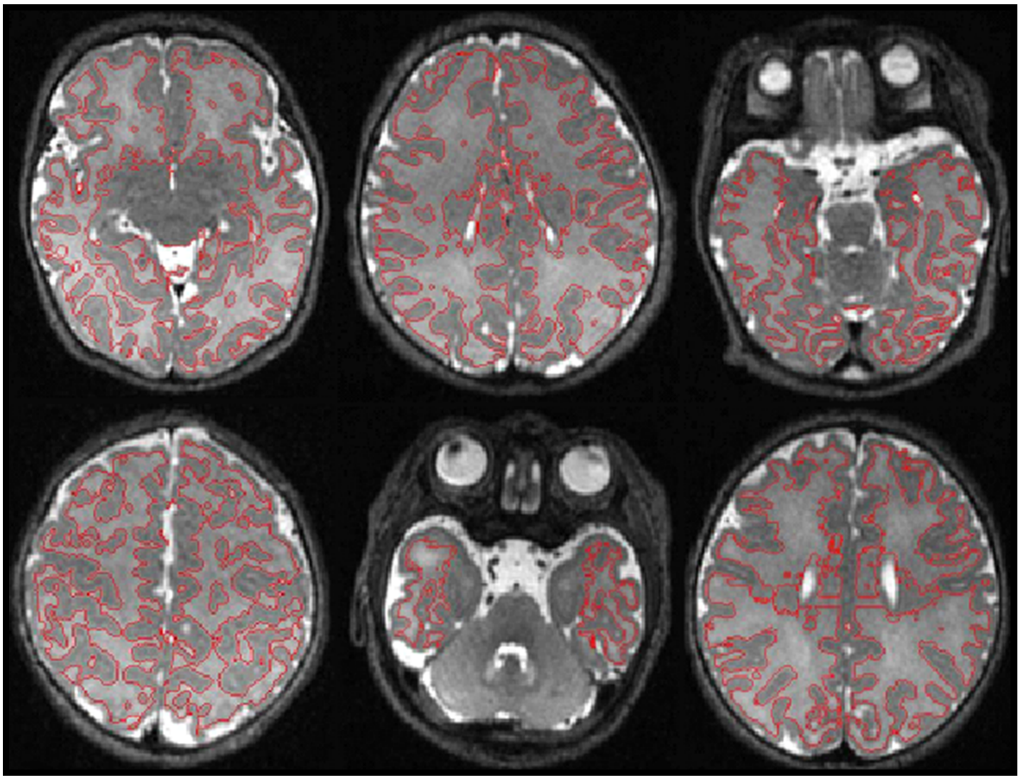

Figure 6.14: White matter segmentation results when applied to brain MRI for infants born at term.

The recent trend in the development of brain segmentation methods is to implement the registration, bias field and segmentation simultaneously using an EM technique. The aim of this is to improve the general performance. During our investigation, we demonstrated that by performing each segmentation step separately, the entire segmentation procedure can be more robust. This is especially the case when considering the issue of converging to local extrema. This assumption was evaluated by Murgasova [90], who developed an EM technique for the investigation of the brain growth during early childhood.

In the next section, an evaluation is presented which was performed on an independent database of healthy premature infant which were acquired using a 3T scanner.

6.3 3 Tesla Infant Data

Brain volume MRI of healthy premature infant have been provided by the Image Sciences Institute[2]. ISI stated that no brain abnormalities are visible and after a follow-up at 15 months, the brain shows a normal structure. The three datasets consist of healthy pre-

---

[2] available on the web page: www.neobrains12.isi.uu.nl (accessed 20/11/2013)

mature infants MR images which were scanned at 40 weeks age. All images were acquired using a 3 Tesla Philips scanner. The T2-weighted images (TR=6293; TE=120; FOV=180×180) have a thickness of $2mm$ and a resolution matrix of 0.35×0.35 mm^2. This datasets were acquired without any post-processing and the dicom format was transformed into mhd and raw format. The database contains the images of a total of three patients where each patient includes 50 images. The numerical evaluation was performed by the scientists of the Image Sciences Institute.

6.3.1 Evaluation

The manual segmentations used in this evaluation were generated by trained medical students at the Image Sciences Institute. The manual segmentations were independently verified by three neonatologists with each of them having at least seven years of experience in reading neonatal MRI scans. In their study, each voxel was assigned to only one of the nine tissue classes (cortical grey matter, deep grey matter, unmyelinated white matter, brain stem, cerebellum, ventricles, CSF, basal ganglia and thalami and myelinated white matter). Three MRI datasets were made available for the NeoBrainS12 challenge and the results are independently evaluated by the scientists from the Image Sciences Institute using the Dice Similarity Measurement (DSM) and a modified Hausdorff distance (MHD) (MHD)[32] (defined as the 95th-percentile Hausdorff distance).

The segmentation algorithm proposed in this thesis has returned precise and accurate results by indicating an average Dice Similarity Measurement of 83% for the white matter segmentation when applied to 3T data. This accuracy is in the same range with the DSM obtained for 1.5T MRI data used in the evaluation of this study (see Section 6.2.2)), which is 82.8%. Figure 6.15 illustrates some results that were obtained when the proposed algorithm was applied to 3T MRI data.

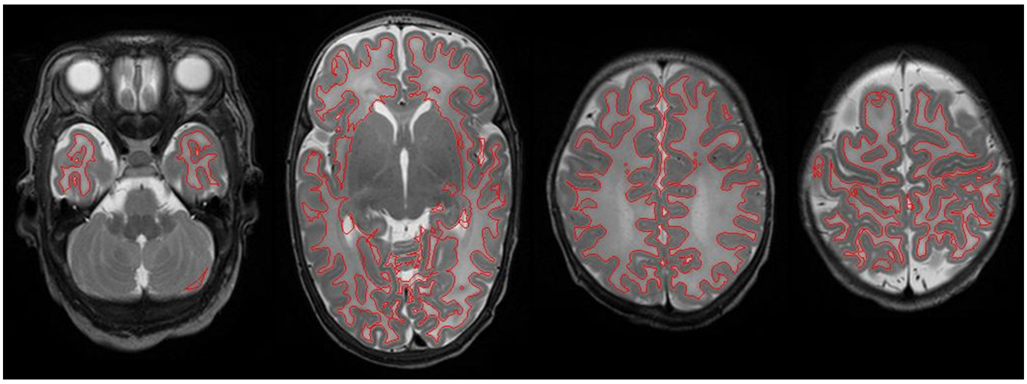

Figure 6.15: White matter segmentation results using 3T infant brain MRI data.

The aim of the NeoBrainS12 challenge was to compare different algorithms that are developed for infant brain segmentation. As mentioned before, this challenge addressed the segmentation of nine tissue types but in our study only the non-myelinated white matter was of interest. The following research teams developed brain tissue segmentation algorithms for the NeoBrainS12 challenge:

- The team from the University of Oxford developed an atlas-based segmentation method. This approach is based on the SPM software [116] and it is used in conjunction with a neonatal probabilistic atlas[3]. The initial segmentation results are further processed to extract the brainstem, the basal ganglia and the thalami using the intensity information in T1 and T2 images.
- FER-UMCU proposed an atlas-based segmentation algorithm which includes a supervised voxel classification. In order to generate the atlas, the authors manually segmented seven infant datasets which were provided by the NeoBrainS12 challenge for algorithm training. The data is initially pre-processed using the BET method [40] [112]], and then, during the supervised voxel classification process, the results were refined using morphological operations such as closing and dilation. This is followed by assigning each voxel to a tissue class by combining the atlas with the T1 and T2 intensity information using a kNN classifier.
- The team from Imperial College London proposed an EM-based segmentation approach for T2 infant MRI datasets. The MRI data is pre-processed using the BET algorithm and N4 method [122]], and the k-means is used to generate a subject-specific atlas. This atlas guides the EM segmentation procedure which embeds an MRF algorithm [30] to incorporate the spatial dependencies that are associated with each tissue.
- " The team from the University College London (UCL) proposed an extension on infant brain segmentation algorithm proposed by Cardoso et al. [31]]. This algorithm includes the segmentation of the myelinated white matter tissue and the separation of the ventricle from the overall CSF tissue. The algorithm consists of a MAP-EM based segmentation technique that includes bias field correction, MRF to model spatial dependencies and a step that deals with the PVE voxels. The relaxation strategy presented in the Cardoso et al. [31] was developed to guide the segmentation of infant MRI data with abnormal anatomical structure. This relaxation process was not included in the algorithm developed by the UCL team because the data made available by the NeoBrainS12 challenge did not include patients with pathologies.

---

[3] available at brain-development.org

- " The team from the University of Pennsylvania (UPenn) proposed an EM-based segmentation algorithm for infant brain MRI data. This algorithm initially applies a registration method which is available in the Advanced Normalization Tools (ANTs) [5]. The bias field correction is performed using the N4 algorithm. To segment the brain tissues, an EM algorithm which incorporates an MRF is applied with an atlas[4] that is used to guide the segmentation process.
- The team UMCU1 have not provided any information about their segmentation algorithm.

The average results obtained by all algorithms for white matter segmentation are presented in Table 6.3.

Team Name	WM DSM	WM MHD
Imperial	0.89	0.63
FER-UMCU*	0.91	0.40
Oxford	0.88	0.70
UCL	0.87	0.99
UPenn	0.85	1.68
UMCU1*	0.88	1.03
DCU	0.83	1.67

Table 6.3: Average white matter segmentation results for all algorithms that participate in the NeoBrainS12 challenge. The algorithms which are indicated by the Asterisk have used additional data provided by the NeoBrainS12 challenge.

The results shown in Table 6.3 were obtained when the algorithms were applied to three healthy infant MRI datasets. It is important to mention that the algorithms developed by FER-UMCU and UMCU1 were trained for this challenge using additional data that was provided by NeoBrainS12. This additional data was used to generate an atlas that was optimised for specific MRI data that is captured at the age of 40 weeks. Clearly, this testing environment is optimal for supervised segmentation algorithms since the anatomic differences between healthy patients are not significant and the use of atlases allow accurate modelling for PVE when dealing with diffuse contours. This observation is also suggested by the modification in the algorithm developed by the UCL team where the relaxation step as used by Cardoso et al. [31] was removed. The aim of this relaxation step in [31] is to reduce the false classifications in infant data that present abnormal anatomical structures. In the algorithm developed by the UCL team this step is removed to maximise the segmentation results when applied to healthy MRI infant data. The proposed algorithm described in this thesis was developed to identify the WM in MRI data

---

[4] available at brain-development.org

with and without pathologies.

The slightly lower DSM results obtained by the proposed algorithm may have been determined by the approach suggested by the clinical collaborators to deal with the classification of the PVE voxels that are positioned on diffuse contours. As mentioned before, the PVE which consists of voxels that are generated by more than one brain tissue type has an impact on the accuracy of brain segmentation methods. Since the MRI data made available for the NeoBrainS12 challenge was acquired using a 2mm thickness, this will enhance the presence of PVEs. Hence, there is a possibility that the evaluation of the PVE has been considered differently than in our study. Unfortunately, this assumption cannot be 100% validated since the segmentation results for the NeoBrainS12 challenge were processed by the researchers from the Image Sciences Institute and no ground truth data was made available to any group involved in the challenge.

Another important issue is that the age of the patients in the NeoBrainS12 data is 40 weeks. At this age the brain structure is better developed than the brain structure in the 1.5T data that was provided by our clinical collaborators from the Temple Street Childrens' Hospital. Although the testing environment using 3T MRI is different than the one used in the segmentation of the WM in 1.5T data, the results presented in Table 6.3 indicate that the algorithm described in this thesis is accurate. This is illustrated by the small MHD achieved by the proposed algorithm, which shows that it does not generate large errors. In addition, the DSM result is slightly lower than the DSM values obtained for other methods (differences are in the range of 2 to 6%).

While the proposed approach was developed for a pre-defined clinical study that analyses 1.5T MRI premature infant data, the tests on 3T MRI data further indicate that the proposed method achieves similar performance when applied unchanged to MRI neonatal data that is captured with a different acquisition protocol.

6.3.2 Discussion

The proposed white matter segmentation method has provided accurate results by processing the blurred contours between the white matter and the grey matter. Some examples that illustrate segmentation results are displayed in Figure 6.16.

Although the scanning parameters used for this preterm MRI data are different than the scanning parameters for 1.5T, the proposed approach produces precise segmentations without any modifications on the algorithm. Figure 6.16 displays segmentation results for the three tested patients where each row illustrates a different patient. It can be observed that the algorithm produced accurate results. As mentioned in Section 6.2.3, the

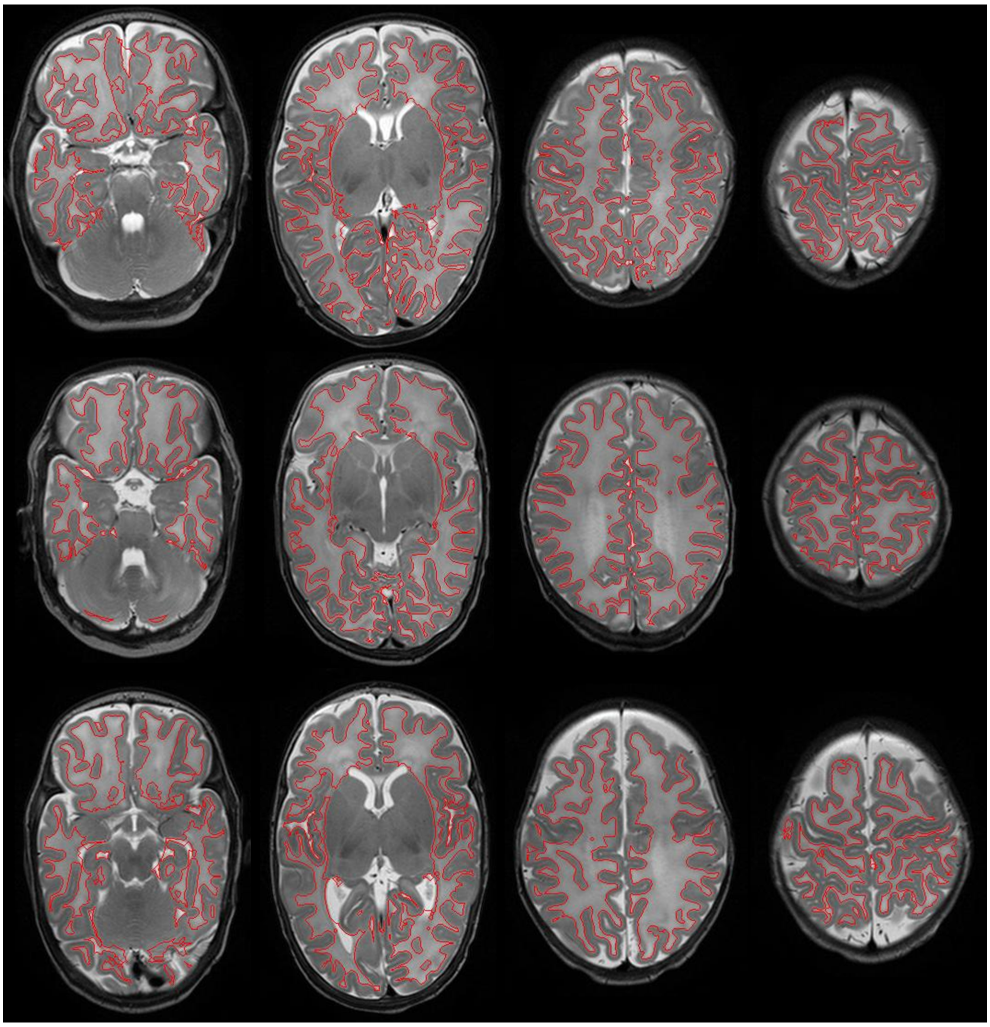

Figure 6.16: White matter segmentation results when the white matter segmentation method was applied to 3T infant brain MRI data provided by the Image Sciences Institute. Each row presents images of a different patient.

partial volume effect impacts on the accuracy of the brain segmentation methods. The 3T data has a thickness of $2mm$ which enhance the PVE. Nevertheless, the combination of 2D and 3D algorithms in the framework has provided accurate results when dealing with this issue.

A common problem in infant MRI segmentation is the strong variation of intensity values within the white matter and some developed methods [52] [31] return under-segmentation especially in regions close to the gyri. Similar to 1.5T data, the reclassification of the PVE and diffused contour voxels in the proposed algorithm returns precise segmentation without being negatively influenced by the inconsistent intensity values. Figure 6.17 illustrates a set of examples that demonstrate the accuracy of the segmentation results.

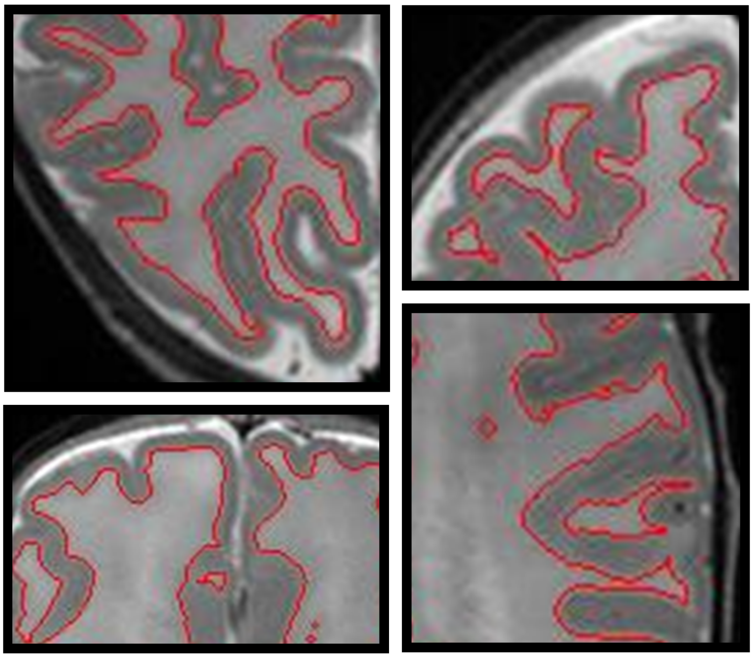

Figure 6.17: Four magnified examples of different segmentation results performed on 3T datasets, which illustrate that the regions surrounded by the gyri are precisely extracted.

Chapter 7

Conclusions and Future Work

The aim of this chapter is to highlight the principal contributions associated with this study and to provide conclusions in relation to the objectives of this research work. In the second section, the future work and its significance for this research is outlined and examined.

7.1 Contributions and Conclusions

This thesis has dealt with the difficulties which emerge during the segmentation of the white matter tissue in brain MRI data from premature infants. Brain segmentation during infancy is a challenging task due to the early stage of brain development. However, precise measurements of specific regions could provide an indicator for an early diagnosis of neurodevelopment impairment. An early diagnosis is of great advantage as an early therapy can improve the state of life significantly. The motivation for this study has raised from the challenge to automatically detect inconsistencies in young brain MRI without facing the issues associated with the manual segmentation. During the development of the proposed technique, a number of major and minor contributions emerged in the area of brain tissue segmentation, brain field correction, variations in the brain structure, and tissue intensity overlapping.

The major contribution of this thesis is the proposed approach to segment and measure the white matter volume in infant brain MRI. The synthesis of the contributions which are presented throughout this thesis (Chapters 3, 4 and 5), represents the maximisation of the white matter segmentation process. The proposed technique is based on intensity-based methods and combines 2D and 3D methods. The state-of-the-art review, presented in Chapter 2, reveals that the majority of the developed techniques are used for adult MRI brain segmentation and suffer from limitations when applied to infant data. These limitations are caused by the brain differences during various stages of development. The use of adult brain data has advantages because the patients are less likely to move during the acquisition as well as the larger head size results in a better image definition. The infant brain segmentation algorithms presented in Chapter 2 are mostly implemented using an EM algorithm and the detection is guided by an atlas. The EM technique has provided precise results in segmenting infant brain MRI and was, therefore, further investigated in this study.

Another important contribution of this thesis, presented in Chapter 3, is the novel brain extraction algorithm, which is composed of data pre-processing, mask generation, brain tissue segmentation and post-processing algorithms. The aim of the brain extraction algorithm is the removal of all non-brain tissues. Due to the fact that our proposed approach is built upon an intensity-based technique, this is essential to avoid misclassification. The proposed skull stripping method is not negatively influenced by intensity inhomogeneities, noise or unclear borders between the brain and non-brain tissue. The main reason is that the algorithm is composed of global processes for the broader extraction and local procedures to reduce the impact of artefact influence. The method does not rely on structure and shape differentiations between patients nor on knowledge about the field of view in which each patient was scanned in. A quantitative evaluation of the designed technique was performed and demonstrated the accuracy and efficiency in extracting the brain tissue when facing significant changes in the MR data.

The next major contribution, addressed in Chapter 4, deals with the intensity inconsistencies associated with the bias field that emerge from the inhomogeneity of the magnetic field during the MRI acquisition. The bias field corruption arises on a slice-by-slice basis and consequently the problem is addressed in the 2D domain. The main idea behind the bias field correction is to distinguish between the two brain tissues where the intensity ranges overlap. This classification issue was solved by segmenting the brain tissue, first into four classes followed by the reduction of those classes into two by using probabilistic calculations. This is important to minimise the influence of the partial volume effects and bias field corruption. A low pass filter emphasises the low frequency signal which allows the separation of the intensity inconsistencies from the image information. During the evaluation of the white matter segmentation, a limitation surfaced, which is given by the misclassification of the tissue on parts with extremely low contrast between the white matter and the grey matter. An evaluation of the designed method is performed and compared to state of the art techniques. The experimental results demonstrate that the intensity inconsistencies are corrected while maintaining the brain structure.

A minor contribution of this thesis is to reduce the influence of the partial volume effects (PVE). A partial volume voxel describes a data point whose intensity is generated by more than one tissue signal. The first time this issue is addressed is in Chapter 3 when creating a mask of the brain tissue which separates the brain tissue from the non-brain tissue. 3D based methods are used to create a volume of the brain including CSF and to reduce the PVE. The second time this issue occurs is during the voxel re-classification which finds the correct boundaries between the white matter and the grey matter. Using a voxel re-classification to classify the partial volume voxels into grey or white matter plays a significant role in minimising the influence of PVE.

A major contribution, presented in Chapter 5, is given by the development of the white matter segmentation technique. Diffuse contours and partial volume effects prevent a single EM algorithm to perform a successful segmentation. In order to improve the white matter segmentation, the EM algorithm is performed twice and each time based on different images. The combination of the two EM results emphasises the differences between the grey matter and the white matter. The generation of a pre-segmented white matter mask is used as a basis for a voxel re-classification which is performed to classify the voxels that lie on diffused contours.

Another contribution is given by the difficult detection of the cerebellum and the deep grey matter. This task is challenging due to the large intensity inconsistencies within these regions. In adult brains the deep grey matter is divided into three parts on each side due to the white matter tissue which runs through it. During infancy, the white matter is not distinguishable from the grey matter within these regions and is, therefore, detected as one region without the distinction of the white matter. However, the white matter tissue contained in these areas influences the appearance of these regions and due to the diffuse boundaries and large intensity changes on a pixel-by-pixel basis, the segmentation remains difficult. Given that the white matter segmentation framework is using intensity-based methods, this additional step is essential for precise and accurate white matter segmentation results.

An important objective of this work was to evaluate quantitatively and qualitatively the proposed white matter segmentation approach when comparing the results to manually segmented data. By testing a large database of preterm and at term born infants' brain MR images, the evaluation revealed that the proposed approach has overcome several challenges which can be listed as follows:

- **The brain extraction** algorithm has provided accurate results. After pre-processing the data, the influence of partial volume voxels and diffused contours is reduced by the generation of a brain mask. The removal of the non-brain tissue is important in order to facilitate the following procedures.

- **Diffused contours** were dealt with by the application of two EM methods, which reduced the ambiguous boundaries and an additional re-classification model was developed to guide the final segmentation.
- **Intensity overlapping** between tissues does not have an impact on the white matter segmentation results.
- **Artefacts** were reduced by the Coherence Enhancing Diffusion filter and the final results show no impact during the segmentation procedure.
- **Evaluation of the bias field correction** proved difficult because a gold standard does not exist. The evaluation of the segmentation approach revealed that the bias field correction algorithm has provided accurate results when correcting the bias field corruption.
- **Manually annotated data** can limit the evaluation process. It is a generally recognised problem that the manual marking is prone to errors due to low contrast structure and weak, missing or diffused boundaries.
- **Partial volume effects** indicated no influence on our approach and this issue was precisely addressed.
- **Structure and shape independence** is an advantage of the proposed approach because it segments infant brain data independent without the guidance of a predefined template. There is a high risk that the preterm infants suffer from large structure and shape abnormalities. This does not automatically mean ill health because the infants can develop normally. To avoid misclassification when guiding the segmentation process by an atlas, the proposed segmentation approach consists of enhancing the images and performing local voxel classifications.

In this study a fully automatic white matter segmentation technique is presented where the main focus is on the segmentation of premature infant brain MRI data. The approach has overcome challenges such as noise, intensity overlapping, bias field corruption and partial volume effects, and provided accurate results. The main focus in this study is the white matter segmentation of premature infant data. The method has also provided accurate results when applied to term-born infant MRI data.

The clinical experts from Temple Street Children Hospital, Dublin, have evaluated the accuracy of the white matter segmentation results and the current research is focused on the evaluation of the proposed segmentation when applied to a larger database.

7.2 Future Work

While the objectives of this study have been fully accomplished, some future work can be considered to advance the ideas in this research domain.

- Neurodevelopment impairment is caused by inconsistencies in the white matter region. One of the inconsistencies can appear in a lack of white matter tissue which is replaced by CSF. The diminishing of the volume does also affect the surrounding tissues. For this reason, an investigation on the volume measurement of the deep grey matter, the grey matter and the cerebrospinal fluid could be performed. The deep grey matter has been detected during the probabilistic segmentation algorithm and would need to be disconnected from the cerebellum. The grey matter could be extracted by subtracting the white matter from the brain tissue volume, however, small CSF parts might remain in this volume and would need to be detected.
- In order to avoid under-segmentation for infants with strong enlarged ventricles, the approach can be improved by generating two ellipses to detect the deep grey matter. Infants with strong enlarged ventricles usually include a strong dissimilarity between the right and left ventricles. The deep grey matter detection algorithm is based on the similarity between ventricles to extract the deep grey matter region by constructing one ellipse and it can result in under-segmentation. A solution is to fit two ellipses at each side of the deep grey matter, which will result in a more precise segmentation.
- An investigation into applying registration techniques to the data can open the application of the framework to other databases. So far the proposed approach has been evaluated on the 1.5T database provided by the collaborating clinicians and the 3T datasets provided by the Image Sciences Institute.

  On a second note, the case that a child could turn the head during the scanning process has not been considered because this problem has not occurred in our database. However, it is likely that this case can emerge and a registration technique would prevent any erroneous segmentation during the 3D procedures.
- A more comprehensive performance of the designed approach can be reached with a larger database of manually segmented data, which allows a larger qualitative evaluation. Secondly, it has been mentioned before that the process of manually marked data is prone to errors. For this reason, the evaluation could benefit from a second set of manually annotated datasets which are marked by a second clinical expert.

Bibliography

[1] M. N. Ahmed, S. M. Yamany, N. Mohamed, A. A. Farag, and T. Moriarty. A modified fuzzy c–means algorithm for bias field estimation and segmentation of MRI data. *IEEE Transactions on Medical Imaging*, 21(3):193–199, 2002.

[2] P. Aljabar, K. K. Bahatia, M. Murgasova, J. V. Hajnal, J. P. Broadman, L. Srinivasan, M. A. Rutherford, L. E. Dyet, A. D. Edwards, and D. Rueckert. Assessment of brain growth in early childhood using deformation–based morphometry. *NeuroImage*, 39(1):348–358, 2008.

[3] M. Altaye, S. K. Holland, M. Wilke, and C. Gaser. Infant brain probability templates for MRI segmentation and normalization. *NeuroImage*, 43(4):721–730, 2008.

[4] E. Angelini, Y. Jin, and A. Laine. *State of the Art of Level Set Methods in Segmentation and Registration of Medical Imaging Modalities*. Topics in Biomedical Engineering. International Book Series. Springer US, 2005.

[5] ANT. available at http://picsl.upenn.edu/software/ants/ (accessed 23/01/2014).

[6] J. Ashburner. *Computational Neuroanatomy – PhD thesis*. University College London, 2000.

[7] J. Ashburner and K. Friston. Multimodal image coregistration and partitioning – A unified framework. *NeuroImage*, 6(3):209–217, 1997.

[8] J. Ashburner and K. Friston. Voxel–Based Morphometry – The Methods. *NeuroImage*, 11(6):805–821, 2000.

[9] J. Ashburner and K. F. Friston. Unified segmentation. *NeuroImage*, 26(3):839–851, 2005.

[10] J. Ashburner and K. J. Friston. Comments and Controversis – Why Voxel–Based Morphometry Should Be Used. *NeuroImage*, 14(6):1238–1243, 2001.

[11] J. Ashburner, C. Hutton, R. Frackowiak, I. Jahnsrude, C. Price, and K. Friston. Identifying global anatomical differences deformation-based morphometry. *Human Brain Mapping*, 6:348–357, 1998.

[12] L. Axel, J. Costantini, and J. Listerud. Intensity Correction in Surface-Coil MR Imaging. *AJR American Journal of Roentgenology*, 148:418–420, 1987.

[13] K. O. Babalola, B. Patenaude, P. Aljabar, J. Schnabel, D. Kennedy, W. Crum, S.Smith, T. Cootes, M. Jenkinson, and D. Rueckert. An evaluation of four automatic methods of segmenting the subcortical structures in the brain. *NeuroImage*, 47(4):1435–1447, 2009.

[14] M. A. Balafar, A. R. Ramli, M. I. Saripan, and S. Mashohor. Review of brain MRI image segmentation methods. *Artificial Intelligent Review*, 33(3):261–274, 2010.

[15] A. G. R. Balan, A. J. M. Traina, M. X. Ribeiro, P. M. A. Marques, and C. Traina-Jr. Head: The Human Encephalon Automatic Delimiter. *Proceedings of the Twentieth IEEE International Symposium on Computer-Based Medical Systems, CBMS'07*, pages 171–176, 2007.

[16] G. Ball, J. Boardman, D. Rueckert, P. Aljabar, T. Arichi, N. Merchant, I. Gousias, A. Edwards, and S. Counsell. The Effect of Preterm Birth on Thalamic and Cortical Development. *Cerebral Cortex*, 22(5):1016–1024, 2012.

[17] W. A. Barret and E. N. Mortensen. Interactive Live–Wire Boundary Extraction. *Medical Image Analysis*, 1(4):331–341, 1997.

[18] M. Bax, M. Goldstein, P. Rosenbaum, A. Leviton, and N. Paneth. Proposed definition and classification of cerebral palsy. *Developmental Medicine and Child Neurology*, 47:571–576, 2005.

[19] P.-L. Bazin, J. Bogovic, D. Reich, J. L. Prince, and D. L. Pham. Belief Propagation Based Segmentation of White Matter Tracts in DTI. *Medical Image Computing and Computer-Assisted Intervention – MICCAI 2009, Lecture Notes in Computer Science (LNCS)*, 5761:943–950, 2009.

[20] B. Belaroussi, J. Milles, S. Carme, Y. M. Zhu, and H. Benoit-Cattin. Intenisty non-uniformity correction in MRI: Existing methods and their validation. *Medical Image Analysis*, 10(2):234–246, 2006.

[21] J. Boardman, C. Craven, S. Valappil, S. Counsell, L. Dyet, D. Rueckert, P. Aljabar, M. Rutherford, A. Chew, J. Allsop, F. Cowan, and A. Edwards. A common neonatal image phenotype predicts adverse neurodevelopmental outcome in children born preterm. *NeuroImage*, 52(2):409–414, 2010.

[22] R. Boer, H. A. Vrooman, F. v. d. Lijn, M. W. Vernooij, M. A. Ikram, A. v. d. Lugt, M. M. B. Breteler, and W. J. Niessen. White matter lesion extension to automatic brain tissue segmentation on MRI. *NeuroImage*, 45(4):1151–1161, 2009.

[23] K. Boesen, K. Rehm, K. Shaper, S. Stoltzner, E. Lueders, and D. Rottenberg. Quantitative comparison of four brain extraction algorithms. *NeuroImage*, 22(3):1255–1261, 2004.

[24] F. L. Bookstein. voxel–based morphometry should not be used with imperfectly registered images. *NeuroImage*, 14(6):1454–1462, 2001.

[25] B. Brinkmann, A. Manduca, and R. Robb. Optimized homomorphic unsharp masking for MR grayscale inhomogeneity correction. *IEEE Transactions on Medical Imaging*, 17(2):161–171, 1998.

[26] J. P. Broadman, K. Bhatia, S. Counsell, J. Allsop, O. Kapellou, M. A. Rutherford, A. D. Edwards, J. V. Hajnal, and D. Rueckert. An evaluation of deformation–based morphometry applied to the developing human brain and detection of volumetric changes associated with preterm birth. *Medical Image Computing and Computer-Assisted Intervention – MICCAI 2003, Lecture Notes in Computer Science (LNCS)*, 2878:697–704, 2003.

[27] J. P. Broadman, S. J. Counsell, D. Rueckert, O. Kapellou, K. K. Bahatia, P. Aljabar, J. V. Hajnal, J. M. Allsop, M. A. Rutherford, and A. D. Edwards. Abnormal deep grey matter development following preterm birth detected using deformation–based morphometry. *NeuroImage*, 32(1):70–78, 2006.

[28] M. Cabezas, A. Oliver, X. Llado, J. Freixenet, and M. Cuadra. A review of atlas-based segmentation for magnetic resonance brain images. *Computer Methods and Programs in Biomedicine*, 104(3):e158–e177, 2011.

[29] V. A. Cardenas, C. Studholme, S. Gazdzinski, T. C. Durazzo, and D. J. Meyerhoff. Deformation based morphometry of brain changes in alcohol dependence and abstinence. *NeuroImage*, 34(3):879–887, 2007.

[30] M. Cardoso, A. Melbourne, G. Kendall, M. Modat, C. Hagmann, N. Robertson, N. Marlow, and S. Ourselin. Adaptive neonate brain segmentation. *Medical Image Computing and Computer–Assisted Intervention - MICCAI 2011, Lecture Notes in Computer Science (LNCS)*, 6893:378–386, 2011.

[31] M. Cardoso, A. Melbourne, G. Kendall, M. Modat, N. Robertson, N. Marlow, and S. Ourselin. AdaPT: An adaptive preterm segmentation algorithm for neonatal brain mri. *NeuroImage*, 65:97–108, 2013.

[32] N. challenge. available at http://neobrains12.isi.uu.nl (accessed 24/01/2014).

[33] J. Chiverton, K. Wells, E. Lewis, C. Chen, B. Podda, and D. Johnson. Statistical morphological skull stripping of adult and infant MRI data. *Computers in Biology and Medicine*, 37(3):342–357, 2007.

[34] K.-S. Chuang, H.-L. Tzeng, S. Chen, J. Wu, and T.-J. Chen. Fuzzy c–means clustering with spatial information for image segmentation. *Computer Medical Imaging and Graphics*, 30(1):9–15, 2006.

[35] M. Cohen, R. DuBois, and M. Zeneih. Rapid and effective correction of RF inhomogeneity for high field magnetic resonance imaging. *Human Brain Mapping*, 10(4):204–211, 2000.

[36] J. Conklin, J. D. Winter, R. T. Thompson, and N. Gelman. High-Contrast 3D Neonatal Brain Imaging with Combined T1- and T2-Weighted MP-RAGE. *Magnetic Resonance in Medicine*, 59(5):1190–1196, 2008.

[37] T. Cootes, G. Edwards, and C. Taylor. Comparison Active Shape Models with Acitve Appearance Models. *In Proceedings of the British Machine Vision Conference, BMVC99*, 1:173–182, 1999.

[38] T. Cootes, G. Edwards, and C. Taylor. Active Appearance Models. *IEEE Transactions on Pattern and Machine Intelligence*, 23(6):681–685, 2001.

[39] T. Cootes and C. Taylor. Using grey-level models to improve active shape model search. *Proceedings of the International Conference on Pattern Recognition, IAPR 1994*, 1:63–67, 1994.

[40] W. R. Crum, D. Rueckert, M. Jenkinson, D. Kennedy, and S. M. Smith. A Framework for Detailed Objective Comparison of Non–rigid Registration Algorithms in Neuroimaging. *Medical Image Computing and Computer-Assisted Intervention – MICCAI 2004, Lecture Notes in Computer Science (LNCS)*, 3216:679–686, 2004.

[41] J. d. Lee, Y. x. Tseng, L. c. Liu, C. h. Huang, S. t. Lee, C. t. Wu, and J. f. Chen. A 2-D Automatic Segmentation Scheme for Brainstem and Cerebellum Regions in Brain MR Imaging. *Proceedings of the Fourth International Conference on Fuzzy Systems and Knowledge Discovery, FSKD 2007*, 4:270–274, 2007.

[42] I. Despotovic, E. Vansteenkiste, and W. Philips. Brain volume segmentation in newborn infants using multi-modal MRI with a low iinter-slice resolution. *Proceedings of the 2010 IEEE Annual International Conference of the Engineering in Medicine and Biology Scociety, EMBC 2010*, pages 5038–5041, 2010.

[43] A. Evans, D. Collins, S. Mills, E. Brown, R. Kelly, and T. Peters. 3d statistical neuroanatomical models from 305 MRI volumes. *Proceedings of the IEEE Nuclear Science Symposium and Medical Imaging Conference*, 3:1813–1817, 1993.

[44] A. X. Falcao and J. K. Udupa. Segmentation of 3D Objects using Live Wire. *Proceeding of the SPIE Conference on Image Processing for Medical Imaging*, 3034(1):228–235, 1997.

[45] A. Fitzgibbon and R. B. Fisher. A buyer's guide to conic fitting. In *In British Machine Vision Conference*, pages 513–522, 1995.

[46] K. J. Friston and W. Penny. Posterior probability maps and SPMs. *NeuroImage*, 19(3):1240–1249, 2003.

[47] R. Gonzales, R. Woods, and S.L.Eddins. *Digital Image Processing Using Matlab*. Pearson Education Inc., 2004.

[48] I. Gousias, A. Edwards, M. Ruthford, S. Counsell, and J. Hajnal. Magnetic resonance imaging of the newborn brain: Manual segmentation of labelled atlases in term-born and preterm infants. *NeuroImage*, 62:1499–1509, 2012.

[49] I. S. Gousias, A. Hammers, S. Counsell, A. D. Edwards, and D. Rueckert. Automatic Segmentation of Pediatric Brain MRIs using a Maximum Probability Pediatric Atlas. *Proceeding of the IEEE International Conference on Imaging Systems and Techniques (IST)*, pages 95–100, 2012.

[50] I. S. Gousias, D. Rueckert, R. A. Heckmann, L. E. Dyet, J. P. Broadman, A. D. Edwards, and A. Hammers. Automatic segmentation of brain MRIs of 2–year–olds into 83 regions of interest. *NeuroImage*, 40(2):672–684, 2008.

[51] W. E. L. Grimson, G. J. Ettinger, T. Kapur, M. E. Leventon, W. M. Wells, III, and R. Kikinis. Utilizing Segmented MRI Data in Image-Guided Surgery. *International Journal of Pattern Recognition and Artificial Intelligence (IJPRAI)*, 11(8):1367–1397, 1996.

[52] L. Gui, R. Lisowski, T. Faundez, P. Hüppi, F. Lazeyras, and M. Kocher. Morphology-driven automatic segmentation of MR images of the neonatal brain. *Magnetic Resonance Analysis*, 16:1565–1579, 2012.

[53] R. Guillemaud and M. Brady. Estimating the Bias Field of MR Images. *IEEE Transactions on Medical Imaging*, 16(3):238–251, 1997.

[54] H. K. Hahn, W. S. Millar, O. Klinghammer, M. S. Durkin, P. K. Tulipano, and H.-O. Peitgen. A reliable and efficient method for cerebral ventricular volumetry

in pediatric neuroimaging. *Methods of Information in Medicine*, 43(4):376–390, 2004.

[55] H. K. Hahn and H.-O. Peitgen. The Skull Stripping Problem in MRI Solved by a Single 3D Watershed Transform. *Medical Image Computing and Computer-Assisted Intervention – MICCAI 2000, Lecture Notes in Computer Science (LNCS)*, 1935:129–145, 2000.

[56] G. Hamarneh, J. Yang, C. McIntosh, and M. Langille. 3D live–wire–based semi–automatic segmentation of medical images. *Proceeding of the SPIE Conference on Image Processing for Medical Imaging*, 5747:1597–1603, 2005.

[57] R. Haralick and L. Shapiro. *Computer and Robot Vision*, volume 1. Addison-Wesley Publishing Company, Inc., 1992.

[58] H. R. Harnsberger, A. G. Osborn, J. Ross, and A. Macdonald. *Diagnostic and Surgical Imaging Anatomy: Brain, Head and Neck, Spine*. Amirsys Inc, 2006.

[59] L. He and N. Parikh. Automated detection of white matter signal abnormality using T2 relaxometry: Application to brain segmentation on term MRI in very preterm infants. *NeuroImage*, 64:328–340, 2013.

[60] A. Huang, R. Abugharbieh, and R. Tam. A Novel Rotationally Invariant Region-Based Hidden Markov Model for Efficient 3-D Image Segmentation. *IEEE Transactions on Medical Imaging*, 19(10):2737–2748, 2010.

[61] T. E. Inder, N. J. Anderson, C. Spencer, S. Wells, and J. J. Volpe. White Matter Injury in the Premature Infant: A Comparison between Serial Cranial Sonographic and MR Findings at Term. *AJNR - American Journal of Neuroradiology*, 24:805–809, 2003.

[62] T. E. Inder, S. Warfield, H. Wang, P. Huppi, and J. Volpe. Abnormal cerebral structure is present at term in premature infants. *Pediatrics*, 115(2):286–294, 2005.

[63] B. Jaehne and H. Haussecker. *Computer Vision and Applications – A guide for students and practitioners*. Academic Press, 2000.

[64] F. Jäger. *Normalization of Magnetic Resonance Images and its Application to the Diagnosis of the Scoliotic Spine – PhD thesis*. Technische Fakultät der Universität Erlangen Nürnberg, 2010.

[65] Z. Ji, Y. Xia, Q. Sun, Q. Chen, D. Xia, and D. D. Feng. Fuzzy Local Gaussian Mixure Model for Brain MR Image Segmentation. *IEEE Transactions on Information Technology in Biomedicine*, 16(3):339–347, 2012.

[66] S. R. Kannan, S. Ramathilagam, R. Devi, and E. Hines. Strong fuzzy c–means in medical image data analysis. *The Journal of Systems and Software*, page In Press, 2012.

[67] J. Kapur, P. K. Sahoo, and A. Wong. A new method for grey-level picture thresholding using the entropy of the histogram. *Computer Vision, Graphics, and Image Processing*, 29(3):273–285, 1985.

[68] M. Kass, A. Witkin, and D. Terzopoulos. Snakes: active contour models. *International Journal of Computer Vision*, 1(4):321–331, 1988.

[69] K. M. Kennedy, K. I. Erickson, K. M. Rodrigue, M. W. Voss, S. J. Colcombe, A. F. Kramer, J. D. Acker, and N. Raz. Age–related differences in regional brain volumes: A comparison of optimized voxel–based morphometry to manual volumetry. *Neurobiology of Aging*, 30(10):1657–1676, 2009.

[70] S. Kobashi, Y. Fujimoto, M. Ogawa, K. Ando, R. Ishikura, K. Kondo, S. Hirota, and Y. Hata. Fuzzy-ASM Based Automated Skull Stripping Method from Infantile Brain MR Images. *Proceedings of the IEEE International Conference on Granular Computing, GRC 2007*, 0:632–635, 2007.

[71] S. Koenig and J. Hesser. Live–Wires Using Path–Graphs. *Methods of Information in Medicine*, 43(4):371–375, 2004.

[72] S. Koenig and J. Hesser. 3D Live–Wires on Pre–Segmented Volume Data. *Proceeding of the SPIE Conference on Image Processing for Medical Imaging*, 5747:1674–1681, 2005.

[73] M. Kuklisova-Murgasova, P. Aljabar, L. Srinivasan, S. Counsell, V. Doria, A. Serag, I. Gousias, J. Boardman, M. Rutherford, A. Edwards, J. Hajnal, and D. Rueckert. A dynamic 4d probabilistic atlas of the developing brain. *NeuroImage*, 54(4):2750 – 2763, 2011.

[74] S.-H. Lai and M. Fang. A dual image approach for bias field correction in magnetic resonance imaging. *Magnetic Resonance Imaging*, 21(2):121–125, 2003.

[75] J.-M. Lee, U. Yoon, S. H. Nam, J.-H. Kim, I.-Y. Kim, and S. I. Kim. Evaluation of automated and semi–automated skull–stripping algorithms using similarity index and segmentation error. *Computers in Biology and Medecine*, 33(6):495–507, 2003.

[76] K. V. Leemput, F. Maes, D. Vandermeulen, and P. Suetens. Automated Model-Based Bias Field Correction of MR Images of the Brain. *IEEE Transactions on Medical Imaging*, 18(10):885–896, 1999.

[77] K. V. Leemput, F. Maes, D. Vandermeulen, and P. Suetens. Automatic model-based tissue classification on MR images of the brain. *IEEE Transactions on Medical Imaging*, 18(10):897–908, 1999.

[78] X. Li, L. CI, R. Wang, and J. Li. A Region Growing Method Based on Fuzzy Connectedness. *Proceedings of the International Conference on Audio, Language and Image Processing, ICALIP 2008*, pages 993–997, 2008.

[79] K. Lim and A. Pfefferbaum. Segmentation of mr brain images into cerebrospnal fluid spaces, white and gray matter. *Journal of Computer Assistes Tomography*, 13(4):588–593, 1974.

[80] J. Liu, J. K. Udupa, P. K. Saha, D. Odhner, B. E. Hirsch, and S. Siegler. Model–based 3D segmentation of the bones of the ankle and subtalar joints in MR images. *Proceeding of the SPIE Conference on Image Processing for Medical Imaging*, 5032:1650–1657, 2003.

[81] X. Llado, A. Oliver, M. Cabezas, J. Freixenet, J. C. Vilanova, A. Quiles, L. V. adn L. Ramiio-Torrenta, and A. Rovira. Segmentation of multiple sclerosis lesions in brain MRI: A review of automated approaches. *Information Sciences*, 186(1):164–185, 2012.

[82] D. Mahapatra. Skull Stripping of Neonatal Brain MRI: Using Prior Shape Information with Graph Cuts. *Journal of Digital Imaging*, pages 1–13, 2012.

[83] J.-F. Mangin. Entropy minimization for automatic correction of intensity nonuniformity. *Proceedings of the IEEE Workshop on Mathematical Methods in Biomedical Image Analysis, 2000*, pages 162–169, 2000.

[84] N. Marlow, D. Wolke, M. A. Bracewell, and M. S. for the EPICure Study Group. Neurologic and Developmental Disability at Six Years of Age after Extremely Preterm Birth. *The New England Journal of Medicine*, 352(1):9–19, 2005.

[85] D. Marr and E. Hildreth. Theory of edge detection. *Proceedings of Royal Society of London, Biological Sciences*, 207(1167):187–217, 1980.

[86] A. M. Mathur, J. J. Neil, and T. E. Inder. Understanding Brain Injury and Neurodevelopment Disabilities in the Premature Infant: The Evolving Role of Advanced Magnetic Resonance Imagine. *Seminar in Perinatology*, 34(1):57–66, 2010.

[87] J. Mazziotta, A. Toga, A. Evans, P. Fox, J. Lancaster, K. Zilles, R. Woods, T. Paus, G. Simpson, B. Pike, C. Holmes, L. Collins, P. Thompson, D. MacDonald, M. Iacoboni, T. Schormann, K. Amunts, N. Palomero-Gallagher, S. Geyer, L. Parsons, K. Narr, N. Kabani, G. L. Goualher, D. Boomsma, T. Cannon, R. Kawashima, and

B. Mazoyer. A probabilistic atlas and reference system for the human brain: International Consortium for Brain Mapping (ICBM). *Philosophical Transactions of the Royal Society of London. Series B: Biological Sciences*, 356(1412):1293–1322, 2001.

[88] C. McIntosh and G. Hamarneh. Medial-Based Deformable Models in Nonconvex Shape-Spaces for Medical Image Segmentation. *IEEE Transactions on Medical Imaging*, 31(1):33–50, 2012.

[89] H. Merisaari, R. Parkkola, E. Alhoniemi, M. Teras, L. Lehtonen, L. Haataja, H. Lapinleimu, and O. S. Nevalainen. Gaussian mixture model–based segmentation of MR images taken from premature infants brains. *Journal of Neuroscience Methods*, 182(1):110–122, 2009.

[90] M. Murgasova. *Segementation of brain MRI during early childhood – PhD thesis*. Imperial College London, 2008.

[91] M. Murgasova, L. Dyet, D. Edwards, M. Rutherford, J. V. Hajnal, and D. Rueckert. Segmentation of Brain MRI in Young Children. *Medical Image Computing and Computer-Assisted Intervention – MICCAI 2006, Lecture Notes in Computer Science (LNCS)*, 4190:687–694, 2006.

[92] N. Otsu. A Threshold Selection Method form Gray-Level Histogram. *IEEE Transactions on Systems, Man, and Cybernetics*, SMC-9(1):62–66, 1979.

[93] P. Perona and J.Malik. Scale-Spacing and Edge Detection Using Anisotropic Diffusion. *IEEE Transactions on Pattern Analysis and Machine Intelligence*, 12(7):629–639, 1990.

[94] R. Pohle and K. D. Toennies. Segmentation of medical images using adaptive region growing. *Proceeding of the SPIE Conference on Image Processing for Medical Imaging*, 4322:1337–1346, 2001.

[95] M. Prastawa, J. H. Gilmore, W. Lin, and G. Gerig. Automatic segmentation of MR image of the developing newborn brain. *Medical Image Analysis*, 9(5):457–466, 2005.

[96] K. Rademaker, C. Uiterwaal, F. Beek, I. C. van Haastert, A. Lieftink, F. Groenendaal, D. Grobbee, and L. S. de Vries. Neonatal cranial ultrasound versus mri and neurodevelopmental outcome at school age in children born preterm. *Archives of Disease in Childhood: Fetal and Neonatal*, 90(6):489–493, 2005.

[97] S. Rajagopalan, R. A. Karwoski, and R. Robb. Robust Fast Automatic Skull Stripping of MRI-T2 Data. *Proceeding of the SPIE Conference on Image Processing for Medical Imaging*, 5747:485–495, 2005.

[98] K. Rehm, K. Schaper, J. Anderson, and R. Woods. Putting our heads together: a consensus approach to brain/non–brian segmentation in T1–weighted MR volumes. *NeuroImage*, 22(3):1262–1270, 2004.

[99] C. Rorden and M. Brett. Stereotaxic display of brain lessions. *Behavioural Neurology*, 12(4):191–200, 2000.

[100] D. Rueckert, L. I. Sonoda, C. Hayes, D. L. G. Hill, M. O. Leach, and D. J. Hawkes. Nonrigid Registration using Free–Form Deformations: Application to Breast MR Images. *IEEE Transactions on Medical Imaging*, 18(8):712–721, 1999.

[101] S. A. Sadananthan, W. Zheng, M. W. Chee, and V. Zagorodnov. Skull stripping using graph cuts. *NeuroImage*, 49(1):225–239, 2010.

[102] N. Saeed and B. Puri. Cerebellum segmentation employing texture properties and knowledge based image processing: applied to normal adult controls and patients. *Magnetic Resonance Imaging*, 20:425–429, 2002.

[103] S. Saha, S. K. Das, and A. Kar. A New Segmentation Technique for Brain and Head from Hight Resolution MR Image Using Unique Histogram Features. *Proceedings of the Second International Conference on Image Processing Theory Tools and Aplications, IPTA*, pages 288–293, 2010.

[104] O. Salvado, C. Hillenbrand, S. Zhang, and D. Wilson. Method to correct intensity inhomogeneity in MR images for atherosclerosis characterization. *IEEE Transactions on Medical Imaging*, 25(5):539–552, 2006.

[105] F. Segonne, A. M. Dale, E. Busa, M. Glessner, D. Salat, H. K. Hahn, and B. Fischl. A hybrid approach to the skull stripping problem in MRI. *NeuroImage*, 22(3):1060–1075, 2004.

[106] Z. Y. Shan, G. H. Yue, and J. Z. Liu. Automated Histogram–Based Brain Segmentation in T1–Weighted Three–Dimensional Magnetic Resonance Head images. *NeuroImage*, 17(3):1587–1598, 2002.

[107] K. Shanthi and M. Sasi Kumar. Skull stripping and automatic segmentation of brain MRI using seed growth and threshold techniques. *Proceedings of the International Conference on Intelligent and Advanced Systems, ICIAS 2007.*, pages 422–426, 2007.

[108] D. W. Shattuck and R. M. Leathy. BrainSuite: An automated cortical surface identification tool. *Medical Image Analysis*, 6(2):129–142, June 2002.

[109] D. W. Shattuck, S. R. Sandor-Leathy, K. A. Shaper, D. A. Rottenberg, and R. M. Leathy. Magnetic Resonance Image Tissue Classification Using a Partial Volume Model. *NeuroImage*, 13(5):856–876, 2001.

[110] F. Shi, P.-T. Yap, J. H. Gilmore, W. Lin, and D. Shen. Neonatal brain MRI segmentation by building multi-region-multi-reference atlases. *Proceedings of the 2010 IEEE International Symposium on Biomedical Imaging: From Nano to Macro, ISBI'10*, pages 964–967, 2010.

[111] J. Sled, A. Zijdenbos, and A. Evans. A nonparametric method for automatic correction of intensity nonuniformity in MRI data. *IEEE Transactions on Medical Imaging*, 17(1):87–97, 1998.

[112] S. Smith, M. Jenkinson, M. Woolrich, C. Beckmann, T. Behrens, H. Johansen-Berg, P. Bannister, M. D. Luca, I. Drobnjak, D. Flitney, R. Niazy, J. Saunders, J. Vickers, Y. Zhang, N. D. Stefano, J. Brady, and P. Matthews. Advances in functional and structural MR image analysis and implementation as FSL. *NeuroImage*, 23(1):S208–S219, 2004.

[113] S. M. Smith. Fast robust automated brain extraction. *Human Brain Mapping*, 17(3):143–155, 2002.

[114] K. Somasundarm and T. Kalaiselvi. Brain Extraction Method for T1-weighted Magnetic Resonance Scans. *Proceedings of the International Conference on Signal Processing and Communications, SPCOM*, pages 1–5, 2010.

[115] K. Somasundarm and P. Kalavathi. A Hybrid Method for Automatic Sull Stripping of Magnetic Resonance Images (MRI) of Human Head Scans. *Proceedings of the International Conference on Computing Communication and Networking Technologies, ICCCNT'10*, pages 1–5, 2010.

[116] SPM8. This software is available at the web adress: http://www.fil.ion.ucl.ac.uk/spm/ (accessed 08/09/2010).

[117] E. Stindel, J. K. Udupa, B. E. Hirsch, D. Odhner, and C. Couture. 3D MR image analysis of the morphology of the rear foot: application to classification of bones. *Computerized Medical Imaging and Graphics*, 23(2):75–83, 1999.

[118] J. S. Suri, S. Singh, and L. Reden. Computer Vision and Pattern Recognition Techniques for 2-D and 3-D MR Cerebral Cortical Segmentation (Part I): A State-of-the-Art Review. *Pattern Analysis and Applications*, 5(1):46–76, 2002.

[119] J. Talairach and P. Tournoux. *Co-planar stereotaxic atlas of the human brain*. Thieme, New York, 1988.

[120] A. Top, G. Hamarneh, and R. Abugharbieh. Spotlight: Automated Confidence-based User Guidance for Increasing Efficiency in Interactive 3D Image Segmentation. *Medical Image Computing and Computer-Assisted Intervention Workshop on Medical Computer Vision – MICCAI MCV 2010, Lecture Notes in Computer Science (LNCS)*, pages 204–213, 2010.

[121] A. Top, G. Hamarneh, and R. Abugharbieh. Active Learning for Interactive 3D Image Segmentation. *Medical Image Computing and Computer-Assisted Intervention – MICCAI 2011, Lecture Notes in Computer Science (LNCS)*, 6893:603–610, 2011.

[122] N. Tustison, B. Avants, P. Cook, Y. Zhang, A. Egan, P. Yushkevich, and J. Gee. N4itk: improved N3 bias correction. *IEEE Transactions on Medical Imaging*, (29):1310–1320, 2010.

[123] A. Viterbi and J. Omura. Trellis encoding of memoryless discrete-time sources with a fidelity criterion. *IEEE Transactions on Information Theory*, 20(3):325–332, 1974.

[124] U. Vovk, F. Pernus, and B. Likar. A Review of Methods for Correction of Intensity Inhomogeneity in MRI. *IEEE Transactions on Medical Imaging*, 26(3):405–421, 2007.

[125] I. W. M. Wells. Adaptive segmmentation of MRI data. *IEEE Transactions on Medical Imaging*, 15(4):429–442, 1996.

[126] L. Wang, F. Shi, P.-T. Yap, J. Gilmore, W. Lin, and D. Shen. Accurate and Consistent 4D Segmentation of Serial Infant Brain MR Images. *Multimodal Brain Image Analysis, Lecture Notes in Computer Science (LNCS)*, 7012:93–101, 2011.

[127] J. Weickert. A review of nonlinear diffusion filtering. *Scale-Space Theory in Computer Vision, , Lecture Notes in Computer Science (LNCS)*, 1252:1–28, 1997.

[128] J. Weickert. Coherence–Enhancing Diffusion Filtering. *Internation Journal of Computer Vision*, 31(2):111–127, 1999.

[129] W. Wieclawek and E. Pietka. Live-Wire-Based 3D Segmentation Method. *Proceedings of the 29th Annual International Conference of the IEEE Engineering in Medicine and Biology Society, EMBS 2007.*, pages 5645–5648, 2007.

[130] L. J. Woodward, P. J. Anderson, N. C. Austin, K. Howard, and T. E. Inder. Neonatal MRI to Predict Neurodevelopmental Outcomes in Preterm Infants. *The New England Journal of Medicine*, 355:685–694, 2006.

[131] X. Xie and M. Mirmehdi. MAC: Magnetostatic Active Contour Model. *IEEE Transactions on Pattern and Machine Intelligence*, 30(4):632–647, 2008.

[132] H. Xue, L. Srinivasan, S. Jiang, M. Rutherford, D. A. Edwards, D. Rueckert, and J. V. Hajnal. Automatic segmentation and reconstruction of the cortex from neonatal MRI. *NeuroImage*, 38(3):461–477, 2007.

[133] C. Yunjie, Z. Jianwei, and W. Shunfeng. A new fast brain skull stripping method. *Proceedings of the Second International Conference on Biomedical Engineering and Informatics, BMEI 2009*, page 5, 2009.

[134] W. Zhao, M. Xie, J. Gao, and T. Li. A Modified Skull-Stripping Method Based on Morphological Processing. *Proceedings of the Second International Conference on Computer Modeling and Simulation, ICCMS 2010*, 1:159–163, 2010.

Appendix A

State-of-the-Art Brain Extraction Comparison Methods

A.1 Comparison Methods

Finding the right tools for a numerical comparison is difficult. The term skull-stripping is by definition the removal of the non-brain tissue. But a precise definition on which parts have to be removed does not exist. In our case, the cortical grey matter, white matter, deep grey matter and cerebellum will be retained after skull stripping. Some brain extraction techniques also remove the cerebellum, other techniques leave the CSF in the RoI. Each existing skull-stripping approach has been developed for a specific medical task, therefore it is very difficult to do a precise evaluation. In our case, we use several well-established state-of-the-art approaches because they were used for comparison in many other studies.

Brain Surface Extraction (BSE) [109], Brain Extraction Tool (BET) [40] [112] and Statistical Parametric Mapping (SPM) [116], are brain segmentation tools available on the internet. The BSE and BET methods have been described in detail in Section 3.1 and the SPM approach was introduced in Section 2.4. BSE has been designed to process T1-weighted MRI, whereas, BET and SPM have been developed for T1 and T2-weighted MRI data. During this investigation, each tool was tuned to achieve the best of their performance when applied to our database. For each software, we had to convert the Dicom database into a Neuroimaging Informatics Technology Initiative (NIfTI-1) format[1].

MRIConvert_2.0 [2] is a medical image file converter tool that converts DICOM files to NIfTI 1.1. NIfTI format is generally recognized with the file ending .nii or a combination of .hdr/.img. The "hdr" file called header includes all valuable information about

---

[1] Additional information about the NIfTI format can be found at http://nifti.nimh.nih.gov/nifti-1/ (accessed 01/09/2010)

[2] available on the web page: http://lcni.uoregon.edu/ jolinda/MRIConvert (accessed 01/09/2010)

images and the "img" file contains the image data. NIfTI was developed by the community of neuroscientists and by the community of developers of informatics tools in order to facilitate the analysis of neuroimaging data and is not an official format. NIfTI-1 can store image data from any imaging modality such as Positron Emission Tomography (PET), MRI, Computed Tomography (CT) and Electroencephalography (EEG).

A.1.1 Brain Surface Extraction

BSE is embedded in the segmentation tool BrainSuite [108], which is a magnetic resonance image analysis tool designed for the identification of tissue types and surfaces in brain MR images. BrainSuite was specifically developed for cortical surface extraction. The software is easy to install and includes a user friendly interface, which was implemented in C++ to allow a fast brain extraction process.

The BSE algorithm functions in a stepwise manner that allows the user to adjust its parameters, which include: diffusion iterations, diffusion constant, edge constant and erosion size. Additionally, the user has the option to add the removal of the neck, brainstem and to dilate the final mask. The only parameter we needed to adjust was the size of the structuring element employed by the erosion algorithm in the final step. A negative aspect of BrainSuite is that we needed to restart the application for each patient data.

A.1.2 Brain Extraction Tool

MRIcroN [99] applies BET (version 1) and FSL [40] [112] applies BET2 (version 2)[3]. MRIcroN is a simple and user friendly tool for medical image analysis, which can be used to create 2D or 3D renderings of statistical overlay maps on brain anatomy images.

FSL runs in a Linux, Mac OS and Windows environment, but with the addition that Windows users have to install a virtualisation platform called VMware Player[4] before installing the FSL Library. FSL is implemented in C++ and provides a fast segmentation.

The best results for both tools have been returned using their default values with a fractional intensity threshold of 0.5. Changing the fractional intensity threshold from its default value of 0.5 will change the overall segmented brain region. If the threshold is smaller than 0.5, the segmented area will become larger. In case the threshold is larger than 0.5, the segmented area will become smaller. This threshold always take values within the range 0 and 1.

---

[3] a detailed description on the newest version of BET used in FSL including the differences to the previous version of BET is available at http://www.fmrib.ox.ac.uk/analysis/research/bet/bet2.pdf (accessed 06/09/2010)

[4] is available at http://www.vmware.com/products/player/ (accessed 02/09/2010)

A.1.3 SPM8

The well-established state of the art tool SPM was applied to our database. Experimentally, we modified the SPM parameters and the best results were obtained by adjusting the bias regularisation to a value of 0.1 and using the native space for the generation of GM, WM and CSF. SPM extracts three regions (GM, WM and CSF) and for each region a volume is generated. In the numerical evaluation, the resulting volumes of GM and WM were combined into one volume and compared against our automatically segmented results.

A.2 Results

We performed a quantitative evaluation of four state-of-the-art methods. This investigation was been carried out to provide comparative results with other algorithms that have been developed for infant MRI brain segmentation [33] [82]. Chiverton et al. [33] employed BET on their 3T MRI database which consists of T1 and T2 datasets. Mahaparta et al. [82] utilised BET and BSE on their 3T MRI database which was as well built upon T1 and T2 datasets. In the case of SPM, the segmented volumes of GM and WM were merged together before measuring the similarity rate. For this evaluation the numerical results have been calculated between the automatically segmented and manually segmented data using five datasets of our database. The evaluation techniques (Dice Similarity Measurement (DSM), False Positive (FP) and the False Negative (FN)) which are applied in these experiments, are described in Section 3.7.1. All results are shown in Table A.1 and the best results are highlighted in bold.

The quantitative results presented in Table A.1 indicate that the methods discussed in the previous section return less accurate results when applied to the skull stripping of brain MRI data of premature infants than the proposed brain extraction algorithm. It has to be clarified that BSE and BET are based on a different definition of skull stripping than the proposed method. In this study, the CSF has been associated as non-brain tissue, whereas, in BSE and BET the CSF was included in the brain tissue which has to be considered when examining the results. The strong false positive rate is an indication for this which is caused by the CSF which is retained in the volume. As mentioned before when regarding SPM, only the results of GM and WM were considered for this evaluation.

Table A.2 reveals the accuracy of each analysed technique in comparison with other brain extraction methods by observing the average results of all the tests. In this experiment, the proposed technique provided the overall best results in the dice similarity, as illustrated in Table A.2. The BET algorithm indicates a low false negative rate but on the other hand, the false positive rate illustrates a high over-segmentation level, which can be explained by the CSF tissue that is included in the brain tissue volume. When

Table A.1: Quantitative performance evaluation for four state-of-the-art implementations. Best results are highlighted in bold

	Methodology	**DSM**	**FP(%)**	**FN(%)**
Patient 1	Proposed method	**0.9609**	**2.14**	5.56
	BET2	0.8800	26.86	**0.31**
	BSE	0.9065	18.29	1.93
	BET	0.7840	38.35	10.78
	SPM	0.9076	16.14	3.50
Patient 2	Proposed method	**0.9656**	3.05	3.81
	BET2	0.8793	26.51	**0.74**
	BSE	0.9029	**1.06**	16.83
	BET	0.8547	30.79	2.39
	SPM	0.9187	12.59	4.33
Patient 3	Proposed method	**0.9602**	**3.01**	4.88
	BET2	0.8838	26.21	**0.16**
	BSE	0.7437	24.60	26.23
	BET	0.7097	45.01	20.23
	SPM	0.8386	27.65	7.83
Patient 4	Proposed method	**0.9525**	5.32	4.22
	BET2	0.8586	32.90	**0.03**
	BSE	0.9044	**0.34**	17.17
	BET	0.8144	38.37	49.45
	SPM	0.8733	27.89	0.86
Patient 5	Proposed method	**0.9603**	**3.50**	4.41
	BET2	0.8955	22.49	**0.69**
	BSE	0.9262	12.62	2.86
	BET	0.8714	25.27	3.28
	SPM	0.8529	15.57	14.06

comparing the two BET results, the newer version provides more accurate results. SPM tends to include non-brain tissue into the brain volume as illustrated in Figure A.1. One reason for this is that the voxel-based morphometry registers an adult brain template to the data. As mentioned in Chapter 2, the registration of adult templates on infant data cause erroneous segmentation.

Every approach has its strength and limitations, which is reflected in the experimental values shown in Table A.1 and Table A.2. Figure A.1 illustrates the results obtained by the different algorithms. Image (A) presents the original image, which is followed by the results for BET2 (B), BSE (C), BET (D), SPM (E) and the outcome of the proposed approach (F). It can be observed that each tool returns some of the CSF after brain extraction except the proposed technique. The experimental results indicate large over-segmentations by including non-brain parts in the brain volume. The outcome of the BSE reveals that the technique does not find the correct contours between brain tissue and non-brain tissue, which results in under-segmentation.

Table A.2: Average values obtained for the entire database.

Methodology	**DSM**	**FP(%)**	**FN(%)**
Proposed method	**0.9599**	**3.40**	4.58
BET2	0.8794	26.99	**0.39**
BSE	0.8767	11.38	13.01
BET	0.8068	35.55	17.23
SPM	0.8782	19.97	6.12

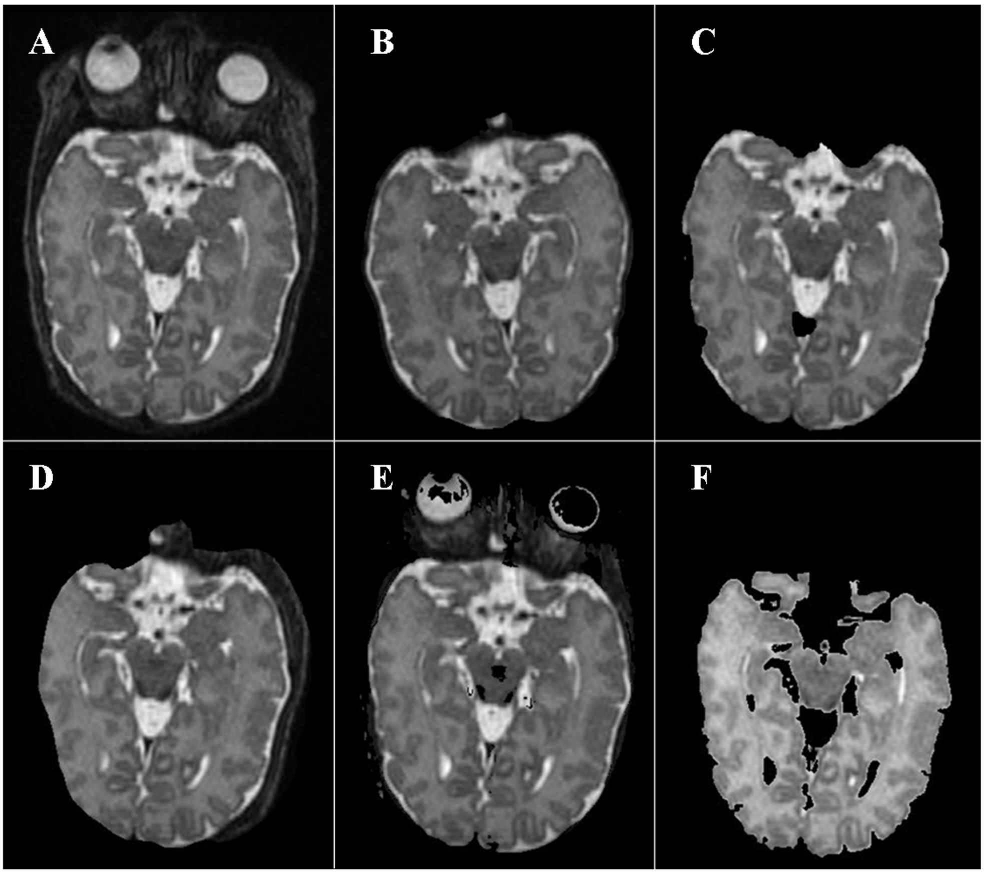

Figure A.1: Results obtained for all brain extraction tools. Image (A) presents the original image, which is followed by the brain segmentation results BET2 (B), BSE (C), BET (D), SPM (E) and the outcome of the proposed approach (F).